

THÈSE

En vue de l'obtention du

DOCTORAT DE L'UNIVERSITÉ DE TOULOUSE

Délivré par :

Institut National Polytechnique de Toulouse (INP Toulouse)

Discipline ou spécialité :

Dynamique des fluides

Présentée et soutenue par :

M. IGNACIO MAYO YAGUE

le vendredi 28 juillet 2017

Titre :

Flow field and heat transfer in a rotating rib-roughened cooling passage

---

Ecole doctorale :

Mécanique, Energétique, Génie civil, Procédés (MEGeP)

Unité de recherche :

Centre Européen de Recherche et Formation Avancées en Calcul Scientifique (CERFACS)

Directeurs de Thèse :

M. LAURENT GICQUEL

M. TONY ARTS

Rapporteurs :

M. LUCA CASARSA, UNIVERSITE D'UDINE

Mme EVA DORIGNAC, UNIVERSITE DE POITIERS

Membres du jury :

M. ROQUE CORRAL, UNIVERSIDAD POLITECNICA DE MADRID, Président

M. BERNHARD WEIGAND, UNIVERSITAT STUTTGART, Membre

Man belongs wherever he wants to go

Wernher von Braun (1912-1977)

Acknowledgments

The result of the work that I have carried out during the last years, including this manuscript, is a combination of the support, advices, experiences and lessons learnt from the people that have been near me. It is difficult to mention the name of every single person that has helped me in this task and contributed to the present work, but I would like to thank everyone who has shared my experiences during these years, inside the workplace as well as outside.

The main supporter of this PhD has been my supervisor, professor and colleague Tony Arts. Since the moment he gave me the opportunity to join the VKI, he has always been an example to make the best of ourselves, to examine in contrast our work and to bring quality above quantity. His door has been always open to listen to everyone, to review, to debate and to bring new ideas. His contribution to this work has been enormous also by bringing the resources needed to continue the pure research, sharing his knowledge and giving countless advices.

My supervisor Laurent Gicquel is the godfather of the present thesis. He has provided me the link to the University of Toulouse and he has given a quick and efficient response whenever I needed help. The discussions on the phone, by email or in person about the CFD aspects of this work and the results have brought always a light bulb moment.

I met great individuals under the roof of the VKI that gave me innumerable unforgettable days. Filippo Coletti is the spark that ignited my willingness to carry out a PhD in the RC-1, he introduced me into the world of experimental fluid dynamics and he taught me the fundamental laboratory survival skills. Also, that the best way to research, learning and creating is to do it with passion. My friend Daisaku Sakaguchi, office mate for a year, has been the example of the hard work, politeness and kindness. In fact, the computer employed to carry out the LES simulations of this thesis used to be his own PC. My laboratory comrades Irene Cresci, Jan Michálek, Can Tümer, Julien Clinckemaillie, Ahmed El-Habib, Benjamin Parres, Lorenzo Ceccherini, Onur Cildir, Özge Ateş, Alessio Pappa, Marco Virgilio, Bogdan Cernat, Koray Sevinç and Dimitra Tsakmakidou have brought me back the feelings that I used to have when I was a kid in the playground, or a teenager playing videogames with friends. It has been a great experience to work together, to learn from them, to interchange ideas and, of course, to talk about life.

Two outstanding scientists, Gian Luca Gori and Aude Lahalle, have left large and deep footprints in this PhD. I had the chance to be at the right place, at the right moment,

together with them. Their extraordinary help to prepare the experimental setup and to analyze the results has allowed us to deliver a work that has been well acknowledged by the community. Julien Desset and Gérard Gossens have provided infinite assistance by giving excellent advises and by carrying out the detailed mechanical design of the facility employed during this work. The colleagues of the VKI atelier have done also a good job by manufacturing and assembling every single piece of the wind tunnel shown in the present thesis. Finally, the TU Department technicians, J-C "van Damme" Desilve, Pierre Londers and Bram Truyaert, have brought creative solutions for those issues that calculations cannot consider.

Outside the VKI there have been very special persons that have supported me in everything I did, they took care of me and charged my batteries for the following days. My friends Manu, Charly and Alex, who were most probably my brothers in previous lives, have been near me in the good and not-so-good moments, have thrust me every single time I was with them. My family, Eusebio, Encarna and Alfredo, have taught me almost everything I know and given me almost everything I have, including their love. My best friend, my companion, my love, Anika, appeared in my life to become the perfect soul mate. Whether at home or in the four corners of the earth, she has brought me with endless grace emotions that cannot be captured by words. I know that without them, I would not be writing these lines.

Thanks my friends, here you have it!

Nacho Mayo

Brussels, February 2017

Abstract

A great effort has been carried out over the recent years in the understanding of the flow field and heat transfer in the internal cooling channels present in turbine blades. Indeed, advanced cooling schemes have not only lead to the increase of the gas turbine efficiency by increasing the Turbine Inlet Temperature above the material melting temperature, but also the increase of the turbine lifespan.

To allow such progresses, modern experimental and numerical techniques have been widely applied in order to interpret and optimize the aerodynamics and heat transfer in internal cooling channels. However, the available data is limited in the case of internal cooling channels in turbine rotor blades. Rotation and temperature gradients introduce Coriolis and centripetal buoyancy forces in the rotating frame of reference, modifying significantly the aerothermodynamics from that of the stationary passages. In the case of turbine rotor blades, most of the investigations are either based on point-wise measurements or are constraint to low rotational regimes.

The main objective of this work is to study the detailed flow and heat transfer of an internal cooling channel at representative engine dimensionless operating conditions. This work introduces a laboratory test section that operates ribbed channels over a wide range of Reynolds, Rotation and Buoyancy numbers. In the present work, the Reynolds number ranges from 15,000 to 55,000, the maximum Rotation number is equal to 0.77, and the maximum Buoyancy number is equal to 0.77. The new experimental facility consists in a versatile design that allows the interchangeability of the tested geometry, so that channels of different aspect ratios and rib geometries can be easily fitted. Particle Image Velocimetry and Liquid Crystal Thermography are performed to provide accurate velocity and heat transfer measurements under the same operating conditions, which lead to a unique experimental data set. Moreover, Large Eddy Simulations are carried out to give a picture of the entire flow field and complement the experimental observations. Additionally, the numerical approach intends to provide a robust methodology that is able to provide high fidelity predictions of the performance of internal cooling channels.

Contents

1 Motivation and goals of the present thesis **1**
- 1.1 The gas turbine . . . 1
- 1.2 The relevance of the Turbine Inlet Temperature . . . 3
- 1.3 Towards high Turbine Inlet Temperature: Turbine cooling . . . 7
- 1.4 Turbine internal cooling under the effects of rotation . . . 10
- 1.5 Aims of the present work . . . 16

2 Case description **17**
- 2.1 Case presentation and nomenclature . . . 17
- 2.2 Application of the Π-Buckingham theorem . . . 19
- 2.3 Dimensionless equations . . . 21
- 2.4 Engine conditions . . . 22

3 Experimental setup **27**
- 3.1 The RC-1 facility . . . 27
- 3.2 Test section . . . 32
- 3.3 Particle Image Velocimetry setup . . . 36
  - 3.3.1 PIV dimensioning . . . 37
  - 3.3.2 PIV test section . . . 40
  - 3.3.3 PIV processing . . . 43
- 3.4 Liquid Crystal Thermography setup . . . 46
  - 3.4.1 LCT channel . . . 47
  - 3.4.2 TLC instrumentation . . . 50
  - 3.4.3 TLC calibration . . . 52
  - 3.4.4 LCT data reduction . . . 54

4 Experimental uncertainty estimation **65**
- 4.1 Test uncertainty . . . 65
- 4.2 PIV uncertainty . . . 67
- 4.3 LCT uncertainty . . . 70
  - 4.3.1 TLC temperature uncertainty . . . 70
  - 4.3.2 Heat transfer uncertainty . . . 74

5 Numerical details **81**
5.1 Physical modeling and flow conditions 81
5.2 Domain and mesh details 83
5.3 Boundary and initial conditions 87
5.4 Solver 89

6 Results **91**
6.1 Experimental results 91
6.1.1 Inlet conditions 91
6.1.2 Isothermal velocity field 92
6.1.3 Heat transfer field 116
6.1.4 Buoyancy effects 132
6.2 Numerical results 138

7 Concluding remarks **161**
7.1 Conclusions 161
7.2 Future work 165

Bibliography **167**

List of Figures

1.1 SFC as a function of the propulsive and thermal efficiency [4] 3
1.2 Rolls-Royce Trent XWB jet engine [5] 4
1.3 Evolution of η_{th} and OPR for different generations of state-of-the-art engines 4
1.4 Development of the TIT over the years, from Ref. [4] 7
1.5 Rolls-Royce Trent 1000 jet engine (left) and detail of the high-pressure section (right) [18] 9
1.6 Detail of the cooling system in a Rolls-Royce XWB turbine blade [5] . . . 9
1.7 Sketch of a channel flow under rotation 11
1.8 Schematic view of the secondary flows system in a rotating ribbed duct [32] 13

2.1 Schematic view of the channel 18
2.2 Ranges of Re, Ro and Bo in published experimental investigations [15] . 23
2.3 Sketch of the turbine flow path (a) and turbine rotor cooling system (b) given in Ref. [49] 24

3.1 Frontal view of the RC-1 original setup [30] 29
3.2 Stream-wise velocity contours and in-plane streamlines in the symmetry plane of a rotating ribbed channel: Leading Side, $Ro = 0.30$ (a); static, $Ro = 0$ (b); Trailing Side, $Ro = 0.30$ [32] 30
3.3 Comparison of the operational range between the new and the original facilities 31
3.4 Test section sketch (as introduced in Ref.[53]) 32
3.5 Sketch of the turning vanes in the U-bend 33
3.6 Sketch of the inlet contraction 34
3.7 Sketch of the tested model 35
3.8 Example of a PIV image (left) and the corresponding instantaneous velocity field (right). Only one out of nine velocity vectors are represented . 37
3.9 PIV setup 41
3.10 Fields of View for the experiments with the 50 mm lens (left) and with the 35 mm lens (right) 42
3.11 sketch of the PIV setup and location of the measurement plane 44

3.12 Comparison of a raw image (left) and its corresponding enhanced image (right) . . . 45
3.13 Comparison of the PIV measurements with reduced and large FoV in static conditions, $Re = 15{,}000$ . . . 47
3.14 LCT experimental setup . . . 48
3.15 Inconel connection: detail (left) and sketch (right) . . . 49
3.16 Sketch of the different layers in the channel cross section [78] . . . 50
3.17 Sketch of the channel model for the LCT measurements [78] . . . 51
3.18 Relative position of the camera and light sources with respect to the channel . . . 52
3.19 TLC calibration rig . . . 53
3.20 Color distribution on the calibration rig, background picture (a), active TLCs with linear temperature profile (b) and final picture after background subtraction (c) . . . 53
3.21 Mean Hue and temperature distributions in the calibration rig (a), and final Hue-temperature calibration curve (b) . . . 54
3.22 Raw picture (a) and corresponding Hue (b) and temperature (c) distributions between the 6th and 7th ribs at $Re = 15{,}000$, $Ro = 0$ . . . 55
3.23 Sketch of the considered heating element and energy balance (dimensions given in [mm]) . . . 56
3.24 Joule power per unit area in the heating foil as a function of the voltage of the power supply . . . 57
3.25 Comparison of the span-wise averaged Nusselt number with and without lateral conduction losses in the analysis . . . 60
3.26 Overall heat transfer per unit area in the region between the 6th and 7th ribs at different conditions . . . 61
3.27 Nusselt and Enhancement Factor contours between the 6th and 7th ribs at $Re = 15{,}000$, $Ro = 0$ . . . 63

4.1 Systematic and random errors for the static case, $Re = 15{,}000$, and reduced Field of View . . . 69
4.2 Systematic and random errors for the static case, $Re = 15{,}000$, and large field of view . . . 69
4.3 Uncertainty of the dimensionless mean stream-wise velocity at Re=15,000, Ro=0 in the experiments with reduced field of view . . . 71
4.4 Uncertainty of the dimensionless mean stream-wise velocity at Re=15,000, Ro=0 in the experiments with large field of view . . . 71
4.5 Estimated uncertainty evaluation of the TLC calibration . . . 74
4.6 Influence of the primitive magnitudes in the final EF relative standard uncertainty, at $Re = 15{,}000$ and $Ro = 0$ . . . 80
4.7 Influence of the primitive magnitudes in the final EF relative standard uncertainty, at $Re = 55{,}000$ and $Ro = 0.21$, counter-clockwise rotation . . . 80

5.1 Simulated geometry (a) and computational domain (b) . . . 85

5.2 Detailed view of the mesh in planes xy and yz 85
5.3 y^+ distribution on the walls (top) and on the rib (bottom) 86
5.4 Instantaneous y^+ distribution on the channel walls ($Ro = 0.30$, counter-clockwise rotation) 87
5.5 Mean turbulence resolution magnitude ($\overline{M_T}$) contours in the symmetry plane ($Ro = 0.30$ counter-clockwise rotation) 88
5.6 Overall temperature in the domain as a function of the dimensionless time 90

6.1 Inlet mean stream-wise velocity contours in static conditions 92
6.2 Inlet mean stream-wise velocity profiles 93
6.3 Inlet turbulent stream-wise velocity profiles 94
6.4 Stream-wise velocity contours and in-plane streamlines, Re = 15,000: present investigation, Leading Side, $Ro = 0.30$ (a); present investigation, Static, $Ro = 0$ (b); present investigation, Trailing Side, $Ro = 0.30$ (c); Coletti et al. (2012), Leading Side, $Ro = 0.30$ (d); Coletti et al. (2012), Static, $Ro = 0$ (e); Coletti et al. (2012), Trailing Side, $Ro = 0.30$ (f) . . . 96
6.5 Stream-wise velocity profiles: Leading Side, $Ro = 0.30$ (a); Static (b); Trailing Side, $Ro = 0.30$ (c) 98
6.6 Stream-wise turbulent velocity profiles: Leading Side, $Ro = 0.3$ (a); Static (b); Trailing Side, $Ro = 0.30$ (c) 99
6.7 In-plane velocity modulus contours and in-plane streamlines, $Re = 15{,}000$: Leading Side, $Ro = 0.77$ (a); Leading Side, $Ro = 0.38$ (b); Static, $Ro = 0$ (c); Trailing Side, $Ro = 0.38$ (d); Trailing Side, $Ro = 0.77$ (e). Data obtained with the 50 mm objective (Table 3.3) 101
6.8 In-plane velocity modulus contours and in-plane streamlines, $Re = 15{,}000$: Leading Side, $Ro = 0.77$ (a); Leading Side, $Ro = 0.30$ (b); Static, $Ro = 0$ (c); Trailing Side, $Ro = 0.30$ (d); Trailing Side, $Ro = 0.77$ (e). Data obtained with the 35 mm objective (Table 3.4) 102
6.9 Mean stream-wise velocity contours, Re = 15,000: Leading Side, $Ro = 0.77$ (a); Leading Side, $Ro = 0.38$ (b); Static, $Ro = 0$ (c); Trailing Side, $Ro = 0.38$ (d); Trailing Side, $Ro = 0.77$ (e). Data obtained with the 50 mm objective (Table 3.3) 105
6.10 Mean stream-wise velocity contours, Re = 15,000: Leading Side, $Ro = 0.77$ (a); Leading Side, $Ro = 0.30$ (b); Static, $Ro = 0$ (c); Trailing Side, $Ro = 0.30$ (d); Trailing Side, $Ro = 0.77$ (e). Data obtained with the 35 mm objective (Table 3.4) 106
6.11 Mean wall-normal velocity contours, Re = 15,000: Leading Side, $Ro = 0.77$ (a); Leading Side, $Ro = 0.38$ (b); Static, $Ro = 0$ (c); Trailing Side, $Ro = 0.38$ (d); Trailing Side, $Ro = 0.77$ (e). Data obtained with the 50 mm objective (Table 3.3) 107

6.12 Mean wall-normal velocity contours, Re = 15,000: Leading Side, Ro = 0.77 (a); Leading Side, Ro = 0.30 (b); Static, Ro = 0 (c); Trailing Side, Ro = 0.30 (d); Trailing Side, Ro = 0.77 (e). Data obtained with the 35 mm objective (Table 3.3) 108

6.13 Stream-wise turbulent velocity contours, Re = 15,000: Leading Side, Ro = 0.77 (a); Leading Side, Ro = 0.30 (b); Static, Ro = 0 (c); Trailing Side, Ro = 0.30 (d); Trailing Side, Ro = 0.77 (e). Data obtained with the 35 mm objective (Table 3.3) 110

6.14 Wall-normal turbulent velocity contours, Re = 15,000: Leading Side, Ro = 0.77 (a); Leading Side, Ro = 0.30 (b); Static, Ro = 0 (c); Trailing Side, Ro = 0.30 (d); Trailing Side, Ro = 0.77 (e). Data obtained with the 35 mm objective (Table 3.3) 111

6.15 In-plane turbulent kinetic energy contours, Re = 15,000: Leading Side, Ro = 0.77 (a); Leading Side, Ro = 0.30 (b); Static, Ro = 0 (c); Trailing Side, Ro = 0.30 (d); Trailing Side, Ro = 0.77 (e). Data obtained with the 35 mm objective (Table 3.3) 112

6.16 Richardson number contours, Re = 15,000: Leading Side, Ro = 0.77 (a); Leading Side, Ro = 0.30 (b); Trailing Side, Ro = 0.30 (c); Trailing Side, Ro = 0.77 (d). Data obtained with the 35 mm objective (Table 3.3) . . . 114

6.17 Energy spectra at $(X/H, Y/H)$ = (1, 1) 115

6.18 Combination of the experimental Enhancement Factor and in-plane turbulent kinetic energy at Re = 15000, Ro = 0 117

6.19 Comparison of the present span-wise-averaged Enhancement Factor in static conditions with the data provided by Ekkad and Han [104], as shown in Ref. [78] 118

6.20 Centerline Enhancement Factor, in-plane turbulent kinetic energy and streamlines at Re=15,000: Leading Side - Ro = 0.77 (PIV) - 0.83 (LCT) (a), Leading Side - Ro 0.30 (b), static case (c), Trailing Side - Ro = 0.30 (d) and Trailing Side - Ro = 0.77 (PIV) - 0.83 (LCT) (e) 120

6.21 Combination of the experimental Enhancement Factor and in-plane turbulent kinetic energy at Re = 15000 122

6.22 Combination of the experimental Enhancement Factor and in-plane turbulent kinetic energy at Re = 15000 124

6.23 Enhancement Factor contours at Re = 15,000: Static (a), Leading Side - Ro = 0.30 (b), Leading Side - Ro = 0.83 (c), Trailing Side - Ro = 0.30 (d), Trailing Side - Ro = 0.83 (e) 125

6.24 Enhancement Factor contours at Re = 15,000 (a), 30,000 (b) and 55,000 (c) 126

6.25 Enhancement Factor contours at Ro = 0.20: Leading Side (LS) - Re = 15,000 (a), LS - Re = 30,000 (b), LS - Re = 55,000 (c), Trailing Side (TS) - Re = 15,000 (d), TS - Re = 30,000 (e), TS - Re = 55,000 (f) 128

6.26 Enhancement Factor contours at $Ro = 0.47$: Leading Side (LS) - Re = 15,000 (a), LS - Re = 30,000 (b), Trailing Side (TS) - Re = 15,000 (c), TS - Re = 30,000 (d) . . . 130
6.27 Enhancement Factor contours at Re = 15,000, Ro = 1.0: Leading Side (a), Trailing Side (b) . . . 131
6.28 Area-averaged Enhancement Factor as a function of the Rotation and Reynolds numbers[53] . . . 132
6.29 Normalized average Enhancement Factor at Re = 15,000 and comparison with similar data present in the open literature[78] . . . 133
6.30 Mean wall-normal velocity contours, Re = 15,000: Leading Side, Ro = 0.77, Bo = 0.77 (a); Leading Side, Ro = 0.77, Bo = 0 (b); Static, Ro = 0 (c); Trailing Side, Ro = 0.77, Bo = 0 (d); Trailing Side, Ro = 0.77, Bo = 0.77 (e) . . . 135
6.31 Mean wall-normal velocity contours, Re = 15,000: Leading Side, Ro = 0.77, Bo = 0.77 (a); Leading Side, Ro = 0.77, Bo = 0 (b); Static, Ro = 0 (c); Trailing Side, Ro = 0.77, Bo = 0 (d); Trailing Side, Ro = 0.77, Bo = 0.77 (e) . . . 136
6.32 Mean wall-normal velocity contours, Re = 15,000: Leading Side, Ro = 0.77, Bo = 0.77 (a); Leading Side, Ro = 0.77, Bo = 0 (b); Static, Ro = 0 (c); Trailing Side, Ro = 0.77, Bo = 0 (d); Trailing Side, Ro = 0.77, Bo = 0.77 (e) . . . 137
6.33 Stream-wise turbulent velocity contours, Re = 15,000: Leading Side, Ro = 0.77, Bo = 0.77 (a); Leading Side, Ro = 0.77, Bo = 0 (b); Static, Ro = 0 (c); Trailing Side, Ro = 0.77, Bo = 0 (d); Trailing Side, Ro = 0.77, Bo = 0.77 (e) . . . 139
6.34 Wall-normal turbulent velocity contours, Re = 15,000: Leading Side, Ro = 0.77, Bo = 0.77 (a); Leading Side, Ro = 0.77, Bo = 0 (b); Static, Ro = 0 (c); Trailing Side, Ro = 0.77, Bo = 0 (d); Trailing Side, Ro = 0.77, Bo = 0.77 (e) . . . 140
6.35 In-plane turbulent kinetic energy contours, Re = 15,000: Leading Side, Ro = 0.77, Bo = 0.77 (a); Leading Side, Ro = 0.77, Bo = 0 (b); Static, Ro = 0 (c); Trailing Side, Ro = 0.77, Bo = 0 (d); Trailing Side, Ro = 0.77, Bo = 0.77 (e) . . . 141
6.36 Energy spectra under the buoyancy effects at $(X/H, Y/H) = (1, 1)$ . . . 142
6.37 Mean stream-wise velocity profiles (top) and centerline Enhancement Factor (bottom) obtained in static conditions (Re = 15,000, Ro = 0) during the experimental campaign and by means of LES in Mesh A and Mesh B. 143
6.38 Mean λ_2 iso-surface and vertical velocity contour in the plane X/H = -0.5, static case . . . 145
6.39 Dimensionless temperature contour and in-plane streamline in the plane X/H = 3.33 in static conditions . . . 146
6.40 Enhancement Factor contours in the static case (Ro = 0): experiments (a), LES (b) . . . 148

6.41 3D representation of the flow field and heat transfer provided by the LES in static conditions 148
6.42 Mean stream-wise velocity profiles, from top to bottom: Trailing Side - $Ro = 0.77$, Trailing Side - $Ro = 0.30$, static case, Leading Side - $Ro = 0.30$ and Leading Side - $Ro = 0.77$ 151
6.43 Stream-wise turbulent velocity profiles, from top to bottom: Trailing Side - $Ro = 0.77$, Trailing Side - $Ro = 0.30$, static case, Leading Side - $Ro = 0.30$ and Leading Side - $Ro = 0.77$ 152
6.44 Centerline Enhancement Factor: Leading Side - $Ro \simeq 0.8$ (a), Leading Side - $Ro \simeq 0.3$ (b), static (c), Trailing Side - $Ro \simeq 0.3$ (d), Trailing Side - $Ro \simeq 0.8$ (d) 153
6.45 Dimensionless temperature contours and in-plane streamlines in the plane $X/H = 3.33$, Leading Side case (clockwise rotation): $Ro = 0.30$ (left), $Ro = 0.77$ (right) 154
6.46 Enhancement Factor contours in the Leading Side case: Experiments - $Ro = 0.29$ (a), Experiments - $Ro = 0.82$ (b), LES - $Ro = 0.30$ (c), LES - $Ro = 0.77$ (d) 155
6.47 3D representation of the flow field and heat transfer provided by the LES under clockwise rotation: $Ro = 0.30$ (left), $Ro = 0.77$ (right) 156
6.48 Dimensionless temperature contours and in-plane streamlines in the plane $X/H = 3.33$, Trailing Side case (counter-clockwise rotation): $Ro = 0.30$ (left), $Ro = 0.77$ (right) 157
6.49 Enhancement Factor contours in the Trailing Side case: Experiments - $Ro = 0.29$ (a), Experiments - $Ro = 0.83$ (b), LES - $Ro = 0.30$ (c), LES - $Ro = 0.77$ (d) 158
6.50 3D representation of the flow field and heat transfer provided by the LES under counter-clockwise rotation: $Ro = 0.30$ (left), $Ro = 0.77$ (right) . . 159
6.51 Normalized EF on the bottom wall as a function of the Rotation number 159
6.52 Normalized mean friction factor as a function of the Rotation number . . 160

List of Tables

1.1 Engine components figures of merit employed in the analysis of η_{th}. Data adapted from Ref. [6] 5
1.2 Direct impact estimation of the TIT variations on η_{th} 6

2.1 Physical parameters 20
2.2 Absolute units in the dimensional analysis 20

3.1 Test matrix for the PIV experiments with the 50 mm lens (Re = 15,000), performed experiments are colored 42
3.2 Test matrix for the PIV experiments with the 35 mm lens (Re = 15,000), performed experiments are colored 43
3.3 Summary of the PIV parameters for the experiments with reduced Field of View (Fig. 3.10-left) 45
3.4 Summary of the PIV parameters for the experiments with large Field of View (Fig. 3.10-right) 46
3.5 Test matrix for the TLC experiments. The investigated Re-Ro combinations are colored 51

4.1 Comparison the TLC temperature measurement uncertainty 75
4.2 Summary of the primitive uncertainties 76
4.3 Summary of the heat transfer uncertainties at Re = 15,000, Ro = 0 . . . 78
4.4 Summary of the heat transfer uncertainties at Re = 55,000, Ro = 0.21 counter-clockwise 78

5.1 Cases studied by LES (Re = 15000, Pr = 0.72) 84

List of Symbols

Acronyms

AU	Arbitrary Units
CCD	Charge-Coupled Device
CFD	Computational Fluid Dynamics
CFL	Courant - Friedrichs - Lewy
C.L.	Confidence Level
CMOS	Complementary Metal Oxide Semiconductor
DNS	Direct Numerical Simulation
FOV	Field of View
FTT	Flow Through Time
HSC	High Speed Camera
ISA	International Standard Atmosphere
LCT	Liquid Crystal Thermography
LDKSGS	Localized k-Equation Subgrid-Scale
LES	Large Eddy Simulation
LETOT	Large Eddy Turn-Over Time
OPR	Overall Pressure Ratio
PIV	Particle Image Velocimetry
RANS	Reynolds-Averaged Navier-Stokes
RGB	Red, Green, Blue
RSM	Reynolds Stress Model
SFC	Specific Fuel Consumption
SGS	Sub-Grid Scale
SLR	Single-Lens Reflex
TIT	Turbine Inlet Temperature
TLC	Thermo-Chromic Liquid Crystal
TR	Time-Resolved
URANS	Unsteady Reynolds-Averaged Navier-Stokes
VKI	von Karman Institute
WALE	Wall-Adapting Local Eddy
XPS	Extruded Polystyrene

Roman symbols

A_1	pipe area	m^2
A_2	nozzle throat area	m^2
B	blue color intensity	AU
Bo	Buoyancy number	-
C_S	Smagorinsky constant	-
c_{blade}	blade chord	m
c_p	specific heat capacity at constant pressure	$J/\left(kg \cdot K\right)$
c_ν	turbulence model constant	-
D_H	hydraulic diameter	m
D_I	interrogation window size in the image plane	m
d_I	interrogation window size in the real plane	m
d_r	pixel size	m
Ec	Eckert number	-
EF	Enhancement Factor	
$\mathbf{e_x}$	stream-wise unit vector	-
$\mathbf{e_y}$	vertical unit vector	-
$\mathbf{e_\Omega}$	angular velocity unit vector	-
F_{HV}	fuel calorific value	J/kg
FP_{in}	turbine corrected mass flow	$\frac{\left[LBM \cdot (^oR^{1/2})\right]}{(s \cdot psia)}$
f	lens focal length	m
f_{acq}	acquisition frequency	Hz
G	green color intensity	AU
g	gravitational acceleration	m/s^2
H	rib height	m
He	height of the contraction's cross section	m
He_0	height of the settling chamber	m
He_L	channel height	m
h	heat transfer coefficient	$W/\left(m^2 \cdot K\right)$
k	thermal conductivity	$W/\left(m \cdot K\right)$
k_f	film thermal conductivity	$W/\left(m \cdot K\right)$
k_{XPS}	XPS thermal conductivity	$W/\left(m \cdot K\right)$
L	length of the contraction	m
L_X	sensor width	m
L/D	overall aerodynamic efficiency	-
l	length scale	m
l_x	Field of View	m
M	Mach number, mapping function	-
M_T	turbulence resolution measure	-
$\dot{m}$	mass flow	kg/s
$\mathbf{n}$	unit surface vector	-
Nu	Nusselt number	-

Nu	reference Nusselt number	-
P	rib pitch	m
Pr	Prandtl number	-
Pr_t	turbulent Prandtl number	-
p	pressure	Pa
$\overline{p}$	mean pressure	Pa
p_0	reference pressure	Pa
p^*_{eff}	dimensionless effective pressure	-
Q	heat flux	W
q_{cond}	conductive heat loss unit area	W/m^2
q_{conv}	convective heat transfer per unit area	W/m^2
q_{Joule}	heating power produced by Joule effect per unit area	W/m^2
q_{rad}	radiative heat loss per unit area	W/m^2
R	red color intensity	AU
R_{air}	air specific gas constant	$J/(kg \cdot K)$
Re	Reynolds number	-
Ri	gradient Richardson number	-
Ro	Rotation number	-
r	distance to the axis of rotation	m
r_{corner}	corner radius	m
S	local rotation number	-
S_{ij}	strain stress tensor	$1/s$
T	temperature	K
T_0	ambient temperature	K
T_b	bulk temperature	K
T_c	fluid temperature at the center of the cross section	K
T_w	local wall temperature	K
T_w	overall wall temperature (chapter 2)	K
$T_{w,ext}$	mean external wall temperature	K
T_∞	temperature of the surrounding elements	K
t_c	characteristic time	s
t_I	Inconel foil thickness	m
t_{XPS}	XPS wall thickness	m
U	mean stream-wise velocity	m/s
$\mathbf{u}^*$	dimensionless velocity vector	-
u	stream-wise velocity	m/s
u	uncertainty	case dependent
U_b	bulk velocity	m/s
V	mean vertical velocity	m/s
V_0	flight velocity	m/s
V_{GEN}	voltage provided by the power supply	V
v	vertical velocity	m/s
W	mean span-wise velocity	m/s

Wi	width of the contraction's cross section	m
Wi_0	width of the settling chamber	m
Wi_L	channel width	m
$W_{initial}$	aircraft initial weight (mass)	$N(kg)$
W_{final}	aircraft final weight (mass)	$N(kg)$
w	span-wise velocity	m/s
X	axial coordinate in the image plane	-
x	axial coordinate	m
y	vertical coordinate	m
y^+	dimensionless wall distance	-
Z_0	distance from the lens to the camera sensor	m
z	span-wise coordinate	m
z_0	distance from the measurement plane to the lens	m

Greek symbols

β	driving pressure gradient	Pa/m
Δp	pressure difference	Pa
$\Delta p_{Venturi}$	pressure difference in the Venturi nozzle	Pa
ΔTIT	TIT variation	K
Δt	separation time	s
ΔX	particle displacement in the image plane	m
Δx	particle displacement in the real plane	m
$\Delta \rho$	overall density difference	kg/m^3
$\tilde{\Delta}$	filter length	m
$\delta()$	estimated measurement error/ variation of a variable	-
δ_{ij}	Kronecker Delta	-
δx	length in the stream-wise direction of an infinitesimal element	m
δz	length in the span-wise direction of an infinitesimal element	m
ε_{TLC}	TLC emissivity	-
ε_{ijk}	Levi-Civita symbol	-
γ	air heat capacity ratio	-
η_{comp}	compressor isentropic efficiency	-
η_P	propulsive efficiency	-
η_{th}	thermal efficiency	-
η_{turb}	turbine isentropic efficiency	-
Θ	dimensionless temperature	-
μ	molecular viscosity	$kg/\left(m \cdot s\right)$
ν	kinematic viscosity	m^2/s
ν_T	SGS eddy viscosity	m^2/s
ρ	fluid density	kg/m^3
ρ_0	reference density	kg/m^3
σ	Stephan-Boltzmann constant	$W/(m^2 \cdot K^4)$
τ_{ij}	SGS stress tensor	m^2/s^2
Π	cross section perimeter	m
Φ^*	dimensionless viscous dissipation tensor	-
Ω	system angular velocity	rad/s

Sub- and Superscripts

eff	effective
$film$	film conditions
in	inlet
lat	lateral
out	outlet
r	random
sgs	subgrid-scale
T	total conditions
x	stream-wise direction
z	span-wise direction
$*$	dimensionless value
$\overline{\phi}$	mean value of the variable ϕ
$\tilde{\phi}$	filtered value of the variable ϕ

Chapter 1

Motivation and goals of the present thesis

1.1 The gas turbine

Gas turbines are power plants that are widely employed to produce mechanical energy. Numerous applications of gas turbines are present in the world, such as power generators in means of transport and industrial facilities. Boyce [1] presents an economic comparison between different power generation technologies: diesel engine, gas engine, simple cycle gas turbine, fuel cell, biomass, etc. The suitability of these systems depends on the fuel cost, system efficiency, maintenance costs and capital costs. According to Boyce [1], the new power plants are based on combined cycles with the gas turbine as main character, with a design focused on the:

- efficiency
- reliability
- ease of use
- simplicity of installation and commissioning
- agreement with the environmental standards
- incorporation of accessories and control systems
- adaptability to service and fuel needs.

In the case of aircraft propulsion at moderate-high speeds (jet aircraft) the requirements for the gas turbines are more severe. Despite the fact that the technical and economic risks involved in the production of aircraft engines are extremely high, a successful engine may provide large benefits to the manufacturers. For instance, the Rolls-Royce

RB211 engine family (first run in 1969) had an arduous origin that resulted in the insolvency of the company. Due to the strategic importance of the company, Rolls-Royce was nationalized by the UK Government in the early 70s. Nevertheless, the engine development supposed the inception of the first three-spool jet engine. Several upgraded models have been released since then, indicating the room for development of a new engine family and the chance of success several years after the engine birth. Moreover, the advances achieved in the RB211 engine have allowed the creation and evolution of the Rolls-Royce Trent family.

Another example of the difficult beginning for an aircraft gas turbine is the General Electric GE90 turbofan engine (first run in 1993). The GE90 was designed to power specifically the Boeing B-777 aircraft, becoming the most powerful turbofan engine. The GE90 program was extremely challenging and required the collaboration of General Electric, SNECMA, IHI, and Fiat Avio. For instance, the initial investment in the program was of €2000 million for General Electric, and no profit was expected in the 15-20 years after the beginning of the program [2].

It is clear that the aircraft propulsion industry is highly competitive and changing. As stated by Birch [3], the development of engines is nowadays directed towards:

- optimization of the engine efficiency and fuel consumption reduction
- weight reduction
- environmental impact minimization (noise and emissions)
- reduction of the ownership cost (product unit cost, maintenance costs and reliability)

The aircraft fuel consumption has been reduced by 70% in the period 1960-2005 due to the improvements in the aircraft and the engine design. In particular, the impact on the fuel consumption reduction by the jet engine development is estimated to be two-thirds of the total reduction [3]. The specific fuel consumption, SFC, is defined as the fuel consumption per unit of thrust and constitutes one of the main figures of merit of a jet engine. The SFC is often expressed as

$$SFC = \frac{V_0}{\eta_P \eta_{th} F_{HV}} \tag{1.1}$$

where V_0 is the aircraft speed, η_P is the propulsive efficiency, η_{th} is the thermal efficiency and F_{HV} is the fuel calorific value. Equation (1.1) identifies the prime elements that need to be optimized in order to minimize the SFC. Since V_0 is in general given by the preliminary aircraft design, and F_{HV} is known for the existing fuel, aircraft engine designers are requested to increase the propulsive and thermal efficiencies.

Haselbach and Parker [4] (Fig. 1.1) show the dependency of the SFC with respect to the thermal and propulsive efficiencies, for a given flight speed (flight Mach number of 0.8) and fuel. The state-of-the-art engines present thermal and propulsive efficiencies up

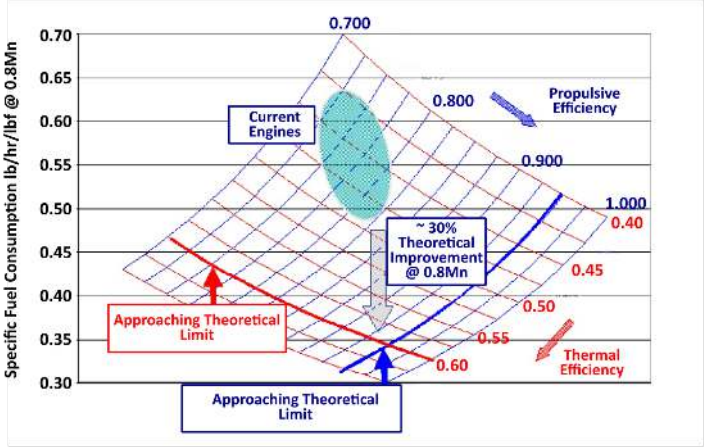

Figure 1.1 : SFC as a function of the propulsive and thermal efficiency [4]

to 0.475 and 0.80, respectively. Nevertheless, the theoretical improvement in the SFC can be of 30 % if η_{th} and η_P are improved.

The followed strategy to increase the propulsive efficiency is to reduce the engine exit velocity, which in turn requires high mass flows to achieve the desired thrust. In the 1940s, the architecture of the jet engines was modified to include a fan in the first stage of the engine to move higher mass flows and reduce the overall exit speed. This resulted in the turbofan engine, in which a part of the mass flow that across the fan enters the core of the engine in order to produce mechanical energy as in the early turbojets, and the rest of the mass flow moves through the bypass duct and is accelerated to speeds slightly higher than V_0. The ratio between the secondary mass flow and the core mass flow is known as the bypass ratio, and it has experienced an important evolution towards large values. Nowadays, ultra-high bypass ratio engines offer bypass ratios up to 10, and open rotor architectures in development are expected to offer bypass ratios up to 50. The expected propulsive efficiencies of such engines are to be up to $\eta_P \sim 0.92$ - 0.95. Nevertheless, limitations in the bypass ratio are present, such as the weight increase and mechanical constraints.

1.2 The relevance of the Turbine Inlet Temperature

On the other hand, the thermal efficiency can be enhanced mainly by increasing the overall pressure ratio (OPR), the turbine inlet temperature (TIT) and the components efficiencies. The study of the turbojet thermodynamic cycle reveals the dependency of the thermal efficiency on the latter parameters:

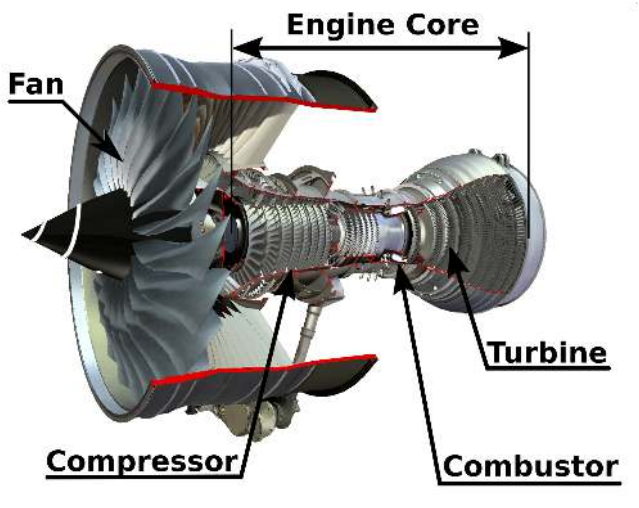

Figure 1.2 : Rolls-Royce Trent XWB jet engine [5]

$$\eta_{th} = \frac{\left[1 - \frac{1}{OPR^{\frac{\gamma-1}{\gamma}}}\right]\left[\eta_{comp}\eta_{turb}\frac{TIT}{T_0} - OPR^{\frac{\gamma-1}{\gamma}}\right]}{1 + \eta_{comp}\left[\frac{TIT}{T_0} - 1\right] - OPR^{\frac{\gamma-1}{\gamma}}} \tag{1.2}$$

where γ is the air heat capacity ratio, η_{comp} is the compressor isentropic efficiency, η_{turb} is the turbine isentropic efficiency and T_0 is the total temperature of the air at the entrance of the engine.

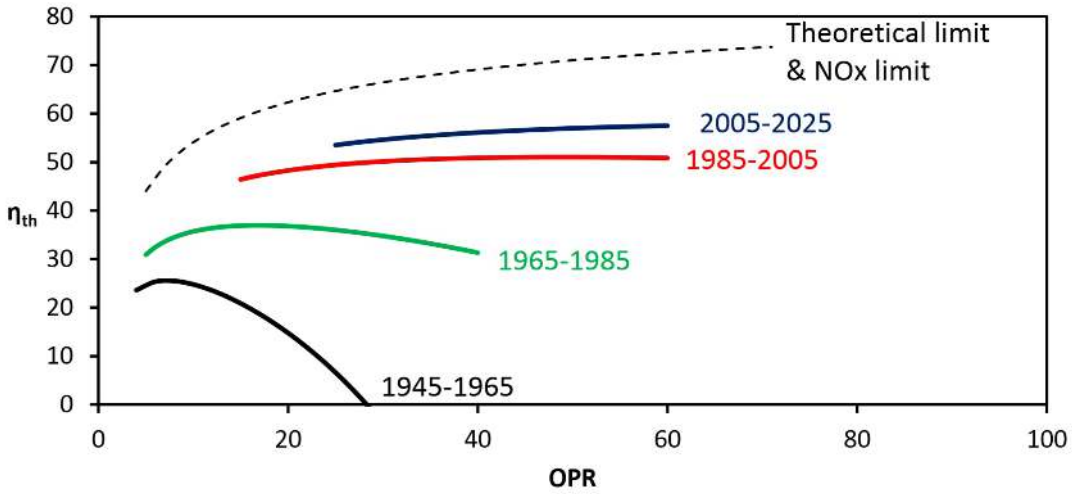

Figure 1.3 : Evolution of η_{th} and OPR for different generations of state-of-the-art engines

Table 1.1 : Engine components figures of merit employed in the analysis of η_{th}. Data adapted from Ref. [6]

		Period			
Component	Figure of merit	1945-1965	1965-1985	1985-2005	2005-2025
Compressor	η_{comp}	0.71	0.76	0.81	0.84
Turbine	η_{turb}	0.83	0.85	0.89	0.91
Turbine	TIT[K]	1110	1390	1780	2000

Figure 1.3 shows the dependency of the thermal efficiency (Eq. (1.2)) and OPR over the last decades. The level of technology has been allocated in periods of 20 years from 1945. The components efficiencies and TIT employed in the estimation of η_{th} are shown in Table 1.1, adapted from the data presented in Ref. [6]. All these figures of merit have been continuously improved to enhance the gas turbine efficiency. In order to simplify the model, the air heat capacity ratio γ has been assumed constant and equal to 1.4, whereas T_0 has been taken as the ambient temperature 10 km above the sea level in an International Standard Atmosphere (ISA) standard day. It is clear from Fig. 1.3 that the improvement in the level of technology through the years affects positively the thermal efficiency. For a fixed period of time, there exits an optimum value of the OPR that provides a maximum η_{th}. Nevertheless, the sensitivity of η_{th} on the OPR is reduced as the gas turbine technology is enhanced, and such an optimum is only found at ultra-large pressure ratios. On the other hand, the impact of the TIT on the η_{th} can be estimated for the values of the OPR, TIT, η_{comp} and η_{turb} corresponding to the present days. By taking the derivative of Eq. (1.2), it is possible to relate the expected variation of the thermal efficiency for a given increase of the Turbine Inlet Temperature ΔTIT:

$$\frac{\Delta\eta_{th}}{\eta_{th}} = \left[\frac{\eta_{comp}\eta_{turb}}{\eta_{comp}\eta_{turb}\frac{TIT}{T_0} - OPR^{\frac{\gamma-1}{\gamma}}} - \frac{\eta_{comp}}{1 - OPR^{\frac{\gamma-1}{\gamma}} + \eta_{comp}\left(\frac{TIT}{T_0} - 1\right)} \right] \cdot \frac{\Delta TIT}{T_0} \tag{1.3}$$

Assuming TIT, η_{comp} and η_{turb} equal to the values in the period 2005-2025 (Table 1.1) and an OPR of 50, the direct variation of η_{th} with respect to the TIT increase is given in Table 1.2. Despite of the fact that several assumptions have been made to obtain the relation in Eq. (1.3), it provides the order of magnitude of the TIT impact on the thermal performance. For a variation of 1 K, the improvement of the thermal efficiency is only of order of 0.01 %. However, the improvement on η_{th} is about 0.1 % for

Table 1.2 : Direct impact estimation of the TIT variations on η_{th}

ΔTIT [K]	$\Delta\eta_{th}/\eta_{th}$ [%]
1	0.01
10	0.13
50	0.64

a TIT increase of 10 K, which is the typical variation seen per year. In the same way, the estimated improvement reaches 0.6 % for the typical 5-year TIT increase (50 K).

The corresponding improvement on the SFC due to the η_{th} increase can be evaluated as:

$$\frac{\Delta SFC}{SFC} = \frac{\Delta\eta_{th}}{\eta_{th}} \tag{1.4}$$

Therefore, the relative variation of the SFC is the same as that of η_{th} when the TIT is increased. The consequent impact on the aircraft performance can be analyzed by considering the Bréguet Range Equation [7], applied in the case of horizontal and straight flight at constant speed (V_0) and overall aerodynamic efficiency (L/D):

$$Range = \frac{V_0(L/D)}{g \cdot SFC} \ln\left(\frac{W_{initial}}{W_{final}}\right) \tag{1.5}$$

where g is the gravitational acceleration, $W_{initial}$ is the initial aircraft weight and W_{final} is the final aircraft weight. From Eq. (1.5), it can be deduced that the relative gain in the flight range is the same as the relative SFC variation:

$$\frac{\Delta Range}{Range} = \frac{\Delta SFC}{SFC} \tag{1.6}$$

Thus, a TIT increment of 10 K represents an increase of about 0.1 % of the aircraft range, whereas an increment of 50 K represents an increase of 0.6 % of the aircraft range. Note also that the enhancement of the thermal efficiency supposes a reduction in size of the engine's core for a specified output power. In turn, the engine bypass ratio is enlarged, which provides an increase of the propulsive efficiency. Therefore, the TIT increase does not affect only the thermal efficiency, but also the propulsive efficiency, which yields a further decrease of the SFC. On the other hand, a reduction of the fuel consumption allows a larger payload for a fixed flight range, which increases the profit margin.

It is noteworthy to stress that fuel is typically the most important factor of the airline operational costs. The ratio of the fuel costs to the airline operational costs varies in time due to its strong relation with the fuel price. In 2016, fuel will represent about 20% of the operational costs (the lowest since 2005). With the previous model, the ability to

design a jet engine with a TIT 100 K higher, may represent a reduction of 0.1% of the airline operational cost.

Even though this analysis is to some extent a simplification of a real case, it provides the order of magnitude of the influence of the TIT of the gas turbine and aircraft performance and operational costs. In a more elaborated model of a mixed-flow, two-shaft and high bypass turbofan, Cumpsty [8] estimates the impact of the Turbine Inlet Temperature on the engine performance. For the selected design parameters, an increase of the TIT from 1450 to 1550 K, the specific fuel consumption is reduced by about 2.8%, which would lead to significant fuel savings to airline companies (for example, the fuel, oil and emissions costs for International Airlines Group were about €6 billion in 2015 [9]). The data provided by the International Air Transport Association (IATA) shows that the fuel costs represented in average 27.5% of the airline operational cost, and a global cost of US$181 billion [10]. Therefore, by reducing the SFC by 2.8%, the fuel savings would present an order of magnitude of US$5 billion per year, only in the civil aircraft engine segment. In the segment of combined cycle power plants, the fuel costs can represent up to 75% of the plant life costs [1]. Thus, it is clear that the design of gas turbines operating at high Turbine Inlet Temperature has a large economic impact.

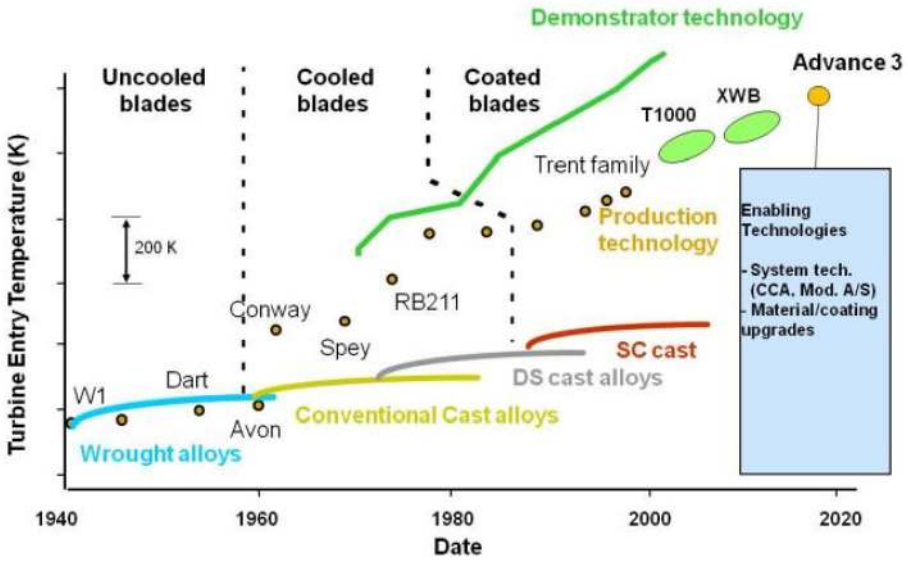

Figure 1.4 : Development of the TIT over the years, from Ref. [4]

1.3 Towards high Turbine Inlet Temperature: Turbine cooling

The increase of the design TIT has been possible mainly due to the improvement of materials and their mechanical properties, the application of protective coatings and the optimization of cooling techniques. In fact, Unger and Herzog [11] addressed the

advances in the cooling and material fields as the main technological factors that lead to the gas turbine success. Figure 1.4 shows that the contribution of materials development to the TIT gain has been about 200-300 K since 1940, or equivalently 2.9-4.3 K/year. The first wrought turbine components were able to withstand around 1100 K, whereas the modern cast nickel-base alloys can reach metal temperatures of about 1300 K during operation [12]. However, the challenge in the material science research applied to gas turbines does not consist only to stand high levels of stress at high temperatures, but also to present excellent resistance to oxidation and corrosion due to combustion.

At the same time, cooling technology has been applied to achieve fluid temperatures higher than the material creep temperature. In the example of Fig. 1.4, the difference between the TIT and the metal temperature reaches values of about 550-600 K nowadays. Thanks to the cooling contribution, the TIT increase is about 10 K/year. According to Auxier [13], the introduction of cooling technology in gas turbines has been the main factor that has allowed high temperature in combustors, exhaust nozzles and turbines. As a result, the reduction of fuel consumption has resulted for about 70% since the introduction of internal cooling schemes in the 1960s to 2005.

A detail of the high pressure section of a modern jet engine is shown in Fig. 1.5. Typically, 20 to 30 % of the mass flow of the high pressure compressor (upstream of the combustion chamber) is used to cool the engine hot section [13, 14]. The mass flow bled from the compressor is introduced in the internal cooling channels present in the turbine blades to extract the maximum amount of heat out of the blade. As TIT increases, the total amount of heat transferred to the blade increases. Therefore, a good design of the cooling scheme is fundamental to transfer that heat to the internal cooling flow. An example of a state-of-the-art blade cooling scheme is given in Fig. 1.6. In order to maximize the heat transfer with minimum pressure losses, great efforts have been made by investigating different geometry factors and operating regimes. A wide review of the state of the art in internal cooling techniques is provided by Ligrani [15]. A part of the cooling flow is ejected from the internal channels through small holes in order to create a protective film that seeks the insulation of the turbine blade from the mass flow exiting the combustion chamber. This technique is known as film cooling, and it is also widely employed as a method to increase the flow temperature in the hot section. Generally, film cooling holes are located in regions where heat transfer and mechanical stresses are critical. In the example of the blade of Fig. 1.6, film cooling holes are present at the leading and trailing edges, pressure side and endwalls. A complete description of the turbine heat transfer and blade cooling is provided by Han et al. in Ref. [16], whereas a recent outlook for the future in hot section cooling techniques is provided by Bunker [17].

On the other hand, an increase of the cooling flow leads to the reduction of the turbine performance. In the analysis made by Cumpsty [8], an increase of the cooling mass flow from 10% to 20% of the compressor mass flow would suppose an increase of about 3.8 % in the specific fuel consumption, if the TIT is kept unchanged. Therefore, a tradeoff between the thermodynamic cycle degradation by the amount of cooling flow and the capability to increase the TIT must be found.



Figure 1.5 : Rolls-Royce Trent 1000 jet engine (left) and detail of the high-pressure section (right) [18]

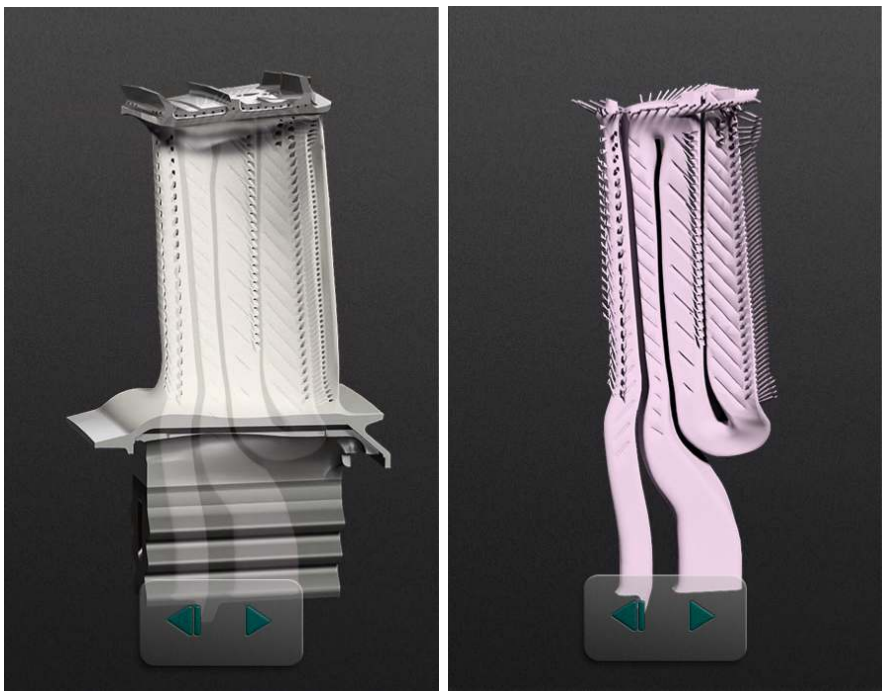

Figure 1.6 : Detail of the cooling system in a Rolls-Royce XWB turbine blade [5]

Many works about turbine cooling can be found in the open literature investigating numerous concepts and regimes. Nevertheless, there is still a lot of work to be done. In the words of Auxier [13]:

> "the industry has come a long way in turbine cooling technology but [...] the hard part is yet to come."

The present dissertation focuses on the physics in internal cooling channels under rotation. Due to the complexity necessary to investigate experimentally the fluid motion and heat transfer of rotating flows, the detailed understanding of the flow subjected to rotation is limited. This work introduces a new experimental setup that allows the measurement of detailed velocity and heat transfer fields at different regimes in order to finally provide a clear picture of the phenomena taking place in the rotating internal cooling channels at engine representative dimensionless conditions. The data obtained experimentally are also aimed to be used as test cases for numerical simulations. Indeed, the second part of this work focuses on the research of a numerical strategy able to reproduce the same quantities at the same conditions with high fidelity and reliability, and reduced cost. These numerical results are furthermore employed to confirm and extend the experimental observations.

1.4 Turbine internal cooling under the effects of rotation

The flow field and heat transfer in rotating cooling channels differ greatly from those in static conditions. There are three main effects introduced by rotation

1. redistribution of the momentum in the rotating frame of reference, resulting in a mean velocity gradient $\partial\overline{U}/\partial y = 2\Omega$ (see Fig. 1.7),

2. redistribution of the turbulence structure,

3. generation of secondary flows

Lezius and Johnston [19] demonstrated that even in the simple case of a two-dimensional, inviscid and parallel shear flow under rotation, the absolute vorticity remains constant, leading to the tilting of the mean relative velocity profile ($\partial U/\partial y \simeq 2\Omega$). Later, Kristoffersen and Andersson [20] confirmed the momentum redistribution in the central region of the flow at several Rotation numbers by means of DNS. However, the most characteristic effect of rotation is the influence of the Coriolis force on the turbulence characteristics. Depending on the sense of rotation and the local relative velocity gradient, the flow can be stabilized or destabilized by the Coriolis force. In a fully developed isothermal flow, Johnston et al. [21] associate the local flow stability to the local rotation number,

$$S = \frac{-2\Omega}{\frac{\partial\overline{U}}{\partial y}} \tag{1.7}$$

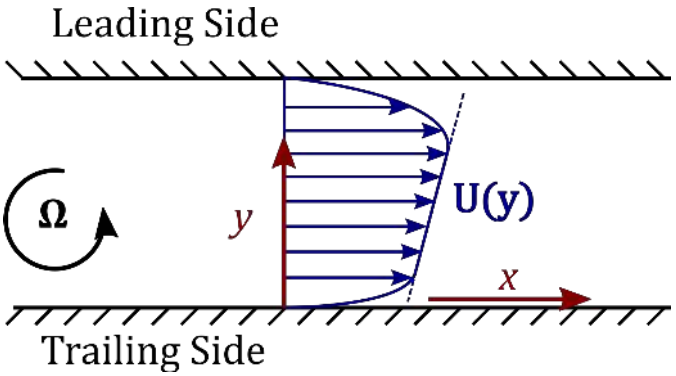

Figure 1.7 : Sketch of a channel flow under rotation

where Ω is the system angular velocity and $\frac{\partial \overline{U}}{\partial y}$ is the mean local relative vorticity. The flow is defined as cyclonic when the mean local relative vorticity presents the same sense as the rotation, resulting in a $S>0$. On the contrary, i.e. anti-cyclonic rotation, $S<0$. Lezius [19] and Johnston et al. [21] established a stability criterion based on the gradient Richardson number:

$$Ri = S(S+1) \tag{1.8}$$

When the flow is cyclonic, the gradient Richarson number is positive and the flow is stabilized by rotation. When the flow is anti-cyclonic, the flow can be stabilized or destabilized by rotation. Typically, from low to moderate rotational speeds, anti-cyclonic rotation leads to a destabilization of the flow. In the experimental observations by Johnston et al. [21] in a high aspect ratio channel, rolling structures oriented in the stream-wise direction were found in the area close to the wall, when the rotation was anti-cyclonic. These structures, identified as Taylor-Gortler vortices by Lezius and Johnston [19], were fully characterized by means of Direct Numerical Simulations (DNS) by Kritoffersen and Andersson [20]. However, the flow can be stabilized if the system rotation is sufficiently high, driving to $S<-1$. This concept is very important in the analysis of rotating internal cooling channels, where the mean relative vorticity presents different values through the section, hence presenting areas with stabilized and destabilized flow. As a result, the aero-thermal performance of the cooling channel is expected to vary with the rotational speed.

In the case of low aspect ratio channels, like those present in many internal cooling schemes, rotation induces large secondary flows oriented in the stream-wise direction. These secondary flows are induced by the unbalance between the Coriolis and pressure forces in some regions of the channel. Due to this unbalance, the fluid close to the walls moves perpendicularly to the main flow direction, generating large rolling structures occupying a considerable area. Due to the strength of these Coriolis-induced secondary flows, the momentum may be distributed even in the central region of the channel. The channel aspect ratio and orientation are the determinant factors on the impact of the secondary flows [22].

In incompressible flows, the centrifugal force is conservative and inconsequential to the resulting flow dynamics [21]. However, when large density gradients are present, the centrifugal force is not uniform and can introduce important buoyancy forces influencing the momentum distribution and the stability of the fluid motion. In the case of an infinite aspect ratio channel, Shat et al. [23] established a stability criterion based not only on the angular velocity and local vorticity, but also on the temperature gradient and thermal properties of the fluid. In the case of internal cooling channels in turbine rotors, the temperature gradients are significant, and do raise the importance of the buoyancy effects.

The dimensional analysis of the flow in internal cooling channels shows that the dimensionless parameters that influence the flow dynamics in a given geometry are the Reynolds (Re), Prandtl (Pr), Rotation (Ro) and Buoyancy (Bo) numbers:

$$Re = \frac{\rho_0 U_b D_H}{\mu} \tag{1.9}$$

$$Pr = \frac{\mu c_p}{k} \tag{1.10}$$

$$Ro = \frac{\Omega D_H}{U_b} \tag{1.11}$$

$$Bo = \frac{\Delta\rho}{\rho_0} Ro^2 \frac{r}{D_H} \tag{1.12}$$

where ρ_0 is the reference density of the fluid, U_b the bulk relative velocity, D_H the hydraulic diameter of the section, μ the molecular viscosity of the fluid, c_p the specific heat capacity of the fluid at constant pressure, k the thermal conductivity of the fluid, Ω the angular velocity, $\Delta\rho$ the overall density gradient and r the distance to the axis of rotation.

Many works investigating different geometries at diverse operating ranges are present in the literature. One of the most representative works applied to rotating internal cooling channels is the one carried out by Hajek et al. [24] and by Johnson et al. [25] during the NASA HOST Program. In the latter, the overall dimensionless heat transfer was measured in serpentine channels with different rib geometries and operating conditions. At the same time, the experiments aimed to provide reliable data to assess the Computational Fluid Dynamics (CFD) capabilities. Additional fundamental references are available in the reviews by Han et al. [16] and Ligrani [15]. However, most of the experimental data in rotating internal cooling channels provided in the literature are based on overall and point-wise measurements. Therefore, details on the flow dynamics and heat transfer in experimental studies are hardly ever documented in the open literature. Often, CFD results are validated with the point-wise available data, and used to provide a detailed vision of the phenomena taking place in the internal cooling scheme. However, CFD models are generally subjected to strong assumptions - especially in engineering applications- introducing high uncertainty. The goal of the present thesis is firstly to provide detailed heat transfer and fluid flow measurements within a large op-

erating range, and then to propose a CFD procedure to provide high-fidelity numerical predictions and to give a detailed picture of the entire flow field.

To understand the flow field and heat transfer in rotating cooling channels, Bons and Kerrebrock [26] performed Particle Image Velocimetry (PIV) and infrared measurements in a rotating smooth duct. The velocity measurements revealed the importance of the Coriolis-induced secondary flows and the effects of rotation on the turbulence and heat transfer. The dimensionless heat transfer coefficient distribution revealed the disparity of the thermal performance on the different walls of the duct. Recent works deal with more complex geometries, closer to the ones present in modern turbines. For instance, Elfert et al [27] employ PIV to investigate the secondary flows in a two-pass trapezoidal rotating cooling channel; Armellini et al [28] studied the flow in a modern trailing edge cooling scheme, and Furlani et al. [29] provided measurements in a triangular channel representative of a leading edge cooling channel.

Like in the previous examples, most of the experimental facilities used to investigate the detailed heat transfer and velocity field in rotating channels use the instrumentation in a stationary frame of reference, while the channel is rotating. This approach introduces a measurement error in the characterization of the flow boundary layer and specific algorithms need to be applied. To maximize the robustness and accuracy of measurements in rotating channels, the von Karman Institute (VKI) developed the RC-1 facility, were the instrumentation is fixed to the rotating frame. First, Di Sante et al. [30, 31] performed measurements in rotating divergent channels to investigate the flow physics in low Reynolds number centrifugal compressors. Later, Coletti et al. adapted the facility to perform PIV experiments in ribbed channels under the effects of the Coriolis forces [32] and centripetal buoyancy [33]. The investigated operating conditions corresponded to a Re equal to 15,000, a maximum Ro equal to 0.38 and a maximum Bo equal to 0.31. The geometry consisted in a channel with a low aspect ratio cross section and turbulators placed on one of the sides of the channel. A sketch of the geometry and the main flow features in static and rotating conditions is presented in Fig. 1.8, introduced by Coletti et al. [32].

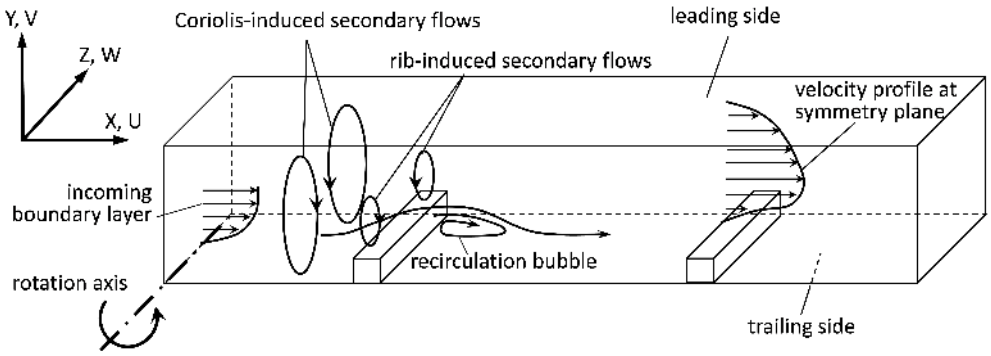

Figure 1.8 : Schematic view of the secondary flows system in a rotating ribbed duct [32]

The main characteristic of the flow in a ribbed cooling channel is the recirculation area that appears just downstream of the rib. The flow accelerates on the top of the rib, and due to the sudden change of section a strong shear layer is generated. The flow recirculates in the area between the shear layer and the wall. In internal cooling channels, the rib is introduced to increase the heat transfer area and to generate the shear layer to enhance the turbulent mixing and the heat transfer. The shear layer generated by the rib can reattach depending on the shear strength and the rib pitch. Therefore, the shape of the rib and the pitch are parameters that are widely investigated in the literature. Note also that due to the interaction between the rib and the lateral walls (planes at constant Z in Fig. 1.8), secondary flows are induced. These secondary flows are usually referred as *rib-induced secondary flows*, and have been rigorously characterized by Rau et al. [34] and Casarsa and Arts [35] in static conditions.

When the channel is rotating around the span-wise direction, as in Fig. 1.8, it is said that the channel is subjected to span-wise rotation. When rotation takes place, the wall leading the channel motion is generally addressed as *Leading Side* (LS), and the opposite side as *Trailing Side* (TS). Near the TS, the mean vorticity of the flow and the angular velocity vector present opposite directions. For this reason, the flow is called anti-cyclonic. On the contrary, the flow is cyclonic in the vicinity of the LS. Coletti et al. [32] and [33], investigated the effect of cyclonic and anti-cyclonic rotation in ribbed channels, showing the impact on the mean velocity and turbulence statistics. The previous experimental investigations showed that the turbulence activity is enhanced on the TS by rotation, hence reducing the size of the recirculation bubble after the obstacle. When the ribs are placed on the LS, the turbulence is greatly reduced, resulting in a large recirculation bubble. Moreover, due to the presence of lateral walls (sides perpendicular to the Z direction in Fig. 1.8), the Coriolis forces generate secondary flows occupying a large part of the test section. Close to the lateral walls, the Coriolis-induced secondary flows push fluid from the TS towards the LS. In the case of low aspect ratio channels such as in Refs. [32, 33], the Coriolis-induced secondary flows push the fluid back towards the TS in the midspan region of the channel. The measurements provided by Coletti et al. showed an increase of momentum close to the TS, and a reduction near the LS.

At higher rotation rates, however, the number of secondary flow cells may increase. The direct simulations by Kristoffersen and Andersson [20], showed that rotation thickens the laminar layer, reducing the effective area of turbulent flow where large stream-wise vortices appear. As a result, the size of these individual stream-wise vortices is also reduced, leaving room for an additional couple of vortices. To the author's best knowledge, there are no experimental investigations documenting the increase (or decrease) of the number of secondary flow cells in rapidly-rotating rib-roughened channels. Nevertheless, the Large Eddy Simulations (LES) by Addel-Wahab and Tafti [36] suggested the increase of the number of secondary flow cells at high rotation numbers in an internal cooling channel.

Several numerical investigations concerning rotating internal cooling channels are also found in the literature. Reynolds-Averaged Navier-Stokes (RANS) simulations are usually employed in the design process, due to the low computational cost and the relatively

acceptable results. For the same reasons, optimization algorithms employ RANS modeling to obtain the optimum design at a reasonable cost. Iacovides [37] compares effective viscosity and low-Re differential stress RANS models, finding a disparity with respect to experimental data of about 20% in the dimensionless heat transfer coefficient. Also, Unsteady-RANS (URANS) have been employed by Saha and Acharya [38], obtaining a good agreement with the experimental data of Johnson et al. [25] at different Rotation numbers. A Reynolds Stress Model (RSM) was employed by Sleiti and Kapat [39] to investigate the heat transfer and flow evolution in a serpentine channel under rotation, finding a good agreement with the experimental data provided at NASA [25].

Large Eddy Simulations are employed to investigate the phenomena in rotating ribbed channels with high reliability, but at higher computational costs. Murata and Mochizuki [40, 41] studied the flow and heat transfer by mean of LES taking into account the effects of the Coriolis and centripetal buoyancy forces. To reduce the computational costs, the Reynolds number of these simulations was somewhat lower than the one in real gas turbines. Nevertheless, the Reynolds number was high enough to guarantee fully turbulent flow, hence leading to representative flow and heat transfer. Adbel-Wahab and Tafti [36] and Sewall and Tafti [42] employed LES at representative Reynolds numbers (Re=20,000) although reducing the computational domain to one rib pitch and applying periodic boundary conditions. However, the validation was only possible by comparing with the overall experimental data provided by Johnson et al. [25] since no detailed experimental results were available for that specific geometry. The experiments of Coletti et al. [32] were used to validate the LES by Fransen et al. [43] and by Borello et al. [44]. Fransen et al. [43], simulated the entire test section in the experiments of Ref. [32] using the Wall-Adapting Local Eddy (WALE) viscosity model and an unstructured mesh. The simulations led to a good agreement in the static and stabilizing rotation cases. In the destabilizing rotation case, the numerical results did not fully reproduce the experimental mean statistics, likely due to the need for a refined mesh and the potential need to take into account the rotation effects adequately by the sub-grid scale (SGS) model. A finer mesh was presented by Borello et al. [44], yet reducing the length of computational domain to a single rib pitch and assigning periodic boundary conditions. The latter LES provided a good agreement with the data of Ref. [32] and a clear view of the secondary flows at the different rotating regimes. Recently, hybrid RANS/LES was applied by Kubacki et al. [45] and by Xun and Wang [46] in the same configuration as in Ref. [32]. This methodology does not require such a refined mesh, yet reproducing the main flow features under rotating conditions.

Note that in parallel to these LES studies, Narasimhamurthy and Andersson [47] obtained high-fidelity flow statistics by means of DNS in a ribbed channel subjected to system rotation. However, the mesh refinement required in DNS limits the Reynolds number in the simulated case. Moreover, the case investigated in Ref. [47] represents an infinite aspect ratio channel, that is, no lateral walls are present. Therefore, the Coriolis-induced secondary flows present in turbine cooling channels were not generated.

1.5 Aims of the present work

According to the literature review, there are still several questions concerning the flow in rotating internal cooling channels. The increase/decrease of turbulence by rotation and the interaction between the Coriolis-induced secondary flows, rib-induced secondary flows and separation bubbles lead to a complex fluid flow and heat transfer distribution highly dependent on the operating regime. The main objective of the present thesis is to provide a detailed description of the flow and heat transfer in rotating cooling channels at different regimes, sustained by highly reliable experimental data.

This work introduces a laboratory test section that can operate ribbed channels over a wide range of Reynolds, Rotation and Buoyancy numbers. In the present work, the Reynolds number ranges from 15,000 to 55,000, a maximum Rotation number equal to 0.78, and a maximum Buoyancy number equal to 0.78. The new experimental facility consists in a versatile design that allows the interchangeability of the tested geometry, so that channels of different aspect ratios and rib geometries can be easily fitted.

The geometry selected to perform the present investigation corresponds to a magnified version of the channel studied by Coletti et al. [32, 33] in order to achieve larger Reynolds and Rotation numbers. This geometry does not mimic the specific shape of the internal cooling channels of modern turbine blades, but is able to represent the main mechanisms that rule the behavior of the fluid motion and heat transfer. Due to the simple geometry, the experimental setup requirements are simplified and the measurement uncertainty is largely reduced.

Since the measurement uncertainty is generally large in heat transfer investigations, a substantial effort was made to asses the sources of measurement error. A methodology for heat transfer measurements and uncertainty estimation in rotating cooling channels has been developed in the present study. Additionally, the uncertainty in the velocity measurements is also provided. In this way, the experimental results are well documented to be used as CFD validation data.

Furthermore, Large Eddy Simulations are performed to provide information about the flow field and heat transfer over the whole domain. Since the experimental techniques provide information in limited areas of the region of interest, the use of Large Eddy Simulations is interesting to support the experimental observations, thereby providing the full picture of the flow field and heat transfer phenomena, and to set a solid procedure for reliable CFD predictions. The present work aims to provide a methodology (algorithms, mesh quality, turbulence modeling) that leads to high-fidelity results at dimensionless engine operating conditions. Moreover, the numerical results are obtained by means of an open source CFD toolbox, which would allow the community to reproduce them.

Chapter 2

Case description

2.1 Case presentation and nomenclature

The present work aims to analyze the flow field and heat transfer in a rotating cooling channel as shown in Fig. 2.1. Since the conditions that exist in advanced turbine blades are extreme, it is extremely complex to perform detailed laboratory experiments within the same environment (temperatures, pressures, etc.). However, dimensional analysis [48] shows that it is possible to reproduce the specific phenomena if the dimensionless governing parameters are preserved. In this way, tests are carried out with magnified models at pressures and temperature close to the ambient conditions. However, the results that are obtained in the laboratory need to be non-dimensionalized in order to be applicable to real engine conditions. In other words, the dimensionless velocity and heat transfer coefficients provided by the experiments will be equal to those found in real engines if every dimensionless governing parameter is maintained.

In this chapter, the magnitudes that affect the flow and heat transfer phenomena are analyzed to determine these relevant dimensionless parameters. The case under consideration is a simplification of a modern internal cooling channel such as that shown in Fig. 1.6, in order to reproduce the main flow physics and provide a complete view. The configuration studied in the present investigation is depicted in Fig. 2.1. The cross-section of the channel is almost square, that is, of low aspect ratio. One of the channel walls is equipped with ribs in order to generate a highly turbulent flow and to enhance the heat transfer. These ribs are placed perpendicularly to the main flow direction. The fluid motion is investigated in a frame of reference fixed to the rotating channel. This relative frame of reference is such that the X-axis corresponds to the stream-wise direction, the Y-axis is perpendicular to the ribbed wall, and the Z-axis corresponds to the span-wise direction. Therefore, each point in the domain is defined by the x, y and z coordinates in that frame of reference. The channel is rotating around the Z axis at an angular speed Ω. This kind of channel rotation is often called span-wise or orthogonal rotation due to the relative orientation of the main flow direction and the axis of rotation. In the present work, Ω is taken as positive if the angular velocity vector is directed in the positive sense of the Z axis, as in Fig. 2.1, and negative in the opposite

case.

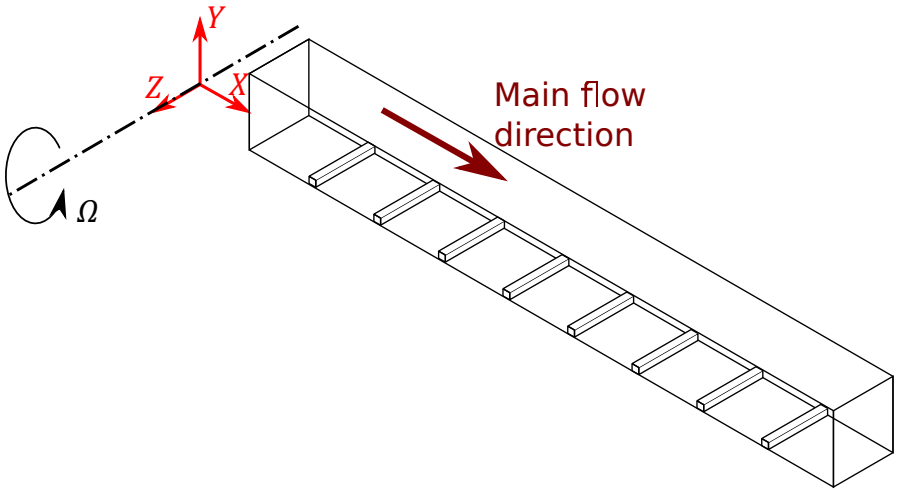

Figure 2.1 : Schematic view of the channel

The fluid enters the channel with a density ρ_0, a pressure p_0 and a temperature T_0. The molecular viscosity of the fluid is represented by μ, the thermal conductivity by k and the specific heat at constant pressure by c_p. The characteristic speed is the bulk velocity U_b, which is the mean flow velocity in the relative frame of reference. At each location, the mean velocity components are represented by U (stream-wise), V (vertical) and W (span-wise), whereas the mean pressure is designated as $\overline{p}$. In the present configuration the wall is heated up, presenting an overall temperature T_w, and leading to a non-uniform temperature field and density variations. The mean temperature at each location is designated as T, and the density variations as $\Delta\rho$. In this way, the local density ρ is related to the density variations as $\rho = \rho_0 + \Delta\rho$.

The capabilities of the experimental facilities to test the flow field and heat transfer in models of internal cooling channels inside turbine rotor blades are under analysis (Fig. 1.8). The non-dimensional parameters which assure the appropriate representation of the phenomena in laboratory experiments are determined: Reynolds (Re), Prandtl (Pr), Rotation (Ro) and Buoyancy (Bo) numbers, apart from the geometric similarity. Once provided, the non-dimensional velocity and pressure fields as well as the heat transfer to the surrounding solid are determined. These values, constituted as overall quantities, may vary along the length of the channel since the flow conditions vary with the position, and lead to local effects. In order to quantify these variations in a real gas turbine cooling channel, the preliminary design of the cooling system presented in the NASA CR-165608 report [49] is evaluated in section 2.4.

2.2 Application of the Π-Buckingham theorem

To determine the dimensionless parameters that define the physical state of the system, the Π-Buckingham theorem [48] is employed. Table 2.1 provides the 18 dimensional parameters that are involved in the present case, including the spatial location, velocities and thermodynamic properties. On the other hand, Table 2.2 provides the absolute units that define the dimensional magnitudes of the problem. For the sake of brevity, the geometrical characteristics of the system are omitted, with the exception of the hydraulic diameter. Also, time has not been included due to the chaotic nature of the fluid motion. By applying the Π-Buckingham theorem we are able to determine a reduced group of 14 non-dimensional parameters which describe the physical system:

$$\psi\left(\frac{x}{D_H},\frac{y}{D_H},\frac{z}{D_H},\frac{u}{U_b},\frac{v}{U_b},\frac{w}{U_b},\frac{p}{\rho_0 U_b^2},\frac{\mu}{\rho_0 U_b D_H},\frac{\Omega D_H}{U_b},\frac{\Delta\rho}{\rho_0},\frac{T}{T_0},\frac{T_w}{T_0},\frac{\mu c_p}{k},\frac{c_p T_0}{U_b^2}\right)=0 \tag{2.1}$$

or in the usual dynamic parameters employed in the Navier-Stokes equations,

$$\psi\left(\frac{x}{D_H},\frac{y}{D_H},\frac{z}{D_H},\frac{u}{U_b},\frac{v}{U_b},\frac{w}{U_b},\frac{p}{\rho_0 U_b^2},Re^{-1},Ro,\frac{\Delta\rho}{\rho_0},\frac{T}{T_0},\frac{T_w}{T_0},Pr,Ec^{-1}\right)=0 \tag{2.2}$$

Now, if the problem is modeled by means of the continuity, momentum, energy and state equations we find a system of 6 equations defined by the 14 parameters shown in Eq. (2.2), hence providing 8 degrees of freedom. Thus, if we fix 8 of these parameters, the others are determined. For example, by fixing the position (x/D_H,y/D_H,z/D_H), Re, Pr, Ro, Ec, and T_w/T_0 we would obtain the dimensionless velocity, pressure gradient, temperature and density. If time is included as a parameter, the initial condition of the system and the time value would need to be specified in order to determine the complete final state.

It is important to note that even if this analysis has provided a great simplification, it is necessary to use the Navier-Stokes equations in order to find practical relations between variables. For instance, we shall see that the Pr number does not have a direct impact neither on the velocity nor on the pressure fields under the conditions of the present case. Moreover, the magnitude of these dimensionless parameters need to be determined in order to allow the reproducibility of the results in experimental models run at similar conditions.

Table 2.1 : Physical parameters

#	Symbol	Description	Units
1	ρ_0	Reference density	kg/m^3
2	p_0	Reference pressure	kg/m^3
3	T_0	Reference temperature	K
4	D_H	Reference length	m
5	U_b	Reference velocity	m/s
6	T_w	Reference wall temperature	K
7	u	Stream-wise velocity	m/s
8	v	Vertical velocity	m/s
9	w	Span-wise velocity	m/s
10	p	Pressure	kg/m^2
11	μ	Molecular viscosity	$kg/(m \cdot s)$
11	x	Stream-wise position	m
12	y	Vertical position	m
13	z	Span-wise position	m
14	Ω	Angular velocity	rad/s
15	T	Temperature	K
16	c_p	Specific heat capacity at constant pressure	$J/(kg \cdot K)$
17	k	Thermal conductivity	$J/(s \cdot m \cdot K)$
18	$\Delta\rho$	Reference density variations	K

Table 2.2 : Absolute units in the dimensional analysis

#	Absolute units
1	kg
2	m
3	s
4	K

2.3 Dimensionless equations

The fluid motion is investigated in the rotating frame of reference represented in Fig. 2.1, fixed to the rotating channel. Therefore, the Navier-Stokes equations are expressed in terms of the fluid velocity relative to this frame. In order to simplify the equations, the density variations in space and time are assumed to be small with respect to the mean value. In this way, $\rho/\rho_0 = 1 + \Delta\rho/\rho_0$, with $\Delta\rho/\rho_0 \ll 1$. Under these conditions, the fluid motion equations in the rotating frame of reference are written as follows:

- continuity

$$\nabla \cdot \mathbf{u}^* = 0 \tag{2.3}$$

- momentum

$$\frac{\mathrm{D}\mathbf{u}^*}{\mathrm{D}t} = -\nabla p^*_{eff} + \frac{1}{Re}\nabla^2\mathbf{u}^* - 2Ro \cdot \mathbf{e}_\Omega \times \mathbf{u}^* + \frac{\Delta\rho}{\rho_0} \cdot Ro^2 \cdot (x^* \cdot \mathbf{e_x} + y^* \cdot \mathbf{e_y}) \tag{2.4}$$

- energy

$$\frac{\mathrm{D}\Theta}{\mathrm{D}t} = \frac{1}{Re}\frac{1}{Pr} \cdot \nabla^2\Theta + \frac{Ec}{Re} \cdot \Phi^* \tag{2.5}$$

- state

$$p = \rho RT \iff \frac{p}{\rho_0 U_b^2} = \left(1 + \frac{\Delta\rho}{\rho_0}\right) \cdot \frac{\gamma - 1}{\gamma} \cdot \frac{1}{Ec} \cdot \left[\left(\frac{T_w}{T_0} - 1\right)\Theta + 1\right] \tag{2.6}$$

where $\mathbf{u}^* = \frac{\mathbf{u}}{U_b}$ is the dimensionless velocity vector in the rotating frame of reference, $p^*_{eff} = \frac{p - 1/2\rho_0\Omega^2\left(x^2+y^2\right)}{\rho_0 U_b^2}$ the dimensionless effective pressure, $\Theta = \frac{T - T_0}{T_w - T_0}$ the dimensionless temperature, $x^* = \frac{x}{D_H}$ and $y^* = \frac{y}{D_H}$ are the dimensionless axial and vertical coordinates, Φ^* the dimensionless viscous dissipation tensor, and γ the fluid heat capacity ratio. The effective pressure gradient can be interpreted as the combination of the static pressure gradient with the centrifugal force gradient to which the fluid is subjected as the flows evolves in the x and y directions.

At low buoyancy, $Bo \approx \frac{\Delta\rho}{\rho_0} \cdot Ro^2 \cdot x^* \ll 1$, the last term of Eq. (2.4) vanishes. In such a case, the continuity and momentum equations are uncoupled from the energy and state equations. Therefore, if Re and Ro are provided, the dimensionless velocity vector and effective pressure are determined.

Besides, the dimensionless heat transfer distribution, i. e. Nusselt number, defined as

$$Nu = \frac{hD_H}{k} \tag{2.7}$$

can be approximated as

$$Nu \approx -\frac{k\nabla T \cdot \mathbf{n}}{T_w - T_b} \cdot \frac{D_H}{k} = -\nabla\Theta \cdot \mathbf{n} \cdot \frac{T_w - T_0}{T_w - T_b} \approx -\nabla\Theta \cdot \mathbf{n} \tag{2.8}$$

if the thermal conductivity, k, does not present important variations ($\mathbf{n}$ represents the unit surface vector), T_b is taken as the reference temperature of the flow (T_0), and $\nabla T \cdot \mathbf{n}$ represents the wall-normal temperature gradient. Thus, if the Pr is given, the dimensionless temperature Θ and the Nusselt number are determined.

However, important temperature and density variations are linked to centripetal buoyancy and may also lead to relevant variations of the thermodynamic properties. Thus, the resulting velocity and pressure fields and heat transfer on the walls may be totally different from the previous case. Therefore, the work in the present thesis considers the low and high centripetal buoyancy scenarios in order to assess the fluid dynamics in cooling channels over a wide operating range.

2.4 Engine conditions

A stated above, the performance of the cooling design is determined mainly by the Reynolds, Prandtl, Rotation and Buoyancy numbers. Based on investigations present in the open literature, Ligrani [15] (Fig. 2.2) provides a notion of the typical Reynolds, Rotation and Buoyancy numbers in rotating internal cooling channels. The Reynolds number presents an order of magnitude ranging from 10^4 to 10^5; the Rotation and Buoyancy numbers range from 0 to 1. Nevertheless, the actual operating conditions in commercial gas turbines are hardly ever reported.

One of the few examples concerning real internal cooling geometries is the article by Lott et al. [50]. In this paper, aerothermal optimizations are carried starting from designs given by MTU and SNECMA. The Reynolds numbers in the cooling channels are 20,000 and 13,000, respectively. In the case of the SNECMA cooling channel, the optimization is carried out under rotation, with Ro = 0.16 - 0.3.

In the present section, the NASA report CR-165608 [49] has been analyzed to estimate the order of magnitude of the non-dimensional parameters in a real jet engine, as well as the fluid properties. From the Table 4.1-I in Ref. [49] we see that the corrected mass flow through the turbine at design conditions (M=0.8, 35,000 ft) is $FP_{in}\left(W\,[LBM/s]\cdot\sqrt{T_T\,[^oR]}/p_T\,[psia]\right)$ =16.984, while the total temperature is 2940°R (1633K) and the total pressure is 192.1 psia (1,324,491 Pa). Assuming the conditions of the International Standard Atmosphere, the ambient pressure at 35,000 ft is 41,390 Pa, so that the overall pressure ratio of the engine is about 32. This value is in accordance with the typical values of the overall pressure ratio of the jet engines from the 80s. On the other hand, it is mentioned that the cooling system design condition corresponds to the takeoff in a hot day at the sea level. Under these conditions, the total pressure at the turbine inlet should be about 435 psia (3 MPa) and the total temperature is 3076°R (1709 K). Assuming that the reduced mass flow at takeoff is equal to the one at the design condition, the turbine mass flow in the cooling design condition is about 133 LBM/s, that is, 60 kg/s.

It is reported that during takeoff, the coolant flow through these channels is equal to the 1.72 % of the core engine inlet flow. Therefore, the coolant flow through the serpentine channels in the rotor is, 1 kg/s. Since the number of rotor blades is 54, the

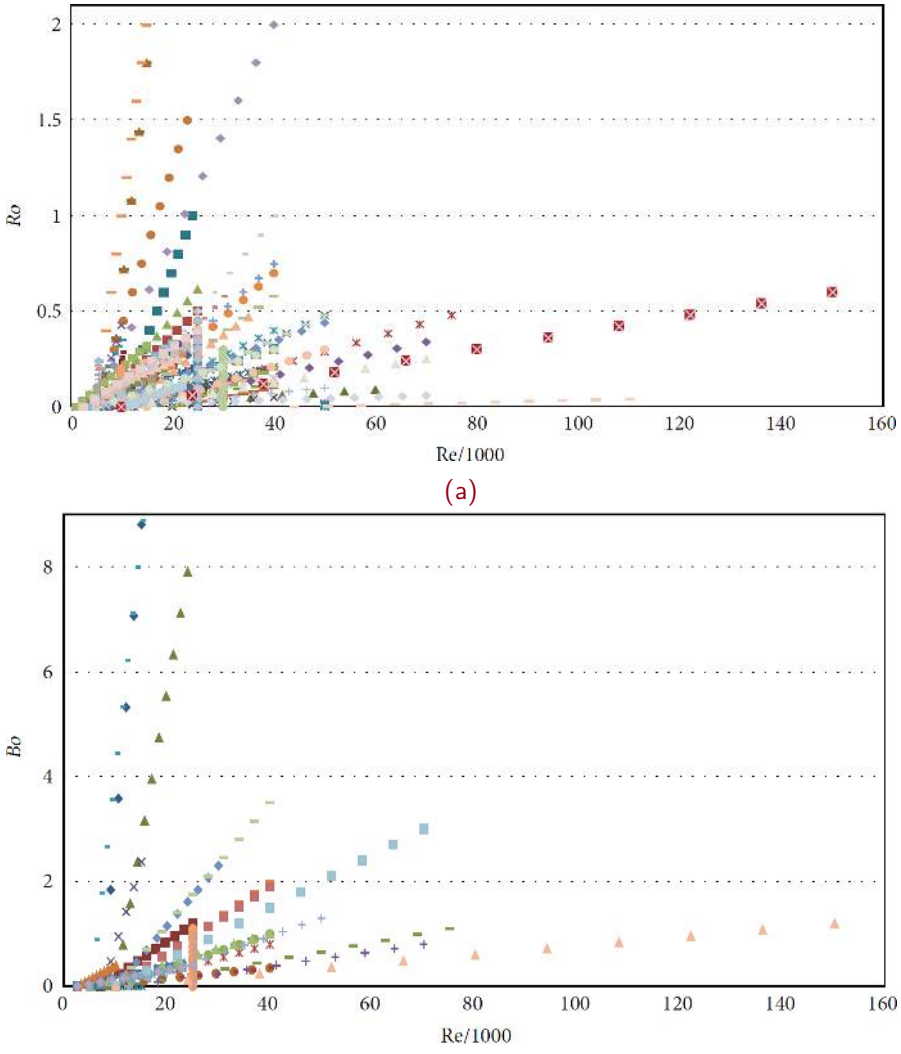

Figure 2.2 : Ranges of Re, Ro and Bo in published experimental investigations [15]

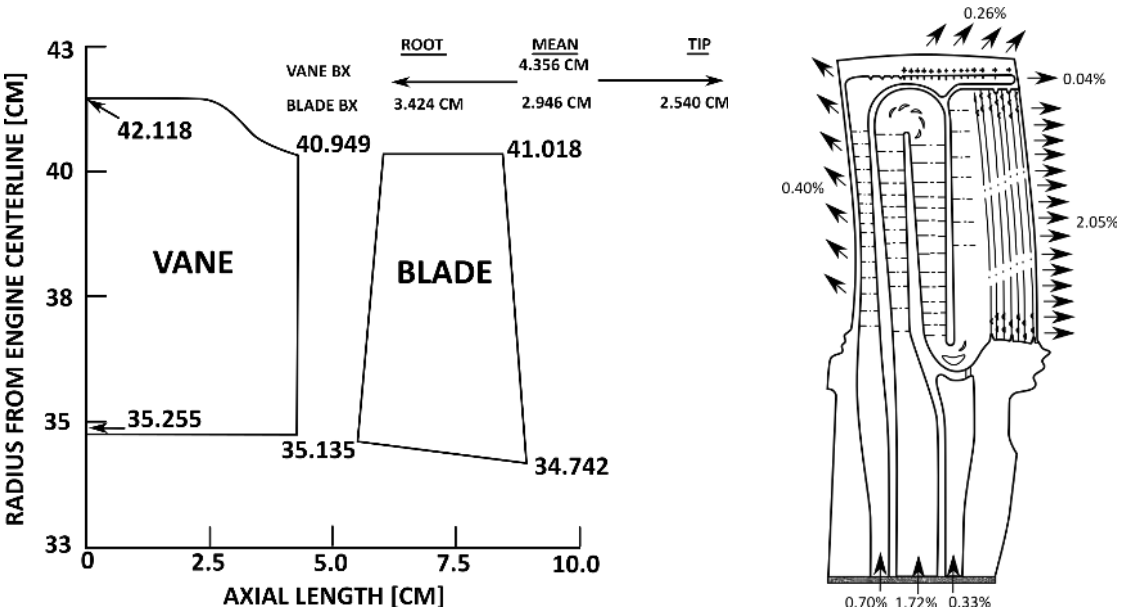

Figure 2.3 : Sketch of the turbine flow path (a) and turbine rotor cooling system (b) given in Ref. [49]

mass flow in each internal cooling channel is about 20 g/s. Knowing the mass flow in the channel, its cross section area and the fluid density, it is possible to obtain the bulk velocity. The fluid at the inlet of the cooling system is at 1.7 MPa and 550°C. Thus, the density of the fluid is 7 kg/m^3. Taking the cross section area of the cooling channel equal to 30 mm^2, and provided the mass flow, the bulk velocity is estimated to about 90 m/s. The corresponding Mach number is of order of 0.15. All obtained quantities lead to a Reynolds number of about 20,000. Since the rotational speed of the rotor at the design point is 13232 rpm, the Rotation number presents an order of magnitude equal to 10^{-1}.

In order to estimate the Eckert and Buoyancy numbers, it is necessary to consider the difference in temperature between the fluid and the metal. Since this difference is nearly 400K the resulting Eckert number is of the order of 10^{-3}, whereas the Buoyancy number, $Bo = \frac{\Delta\rho}{\rho_0} Ro^2 \frac{r}{D_H}$, is of order 10^{-1}.

However, because of the pressure losses and heat transfer, the properties of the fluid and solid change along the channel. The pressure gradient in the channel is of the order of the momentum flux, so that the pressure loss in a length x scales as $\Delta p \sim \rho_0 U_b^2 x/D_H$. For a typical length of 40 mm, and with the properties previously estimated, $\Delta p \sim 4\times10^5$ Pa, so that $\Delta p/p_0 \sim 20\%$. Regarding the temperature variations, it is necessary to apply an energy balance between the fluid and the solid in order to assess the bulk temperature T_b at a distance x downstream of the inlet:

$$\dot{m}c_p\left[T_b(x)-T_0\right] \sim h\left(T_w-T_0\right)\cdot\Pi\cdot x = \frac{Nu\cdot k}{D_H}(T_w-T_0)\cdot\Pi\cdot x \tag{2.9}$$

where Π is the cross section perimeter. The Nusselt number, Nu, presents an order of magnitude equal to the one extracted from the Dittus-Boelter correlation at the same Reynolds number and with a fluid with the same Prandtl number, that is, $Nu \sim 50$. For a typical perimeter of 20 mm, and a channel length of 40 mm, the relative bulk temperature variation is hence

$$\frac{T_b(x)-T_0}{T_w-T_0} \sim \frac{Nu\cdot k}{D_H}\cdot x\cdot\Pi\cdot\frac{1}{\dot{m}c_p} \sim 1\% \tag{2.10}$$

These values have been calculated with averaged, and roughly estimated, quantities of the physical properties of the system. Thus, they do not constitute an accurate measurement of the real quantities found in the real model, but rather an estimation of the non-dimensional parameters. The present work addresses the flow field and heat transfer phenomena at a representative operational range, with Re = 15,000 - 55,000, Ro = 0 - 0.78, Bo = 0 - 0.78 and Pr = 0.72.

Chapter 3

Experimental setup and data reduction

3.1 The RC-1 facility

The development of the RC-1 facility at the von Karman Institute for Fluid Dynamics started in the year 2004 with the objective of providing detailed and accurate data of the flow in centrifugal compressors of micro gas turbines, and in the internal cooling channels of turbine rotor blades. Di Sante (2005, 2010) presented a review of the existing investigations in the open literature, and demonstrated the possibility to provide highly accurate data with the recent advances in CMOS recording devices and laser systems. Prior to that, most of the experimental data concerning rotating channels were based on overall quantities or point-wise measurements. Therefore, no velocity gradients and flow structures were able to be characterized. Very few exceptions such as the work of Bons and Kerrebrock (1998) were able to provide the full velocity field and heat transfer on different planes. Nevertheless, the instrumentation was placed in a fixed frame of reference while the test section was rotating, which introduced important errors in the velocity measurement. The resulting bias error was indeed about 4%.

The key decision taken during the RC-1 design process was to place the required instrumentation in the rotating frame of reference on which the test section was installed; this allowed to obtain the same measurement resolution and accuracy as in a stationary facility. Di Sante (2010) demonstrated that it was possible to reduce the measurement uncertainty by one or two orders of magnitude (depending on the rotational speed) with respect to the case of a stationary PIV system performing measurements of a rotating boundary layer. However, an innovative selection of the PIV instrumentation was also necessary. The PIV components were required to provide accurate measurements while being robust enough to withstand the large centrifugal forces, and light enough to minimize mechanical stresses on the facility. To reduce the weight of the setup, an air-cooled compact continuous laser module of 25W was selected to illuminate the seeding particles instead of a large laser commonly used in PIV applications.

The typical PIV system employed at that time consisted in a large and high-power Nd:YAG laser and a CCD camera with a large sensor and reduced pixel size. The high-power laser allowed obtaining low noise particle images, whereas the CCD camera provided a large dynamic range in terms of spatial resolution and velocity measurement. However, the size and weight of the laser were the primary factors that limited its operation in the rotating facility. In the mean time, light and compact diode lasers were available on the market providing a power of 10-30 W at a reasonable price. These lasers were not common in PIV applications due to their limited power, but they were ideal to obtain low-noise PIV images at low fluid velocities (about 1-5 m/s) with a minimal weight. The laser selected by Di Sante et al. [30, 31] was a Unique Mode UM25k diode laser, which provided a 25W laser beam at 806 nm. Additionally, an optical fiber was connected to the laser beam exit, which increased the robustness of the optical setup: optical mirrors and supports were not needed anymore due to the capability of the optical fiber to bring the laser beam anywhere in the facility. At the end of the optical fiber, a compact optical module was installed to generate the laser sheet required to illuminate the region of interest.

In order to record the light scattered by the PIV seeding particles at the laser wavelength, a Phantom 7.1 CMOS high speed camera was employed. Note that the sensitivity of conventional PIV cameras was drastically reduced at the laser wavelength, whereas the selected camera still presented high sensitivity. Moreover, the use of a high speed camera allowed Time-Resolved PIV (TR-PIV) measurements, which provided the time evolution of the velocity field and its coherent structures. In order to increase the accuracy of the mean velocity fields, a memory gate controller was designed and connected to the high speed camera. This controller allowed to increase the time between consecutive PIV realizations, resulting in statistically independent velocity fields. In this way, the statistics resulting from a series of PIV realizations were more representative of the actual mean velocity field.

Figure 3.1 shows the original experimental setup and first configuration tested in the RC-1 facility. The test section selected for the first investigations [31, 51] consisted in a diverging smooth channel to study the Coriolis force effects in the boundary layers of low Re centrifugal compressors. The investigations carried out were especially important in the case of micro gas turbines, where the rotational effects are significant due to the large angular velocity. Later, Coletti et al. adapted the facility to investigate the flow field in ribbed channels in static [52] and rotating conditions [32, 33]. The channel cross section was kept constant in the stream-wise direction, a rectangle of 75×83 mm^2 (the size of the inlet in Refs.[31, 51]). Eight ribs with squared cross section were placed on one wall perpendicularly to the main flow direction. Moreover, the ribbed wall in ref. [33] was made of copper and was heated up in order to generate centripetal buoyancy effects. Despite the fact that the geometry did not replicate the actual geometry of internal cooling channels of turbine blades, it allowed to reproduce the main flow mechanisms at engine-like conditions. The accuracy of the data and the interpretation of the flow presented in Refs. [32, 33, 52] turned this research into a fundamental reference in the internal cooling field. Figure 3.2 shows an example of the measurements presented



Figure 3.1 : Frontal view of the RC-1 original setup [30]

in Ref.[32], taken in the symmetry plane of the channel several hydraulic diameters downstream of the inlet, between the 6th and 7th ribs. The measurements demonstrated and quantified the effects of rotation in internal cooling channels, presenting accurate data in the region close to the wall at different rotation regimes. Additionally, several works have addressed the data in Refs.[32, 33, 52] for turbulence modelling and CFD validation purposes [43–46].

The investigations carried out in the RC-1 facility were limited in terms of Reynolds and Rotation numbers due to the reduced length of the test section. Since the measurements are typically performed 6 - 7 rib pitches downstream of the inlet, the channel length is required to be at least equal to 9 times the rib pitch to avoid exit disturbances. The space available in the RC-1 facility was equal to the disk radius minus the length of the inlet elbow, that is, about 750 mm. In this way, the selected rib pitch was equal to 80 mm. One of the goals of the present work was to introduce a scaled-up test section, similar to those of Refs. [32, 33], taking advantage of the whole disk diameter to increase the channel dimensions and the Reynolds number. For a given Reynolds number, the bulk velocity can be expressed as

$$U_b = \frac{Re \cdot \nu}{D_H} \tag{3.1}$$

Therefore, an increase of the hydraulic diameter reduces the required bulk velocity. This is a very important fact for the nature of the PIV system employed in this investiga-

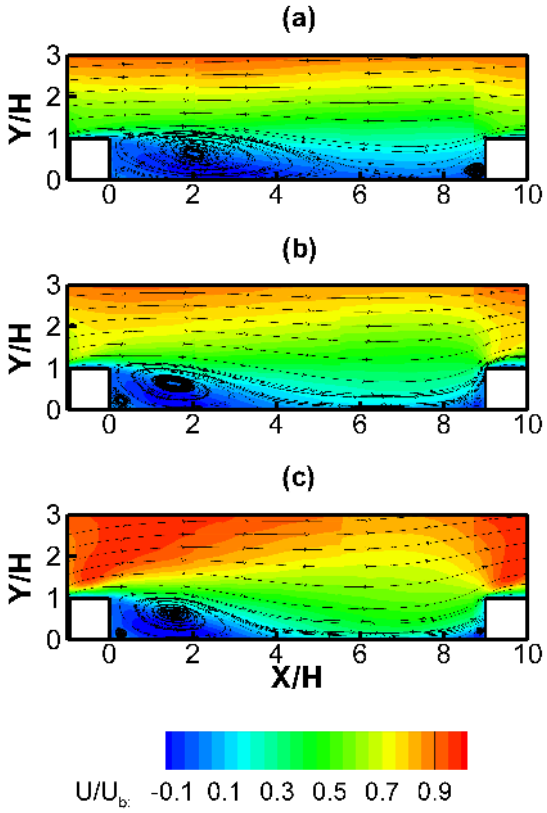

Figure 3.2 : Stream-wise velocity contours and in-plane streamlines in the symmetry plane of a rotating ribbed channel: Leading Side, $Ro = 0.30$ (a); static, $Ro = 0$ (b); Trailing Side, $Ro = 0.30$ [32]

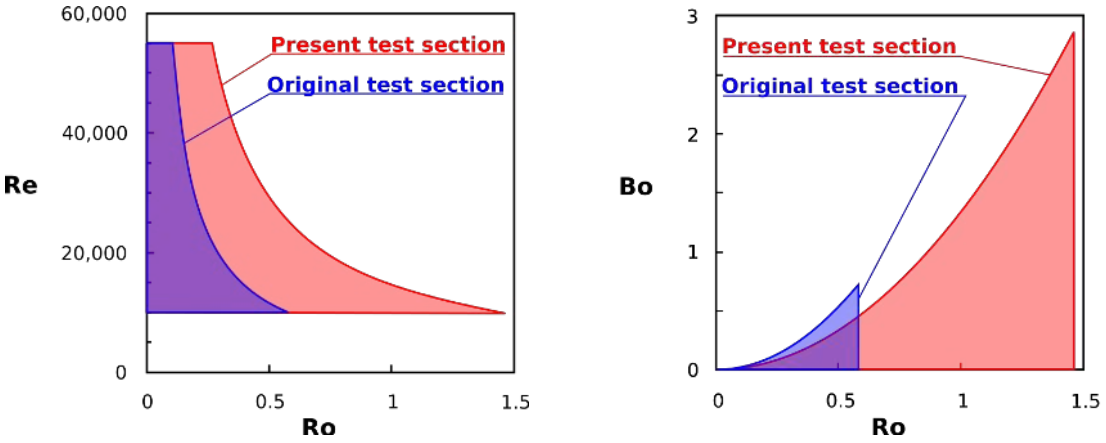

Figure 3.3 : Comparison of the operational range between the new and the original facilities

tion, since the maximum measurable U_b is determined by the laser power and sensitivity of the camera. Thus, an increase of the hydraulic diameter also allowed increasing the Reynolds number. On the other hand, the Rotation number can be expressed as

$$Ro = \frac{\Omega \cdot D_H^2}{Re \cdot \nu} \tag{3.2}$$

Equation (3.2) shows that the increase of the hydraulic diameter has a large impact on the Rotation number. Therefore, an increase of the hydraulic diameter brings more freedom to select the operating regime in terms of Reynolds and Rotation numbers. However, the increase of the channel dimensions leads to a heavier test section and a limitation of the maximum rotational speeds for safety reasons.

The test section introduced in the present work allowed measurements in a wide operational range, with the Reynolds number ranging from 15,000 to 55,000, and a maximum Rotation number equal to 0.2 in the case of Re = 55,000, and equal to 1.0 in the case of Re = 15,000. A comparison of the operational range between the new test section and the original one is represented in Fig. 3.3. Although the facilities were able to investigate flows at Re < 10,000, this range has not been included in Fig. 3.3 for the sake of clarity. Moreover, the versatile design of the test section permits the easy interchange of the channel geometry, such as the aspect ratio, rib geometry, etc. A second objective was to perform Liquid Crystal Thermography (LCT) to study the heat transfer performance of the selected geometry at the same conditions as in the PIV experiments. The possibility of combining the dimensionless velocity and heat transfer fields in the same experimental conditions is one of the qualities that makes the RC-1 facility an unique system for internal cooling research. Additionally, a significant effort was made to quantify and to reduce the measurement uncertainty, leading to highly reliable results.

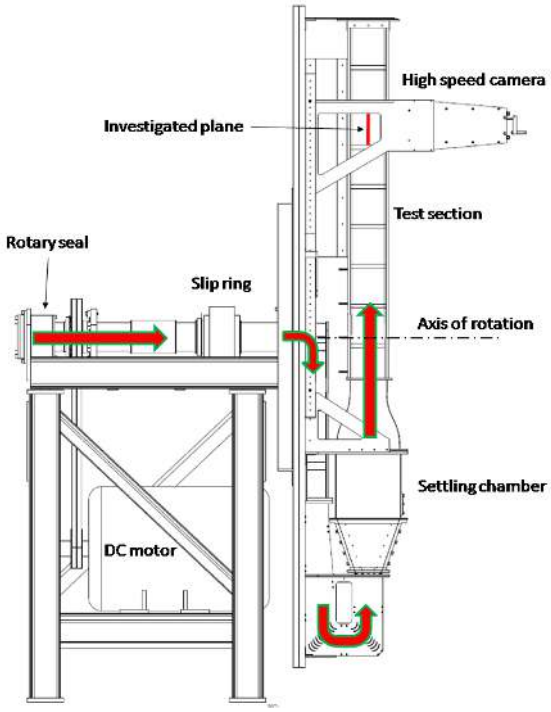

Figure 3.4 : Test section sketch (as introduced in Ref.[53])

3.2 Test section

A sketch of the test section employed in the present investigation is shown in Fig. 3.4. Basically, the channel shown in Fig. 3.1 was substituted by wind tunnel mounted on the rotating disk. The modification of the test section on the RC-1 facility has been performed according to the following goals:

- maximization of the hydraulic diameter in order to achieve large Reynolds and Rotation numbers,
- design of a smooth test section inlet to obtain a symmetric inlet velocity profile, free of secondary flows and large turbulent fluctuations,
- versatile design, allowing a simple interchange of the experimental models.

Several design constraints were present, such as the minimization of the weight and mechanical stresses, the available space and some manufacturing limitations. The use of wood or acrylic glass as base material was discarded due to the expected vibrations and mechanical stresses. Instead, aluminum was employed to manufacture most of the wind tunnel components, with the exception of the test model. The use of aluminum lead to a robust design (especially in compromised areas such as flanges), reduced the facility weight and simplified the manufacturing process.

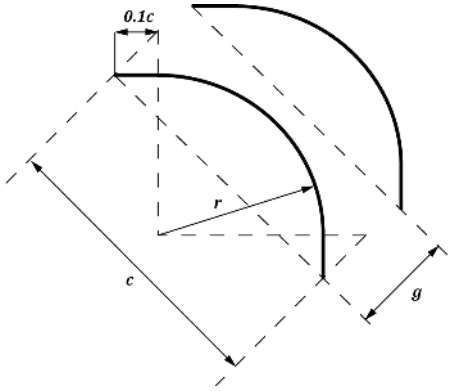

Figure 3.5 : Sketch of the turning vanes in the U-bend

Figure 3.4 also shows the main flow path in the final test section. The air crosses the center of the disk to turn into a 90 degrees bend, and then it moves radially outwards until reaching a U-bend equipped with turning vanes. The turning vanes are disposed in two cascades of 10 blades, at each corner of the U-bend. The design of the turning blades was carried out following the considerations given by Pankhurst and Holder [54] in order to avoid separation and minimize pressure losses. The shape of the blades consist in a circular arc with leading and trailing edge plates, as shown in Fig. 3.5. The total blade chord, c_{blade}, is related to the corner radius, r_{corner}, as

$$c_{blade} = \frac{r_{corner}}{\frac{1}{\sqrt{2}} - 0.1} \tag{3.3}$$

For a $r_{corner} = 25$ mm, the resulting blade chord is about 41 mm. The blade pitch to chord ratio is equal to 0.3, which leads to a blade pitch of 12.3 mm. Downstream of the U-bend, a honeycomb and two screens have been glued to reduce the turbulent fluctuations and the velocity shear in the core of the flow. The honeycomb cell size and length are respectively equal to 3 mm and 19 m. The resulting honeycomb length to cell size ratio is between 6 and 8, as recommended by Sheiman [55]. The distance from the honeycomb to the first screen is equal to 15 mm, 5 times the honeycomb cell size, which is the maximum distance recommended by Farell and Youseff [56] and Loeherke and Nagib [57]. A second screen is placed 40 mm downstream of the first one, in order to optimize the turbulence reduction [55]. Further downstream, the flow crosses a diffuser equipped with 5 equidistant screens to avoid separation and turbulence generation. The number of screens has been calculated by balancing the turbulence increase in the present diffuser with the turbulence reduction caused by the screens [58]. Then, the fluid enters the settling chamber, where the velocity and turbulent fluctuations are drastically reduced due to the large cross section. Moreover, a honeycomb and two screens with the same characteristics as those located downstream of the U-bend are installed in the settling chamber. After the settling chamber, the flow crosses a contraction that is adapted to the selected experimental model and enters finally the test model. The length of the

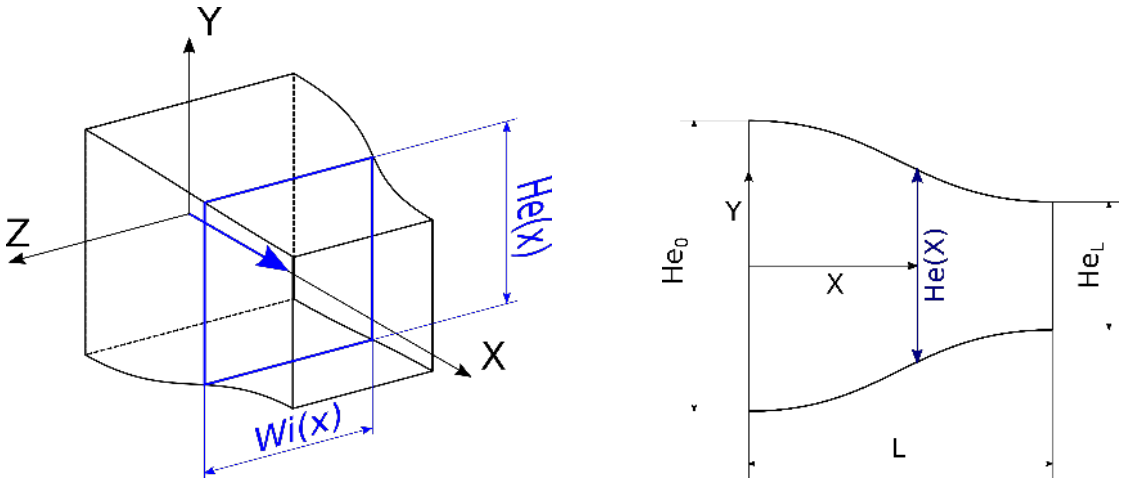

Figure 3.6 : Sketch of the inlet contraction

contraction is the same as the settling chamber width. The height and width of the contraction at a given axial position follow a 7th-degree polynomial in order to have a smooth curvature transition from the settling chamber to the investigated channel [59]. Four conditions are imposed at the inlet and outlet of the contraction: dimensions, zero slope, zero curvature, and zero curvature derivative. As a result, the height, He, and width, Wi of the contraction at a given x can be expressed as

$$\frac{He - He_0}{He_L - He_0} = \left(\frac{x}{L}\right)^4 \cdot \left[-20 \cdot \left(\frac{x}{L}\right)^3 + 70 \cdot \left(\frac{x}{L}\right)^2 - 84 \cdot \left(\frac{x}{L}\right) + 35\right] \tag{3.4}$$

$$\frac{Wi - Wi_0}{Wi_L - Wi_0} = \left(\frac{x}{L}\right)^4 \cdot \left[-20 \cdot \left(\frac{x}{L}\right)^3 + 70 \cdot \left(\frac{x}{L}\right)^2 - 84 \cdot \left(\frac{x}{L}\right) + 35\right] \tag{3.5}$$

where L is the contraction length, He_0 and Wi_0 are respectively the settling chamber height and width, and H_L and W_L are respectively the channel height and width. In the test section redesign, He_0, Wi_0 and L are equal to 240 mm. This value is limited by the position of the high-speed camera, which has to be close enough to the disk in order to reduce mechanical stresses. However, the dimensions of the channel He_L and Wi_L can be varied in order to investigate additional configurations. For a given channel cross section, only the contraction has to be modified according to Equations (3.4) and (3.5).

In the present investigation, the values of He_L and Wi_L are respectively equal to 153 mm and 138 mm, resulting in a hydraulic diameter (D_H) equal to 0.145 mm. A schematic of the tested model is given in Fig. 3.7. The total length of the channel is equal to 1390 mm, and it is equipped with eight ribs placed on its bottom wall, perpendicularly to the main flow direction. The rib pitch, P, is equal to 150 mm. The cross section of the rib is a square of 15 mm side (H), resulting in a blockage ratio equal to 10% and a rib pitch to height ratio equal to 10. The coordinate system selected for this investigation is

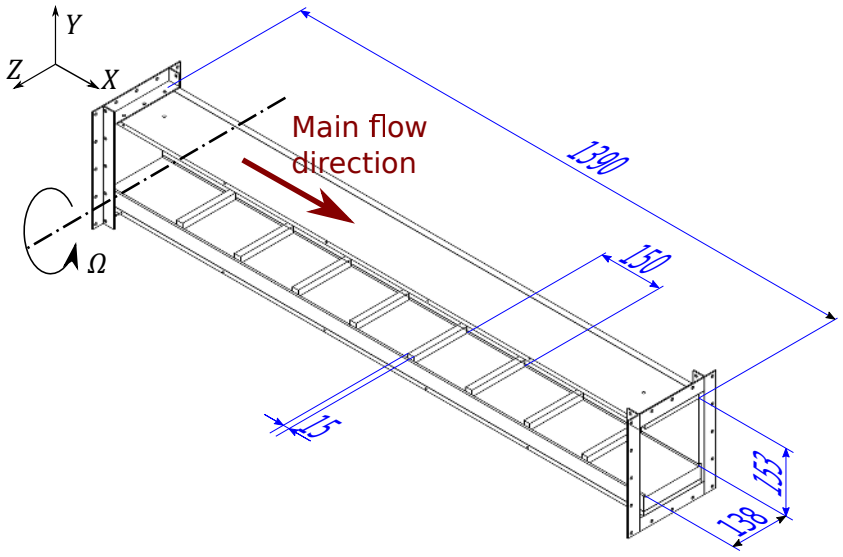

Figure 3.7 : Sketch of the tested model

also shown in Fig. 3.7, with the x axis representing the stream-wise direction, the y axis vertical to the ribbed wall and the z axis the span-wise direction. The tested model can be rotated around the z axis in both senses of rotation. The rotation is counter-clockwise when the angular velocity vector presents the same sense as the z axis, clockwise in the opposite case. The distance from the exit of the contraction (inlet of the test section) to the first rib is equal to 155 mm.

The working fluid for the aerodynamic and heat transfer investigations is air, which is provided by a centrifugal blower. The air is taken from the room at ambient conditions and it is introduced in a stationary pipe equipped with a Venturi nozzle. The angular velocity of the centrifugal compressor is controlled to obtain the pressure drop in the Venturi nozzle, $\Delta p_{Venturi}$, that corresponds to the required Reynolds number. The pressure drop is monitored by means of a Betz micromanometer, with an operational range of 500 mmH_2O and a resolution of 0.2 mmH_2O.The fluid density is calculated by applying the ideal gas equation of state:

$$\rho = \frac{p}{R_{air} \cdot T} \tag{3.6}$$

where p is the ambient pressure, R_{air} the air specific gas constant (equal to 287.06 $\frac{J}{kg \cdot K}$) and T is the ambient temperature. Since the flow is assumed to be incompressible, the air density in the test section is considered equal to the ambient air density.

After the Venturi nozzle, the air crosses a rotary seal (Fig. 3.4) to enter a rotating pipe. The axis of the pipe is equal to the axis of rotation of the facility. Then, the air crosses the center of the disk to enter the rotating test section.

The facility is rotated by means of a variable speed DC electrical engine in gear with the rotating pipe. The rotational speed of the facility is monitored by a photomultiplier adapted to a cogwheel installed on the shaft. Although the facility was able to reach 160 rpm in its original configuration (Fig. 3.1), the maximum speed was limited to 100 rpm in the present setup due to the significant weight increase. The facility is balanced by adjusting the position of the weights shown in Fig. 3.1. Once the facility is balanced, the center of gravity falls on the rotation axis. However, the center of gravity does not fall in the plane of the bearings on which the disk is supported. The limiting factor of the rotational speed arises from the distance between the center of gravity and the supporting bearings, which induces larger stresses as the distance increases. In practice, the maximum rotational speed is determined by monitoring the vibrations of the facility by means of an accelerometer until the maximum admissible acceleration is reached.

Two sliprings are installed on the rotating shaft. The first one was already present in the original investigations by Di Sante [30]. It is able to transmit up to 1000 V_{RMS} and 7.5 A per channel. This slipring is employed to supply the power to the electronic devices mounted on the disk (High Speed Camera, SLR camera, thermocouple amplifiers, ...) and to transmit thermocouples and triggering signals. The second slipring was acquired to allow larger intensities, up to to 30 A. In the case of the heat transfer investigation, an Inconel foil is heated up by Joule effect, which requires intensities up to 13 A.

3.3 Particle Image Velocimetry setup

Particle Image Velocimetry (PIV) is a non-intrusive measurement technique that aims to obtain the fluid velocity distribution in a plane. In a PIV experiment, the motion of seeding particles introduced in the flow is recorded by a camera. To do so, the investigated plane is illuminated typically by a laser sheet, and the camera records the light scattered by the seeding particles. Each PIV realization is composed by two images separated by a short separation time, Δt, on which the particle displacement is evident. Then, the images are divided into small interrogation windows, where the mean particle displacement is determined by a PIV processing algorithm.

The displacement of the interrogation window, as observed by the camera, is expressed here as ΔX. A typical displacement equals 8 pixels, which for a camera whose pixel size is equal to 5 μm, would result in $\Delta X \sim 8\times\ 5\ \mu m = 40\ \mu$m. In order to relate the interrogation window displacement to the one in the real plane (Δx), a mapping function, M, that relates the position in the real plane with the position in the image plane is necessary:

$$X = M \cdot x \tag{3.7}$$

where X is the coordinate in the sensor plane and x is the coordinate in the real plane. In planar two dimensional PIV with no image aberrations, the mapping function is a constant, and is determined by introducing a calibration grid in the measurement plane. In this case, the mapping function represents the magnification factor, which is the ratio between the distances in the image plane (camera sensor) and those in the real plane.

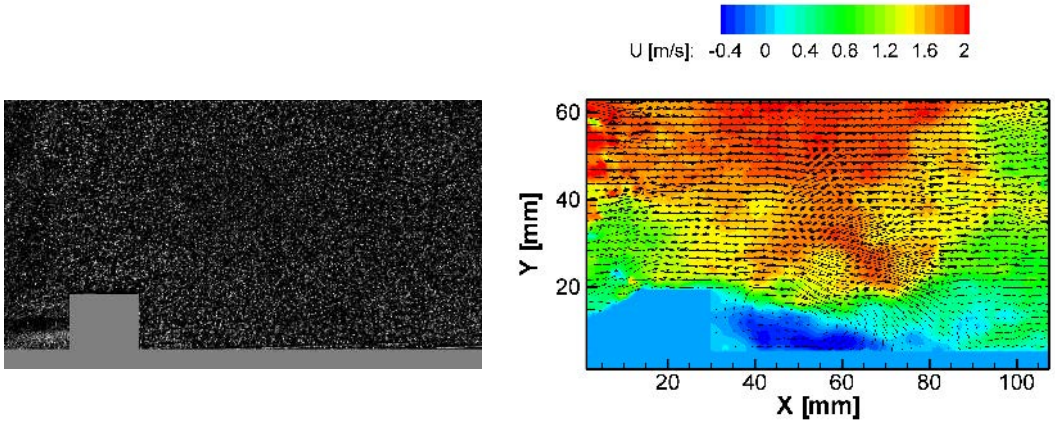

Figure 3.8 : Example of a PIV image (left) and the corresponding instantaneous velocity field (right). Only one out of nine velocity vectors are represented

By deriving Eq. (3.7), the displacement in the image plane is related to the one in the real plane:

$$\Delta X = M \cdot \Delta x \tag{3.8}$$

Finally, the velocity corresponds to the calculated displacement divided by the known separation time,

$$u = \frac{\Delta x}{\Delta t} = \frac{\Delta X}{M \cdot \Delta t} \tag{3.9}$$

An example of one PIV image and an instantaneous velocity field is shown in Fig. 3.8 Many review works have summarized the PIV principles, such as the textbooks of Adrian and Westerweel [60] and Raffel et al. [61], and the reviews by Adrian [62, 63].

The PIV setup employed in the present work has been modified with respect to that in Refs. [30–33] due to the increase in size of the test section and to bring the possibility to investigate larger Reynolds numbers. The procedure to estimate the main parameters needed to select a PIV system is presented in subsection 3.3.1, whereas the component details are given in 3.3.2.

3.3.1 PIV dimensioning

The direct measurement that the PIV system provides is the displacement of each interrogation window in which the observed area is divided, ΔX. The measurement error related to ΔX is due to different factors such as the seeding density, the particle motion perpendicular to the laser sheet, the loss of particles within the interrogation window of the second frame, the velocity gradients and the laser sheet misalignment. In a satisfactory experiment, the measurement error is a fraction of the camera pixel size,

d_r. Typically,

$$\delta(\Delta X) \sim 0.1 d_r \tag{3.10}$$

where $\delta(\Delta X)$ is the particle displacement measurement error. In the present investigation, the objective is to have an overall relative error of about 1-2%. In that case,

$$\frac{\delta(\Delta X)}{\Delta X} \sim \frac{0.1 d_r}{\Delta X} \sim 0.01 \tag{3.11}$$

which implies $\Delta X \sim 10 d_r$. The particle displacement in the image plane should be of order of 10 pixels. The High Speed Camera (HSC) that is employed in the present investigation presents a pixel size of 22 μm, which leads to $\Delta X \sim 220$ μm. On the other hand, the interrogation window size in the image plane (D_I) should be approximately 4 times the displacement [62]. With iterative refinement PIV algorithms [64], the final interrogation window size can be reduced. In this way, $D_I \sim 2\Delta X = 20$ pixel $= 440$ μm. The spatial resolution is given by the interrogation window size in the real plane (d_I), which is related to the mapping function and the interrogation window size in the image plane. Similarly to Eq. (3.8):

$$d_I = \frac{D_I}{M} \tag{3.12}$$

In the present investigation, a resolution of about 1.5 mm is required, corresponding to one tenth of the rib height. Therefore, the magnification factor or mapping function would present a value of

$$M = \frac{D_I}{d_I} \sim \frac{0.440\text{mm}}{1.5\text{mm}} \sim 0.3 \tag{3.13}$$

With the value of the magnification factor, it is possible to determine the Field of View (FOV) expressed here as l_x. In the present case, the sensor width, L_X, is equal to 17.6 mm (800 pixels), resulting in

$$l_x = \frac{L_X}{M} \sim \frac{17.6\text{mm}}{0.3} \sim 59mm \tag{3.14}$$

Note that an increase of the magnification factor, reduces the FOV, hence the system focuses on a reduced region of the flow. Since the interrogation window size in the image plane (D_I) is fixed due to the requirements in the accuracy, the resolution increases (d_I decreases, Eq. (3.12)). This is usually done by changing camera lens, or by moving the camera closer to the investigated plane. Differently, if the magnification factor increases but the spatial resolution remains unchanged, the interrogation window size in the image plane must increase (Eq. (3.12)). The increase of D_I allows larger particle displacements (note that the separation time can be tunned to find the desired displacement), leading to an accuracy increase. This is due to the fact that the measurement error is a fraction of the pixel size, as described in Eq. (3.10). In summary, the resolution and accuracy of the PIV setup can be finely tunned by varying the magnification factor. For this reason, two different PIV experimental campaigns were carried out. The first one is performed

with a large magnification factor in order to minimize the measurement error, whereas the second campaign is executed with a small magnification to study a larger FOV.

The corresponding particle displacement in the image plane (Eq. (3.8)) is $\Delta x \sim 220\mu\text{m}/0.3 \sim 733$ μm. For a Reynolds number equal to 15,000, the bulk velocity U_b is about 1.56 m/s, whereas the typical velocity close to the wall is slightly lower. For a velocity u of about 1 m/s, the separation time between the two pictures of a PIV realization is requested to be $\Delta t = \Delta x/U \sim 733$ μs.

On the other hand, the three dimensional motion leads to the loss of particles in the interrogation window due to the displacement in the direction normal to the laser sheet -span-wise direction-. In order to minimize the error due to this particle loss, the laser sheet thickness is recommended to be at least four times the displacement normal to the laser sheet [62]. In the present case, the velocity is measured in the symmetry plane of the channel, resulting in a negligible mean velocity in the span-wise direction. However, the flow is highly turbulent, with a turbulence level of about 20% of the bulk velocity, that is, 0.3 m/s. The corresponding normal displacement is 0.3 m/s $\times$ 733 μs = 0.23 mm. For a typical 1.5 mm laser sheet thickness, the separation time is short enough to avoid the loss of pairs.

Additionally, the seeding density needs to be high enough to optimize the measurement accuracy. According to Adrian [62], the amount of particles in an interrogation window should be at least equal to 10. For a PIV experiment with interrogation windows of about 1.5×1.5×1.5 mm^3, the required seeding density is equal to 3 particles/mm^3. In the present experiments, the flow rate $U_b \times Wi_L \times He_L$ is about 0.033 m^3/s, for which at least 10^8 particles/s are needed.

The camera lens employed for the investigation of such a FOV presents usually a focal length f equal to 50 mm. If the lens is modeled as a Gaussian thin lens,

$$\frac{1}{f} = \frac{1}{z_0} + \frac{1}{Z_0} \tag{3.15}$$

where z_0 is the distance from the measurement plane to the lens, and Z_0 is the distance from the lens to the camera sensor. The magnification factor can be defined also as

$$M = \frac{Z_0}{z_0} \tag{3.16}$$

and therefore,

$$z_0 = f \times \left(1 + \frac{1}{M}\right) = 50\text{mm} \times \left(1 + \frac{1}{0.3}\right) = 217\text{mm} \tag{3.17}$$

Therefore, the working distance is about 220 mm. This z_0 is shorter than the usual minimum focusing distance, hence an extension ring is needed. Additionally, the extension ring brings the possibility of changing the distance Z_0 and therefore modifies the lens

magnification factor to the present needs. The magnification factor can be expressed as

$$M = \frac{Z_0}{f} - 1 \tag{3.18}$$

showing that if Z_0 is increased, the magnification factor increases. For a typical 50 mm lens without extension ring, $M \sim 0.15$ [65, 66], hence $Z_0 \sim 57.5$ mm. However, if we request a magnification factor equal to 0.3, $Z_0 = f \times (M + 1) \sim 65$ mm. Therefore, an extension tube of at least (65 - 57.5) mm $\sim$ 8 mm must be installed.

3.3.2 PIV test section

A picture of the test section with the PIV instrumentation is shown in Fig. 3.9. The channel lateral and top walls have been manufactured in acrylic glass to provide optical access to the laser and camera. The bottom wall has been manufactured in copper, under which ten Minco heating resistances have been installed. The heaters are employed in the cases where Buoyancy effects are included. In the heating case, the wall was heated up to a temperature of about 95°C. The temperature is monitored in five locations by means of type-K thermocouples, showing a maximum deviation below 2°C due to the high conductivity of the copper. A 250 V AC power supply was employed to provide the energy to the heating resistances. A PID controller connected to a Pt100 sensor inserted in the 6th rib is employed to monitor and control the wall temperature, which is requested to be steady. Below the heaters, a bakelite wall was added in order to reduce the heat losses to the ambiance.

The camera employed to record the PIV images is the same as the one used by Di Sante et al. [31] and Coletti et al. [32, 33] in the RC-1 facility. The device is a Phantom v7.1 High Speed Camera (HSC) by Vision Research, with a resolution of 800×600 pixel^2, a pixel size equal to 22×22 μm^2, and a maximum frame rate equal to 4,800 pictures per second. The camera frequency was operated in the range 1,000 - 1,400 Hz, depending on the FOV. The PIV separation time, Δt, is equal to the inverse of the camera frequency. Therefore, Δt is set to 1,000 and 714 μs in the different PIV experimental campaigns.

The operation of the HSC in PIV measurements provides the time-evolution of the velocity field at the camera frequency. Since the camera memory is limited to 1450 images at the present resolution, the experiment is about 1 second long, that is, 10 times the Large Eddy Turn-Over Time (LETOT). In order to obtain representative statistics, an in-house memory gate controller was developed during the PhD work of Di Sante [30] to set the sampling frequency differently from the camera frequency. With the memory controller enabled, the time between each PIV realization can be increased to about 900 times the separation time. In this way, 724 statistically independent PIV realizations can be acquired in a longer experiment (about 10 minutes), similarly to a typical PIV experiment. In the present work, both the Time-Resolved and typical PIV modes are employed.

Additionally, two camera lenses were used. The first lens employed was a Nikon Nikkor 50mm f/1.8, together with an extension ring, to obtain a large magnification factor and

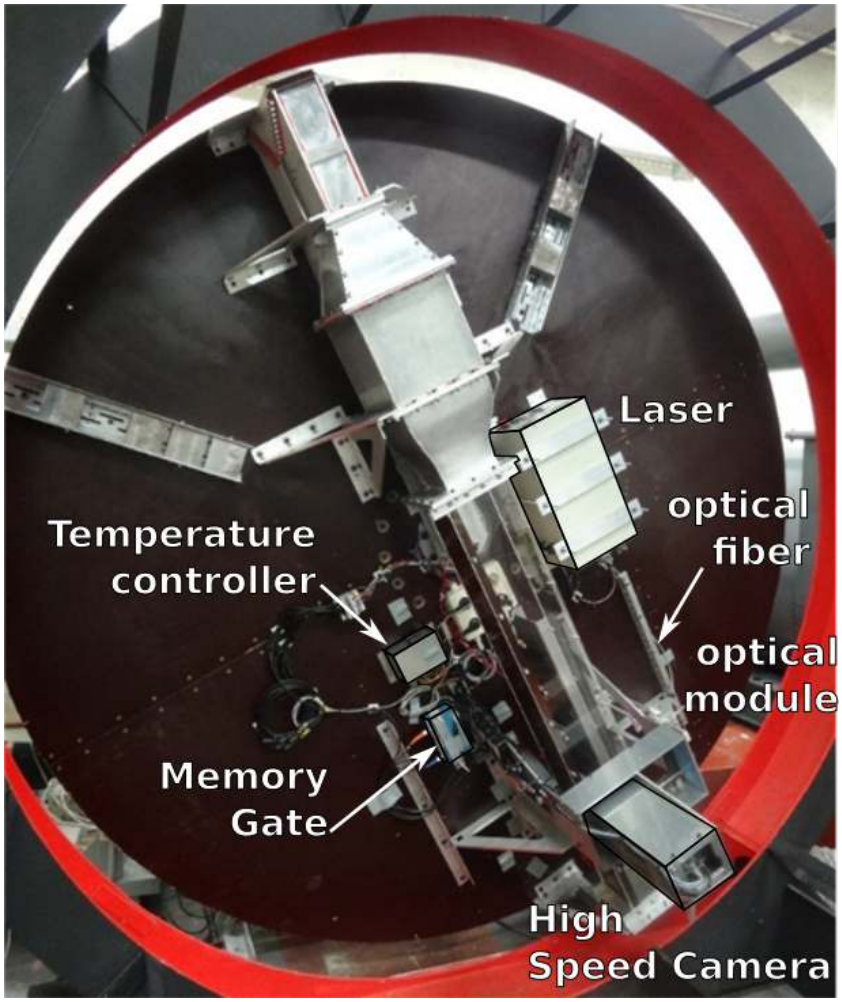

Figure 3.9 : PIV setup

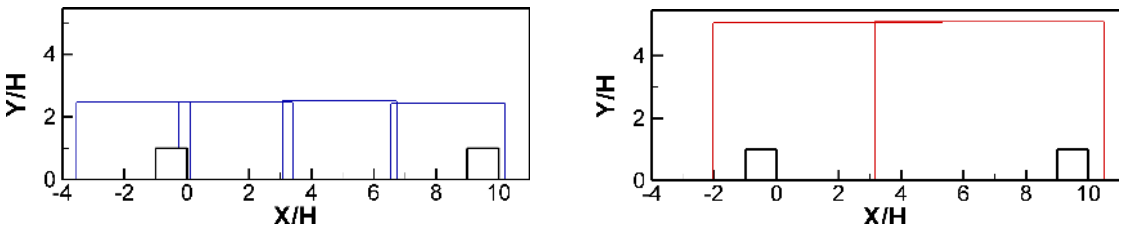

Figure 3.10 : Fields of View for the experiments with the 50 mm lens (left) and with the 35 mm lens (right)

Table 3.1 : Test matrix for the PIV experiments with the 50 mm lens (Re = 15,000), performed experiments are colored

	Bo	
	0	0.77
$Ro = 0$		
$Ro = \pm 0.38$		
$Ro = \pm 0.77$		

therefore to increase the resolution and accuracy. The resulting magnification factor is equal to 0.30, that is, 0.073 mm/pixel. For a typical interrogation window of 20 pixels, the resolution is equal to 1.5 mm. The FOV of each PIV experiment was about 53×40 mm^2.

The second camera lens was a Nikon Nikkor 35mm f/2.8, leading to a FOV of about 83×62 mm^2. The latter allows the investigation of the velocity field over a larger surface in a single experiment, with the drawback of a reduction of the accuracy and resolution. The resulting magnification factor was equal to 0.15, that is, 0.142 mm/pixel. For an interrogation window of 20 pixel side, the resolution is equal to 2.8 mm. A comparison of the FOVs in both cases is shown in Fig. 3.10.The test matrices for the PIV experiments carried out with each lens are shown in Tables 3.1 and 3.2.

The flow is seeded with corn oil particles provided by a PIVTEC PivPart14 aerosol generator, with a mean particle diameter of about 1 μm. The particles are injected in the main flow just upstream of the rotary seal shown in Fig. 3.4. Only 2 out of the 14 Laskin nozzles of the generator were used, to provide about 2 $\times 10^8$ particles per second. The particles are illuminated by a laser sheet in the symmetry plane of the region between the 6th and 7th ribs as shown in Fig. 3.11. The laser beam is generated by an AMTRON LS453 JO75-CPXF-2Pi continuous laser with a maximum power of 75 W and a mean wavelength equal to 808 nm. The laser is 3 times more powerful than the one employed in the investigations by Di Sante et al. [30, 31] and Coletti et al. [32, 33], allowing the investigation of higher Reynolds number flows. The laser beam is directed by a 400 μm

Table 3.2 : Test matrix for the PIV experiments with the 35 mm lens (Re = 15,000), performed experiments are colored

	Bo	
	0	0.77
$Ro = 0$		
$Ro = \pm 0.30$		
$Ro = \pm 0.77$		

diameter optical fiber connected to an optical module. The optical module is similar to the one introduced by Di Sante [30], but has been adapted to an optical fiber of 400 μm (instead of 200 μm in Ref. [30]) and the required Field of View. In particular, the cylindrical lens was replaced by another with a shorter focal length, equal to 10 mm. In this way, the laser is able to cover an area of about 80 mm, instead of 40 mm [30].

In the present PIV measurements ($Re = 15,000$), the laser power was set to 25 W. Due to the available laser power, higher Reynolds number flows can be investigated. The limitation in the Reynolds number arises from the required exposure time and the reduction of the required separation time (inversely proportional to the velocity). As the velocity increases, the exposure time needs to be reduced in order to observe the particles as point sources instead of streaks. Since the exposure time is reduced, the energy collected by the sensor decreases (proportionally to the exposure time) and therefore larger laser powers need to be employed. If the laser power can be increased by a factor of 3, the maximum Reynolds number can be increased by the same factor. With the current test section and optical module, the setup can reach Reynolds numbers of at least 45,000. With a cylindrical lens with larger focal length, the laser sheet width would be reduced, increasing the laser energy density and allowing even larger Reynolds number flows. The separation time would be reduced by a factor of 3, which requires an increase of 3 times the camera frequency. In the present test section, the camera frequency would need to be set to about 3,000 - 4,500 Hz, which is close to the camera limits (4,800 Hz). In the test section introduced by Coletti et al. [32, 33] for instance, the camera frequency was already set to about 3,300 Hz for Re = 15,000. In that case, the limit Reynolds number would have been about 15,000×4,800/3,300 $\sim$ 22,000 with the same optical parameters. A summary of the settings for each case is shown in Tables 3.3 and 3.4.

3.3.3 PIV processing

In order to enhance the quality of the PIV pictures, several image processing tools have been employed. The first step is to translate each couple of images according to the channel vibrations. Due to the mechanical vibrations, the relative position of the investigated wall with respect to the camera shows a relative motion of about 2-3 pixels

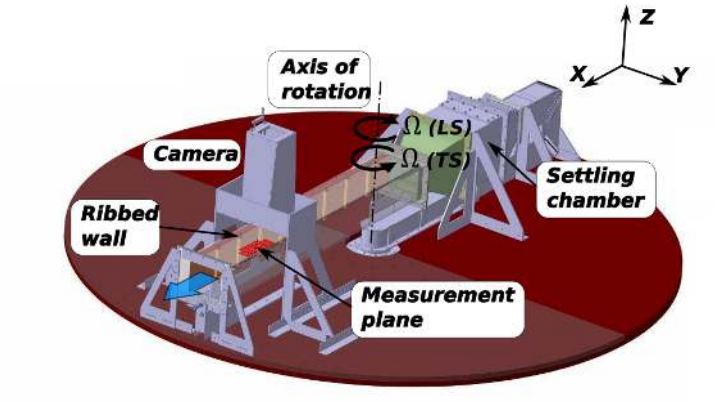

Figure 3.11 : sketch of the PIV setup and location of the measurement plane

during the entire experiment, which can lead to a positioning error of order of 0.2 - 0.4 mm. It is possible to monitor the instantaneous position of the wall with respect to the camera by observing the position of the rib in the image, and to translate each PIV image pair to the original frame of reference. Note that this positioning error does not affect to the PIV accuracy in a single realization, since the wall displacement within the PIV separation time is negligible. However, the statistics are required to be performed at the same exact location in order to improve the accuracy. After the translation, a background image is generated. The intensity at each pixel of the background image corresponds to the minimum intensity value observed at that pixel during the entire experiment. Then, the background picture is subtracted to each PIV image [67], in order to remove the wall reflections and enhance the particle images. Once the background is subtracted, a minimum-maximum filter [60] is applied in windows of 10×10 pixel^2 to normalize the particle images with respect to the background. Finally, a Gaussian filter with a size equal to 3×3 pixel is applied to the resulting picture, in order to smooth the particle images and reduce the pixel-locking effects [60]. Figure 3.12 shows the comparison between a raw image and the corresponding processed image.

An iterative multigrid PIV image processing with interrogation window offset and deformation algorithm [64, 68] has been employed to obtain the velocity fields in each of the PIV realizations. The processing was made in three steps: the first one with interrogation windows of 80×64 pixel^2, the second one with 40×32 pixel^2 and the final one with 20×16 pixel^2. The interrogation window overlap is set to 75% of the interrogation window size. The resulting spatial resolution and vector spacing depend on the lens, and therefore on the image magnification, that was selected. Tables 3.3 and 3.4 show the values of the PIV parameters that are not shared.

Figure 3.13 shows a comparison of the mean stream-wise velocity profiles in the investigated plane at $Ro = 0$. Two main conclusions can be made from the comparison: first, the repeatability of the measurements is very positive, since the represented velocity profiles were obtained in two different experiments, considering that the instrumentation was unmounted and installed back between both campaigns; and secondly, there is little

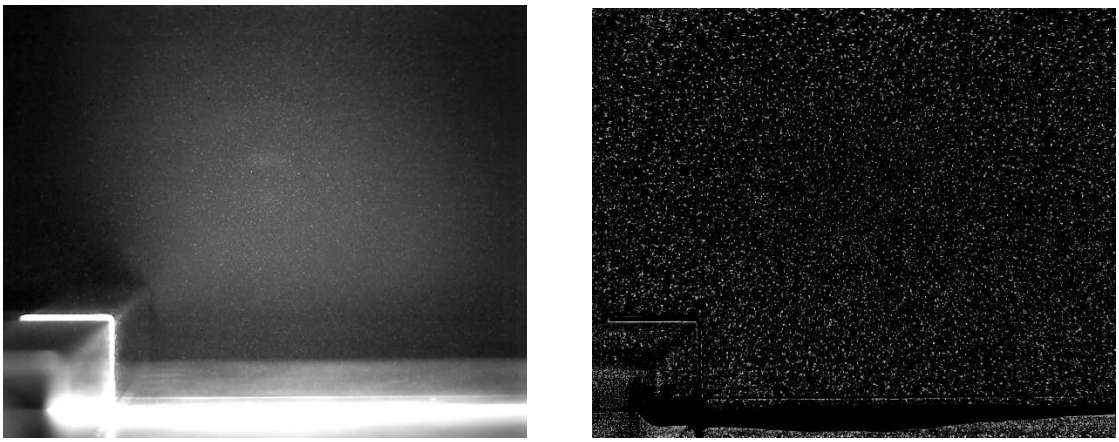

Figure 3.12 : Comparison of a raw image (left) and its corresponding enhanced image (right)

Table 3.3 : Summary of the PIV parameters for the experiments with reduced Field of View (Fig. 3.10-left)

Lens focal length, f	50 mm
Field of View, FOV	56×42 mm^2
Magnification, M	0.3
Resolution	1.47×1.17 mm^2
Vector spacing in the x direction	0.37 mm
Vector spacing in the y direction	0.29 mm
Overall velocity error (95% C.L.)	$0.016U_b$
Separation time, Δt	714 μs
Acquisition frequency, f_{acq}, for statistics evaluation	1.54 Hz
Acquisition frequency, f_{acq}, for Time-Resolved analysis	1400 Hz
Rotation numbers, Ro	0, 0.38, 0.77

Table 3.4 : Summary of the PIV parameters for the experiments with large Field of View (Fig. 3.10-right)

Lens focal length, f	35 mm
Field of View, FOV	90×64 mm^2
Magnification, M	0.15
Resolution	2.8×2.3 mm^2
Vector spacing in the x direction	0.70 mm
Vector spacing in the y direction	0.58 mm
Overall velocity error (95% C.L.)	$0.018U_b$
Separation time, Δt	1 ms
Acquisition frequency, f_{acq}, for statistics evaluation	1.10 Hz
Acquisition frequency, f_{acq}, for Time-Resolved analysis	1000 Hz
Rotation numbers, Ro	0, 0.30, 0.77

difference between the velocity profiles obtained with both lenses. It can be argued that the additional measurement error due to the parallax effect (perspective error) [69, 70] can play a role in the experiments with the 35 mm lens, due to the large angle of view. However, due to the fact that the measurement plane corresponds to the symmetry plane of the channel, and the eventual out-of-plane motion (due to the instantaneous turbulent fluctuations) is low compared to the in-plane velocity, the error is limited, as the profiles in Fig. 3.13 show.

3.4 Liquid Crystal Thermography setup

The channel with the geometrical parameters summarized in section 3.2 (Fig. 3.7) has been adapted to perform Liquid Crystal Thermography (LCT). The temperature of the heated wall is raised by means of a heating foil to induce the heat transfer from the wall to the fluid. The selected material of the foil is Inconel 600, which presents an almost constant resistivity with respect to the temperature. For a typical variation of 5 K, the resistivity change corresponds to about 0.07% of the nominal value. For this reason, the heating power is nearly uniform even if the temperature is uneven over its surface. Due to the three-dimensional character of the flow, the temperature distribution on the wall presents typical variations of ±5 K. In order to obtain the temperature map on the surface, a layer of Thermochromic Liquid Crystals (TLCs) has been deposited on the wall. TLCs are cholesteric liquids that present the characteristic of reflecting light at a wavelength that depends on the temperature. Therefore, the layer of TLCs on the heated wall shows a color distribution which is directly related to the local temperature. Introductions to LCT are given by Ireland and Jones [71] and by Abdullah et al. [72], whereas the methodology employed in the present work to extract the temperature map

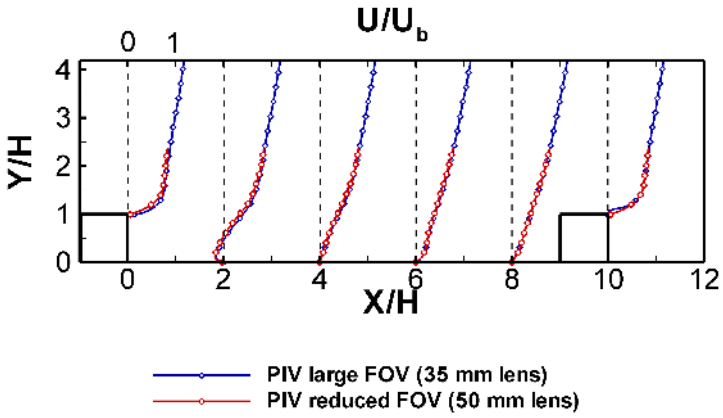

Figure 3.13 : Comparison of the PIV measurements with reduced and large FoV in static conditions, $Re = 15{,}000$

is described by Cukurel et al. [73]. The factors influencing the measurement accuracy are described by Wiberg and Lior [74], Abdullah et al. [72] and Rao and Xu [75].

After obtaining the temperature distribution on the ribbed wall, a heat transfer analysis is carried out on the surface in order to retrieve the dimensionless heat transfer coefficient. The methodology to obtain the dimensionless heat transfer coefficient is an evolution of the methods employed by Çakan [76] and Coletti [77] , and is detailed in section 3.4.4.

3.4.1 LCT channel

The LCT setup on the RC-1 facility is shown in Fig. 3.14. As in the case of the PIV setup, the instrumentation is mounted on the rotating frame of reference to achieve the same resolution and accuracy as in a stationary facility. The power supply to the electronic devices is provided as well through the slip rings placed on the rotating shaft.

The channel employed in the LCT investigation is slightly different from the PIV case, although they present the same geometrical parameters as in Fig. 3.7. The top and lateral walls are also built in acrylic glass in order to provide the optical access to the camera that records the color map on the ribbed surface and to the lights that illuminate the wall. However, the bottom wall is a block of extruded polystyrene (XPS) of 30 mm thickness employed to minimize the heat losses by conduction. A 20 μm thickness Inconel foil is glued on the XPS wall by means of an acrylic adhesive of 60 μm thickness. By applying a current through the Inconel foil, the temperature increases by Joule effect. Therefore, the Inconel foil acts as a heater, leading to a heat transfer by convection to the fluid, conduction to the solid, and radiation to the surrounding elements. The extremities of the heating foil are introduced between two copper plates, one of each connected to a 30 V - 150 A power supply. Figure 3.15 shows a picture and the corresponding sketch of the connection at one of the extremities of the foil to the copper plates. 1 mm thickness teflon plates have been employed to insulate electrically

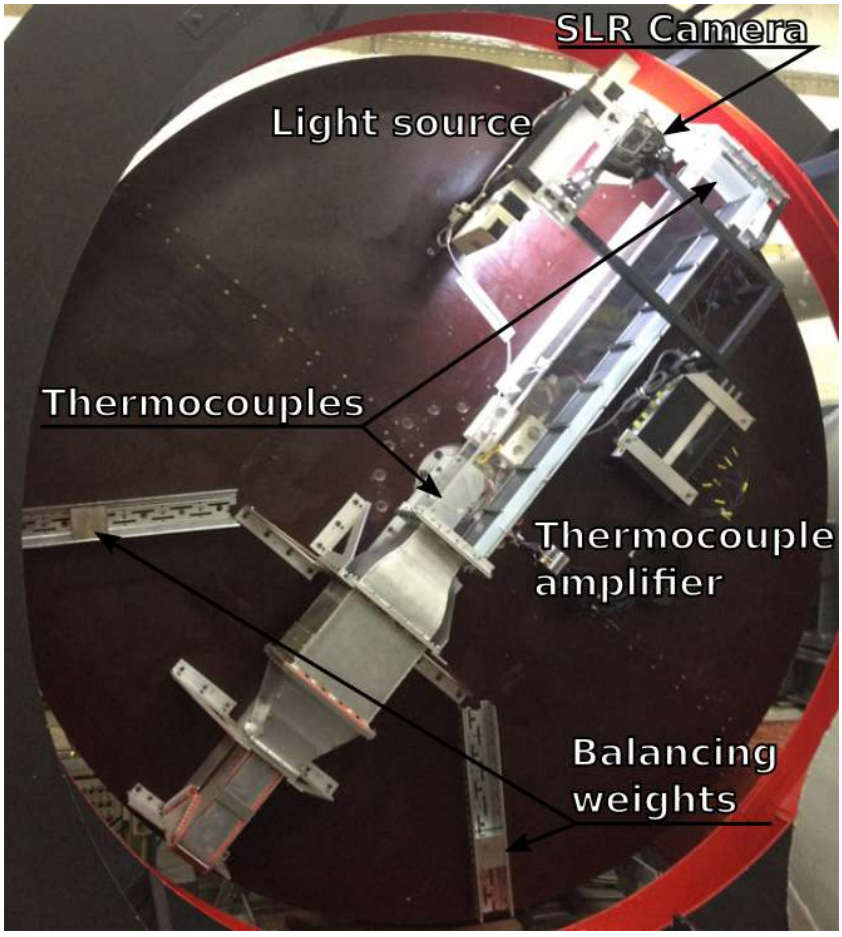

Figure 3.14 : LCT experimental setup

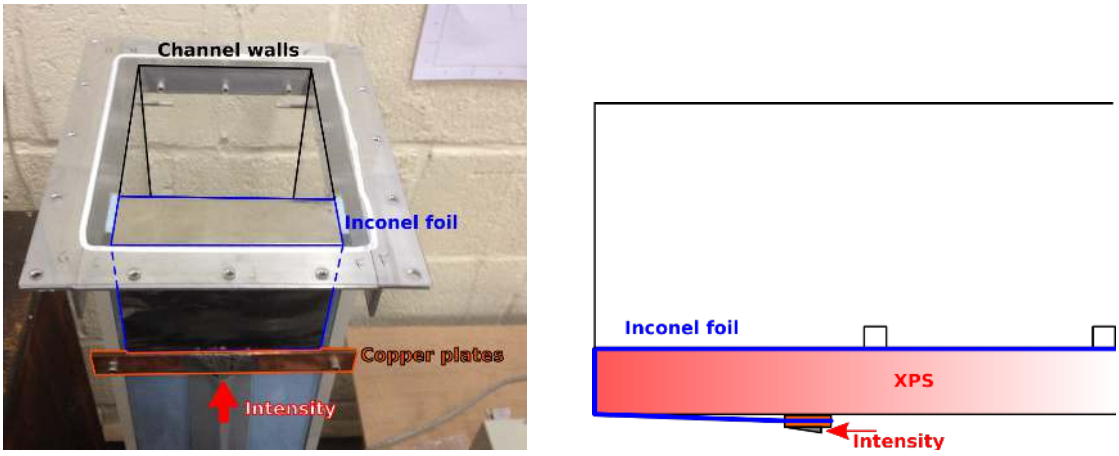

Figure 3.15 : Inconel connection: detail (left) and sketch (right)

the Inconel foil from other metallic elements of the test section, namely the flanges at the inlet and outlet of the channel model.

The Inconel foil has been sprayed with black paint to generate a black mate layer that eliminates reflections and enhances the contrast of the color distribution reflected by the liquid crystals. On top of the black paint, a layer of Hallcrest R35C20W microencapsulated TLCs is sprayed, presenting a starting temperature of about 35°C and a bandwidth of about 20°C. A schematic of the different layers deposited on the XPS wall is given in Fig. 3.16. At temperatures below ∼35°C and above ∼55°C the liquid crystals are not active, and only the black paint is visible. Finally, the ribs (made in acrylic glass) are placed on the top of the liquid crystals. Therefore, the ribs are heated up only in the base by the Inconel foil. In steady conditions, the heat transfered from the heating foil to the rib is balanced by the heat transferred from the rib to the fluid. Two additional XPS blocks have been placed on the lateral sides of the bottom wall, as shown in Fig. 3.16, to minimize lateral conduction effects.

Eight K-type thermocouples have been placed in the channel to monitor the fluid and wall temperatures. Figure 3.17 represents the location of the thermocouples in the channel. Two thermocouples are placed at the center of the inlet and outlet sections to measure the fluid temperature at these locations. A thermocouple is placed downstream of the 8th rib to monitor the wall temperature during the experiments. To reduce the measurement uncertainty, the TLCs are employed in the range of temperatures where the uncertainty is minimized. In the present case, the minimum uncertainty TLC temperature is around 41°C. When varying the Reynolds or Rotation numbers, or the sense of rotation, the heat transferred from the wall to the fluid changes, modifying the wall temperature if the power supplied to the heater is kept constant. Therefore, the power supplied to the heating foil is varied during each experiment to achieve a temperature of about 41°C at the TLC surface. Note that this procedure prevents operating the TLCs out of their active range. The other five thermocouples have been

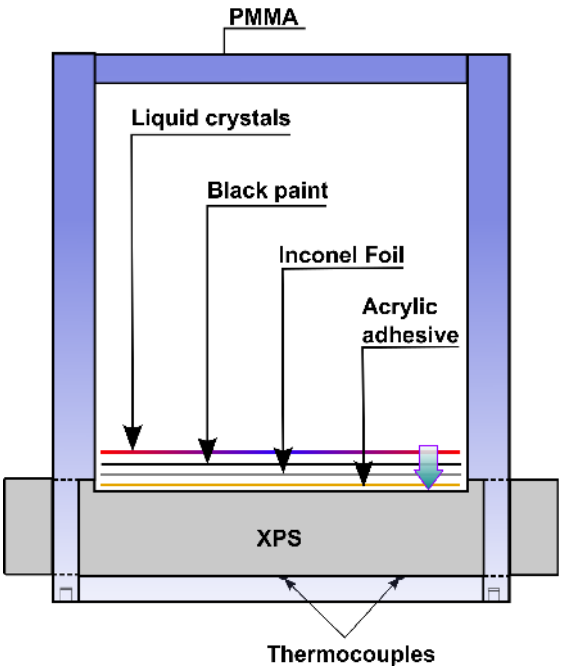

Figure 3.16 : Sketch of the different layers in the channel cross section [78]

placed in the area corresponding to the field of interest (between the 6th and 7th ribs), but on the external face of the XPS wall (Fig. 3.17). Since the temperature of the internal wall is given by the TLCs and the temperature of the external wall is given by the thermocouples, the heat conduction losses can be calculated in the investigated region.

The Reynolds and Rotation numbers investigated during the LCT measurements are set in the same way as during the PIV experiments. Since the complexity of the LCT measurements is lower than the one in the PIV setup, a larger amount of experiments have been performed, including the Reynolds number effect. The final test matrix is given in Table 3.5. The table also shows the Buoyancy number corresponding to each Rotation number. Due to the temperature difference between the wall and the core of the flow and to the increasing Rotation number, the Buoyancy effects are most likely emerging at $Ro > 0.38$, since $Bo > 0.04$.

3.4.2 TLC instrumentation

In order to monitor the color of the TLCs on the ribbed surface, a Nikon D300S SLR camera equipped with a Nikon AF-S DX Nikkor 35mm f1.8G has been employed. The inclination of the camera sensor with respect to the investigated wall is 45°, which is in the range where the TLC sensitivity with respect to the viewing angle is minimum [73]. In order to increase the depth of field of the camera, the f-stop was set to 11. The camera exposure time was set to 1/50 s in order to avoid blurred images due to the mechanical

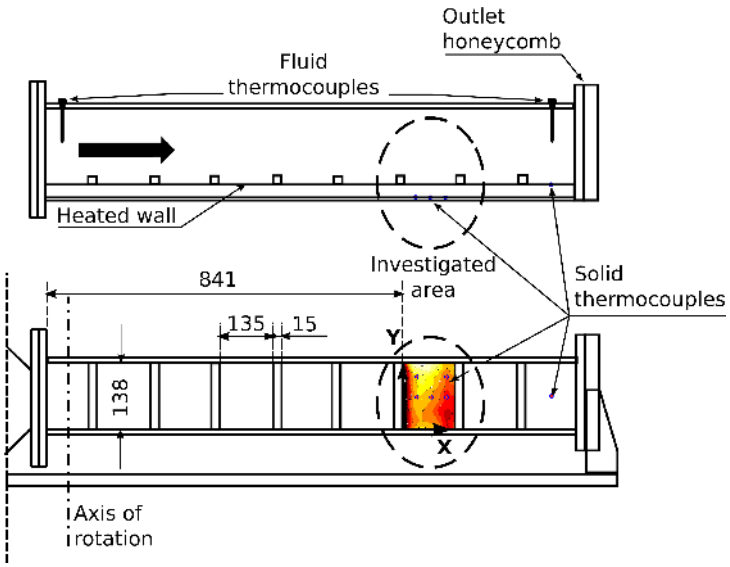

Figure 3.17 : Sketch of the channel model for the LCT measurements [78]

Table 3.5 : Test matrix for the TLC experiments. The investigated Re-Ro combinations are colored

Ro		0	0.06	0.12	0.20	0.30	0.38	0.47	0.69	0.84	1.00
Re	15000										
	30000										
	55000										
Bo		0	0.00	0.01	0.01	0.03	0.04	0.06	0.16	0.26	0.32

vibrations, whereas the ISO value was set to 3200 to maximize the image intensity.

Two Master TL-D 18W/840 fluorescent lamps by Phillips were placed in parallel to the investigated surface to illuminate it uniformly. The white balance temperature of the camera has been set to 4200 K, close to the correlated color temperature of the bulbs (equal to 4000 K) to enhance the color sensitivity of the camera [73]. Figure 3.18 shows the camera and lights setup in the facility.

The background subtraction methodology to obtain the temperature distribution proposed by Cukurel et al. [73] is employed in the present work. The Red, Green and Blue (RGB) distributions of a background picture are subtracted from the RGB picture at each experimental condition. The RGB distribution in the resulting image is employed to extract the Hue values on the wall. A TLC calibration (section 3.4.3) is required to relate the Hue values to the temperature distribution. Finally, the temperature distribution and the energy applied by the heating foil are employed to obtain the heat transfer distribution on the investigated wall. The step-by-step method followed in the present study to obtain the dimensionless heat transfer is explained in section 3.4.4.

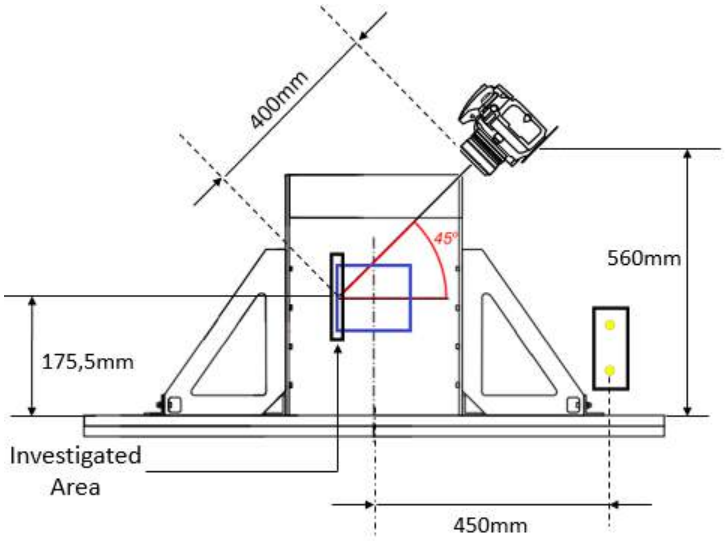

Figure 3.18 : Relative position of the camera and light sources with respect to the channel

3.4.3 TLC calibration

A TLC Hue-temperature calibration was performed prior to the experiments in the rotating channel. The setup and procedure are similar to the ones addressed by Cukurel et al. [73]. The calibration is carried out in a separate rig with the same lamps, camera and settings as those given in the previous section. The calibration rig consists of an aluminum plate that is heated up at one of its extremities by means of a heating resistance, and cooled down at the opposite side by a water cooling circuit. Nine embedded K-type thermocouples provide a linear temperature distribution along the aluminum plate. The TLCs are sprayed on the calibration plate at the same time as the investigated channel, in order to replicate the Hue-temperature relationship. The total TLC surface is equal to 225×100 mm^2. Finally, the relative position of the calibration plate with respect to the camera and lamps is the same as the investigated channel surface (Fig. 3.18). Figure 3.19 shows a picture of the rig during the calibration process.

First, a background picture of the inactive TLC surface is taken at ambient temperature (Fig. 3.20a). Due to the angle of the SLR camera with respect to the calibration plate, the investigated surface is observed as a trapezoid. A perspective transformation is applied on the camera pictures to restore the real shape of the field of interest. Then, a linear temperature profile is imposed on the plate to activate the TLCs on a large surface, as depicted in Fig. 3.19. After stabilization of the temperature, a picture is taken (Fig. 3.20b), and the background subtraction is carried out (Fig. 3.20c).

The Hue distribution on the 225×100 mm^2 TLC surface is obtained from the *RGB*

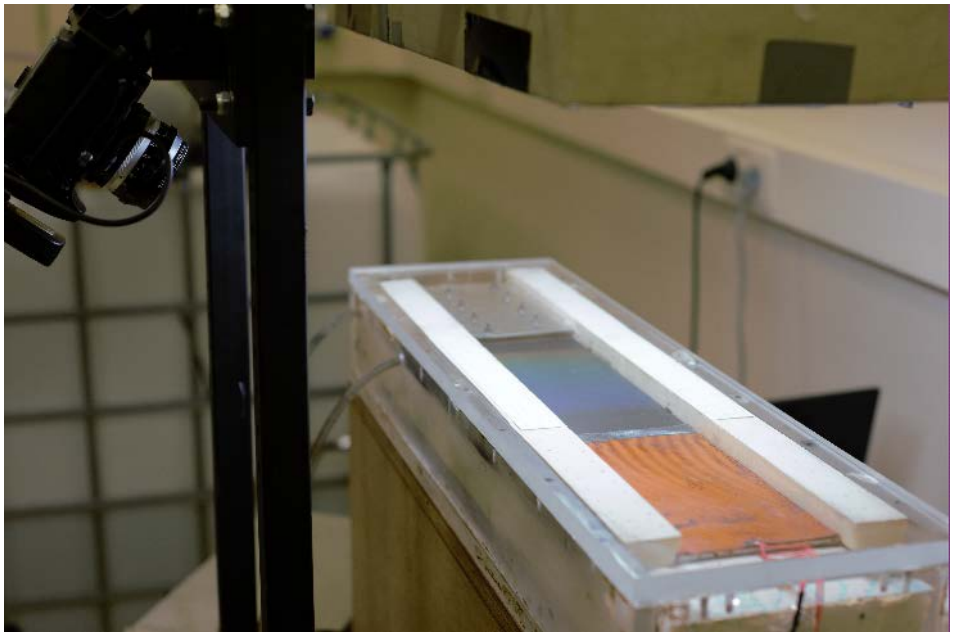

Figure 3.19 : TLC calibration rig



Figure 3.20 : Color distribution on the calibration rig, background picture (a), active TLCs with linear temperature profile (b) and final picture after background subtraction (c)

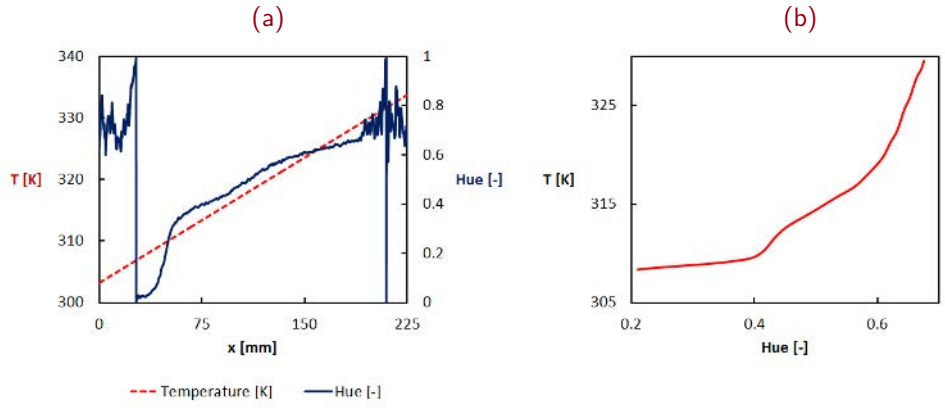

Figure 3.21 : Mean Hue and temperature distributions in the calibration rig (a), and final Hue-temperature calibration curve (b)

values in the resulting image as [73]:

$$Hue = \frac{1}{2\pi} \tan^{-1} \left[\frac{\sqrt{3}\,(G - B)}{2R - G - B} \right] \tag{3.19}$$

where R, G, B are respectively the Hue, Red, Green and Blue values at each pixel. Figure 3.21 shows the temperature and Hue distributions during the calibration of the TLCs used in the present investigation. The Hue distribution represented in Fig. 3.21a corresponds to the span-wise averaged Hue in Fig. 3.20c. Outside of the TLC active range, the Hue shows an irregular distribution due to the low intensity and saturation values, representative of dark colors. The calibration curve is chosen to be in the range 308.5 K $< T <$ 329.5 K, where the Hue-temperature relationship presents a monotonous trend. Figure 3.21b shows the final calibration curve, which is a spline fit of the data shown in Fig. 3.21a in the selected range. It can be observed that the TLCs are remarkably sensitive to the temperature in the range 308.5 K $< T <$ 309.5 K, that is, the response of the TLCs (in terms of the Hue, or color variation) is more sensitive in this range for a given temperature variation. Therefore, this range would be suitable for the TLC operation. However, the wall temperature variations in the ribbed channel are large, about 5 K, and the TLCs need to be operated over a higher temperature in order to avoid inactive areas.

3.4.4 LCT data reduction

Once steady conditions have been reached in the experimental facility a picture of the TLC surface is taken. Figure 3.22a shows an example of a raw image taken by the SLR camera, at $Re = 15{,}000$ and $Ro = 0$. A background picture is subtracted from the previous image and the Hue distribution (Eq. (3.19)) is determined, as shown in Fig.

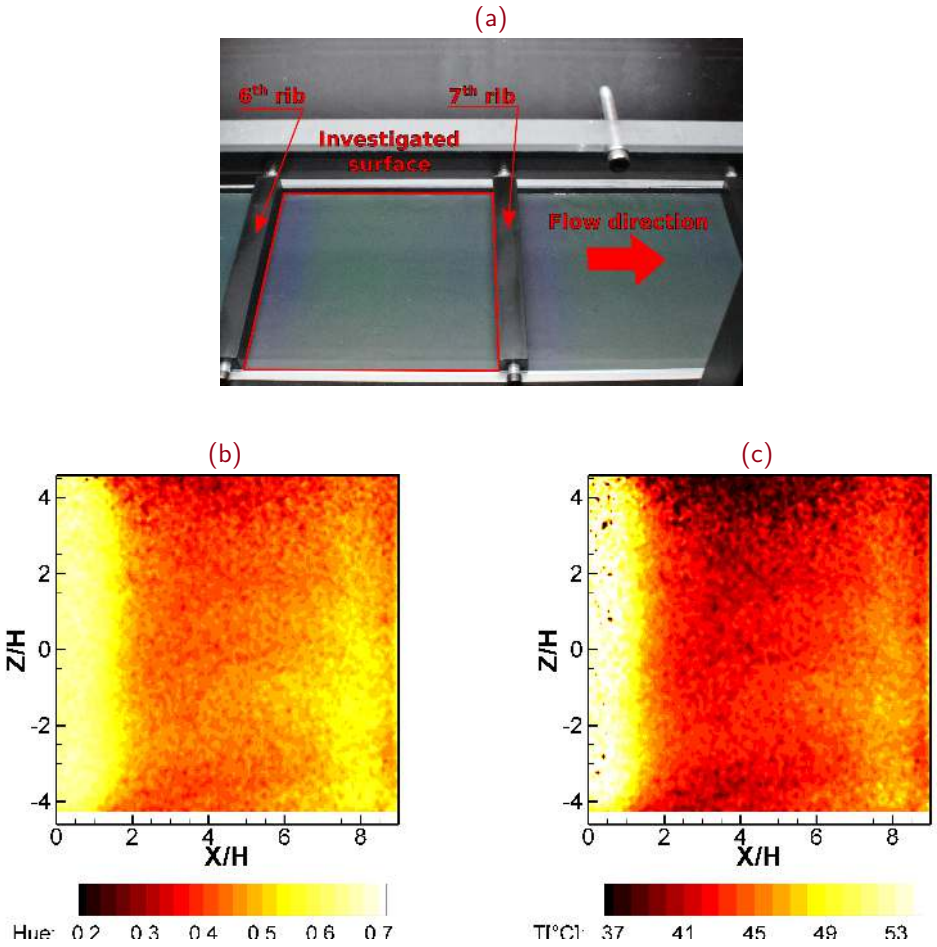

Figure 3.22 : Raw picture (a) and corresponding Hue (b) and temperature (c) distributions between the 6th and 7th ribs at Re = 15,000, Ro = 0

3.22b. In order to transform the image into the physical domain (from pixels to mm), a perspective transformation of the area of interest in the picture is performed. From the Hue-temperature calibration curve, the temperature distribution on the investigated surface is obtained. The corresponding temperature field in the example at $Re = 15{,}000$ and $Ro = 0$ is represented in Fig. 3.22c. After obtaining the temperature distribution in the investigated area, the heat transfer on the wall is investigated. The following data reduction methodology allows to obtain the dimensionless heat transfer coefficient on the TLC surface from the temperature and heating power measurements.

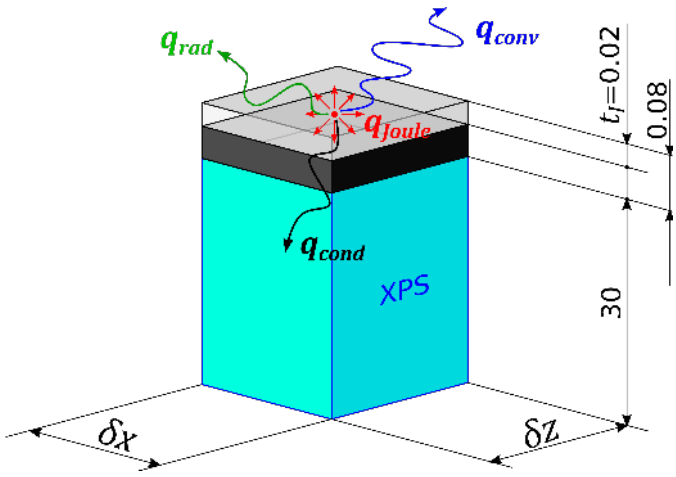

Figure 3.23 : Sketch of the considered heating element and energy balance (dimensions given in [mm])

3.4.4.1 Energy balance and Joule heating power

To obtain the convective heat transfer and the Nusselt number, an energy balance on the heating foil is carried out. A finite volume of the Inconel foil with a size $\delta x \times t_I \times \delta z$ is considered, as depicted in Fig. 3.23. In the present study, the values δx and δz have been set equal to 1 mm, whereas the foil thickness, t_I is equal to 0.02 mm. In the finite volume, the heating power per unit area produced by Joule effect, q_{Joule}, is equal to the heat transferred by convection to the fluid, q_{conv}, by conduction through the solid, q_{conv}, and by radiation to the surrounding elements, q_{rad}, per unit area:

$$q_{Joule} = q_{conv} + q_{cond} + q_{rad} \tag{3.20}$$

The Joule power depends on the electric properties of the heating foil and the voltage or intensity applied. Since the resistivity temperature coefficient of the Inconel is low, the electrical properties of the heating foil are assumed to be uniform. For a typical variation of ± 5 K on the Inconel surface, the change of resistivity of the Inconel foil is below $\pm 0.07\%$ of the nominal value. Typically, the Joule power is obtained by measuring the voltage difference across a section of the heating foil (V) and the intensity (I). The resulting Joule power per unit area would be equal to VI/A, A being the surface area over which the voltage difference is measured.

Since there is not direct access to measure the voltage across the Inconel foil during the experiments in rotation, an alternative methodology to obtain the Joule power is adopted. Prior to the experiments, the connection of the Inconel foil with the power supply is made. With no flow, and in static conditions, the voltage difference and intensity across a section of the heating foil is measured for different voltages of the generator. This procedure allows to relate the Joule power per unit area with the voltage generated by the power supply, as well as to obtain the resistivity of the heating foil.

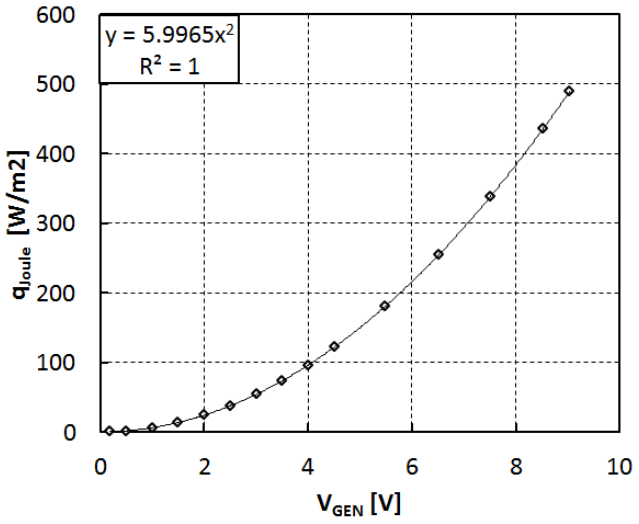

Figure 3.24 : Joule power per unit area in the heating foil as a function of the voltage of the power supply

In the present study, the Inconel surface is equal to 1510×138 mm^2, and the resulting q_{Joule}-voltage relationship is given in Fig. 3.24. The Joule power per unit area can be expressed as

$$q_{Joule} = C \cdot V_{GEN}^2 \tag{3.21}$$

where $C = 5.9965$, and V_{GEN} is the voltage of the generator. The fitting error of this relationship with the experimental points shown in Fig. 3.24 is about 0.13 W/m^2. In the experiment at $Re = 15{,}000$ and $Ro = 0$, q_{Joule} is about $400 W/m^2$, for which the fitting error represents about a 0.03%. It can be stated that the present method to calculate the Joule heating power per unit area is highly accurate and simplifies the measurement chain.

3.4.4.2 Conductive heat transfer

The heat transfer per unit area lost by conduction has been estimated from the temperature measurement of the TLC layer and the external face of the XPS wall, and assuming 1D conduction in the XPS wall,

$$q_{cond} = \frac{k_{XPS}}{t_{XPS}} \left[T_w\left(x,z\right) - \overline{T_{w,ext}} \right] \tag{3.22}$$

where k_{XPS} and t_{XPS} are the thermal conductivity and thickness of the XPS wall, $T_w\left(x,z\right)$ is the temperature given by the TLCs at a location (x,z) and $\overline{T_{w,ext}}$ is the mean temperature of the five thermocouples placed on the external face of the XPS wall (Figs. 3.15 and 3.16). In the present experimental setup $k_{XPS} = 0.033$ W/(m·K) and $t_{XPS} = 30$ mm.

The temperature of the Inconel element, where the energy balance is carried out, is assumed to be the same as the one in the TLC layer. Indeed, their relative distance is of order of 0.1 mm and the conductivity of the TLC, black paint and acrylic adhesive is relatively low (0.2-0.4 $W/(m \cdot K)$). Considering the stationary heat equation in the layer and assuming uniform thermal properties,

$$\frac{\partial^2 T}{\partial x^2} + \frac{\partial^2 T}{\partial y^2} + \frac{\partial^2 T}{\partial z^2} = 0$$

the ratio of the normal gradients to the lateral gradients of the temperature is of the order of the square of the ratio between the normal and lateral length scales (l_z and l_x respectively):

$$\frac{\Delta_z T}{\Delta_x T} \sim \left(\frac{l_z}{l_x}\right)^2$$

The lateral length scale l_x is of order of the rib height, since it can be seen in Fig. 3.22c that the temperature variations take place in a characteristic length of order of H. The normal length scale is of the order of the layer thickness, and therefore ${}^{\Delta_z T}/_{\Delta_x T} \ll 1$. Thus, the temperature gradients in the direction normal to the layer are negligible, and the temperature in the Inconel foil can be assumed equal to that in the TLC layer.

In the example of the experiment at $Re = 15{,}000$ and $Ro = 0$, the mean q_{cond} is about 19 W/m^2, that is, less than 4.8% of the q_{Joule}. The temperature is assumed to be uniform on the external face of the XPS wall, since the standard deviation of the temperature provided by the thermocouples is below 1 K. This deviation introduces an error, δq_{cond}, estimated from the derivation of Eq. (3.22) as

$$\delta q_{cond} \approx \frac{k_{XPS}}{t_{XPS}} \delta T_{w,ext} \tag{3.23}$$

With $\delta T_{w,ext} \sim 1$K, $\delta q_{cond} \sim 1.1$ W/m^2, which represents less than 6% of the overall q_{cond} and less than 0.3% of q_{Joule} in the example at $Re = 15{,}000$ and $Ro = 0$. Note that at larger Reynolds numbers, the convective heat transfer increases and the required Joule power to heat up the TLC layer up to a temperature of about 41°C is larger. However, the magnitude of the conduction losses presents similar values since the boundary conditions of the solid barely change. Therefore, at larger Reynolds numbers, the error due to the non-uniformity of the temperature on the external surface is reduced.

Furthermore, an analysis of the lateral conduction losses in the heating foil has been considered. The net lateral conduction losses in each finite volume (Fig. 3.23) in the x direction has been evaluated as the difference between the heat fluxes on the faces normal to the x direction:

$$Q_{lat,x}(x,z)\,[W] = \left[\frac{k_I}{\delta x}\left[T_w(x,z) - T_w(x+\delta x,z)\right] + \frac{k_I}{\delta x}\left[T_w(x,z) - T_w(x-\delta x,z)\right]\right] \times t_I \delta z$$

where t_I is the heating foil thickness and k_I the Inconel thermal conductivity. Similarly, in the z direction:

$$Q_{lat,z}\left(x,z\right)\left[W\right] = \left[\frac{k_I}{\delta z}\left[T_w\left(x,z\right) - T_w\left(x,z+\delta z\right)\right] + \frac{k_I}{\delta z}\left[T_w\left(x,z\right) - T_w\left(x,z-\delta z\right)\right]\right] \times t_I \delta x.$$

Therefore, the corresponding lateral losses per unit area are

$$q_{lat,x}\left(x,z\right) = \frac{Q_{lat,x}\left(x,z\right)}{\delta x \delta z} = \frac{k_I t_I}{\delta x^2} \cdot \left[2T_w\left(x,z\right) - T_w\left(x+\delta x,z\right) - T_w\left(x-\delta x,z\right)\right] \quad (3.24)$$

$$q_{lat,z}\left(x,z\right) = \frac{Q_{lat,z}\left(x,z\right)}{\delta x \delta z} = \frac{k_I t_I}{\delta z^2} \cdot \left[2T_w\left(x,z\right) - T_w\left(x,z+\delta z\right) - T_w\left(x,z-\delta z\right)\right] \quad (3.25)$$

Figure 3.25 compares the span-wise averaged Nusselt number at Re = 15,000 and Ro = 0 when the lateral conduction losses are taken into account with that in the original analysis. In the present investigation, the lateral conduction losses per unit area are of order of 7% of the normal conduction losses per unit area, which corresponds to about 0.3% of q_{Joule} in the case at Re = 15,000 and Ro = 0. For this reason, only the normal conduction terms (Eq. (3.22)) where considered. The largest variations of the Nu distribution are observed in the region $x/H < 0.7$. In this area, the temperature is the highest, which leads to a higher T_w uncertainty. In some points, the temperature is above the TLC nominal range. For this reasons, the results immediately behind the rib are noisy and present high uncertainty.

3.4.4.3 Radiative heat transfer

The heat loss by radiation per unit area of the heating element considered in Fig. 3.23 is estimated as

$$q_{rad}\left(x,z\right) = \sigma \cdot \varepsilon_{TLC} \cdot \left(T_w\left(x,z\right)^4 - T_\infty^4\right) \quad (3.26)$$

where σ is the Stefan-Boltzmann constant, ε_{TLC} the emissivity of the TLCs, and T_∞ the temperature of the surrounding elements. The value of ε_{TLC} has been chosen to be equal to 0.9, according to Batchelder and Moffat [79]. The temperature of the surrounding solids is assumed to be equal to the ambient temperature, whereas the view factor is chosen equal to 1 since the heating element (Fig. 3.23) is completely surrounded.

3.4.4.4 Convective heat transfer, Nusselt number and Enhancement Factor

The convective heat transfer per unit area is obtained from Eq. (3.20) at each point of the XZ plane as

$$q_{conv}\left(x,z\right) = q_{Joule} - q_{cond}\left(x,z\right) - q_{rad}\left(x,z\right) \quad (3.27)$$

Figure 3.26 shows the mean values of q_{conv}, q_{rad} and q_{cond} in the area between the 6th

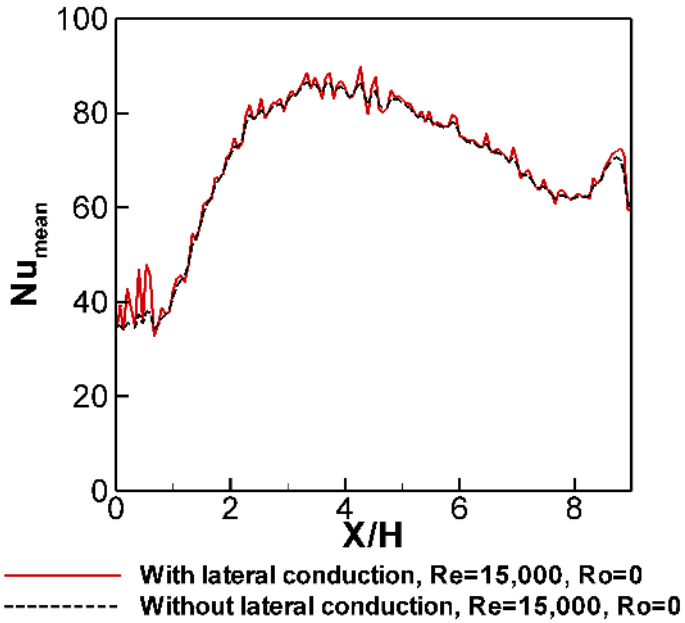

Figure 3.25 : Comparison of the span-wise averaged Nusselt number with and without lateral conduction losses in the analysis

and 7th ribs at different Re, Ro and rotation directions. Depending on these parameters, the q_{Joule} applied to the Inconel foil was varied in order to keep a TLC temperature of about 41°C. It can be observed that the values of q_{rad} and q_{cond} are very similar from experiment to experiment, due to the similar temperature boundary conditions. For a given Ro and rotation direction, it can be observed that q_{conv} increases as Re increases. However, the q_{conv} increase from Re = 30,000 to 55,000 is not as high as initially expected. The latter regime corresponds to the maximum pressure ratio that the centrifugal fan providing the mass flow is able to achieve. In consequence, the temperature of the fluid is higher (about 8 K larger than at Re =15,000), reducing the driving temperature and hindering the heat transfer. On the other hand, it is clear that the heat transfer is promoted when the channel turns in the counter-clockwise sense, at a given Reynolds number. This is due to the flow destabilization close to the investigated wall when the channel rotates in the counter-clockwise sense, whereas the flow is stabilized when the channel rotates in the opposite sense (leading to a heat transfer reduction).

Then, the heat local heat transfer coefficient, h, is calculated as

$$h\left(x,z\right)=\frac{q_{conv}\left(x,z\right)}{T_w\left(x,z\right)-T_c\left(x\right)} \tag{3.28}$$

where $T_c\left(x\right)$ is the estimated temperature at the center of the cross section. T_c is calculated by interpolating between the values of the inlet and outlet fluid temperature

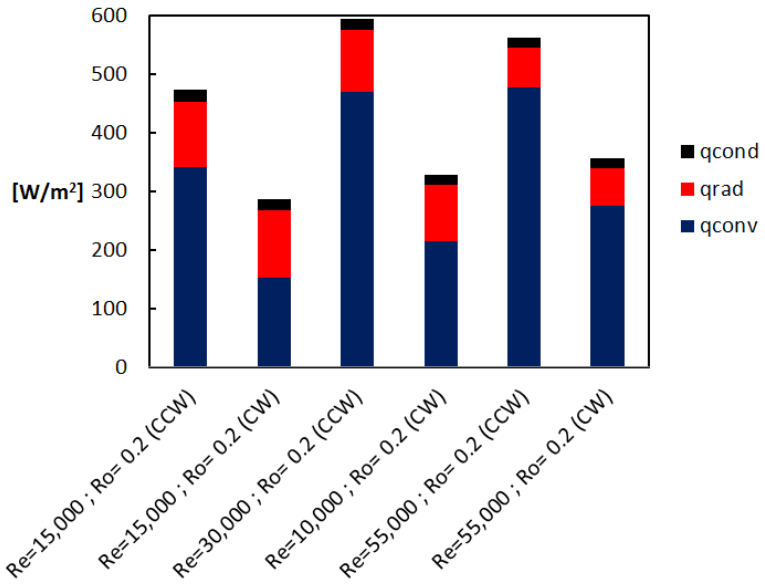

Figure 3.26 : Overall heat transfer per unit area in the region between the 6th and 7th ribs at different conditions

(T_{in} and T_{out}, respectively) at a position x. The difference between T_{in} and T_{out} is always below 1K, which leads to a temperature gradient lower than 0.8 K/m. In the present experiments, the temperature difference $T_{in} - T_{out}$ decreases as the Reynolds number increases. This behavior can be explained due to the importance of the mass flow over the heat transfer increase by the Reynolds number, at a constant driving temperature. If an overall heat transfer balance is made by applying the integral form of the energy equation to the fluid motion in the present conditions, it can be found that the increase of temperature (ΔT) is related to the heat transfer in the following way:

$$\dot{m} c_p \Delta T \simeq Q\,(\Delta x) \tag{3.29}$$

where $\dot{m}$ is the mass flow and Q the total amount of heat introduced in the fluid. Q is estimated as

$$Q \sim h\,(T_w - T_c) \cdot \Pi \cdot \Delta x \sim Nu \cdot \frac{k_f \Pi \Delta x}{D_H} \cdot (T_w - T_c) \tag{3.30}$$

where k_f is the representative fluid thermal conductivity, Π the perimeter of the cross section and Δx the length of the considered section. The Dittus-Boelter correlation as introduced by McAdams [80] proposes $Nu \propto Re^{0.8}$, whereas $\dot{m} = Re \mu D_H$. Therefore,

$$\Delta T \propto Re^{-0.2} \cdot (T_w - T_c) \tag{3.31}$$

Since the driving temperature $T_w - T_c$ presents a value of about 15 K during the experiments, it results that the temperature difference between the outlet and the inlet

decreases as the Reynolds number increases with the power law:

$$\Delta T \propto Re^{-0.2} \tag{3.32}$$

The Nusselt number employed to present the experimental results is defined as

$$Nu\,(x,z) = \frac{h\,(x,z)\cdot D_H}{k_f\,(x,z)} \tag{3.33}$$

The representative fluid thermal conductivity (k_f) has been calculated as the air thermal conductivity at the film temperature, T_{film},

$$T_{film}\,(x,z) = \frac{1}{2}\left[T_w\,(x,z) + T_c\,(x)\right] \tag{3.34}$$

Most of the dimensionless heat transfer data presented in this work are given in terms of the Enhancement Factor (EF), which is the ratio of the local Nusselt number with the one corresponding to a smooth pipe at the same Reynolds and Prandtl numbers:

$$EF\,(x,z) = \frac{Nu\,(x,z)}{Nu_0} \tag{3.35}$$

The Enhancement Factor is a figure of merit that aims to account for the effectiveness of the channel in terms of its heat transfer performance independently from the Reynolds and Prandtl number. The reference Nusselt number, Nu_0, has been determined from the Dittus-Boelter correlation as introduced by McAdams [80, 81]:

$$Nu_0 = 0.023 \cdot Re^{0.8} \cdot Pr^{0.4} \tag{3.36}$$

Figure 3.27 shows an example of the Nusselt number and Enhancement Factor contours, corresponding to the Hue and Temperature fields represented in Fig. 3.22. High (low) temperatures are related to low (high) heat transfer, Nu and EF.

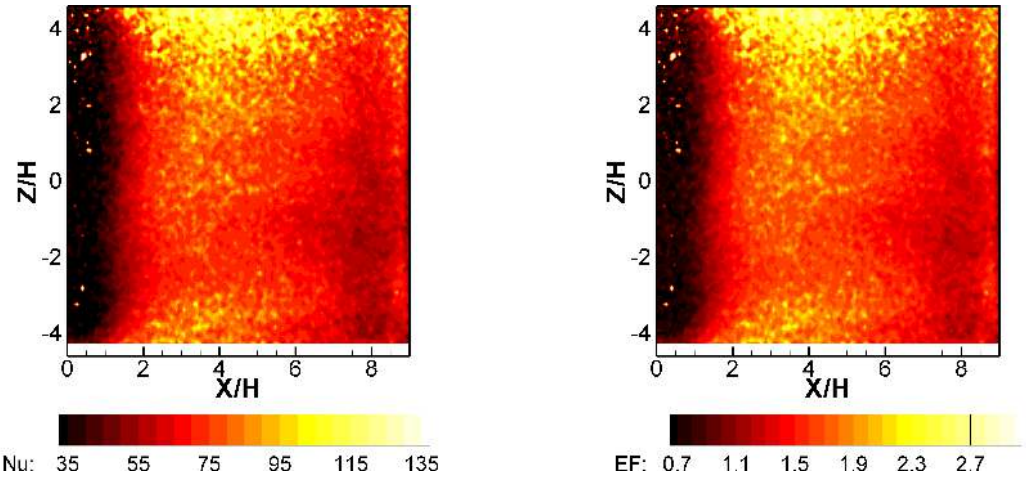

Figure 3.27 : Nusselt and Enhancement Factor contours between the 6th and 7th ribs at Re = 15,000, Ro = 0

Chapter 4

Experimental uncertainty estimation

4.1 Test uncertainty

One of the objectives of the present work is to provide a reliable estimation of the measurement error of the dimensionless velocity and heat transfer in the investigated area. The uncertainty analysis aims to quantify the relative importance of the error sources. In this way, the evaluation has allowed to adapt the experimental setup to minimize the final measurement error.

The uncertainty analysis aims to estimate, from the observed value, the interval where the measured magnitude is expected to lie in with a determined confidence level (C.L.). The expected value of the $\overline{\chi}$ is expressed as

$$\overline{\chi} \pm U_{\overline{\chi}}\,(\text{C.L.}) \tag{4.1}$$

where $\overline{\chi}$ is the observed value and $U_{\overline{\chi}}$ is the expanded estimated uncertainty at a given C.L. In particular, $\overline{\chi}$ can be the value of the velocity, temperature or heat transfer. Numerous textbooks, technical notes, manuals, etc., address different methodologies to assess and to express the measurement uncertainty. In this thesis, the nomenclature suggested by the ASME PTC 19.1-2005 [82] has been adopted due to its simplicity. Other documents, as the ISO Guide to the Uncertainty Measurement [83] and NASA Handbook 8739.19-2 [84], have been employed as references to evaluate the measurement uncertainty in complex cases.

The expanded uncertainty is obtained from the standard uncertainty, $u_{\overline{\chi}}$, to which a correction factor is applied in order to account for the confidence level:

$$U_{\overline{\chi}} = t_{\nu,\text{C.L.}} \cdot u_{\overline{\chi}} \tag{4.2}$$

where $t_{\nu,\text{C.L.}}$ is the Student's t distribution value with ν degrees of freedom and a given confidence level. For a large number of degrees of freedom and a typical C.L. equal to 95%, $t_{\nu,95\%} \approx 2$.

The standard uncertainty is estimated from the systematic and random standard

uncertainties, $b_{\overline{\chi}}$ and $s_{\overline{\chi}}$ respectively, as:

$$u_{\overline{\chi}} = \sqrt{b_{\overline{\chi}}^2 + s_{\overline{\chi}}^2} \tag{4.3}$$

The velocity and heat transfer distributions are calculated from measured values ξ_k (such as the interrogation window displacement, mass flow, wall temperature, ...), each of them with a measurement systematic and random uncertainty, b_{ξ_k} and s_{ξ_k}. Applying the Central Limit Theorem to the known function that relates the final magnitude with the original measured values,

$$\overline{\chi} = f\left(\xi_1, \xi_2, ..., \xi_K\right) \tag{4.4}$$

the contributions of each error source to the final uncertainty are estimated as

$$b_{\overline{\chi}} = \sqrt{\sum_{k=1}^{K} \left(\frac{\partial \overline{\chi}}{\partial \xi_k} b_{\xi_k}\right)^2} \tag{4.5}$$

and

$$s_{\overline{\chi}} = \sqrt{\sum_{k=1}^{K} \left(\frac{\partial \overline{\chi}}{\partial \xi_k} s_{\xi_k}\right)^2} \tag{4.6}$$

K being the number of error sources with systematic and random errors, $\left(b_{\overline{\chi}}^2\right)_k$ and $\left(s_{\overline{\chi}}^2\right)_k$ respectively.

Finally, the degrees of freedom of the Student's t factor, ν_{DoF}, are calculated from the Welch-Satterthwaite equation:

$$\nu_{DoF} = \frac{\left[\sum_{k=1}^{K}\left(b_\xi^2\right)_k + \sum_{k=1}^{K}\left(s_\xi^2\right)_k\right]^2}{\sum_{k=1}^{K}\frac{\left(b_\xi^4\right)_k}{\nu_k} + \sum_{k=1}^{K}\frac{\left(s_\xi^4\right)_k}{\nu_k}} \tag{4.7}$$

being ν_k the degrees of freedom of the variable ξ_k.

In practice, the values of b_{ξ_k} and s_{ξ_k} are either given from the measurement device manufacturer or estimated from calibrations. The number of degrees of freedom of the error source k, ν_k, is assumed to be equal to infinity in the case of not being specified by the device manufacturer. Then, the resulting systematic and random uncertainties are estimated from Eqs. (4.5) and (4.6). The resulting degrees of freedom are estimated from Eq. (4.7) and the Student's t factor is calculated, typically for a probability equal to 95%. Finally, the standard and expanded uncertainties are calculated from Eqs. (4.3) and (4.2), respectively. The methodology and assumptions applied to the present PIV and TLC measurements are summarized in the following sections.

4.2 PIV uncertainty

The magnitude that PIV directly measures corresponds to the mean particle displacement in the given interrogation windows observed by the camera, ΔX. The displacement needs to be translated to the real coordinates by means of the magnification factor, and divided by the separation time in order to obtain the local velocity (Eq. (3.9)):

$$u = \frac{\Delta X}{M \cdot \Delta t}$$

Consequently, the PIV measurement uncertainty depends on the individual uncertainties of ΔX and M. The contribution of the separation time, Δt, is considered negligible. The error on ΔX depends the quality of the PIV experiment and the algorithm employed to process the individual realizations. In the present work, the WIDIM algorithm introduced by Scarano and Riethmuller [64, 68] has been employed to obtain the local particle displacement. The measurement error sources related to the PIV experiment considered in the present work are:

- systematic error due to the sub-pixel window offset, $b_{\Delta X,1}$
- random error due to the sub-pixel window offset, $s_{\Delta X,1}$
- random error due to the displacement gradient (flow shear) $s_{\Delta X,2}$
- random error due to the determination of the magnification factor, s_M
- random error due to the measurement of the bulk velocity, b_{U_b}

In the present work, the measurement uncertainty has been calculated for PIV realization, and then averaged to give a mean representation. The systematic and random errors due to the sub-pixel window offset are related to the capability of the PIV algorithm to provide the interrogation window displacement within a fraction of pixel. Reference [68] provides the corresponding errors for different interrogation window size. For a typical size of 16×16 pixel^2, $b_{\Delta X,1}$ and $s_{\Delta X,1}$ are below 0.01 and 0.005 pixels, respectively.

The random error due to the displacement gradient is related to the capability of the PIV algorithm to find the mean velocity in an interrogation window where the velocity gradient is important. This measurement error is one of the most important since the most interesting area of the flow field, the near-wall region, presents large velocity gradients. This error is a function of the local velocity gradient, and in the present case shows values up to 0.07 pixels on the top of the ribs.

The error due to the determination of the magnification factor arises from the resolution of the camera sensor and to the optical aberrations, which introduce image deformations in certain regions of the image. This error is quantified by measuring the magnification factor in different regions of the image, providing values lower than 0.2% of the magnification factor.

The PIV results are provided in terms of the dimensionless velocity,

$$\frac{u}{U_b} = \frac{\Delta X}{M \cdot \Delta t \cdot U_b} \tag{4.8}$$

Therefore, the error due to the measurement of the bulk velocity, b_{U_b} needs to be included in the analysis. In order to calculate the mass flow measurement uncertainty in the Venturi nozzle, the ISO 5167-1:2003 and ISO 5167-3:2003 standards [85] have been employed. The main contributors to the uncertainty are the discharge coefficient and the expansion ratio. For the typical values measured in the laboratory, the standard uncertainty due to the bulk velocity measurement is estimated to be about 1.4% of the measured value.

The contribution of each of the measurement uncertainties is calculated by deriving Eq. (4.8) with respect to each of the error sources. For instance, the random error due to the magnification factor is estimated as

$$s_M = \frac{\partial}{\partial M}\left(\frac{u}{U_b}\right) \times 0.002M = \frac{u}{U_b} \times 0.002 \tag{4.9}$$

Figures 4.1 and 4.2 compare the contribution of each error source to the dimensionless velocity measurement in two representative cases, both at Re=15,000 and Ro=0, but different Fields of View due to the camera objectives (see Tables 3.3 and 3.4). The figures also show the overall (average in the flow field) and maximum standard uncertainties. In the case of the reduced flow field, it can be observed that the most important contributions are those of the displacement gradient and the bulk velocity measurement. The overall standard uncertainty caused by the displacement gradient is about 0.15% of the bulk velocity, but it reaches values up to 1.1% in the region just above the ribs. The error due to the bulk velocity measurement is weighted by the local flow velocity, providing an overall value of about 0.5% of U_b, and a maximum value of about 1% of U_b in the area of maximum velocity (away from the wall). In the case of the large Field of View, Fig. 4.2, the measurement uncertainty increases as explained in section 3.3. Since the displacement gradient within the interrogation window is larger due to the optical setup, the corresponding error is almost doubled in the near-wall region and on the top of the ribs. In this case, the maximum value of the contribution to the standard uncertainty is about 1.8% of U_b, whereas the overall contribution is estimated to be equal to 0.2% in the region of interest. However, the most important factor of the dimensionless velocity overall uncertainty is the error due to the determination of the bulk velocity. The overall contribution of the latter error source to the final uncertainty is about 0.8% of the bulk velocity, whereas its maximum value is equal to 1.4%.

The resulting systematic and random errors are estimated by applying the Central Limit Theorem to the dimensionless velocity,

$$b_{\overline{u}/U_b} = \sqrt{\left(b_{\Delta X,1}\right)^2 + \left(b_{U_b}\right)^2} \tag{4.10}$$

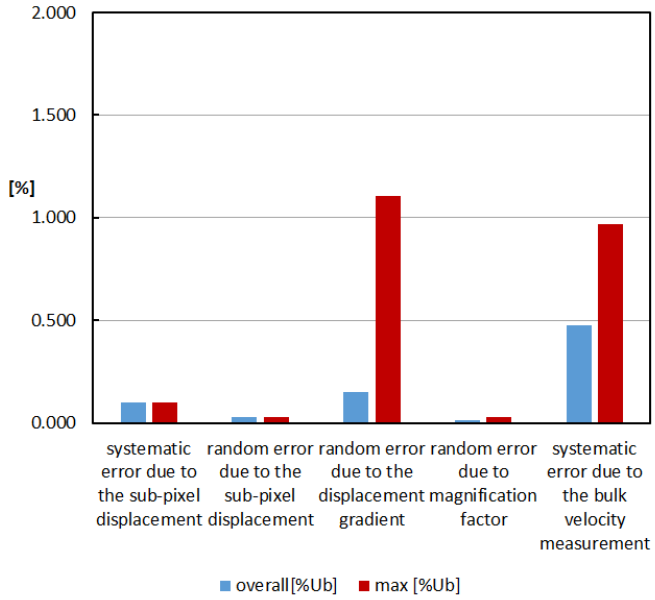

Figure 4.1 : Systematic and random errors for the static case, $Re = 15{,}000$, and reduced Field of View

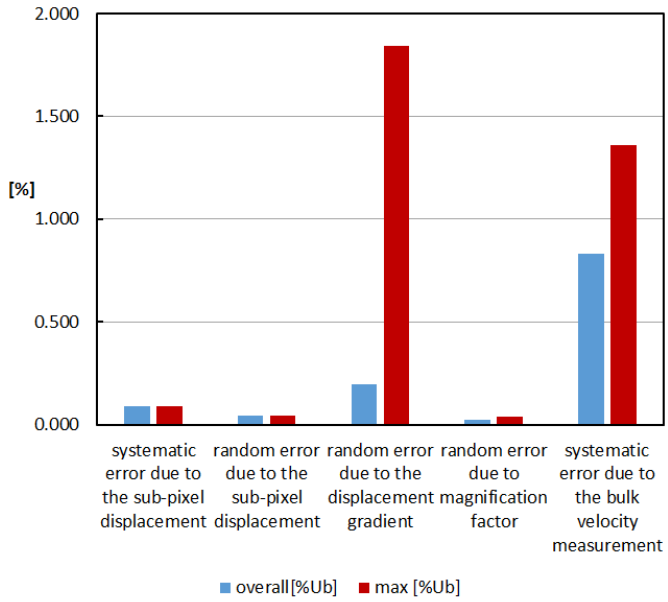

Figure 4.2 : Systematic and random errors for the static case, $Re = 15{,}000$, and large field of view

$$s_{\overline{u}/U_b} = \sqrt{\left(s_{\Delta X,1}\right)^2 + \left(s_{\Delta X,2}\right)^2 + \left(s_M\right)^2} \tag{4.11}$$

whereas the degrees of freedom have been calculated from the Welche-Satterthwaite equation (Eq. (4.7)) The number of degrees of freedom related to the sub-pixel window offset and displacement gradient, $\nu_{\Delta X,1}$, $\nu_{\Delta X,2}$, have been set equal to 10, which is the approximate number of particles in each interrogation window. On the other hand, the degrees of freedom for the magnification factor, ν_M, and the measurement of the bulk velocity, ν_{U_b}, are set to infinity. The degrees of freedom estimated from the Welche-Satterthwaite formula with the present values show an average value in the order of magnitude of 10^3. Therefore, the number of degrees of freedom of the Student's t factor is assumed to be equal to infinity.

The resulting standard uncertainty in the dimensionless stream-wise velocity measurement, u_{u/U_b}, is calculated by applying Eq. (4.3). The corresponding expanded uncertainty, $U_{u/U_b}(95\%)$, is calculated by multiplying u_{u/U_b} by $t_{\infty,95\%}$. Figures 4.3 and 4.4 show the resulting expanded uncertainty at a 95% confidence level of the mean stream-wise velocity, U_{u/U_b} in the reference experiments with reduced and large fields of view. In the case of reduced field of view, the overall expanded uncertainty is about 1.2% of the bulk velocity, showing large uncertainties in the near wall region (i.e. interrogation windows adjacent to the bottom wall). Away from the high-shear region, the uncertainty is reduced, specially in the area where the main velocity is low, that is, just downstream of the rib. As the velocity becomes larger, the uncertainty increases due to the uncertainty in the bulk velocity determination. When the field of view is enlarged (Fig. 4.4), the displacement error becomes more important, specially on the top of the rib. As in the previous case, the expanded uncertainty away from the near-wall region is directly related to the uncertainty in the determination of the bulk velocity. The uncertainty is low in regions of low velocity, and large is areas of high velocity. In this case, the overall expanded uncertainty of the dimensionless stream-wise velocity is estimated to be equal to 1.8% of the bulk velocity at a 95% confidence level.

4.3 LCT uncertainty

The uncertainty analysis of the LCT is made in two steps: the first related to the temperature measurement and the second to the dimensionless heat transfer. The temperature uncertainty is assessed in the calibration rig shown in section 3.4.3, whereas the heat transfer uncertainty analysis is performed with the heat transfer data obtained in the investigated channel.

4.3.1 TLC temperature uncertainty

Several papers have addressed the experimental uncertainty related to LCT [72, 74, 75], focusing on the main error sources in the temperature measurements. However, no detailed application to express and analyze the measurement uncertainty in LCT is given in the open literature. The present work introduces a practical methodology to estimate the temperature uncertainty in wide-band LCT.

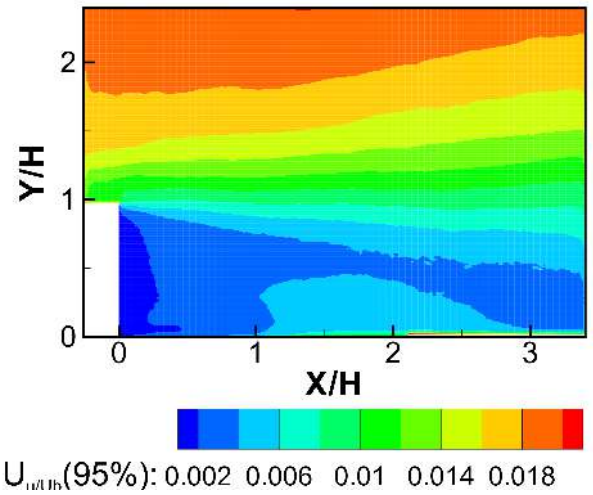

Figure 4.3 : Uncertainty of the dimensionless mean stream-wise velocity at Re=15,000, Ro=0 in the experiments with reduced field of view

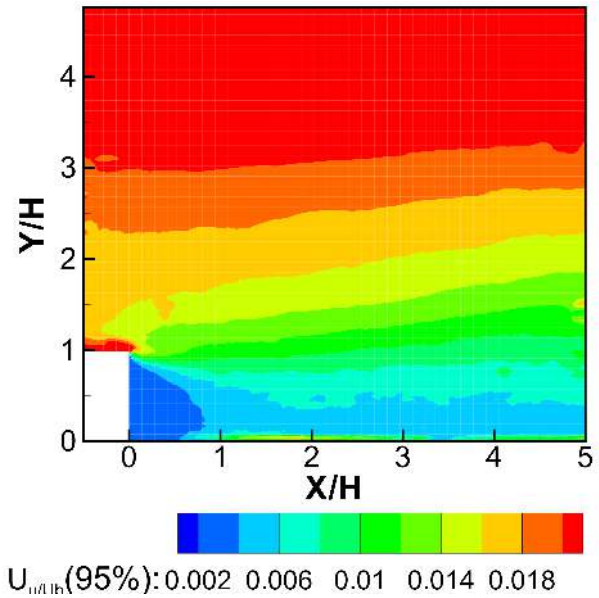

Figure 4.4 : Uncertainty of the dimensionless mean stream-wise velocity at Re=15,000, Ro=0 in the experiments with large field of view

The calibration and measurements in this work are performed in a controlled environment in order to keep constant most of the variables that affect the TLC temperature response, such as the illumination, viewing angles and camera settings. The TLCs were painted at the same time on the calibration rig and the test section in order to get approximately the same film thickness, which notably affects the temperature response. Additionally, the measurements were taken at steady state, about two hours after the experiment starts. To avoid aging effects, the calibration and the full experimental campaign were carried out within a relatively short period of time (7 days). Moreover, repeatability tests were performed to assess the typical test variability. Finally, hysteresis was avoided by operating the TLCs below their maximum working temperature (about 55ºC).

Under these conditions, the measurement error sources considered in the present analysis are:

- systematic uncertainty due to the camera resolution, b_{RGB}
- systematic uncertainty due to the determination of the temperature profile in the calibration rig, b_T
- random uncertainty due to the determination of the temperature profile in the calibration rig, s_T
- random uncertainty due to the non-uniformity of the Hue values in the calibration plate for a given temperature, $s_{non-unif}$
- random uncertainty due to the fitting of the experimental data points to a spline curve, s_{fit}

The systematic uncertainty due to the camera resolution is related to the analog to digital conversion of the RGB signal recorded by the camera. The camera provides a digital signal of the RGB intensities in the range 0 - 255 at each point of the image, with a resolution of 8 bits. The quantization process is assumed to follow a uniform probability distribution [84], and therefore, the corresponding standard uncertainty in the determination of the RGB intensities is equal to

$$b_R = b_G = b_B = \frac{\frac{255}{2^8}}{\sqrt{12}} = 0.288[\text{Arbitrary Units}] \tag{4.12}$$

and therefore,

$$b_{RGB} = b_R \cdot \left[\sqrt{\left(\frac{\partial H}{\partial R}\right)^2 + \left(\frac{\partial H}{\partial G}\right)^2 + \left(\frac{\partial H}{\partial B}\right)^2} \right] \cdot \frac{\partial T}{\partial H} \tag{4.13}$$

The values of $\partial H/\partial R$, $\partial H/\partial G$ and $\partial H/\partial B$ are obtained by deriving Eq. (3.19) and applying the RGB values at each point of the calibration curve (3.21). The value of $\partial T/\partial H$ is obtained from the derivation of the calibration curve shown in Fig. 3.21. On

the other hand, the number of degrees of freedom related to the camera resolution is assumed to be equal to infinity. The resulting b_{RGB} is a function of the temperature, due to the variation of the sensitivity of the temperature-Hue calibration curve over the working range. The average of b_{RGB} over the working range is equal to 0.14 K, with a maximum value equal to 0.35 K, corresponding to the region of high temperatures. In the range 35 - 47°C (308 - 320K), b_{RGB} is about 0.1 K.

The systematic uncertainty due to the determination of the temperature in the calibration plate is related to the limited accuracy of the embedded thermocouples in the plate. An analysis of the thermocouples employed in the present work, based on several calibrations in an oil bath, reveal that the expanded uncertainty of the temperature provided by the thermocouples is about 0.18 K (at a 95% confidence level). The thermocouple calibrations carried out in the oil bath were based on 13 calibration points, and therefore, the number of degrees of freedom of the linear fit employed to express the thermocouple calibration curve is equal to 11. The corresponding Student's t-factor for a 95% confidence level is equal to 2.2, and therefore, the systematic uncertainty b_T is equal to 0.08 K.

The random uncertainty due to the determination of the temperature profile in the calibration plate, arises from the fitting of the temperatures given by the thermocouples embedded in the plate to a linear law. The resulting s_T is equal to 0.10 K, whereas the number of degrees of freedom is equal to 8.

The temperature profile during the calibration process showed a clear linear behavior. Nevertheless, the Hue distribution provided by the TLCs presented reduced variations in the direction perpendicular to the main temperature gradient. These variations are related to the non-uniformity of the plate temperature and the noise of the TLC. The temperature uncertainty related to these non-uniformities, $s_{non-unif}$, is characterized by the standard deviation of the temperature in the direction perpendicular to the main temperature gradient $\sigma_{T,y}$:

$$s_{non-unif} = \frac{1}{N_y} \cdot \sigma_{T,y} = \frac{1}{N_y} \cdot \sqrt{\frac{1}{N_y - 1} \sum_{1}^{Ny} \left[H\left(x, y_j\right) - \overline{H}\left(x\right) \right]^2} \cdot \frac{\partial T}{\partial H} \tag{4.14}$$

where N_y represents the number of point in which the temperature distribution is discretized in the direction normal to the main temperature gradient, $H\left(x, y_j\right)$ is the Hue value at a point (x, y_j) on the calibration plate, and $\overline{H}\left(x\right)$ is the mean hue distribution in the calibration rig (as shown in Fig. 3.21a). The average $s_{non-unif}$ is equal to 0.04 K, whereas its maximum value is about 0.07 K.

The Hue distribution shown in Fig. 3.21a is interpolated by a cubic spline curve with 6 segments. The resulting random uncertainty presents an average equal to 0.10 K, and a maximum value equals 0.17 K when the temperature level is high. The number of degrees of freedom in this case is equal to the number of segments plus the degree of the interpolation, that is, 9 in the present case.

Figure 4.5 shows the comparison of the considered error sources over the operational range of the TLCs. The values of the abscissa axis are normalized with the starting TLC

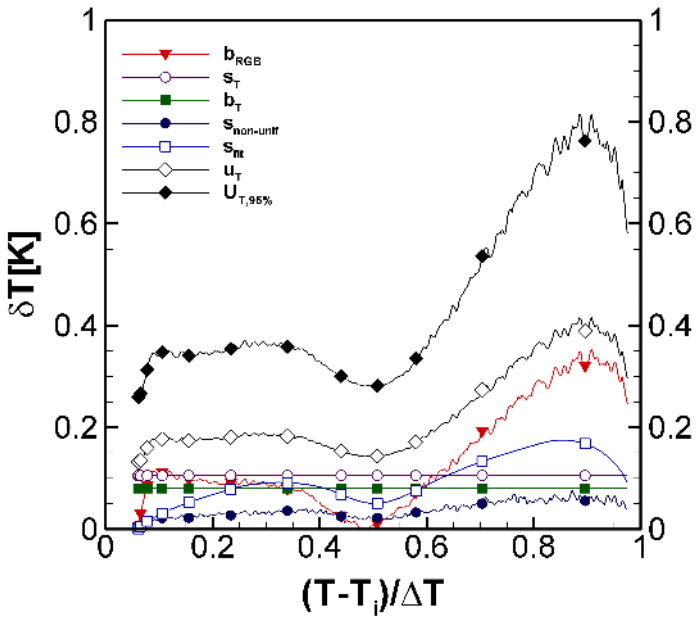

Figure 4.5 : Estimated uncertainty evaluation of the TLC calibration

temperature (T_i, equal to 35 °C) and the measurement range (ΔT, equal to 20°C) in order to allow comparison with TLCs with different operational ranges. The resulting standard and expanded (95% C.L.) uncertainties are also represented in the figure. As a result, the overall expanded temperature uncertainty is 0.45 K, whereas its maximum value is equal to 0.82 K. It is important to note that the uncertainty is below 0.4 K as long as the temperature is below 47.5°C (320.5 K). Above this temperature, the sensitivity of the hue to the temperature is drastically reduced and the errors due to the digital resolution and the spline fit become large. For this reason, the TLCs are preferably operated in the range 35 - 47.5 °C. In turn, the power provided to the heating foil in the experimental section is tunned to achieve a temperature of about 41°C (mean value of the interval 35 - 47.5°C) in the surface thermocouple after the 8th rib.

The uncertainty estimated in the present investigation has been compared with those in the works by Kodzwa and Eaton [86] and Rao and Xu [75] in Table 4.1, obtained by following different methodologies and operational ranges. Table 4.1 shows that the present analysis provides similar values to those given in Refs. [75, 86], in terms of the normalized uncertainty, $U_T/\Delta T$. Therefore, it can be conjectured that the mean uncertainty in the temperature measurement by TLCs is about 2% of the operational range.

4.3.2 Heat transfer uncertainty

The results of the heat transfer analysis are given in terms of the Enhancement factor, which is obtained from the measurement of several primitive quantities, as shown in

Table 4.1 : Comparison the TLC temperature measurement uncertainty

Reference	U_T [K]	ΔT [K]	$U_T/\Delta T$
Kodwa and Eaton [86]	0.20	14	1.4%
Rao and Xu [75]	0.42	20	2.1%
Present investigation	0.45 (95% C.L.)	20	2.3%

section 3.4.4. The uncertainty in the measurement of the primitive values is propagated into the uncertainty of the final result, the Enhancement Factor. In order to calculate the final uncertainty, the sensitivity of the result with respect to the primitive values is calculated from the expressions employed in the data reduction process. The systematic, random and standard uncertainties are calculated with Eqs. (4.3)-(4.6) applied to the Enhancement Factor, whereas the number of degrees of freedom is calculated from expression (4.7). The systematic and bias errors, and the number of degrees of freedom of the primitives variables in the heat transfer experiments are given in Table 4.2.

The systematic uncertainty of the wall external temperature is taken equal to the systematic error of a single thermocouple. On the other hand, the non-uniformity of the wall external temperature is taken into account by the random error, which is equal to the standard deviation of the five thermocouples placed on the external surface (Fig. 3.17). The largest standard deviation in the present experimental campaign was equal to 0.6 K. The uncertainty in the wall temperature measurements depends on the local temperature, as shown in Fig. 4.5. The systematic uncertainty in the Joule heating power per unit area depends on the voltage provided by the generator and its inherent uncertainty. Deriving Eq. (3.21),

$$b_{q_{Joule}} = 2 \cdot C \cdot V_{GEN} \cdot b_{V_{GEN}} \tag{4.15}$$

The voltage supplied by the generator is measured by a digital voltmeter with a resolution of 0.01 V. Therefore, the systematic deviation in the voltage measurement is equal to $0.01/\sqrt{3}$. The applied V_{GEN} depended on the Reynolds and Rotation numbers, and showed values between 7 and 9.6. Thus, the systematic uncertainty in q_{Joule} presents values between 0.49 and 0.68 W/m^2. Additionally, the fitting of the Inconel calibration points to Eq. (3.21) (Fig. 3.24) leading to a random uncertainty equal to 0.13 W/m^2.

On the other hand, the uncertainty of the TLCs emissivity has been estimated from the variation of the emissivities found in the literature. The selected value of ε_{TLC} is equal to 0.90, according to Batchelder and Moffat [79]. However, values as high as 0.95 are present in the literature [87] and therefore $b_{\varepsilon_{TLC}} \simeq 0.05$. Finally, the uncertainty in the mass flow has been estimated following the recommendations of the ISO norms 5167-1:2003 and ISO 5167-3:2003 [85], providing a value below 1.1% of the measured value.

During the calibration of the inlet and outlet thermocouples, 13 calibration points

Table 4.2 : Summary of the primitive uncertainties

Symbol	**Description**	**Units**	**Nominal value**	**Systematic uncertainty**	**Random uncertainty**	**Degrees of freedom**
T_1	inlet temperature	K	295 - 304	0.08	-	11
T_2	exit temperature	K	295 - 304	0.08	-	11
$\overline{T}_{w,ext}$	wall external temperature	K	298 - 301	0.08	0.60	4
T_w	wall temperature	K	308 - 328	Fig 4.5	Fig 4.5	∞
q_{Joule}	Joule heating power	W/m^2	300 - 562	0.49 - 0.68	0.13	13
ε_{TLC}	TLC emissivity	-	0.9	0.05	-	∞
$\dot{m}$	mass flow	kg/s	0.03 - 0.15	$3.4{\cdot}10^{-4}$ - $1.6{\cdot}10^{-3}$		∞

were employed to find the linear relationship between the temperature and the voltage provided by the thermocouples. The corresponding number of degrees of freedom is equal to the number of calibration point minus two, that is, eleven.

In the case of the external wall temperature, the standard deviation of the temperature needs to be taken into account. The number of degrees of freedom related to the spatial variations is equal to the number of thermocouples minus one, that is, four. The corresponding number of degrees of freedom results from the application of the Welche-Satterthwaite formula with the systematic uncertainty and number of degrees of freedom of a thermocouple (0.08 K and 11, respectively) and the random uncertainty and degrees of freedom due to the spatial variations (about 0.6 K and 4, respectively). As a result, the number of degrees freedom is about 4. Note then that the number of degrees of freedom related to the wall temperature is large enough to be considered infinite, as shown in the previous section.

The calibration of the Inconel foil (Fig. 3.24) was obtained from 16 measurement points. Since a parabolic fitting was performed, the resulting number of degrees of freedom concerning the random uncertainty is equal to 16 - 3 = 13. Besides, the contribution to the final number of degrees of freedom of the systematic uncertainty caused by the voltage measurement is negligible. Since the number of degrees of freedom associated to the voltage measurement is equal to infinity, the only contribution in the Welche-Satterthwaite formula corresponds to the random uncertainty due to the fitting. Lastly, the number of degrees of freedom concerning the mass flow and TLC emissivity is estimated to be equal to infinity.

The data shown in Table 4.2 is employed to obtain the uncertainties of the final magnitudes obtained in the experiment. Depending on the Reynolds and Rotation numbers, the heat transfer per unit area is different, which leads to varying uncertainties. Table 4.3 presents the nominal values, and the standard and expanded uncertainties. Given that the values of the temperatures, heat transfer per unit area, etc., are function of the position in the investigated plane, some variations are expected. Table 4.3 shows the area-averaged uncertainty value in the investigated region as well as the maximum uncertainty. The overall uncertainty of the Enhancement Factor is equal to 5.8% (95% C.L.) of the mean Enhancement Factor, whereas the maximum uncertainty is equal to 14.1% (95% C.L.) of the mean Enhancement Factor. The maximum uncertainty values are found in the regions where the secondary flows reduce the wall temperature (close to the lateral walls). The low difference between the wall and fluid temperature results in a high uncertainty in the heat transfer coefficient that is propagated into the Enhancement Factor.

In the case of Table 4.4, the heat transfer is enlarged due to the increase of the Reynolds number and the destabilizing effect by the Coriolis force. The impact of the radiation and conduction losses is reduced due to the higher convective heat transfer. As a result, the relative uncertainty of the Enhancement Factor is slightly reduced to 5.0% (95% C.L.) and the maximum value to 12.5% (95%).

The impact of the primitive magnitudes on the final uncertainty has been analyzed by deriving the expression of the Enhancement Factor with respect to each variable in

Table 4.3 : Summary of the heat transfer uncertainties at Re = 15,000, Ro = 0

Parameter	Units	Mean value	Overall standard uncertainty	Overall uncertainty (95% C.L.)	Maximum uncertainty (95% C.L.)
Re	-	15,116	102	203	203
Ro	-	0	0	0	0
T_c	^{o}C	23.3	0.1	0.2	0.2
T_w	^{o}C	44.4	0.2	0.4	0.8
q_{Joule}	W/m^2	400.4	0.06	1.1	1.1
q_{rad}	W/m^2	125.7	7.1	13.9	22.15
q_{cond}	W/m^2	19.2	0.9	1.8	1.9
q_{conv}	W/m^2	255.5	7.2	14.1	22.3
Nu	-	69.6	2.0	3.9	9.7
EF	-	1.55	0.05	0.09	0.22

Table 4.4 : Summary of the heat transfer uncertainties at Re = 55,000, Ro = 0.21 counter-clockwise

Parameter	Units	Mean value	Overall standard uncertainty	Overall uncertainty (95% C.L.)	Maximum uncertainty (95% C.L.)
Re	-	53,727	351	688	688
Ro	-	0.210	0.002	0.003	0.003
T_c	^{o}C	31.0	0.1	0.2	0.2
T_w	^{o}C	42.3	0.2	0.4	0.8
q_{Joule}	W/m^2	562.6	0.07	1.3	1.3
q_{rad}	W/m^2	69.2	4.1	7.9	17.8
q_{cond}	W/m^2	17.0	1.1	2.1	2.7
q_{conv}	W/m^2	476.4	4.3	8.4	17.9
Nu	-	246.6	5.7	11.2	31.0
EF	-	2.0	0.05	0.10	0.25

Table 4.2. For instance, the effect of the external wall temperature uncertainty on the Enhancement factor is calculated as

$$u_{EF,\overline{T}_{w,ext}} = \frac{\partial EF}{\partial Nu} \cdot \frac{\partial Nu}{\partial h} \cdot \frac{\partial h}{\partial q_{conv}} \cdot \frac{\partial q_{conv}}{\partial q_{cond}} \cdot \frac{\partial q_{cond}}{\partial \overline{T}_{w,ext}} \cdot u_{\overline{T}_{w,ext}} \tag{4.16}$$

which leads to

$$u_{EF,\overline{T}_{w,ext}} = EF \cdot \frac{q_{cond}}{q_{conv}} \cdot \frac{1}{T_w - \overline{T}_{w,ext}} \cdot u_{\overline{T}_{w,ext}} \tag{4.17}$$

Figures 4.6 and 4.7 summarize the impact of the primitive magnitudes on the EF standard uncertainty in the cases of Tables 4.3 and 4.4. For each primitive magnitude, two values are given: the average and maximum standard uncertainties. Finally, the magnitudes represented in the Figures are normalized with the value of the mean EF in each experiment. When Re = 15,000, the largest uncertainty is caused by the TLC emissivity uncertainty, reaching a value about 2.5% of EF. This is due to the fact that the radiative heat transfer losses are important in the energy balance, and because of the high uncertainty on the TLC emissivity. The second most important error source is the wall temperature provided by the TLCs, reaching an average value of 1.4% of the mean EF. It is important to note that the maximum value of the uncertainty caused by the wall temperature is about 3% of the mean EF. This high value appears in the areas where the rib-induced secondary flows are in contact with the investigated wall, reducing the local wall temperature and its difference with respect to the fluid temperature, which leads to an increase of the uncertainty. For the same reason, the maximum impact of the intet and outlet temperatures is somewhat larger than the averaged value: a relatively small error in the fluid temperature is amplified in the region where the fluid-to-wall temperature is reduced.

In the case at Re = 55,000 and Ro = 0.2 (counter-clockwise rotation), the radiative heat transfer is not as important as in the previous case, leading to a reduced impact of the TLC emissivity in the final uncertainty. However, the impact of the wall temperature given by the TLCs is slightly enlarged to become about 2% of the mean EF. This is due to the high fluid temperature, driving to a reduction of the difference between the wall and fluid temperatures.

This analysis reveals the factors whose uncertainty needs to be reduced to obtain EF relative uncertainties below 5%. The main actions that can be taken into account to achieve this goal are:

- determine accurately the emissivity of the TLCs
- increase the driving temperature (fluid-to-wall temperature difference)
- reduce the TLC temperature uncertainty by increasing the resolution of the camera and by using more accurate thermocouples during the calibration

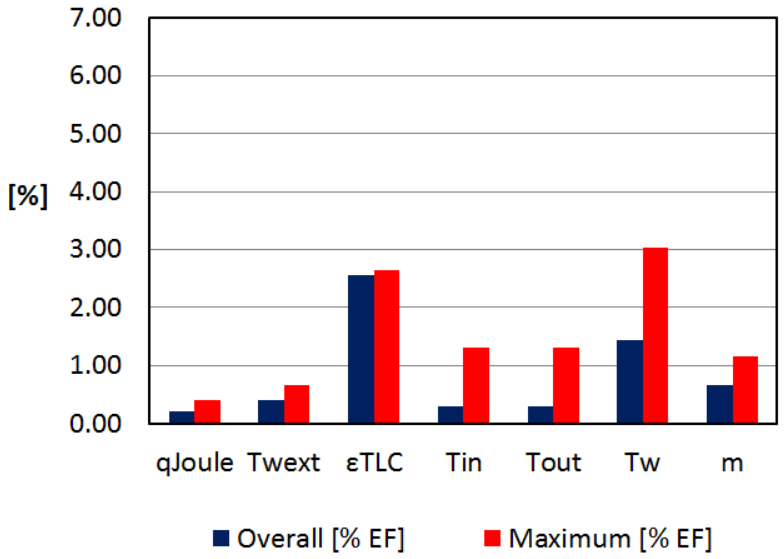

Figure 4.6 : Influence of the primitive magnitudes in the final EF relative standard uncertainty, at $Re = 15{,}000$ and $Ro = 0$

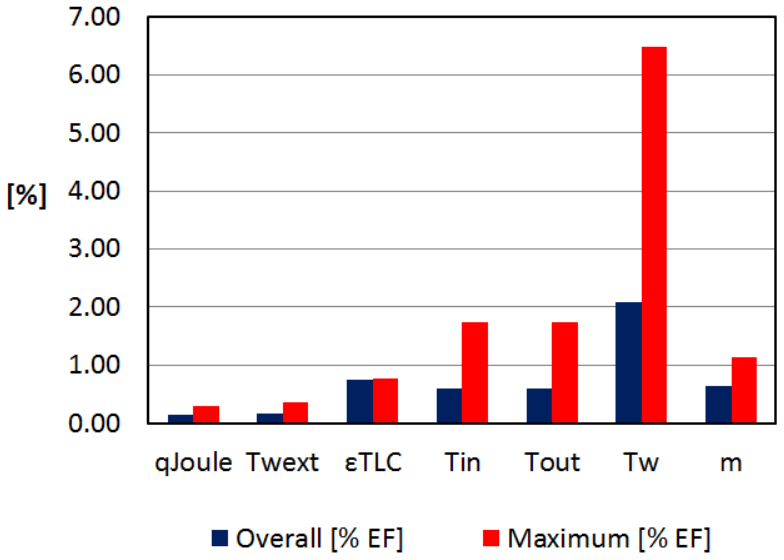

Figure 4.7 : Influence of the primitive magnitudes in the final EF relative standard uncertainty, at $Re = 55{,}000$ and $Ro = 0.21$, counter-clockwise rotation

Chapter 5

Numerical details

5.1 Physical modeling and flow conditions

The present work also aims at introducing a computational procedure that is able to reproduce the main fluid motion and heat transfer phenomena at a reasonable computational cost. After the validation of the numerical data with the experimental measurements, the simulations can indeed provide a reliable picture of the flow field and heat transfer in the whole investigated domain, complementing the measurements and helping the community to fully understand the governing mechanisms. Moreover, it is believed that the methodology introduced in the present work is well suited for the analysis of internal cooling channels with alternative geometrical parameters and operating conditions. Direct Numerical Simulations (DNS) are discarded due to the large amount of grid points required to provide the solution at the present Reynolds number. The most recent DNS in a ribbed channel was carried out by Narasimhamurthy and Andersson [47] at a bulk Reynolds number similar to the one in the present investigation. The case analyzed in Ref. [47] corresponded to an infinite-aspect ratio channel, providing valuable information about the main flow and turbulence budgets, but did not fully reproduce the physics of internal cooling channels due to the lack of lateral walls. Reference [47] also provided an idea of the computational cost that would correspond to DNS of a section of an internal cooling channel. In that case, the grid was built with about 33 million points, one or two orders of magnitude larger than what is often employed in Large Eddy Simulations (LES) [36, 43, 44, 88].

The present study considers LES with the objective of resolving the large-scale motion of the fluid and the resulting heat transfer in an internal cooling channel with a less refined mesh. The unsteady pressure, velocity and temperature fields resolved by the LES correspond to those that would result from filtering the actual turbulent field in the space domain. More details on the filtering, LES principles and practical aspects are given in Refs. [89–91]. In the present work, the " sub-filter-scale" stress tensor that results from the spatial filtering of the Navier-Stokes equations (τ_{ij}) is modeled with an eddy-viscosity model, whereas the "sub-filter-scale" heat flux vector (q_j) is modeled with an eddy diffusivity model. Additionally, the fluid is considered incompressible and

with uniform thermodynamic properties. The resulting filtered continuity, momentum and energy equations in the rotating frame of reference are:

$$\frac{\partial \tilde{u}_i}{\partial x_i} = 0 \tag{5.1}$$

$$\frac{\mathrm{D}\tilde{u}_i}{\mathrm{D}t} = -\frac{\partial}{\partial x_j}\left(\frac{\tilde{p}_{eff}}{\rho}\delta_{ij} + \tau_{ij}\right) + \nu\frac{\partial^2 \tilde{u}_i}{\partial x_j \partial x_j} - 2\varepsilon_{ij3}\Omega\tilde{u}_j \tag{5.2}$$

$$\frac{\partial \tilde{T}}{\mathrm{D}t} = \frac{\partial}{\partial x_j}\left(\frac{\nu}{Pr}\frac{\partial \tilde{T}}{\partial x_j} - q_j\right) \tag{5.3}$$

where $\tilde{u}_i$ ($i = 1, 2, 3$) are the resolved velocity components, t is the time, $\tilde{p}_{eff}$ is the effective pressure, ρ is the fluid density, δ_{ij} is the Kronecker Delta, ν is the kinematic viscosity, ε_{ijk} is the Levy-Civita symbol, Ω is the angular velocity magnitude and $\tilde{T}$ is the resolved temperature field. Note that the temperature acts as a pasive scalar according to this model, and therefore it does not affect the velocity field. Additionally, it can be observed that the Buoyancy terms due to possible density variations have been dropped from the model.

The dynamic viscosity and the Prandtl number of the fluid are set respectively to 1.511×10^{-5} m^2/s and 0.72, which correspond values at the experimental conditions. The resolved effective pressure is defined as

$$\tilde{p}_{eff} = \tilde{p} - \frac{1}{2}\rho\Omega^2 r^2 - \beta x \tag{5.4}$$

where $\tilde{p}$ is the resolved static pressure, r is the distance to the axis of rotation. The supplementary source term β is a part of the solution, and represents the pressure gradient that results from imposing a defined mass flow and periodic boundary conditions for the velocity [92]. In the present computations, the Reynolds number (Eq. (1.9)) based on the bulk velocity and the hydraulic diameter is set equal to 15,000. The value of β is a function of time, and fluctuates around a mean value which depends on the Rotation number. The mean value of β represents the pressure losses in the channel at the given Re and Ro, whereas the standard deviation of β provides the overall level of unsteadiness. These values are reported in section 6.2.

The sub-filter-scale stress tensor and the heat flux vector need to be modeled in order to find the values of $\tilde{u}_i$, $\tilde{p}_{eff}$ and $\tilde{T}$ at each point of the domain. The localized k-equation subgrid-scale (LDKSGS) model proposed by Kim and Menon [93] was employed to model the sub-filter-scale stress tensor due to its relative simplicity and the ability to correctly predict the velocity in high Reynolds number flows. The LDKSGS model expresses the sub-filter-scale stress tensor as a function of the subgrid-scale (SGS) eddy viscosity (ν_T):

$$\tau_{ij} = -2\nu_T\tilde{S}_{ij} + \frac{2}{3}\delta_{ij}k_{sgs} \tag{5.5}$$

where $\tilde{S}_{ij}$ is the resolved strain stress tensor,

$$\tilde{S}_{ij} = \frac{1}{2}\left(\frac{\partial \tilde{u}_i}{\partial x_j} + \frac{\partial \tilde{u}_j}{\partial x_i}\right) \tag{5.6}$$

and k_{sgs} is the SGS kinetic energy. The SGS eddy viscosity is considered by the LDKSGS model to be proportional to the square root of the SGS kinetic energy:

$$\nu_T = c_\nu k_{sgs}^{1/2} \tilde{\Delta} \tag{5.7}$$

To obtain the SGS kinetic energy and eddy viscosity, the subfilter-scale turbulent kinetic energy equation proposed by Yoshizawa [94] is solved, and the procedure introduced by Lilly [95] to obtain the turbulent viscosity coefficient was employed. The LDKSGS model presents several advantages such as the local character of the model constant (no spatial averaging or clipping is needed to increase the stability of the system) and no local equilibrium between the SGS energy production and dissipation is imposed. Additionally, the implementation of the model in rotating flows is relatively easy since the formulation of the subfilter-scale turbulent kinetic energy equation does not change in a rotating frame of reference at constant angular velocity. Nevertheless, the centripetal and Coriolis forces need to be included in the momentum equation.

In practice, the SGS eddy viscosity and stress tensor are iteratively calculated together with the velocity and pressure fields (Eqs. (5.1) and (5.2)) at each time step until the convergence criteria is reached. Then, Eq. (5.3) is solved to obtain the temperature field. In the present work, the eddy diffusivity model that has been used to represent the subfilter-scale heat flux is based on the SGS eddy viscosity and the temperature gradient:

$$\tilde{q}_j = -\frac{\nu_T}{Pr_t}\frac{\partial \tilde{T}}{\partial x_j} \tag{5.8}$$

where Pr_t is the turbulent Prandtl number. In this case, a constant Pr_t equal to 0.5 has been set, in consideration of the work by Moin et al. [96] in a turbulent channel flow. In the case of air ($Pr = 0.72$), the turbulent Prandtl number varied from 1.0 close to the wall, to 0.5 at the edge of the boundary layer. Nevertheless, about 70-80% of the boundary layer presented a value close to 0.5. The value $Pr_t = 0.5$ has also been employed in the LES by Murata and Mochizuki [88] and Sewall and Tafti [97].

Five cases have been considered in the LES analysis, summarized in Table 5.1. The Reynolds, Prandtl and Rotation numbers have been defined following Eqs. (1.9),(1.10), and (1.11). The centripetal buoyancy forces were not included in the momentum equations, hence the buoyancy number is equal to zero in every case.

5.2 Domain and mesh details

The domain selected for the present LES represents a section of the experimental model. The length of the domain is equal to the rib pitch, hence only one rib is retained

Table 5.1 : Cases studied by LES ($Re = 15000$, $Pr = 0.72$)

Case	Ro	Rotation sense
1	0.78	Clockwise
2	0.30	Clockwise
3	0	Static
4	0.30	Counter-clockwise
5	0.78	Counter-clockwise

in the computational domain. The reduction of the domain length to a single pitch is made to increase the spatial resolution for a given amount of grid points, yielding an affordable computational cost. Periodic boundary conditions are applied at the inlet and outlet of the domain to simulate an established flow and heat transfer in the studied model. Despite the actual conditions in the measurement region are not fully established under certain rotation numbers, the present work aims at simulating the main flow structures and provide a physical explanation of the velocity and heat transfer in the entire domain.

Figure 5.1 represents the geometry of the selected domain, similar to the one investigated experimentally. The rib is placed on the bottom wall perpendicularly to the main flow direction. The cross section of the rib is a square of 15 mm side, the width of the channel is equal to 138 mm and the height equals 153 mm. The frame of reference is fixed to the rotating channel, where the x axis corresponds to the stream-wise direction, the y axis to the vertical direction, and the z axis to the span-wise direction. The origin of the frame of reference is placed at the intersection of the symmetry plane, the bottom wall, and the trailing face of the rib. The system is rotated at different angular velocities around the z axis in both senses of rotation. When rotation takes place in the counter-clockwise sense, the angular velocity vector presents the same sense as the z axis. Under clockwise rotation, the angular velocity vector has the sense opposite to the z axis. The distance from the origin of the frame of reference to the axis of rotation has been set equal to 830 mm, which is the distance from the trailing edge of the 6th rib to the axis of rotation in the experimental facility.

The domain is discretized in a multi-block structured grid, represented in detail in Fig. 5.2. The mesh is refined in the areas close to the walls and in the shear layer region. The total amount of cells is 958440; with 97, 150 and 70 elements in the x, y and z directions. The maximum cell aspect ratio is below 30, whereas the maximum adjacent cell volume ratio is below 1.1. The dimensionless wall distance y^+ has been calculated as

$$y^+ = \frac{d_{center} \cdot \sqrt{\nu \cdot \frac{\partial \|\tilde{\mathbf{u}}\|}{\partial n}}}{\nu} \tag{5.9}$$

where d_{center} is the distance from the wall to the center of the first cell, $\|\tilde{\mathbf{u}}\|$ is the

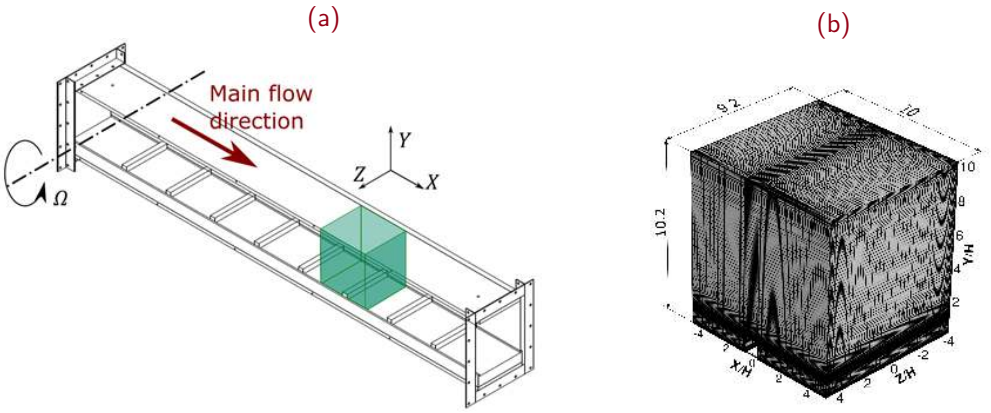

Figure 5.1 : Simulated geometry (a) and computational domain (b)

modulus of the solved velocity vector and n is the wall-normal direction. In the worst scenario, corresponding to the counter-clockwise rotating case at $Ro = 0.30$, the average y^+ value is equal to 1.9 and the maximum y^+ value is equal to 7.1. Figure 5.3 represents the y^+ histogram on the ensemble of the channel walls and on the rib walls. As expected, y^+ is larger on the rib walls, yet the average value is equal to 2.3 and 90% of the cells present a value below 5.

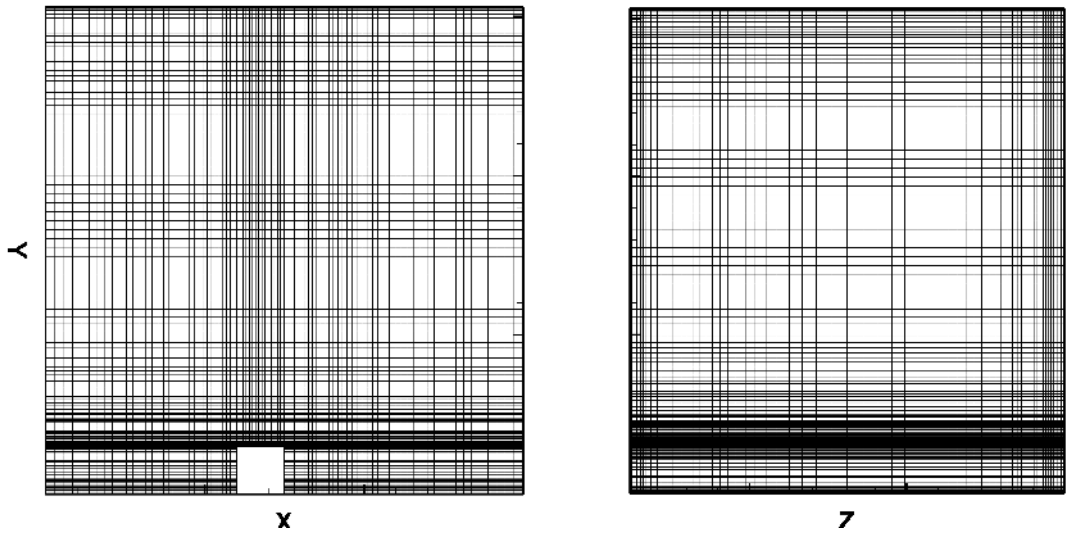

Figure 5.2 : Detailed view of the mesh in planes xy and yz

Figure 5.4 presents the y^+ contours on the channel walls at an arbitrary instant under counter-clockwise rotation with $Ro = 0.30$ and $Re = 15{,}000$. It can be observed that

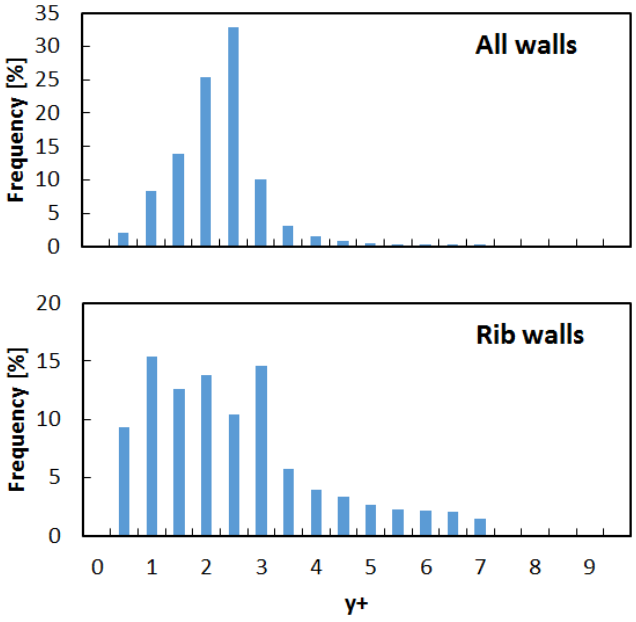

Figure 5.3 : y^+ distribution on the walls (top) and on the rib (bottom)

the most critical region is on the top corner of the rib leading edge, showing y^+ values of about 7.5. The lateral and top walls present $y^+ \sim 4$. In particular, the footprint of the rib-induced secondary flows can be observed on the top walls, close to the lateral corners. There, the y^+ is slightly higher than in the central section due to the velocity gradients caused by the Coriolis-induced secondary flows. On the bottom wall, the y^+ is low due to the grid refinement in this region. In the case of increased Reynolds number, the grid would need to be refined, especially on the rib surface, top and lateral walls.

In order to characterize the mesh resolution, the time-averaged value of the *turbulence resolution measure* [98], M_T, has been calculated as:

$$\overline{M_T} = \frac{\overline{k_{sgs}}}{\overline{\tilde{k}} + \overline{k_{sgs}}} \tag{5.10}$$

where $\overline{\tilde{k}}$ is the mean resolved turbulent kinetic energy and $\overline{k_{sgs}}$ the mean SGS kinetic energy. In the present investigation, $\overline{M_T}$ presents values lower than 0.2. This means that less than 20% of the total turbulent kinetic energy is modeled in some regions of the domain, whereas 80% of the total turbulent kinetic energy resolved by the LES. Figure 5.5 displays the $\overline{M_T}$ contours in the symmetry plane in the case of counter-clockwise rotation and $Ro = 0.30$. $\overline{M_T}$ reaches values of about 0.15 in the core of the flow, and is lower than 10% in the region next to the walls. As a result, the volume-averaged $\overline{M_T}$ is lower than 10%.

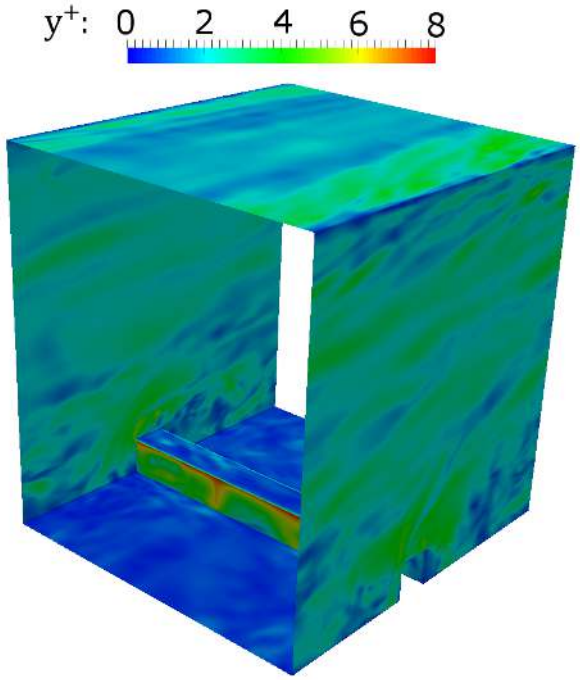

Figure 5.4 : Instantaneous y^+ distribution on the channel walls (Ro = 0.30, counter-clockwise rotation)

5.3 Boundary and initial conditions

The present physical model requires boundary conditions for the velocity, pressure, SGS turbulent kinetic energy and temperature. Periodic boundary conditions are set at the inlet and outlet of the domain (x/H = -5 and 5). The no-slip boundary condition is imposed on the channel walls. The pressure gradient on the walls and the SGS turbulent kinetic energy are also set to zero on the walls. Since the Reynolds number is set equal to 15,000, the flow solver provides a time-dependent pressure gradient β (Eq. (5.4)) which generates the fluid motion with periodic velocity [92].

The selected boundary conditions for the temperature are slightly different from those that are typically applied in the open literature. A tradeoff between the algorithm simplicity and the correspondence to the experimental conditions was intended. The temperature on the bottom wall, excluding the rib, was set equal to 314 K in all the cases. This value is equal to the mean bottom wall temperature during the experiments. However, the temperature over the surface is not uniform in the experiments, which introduces local differences. It is also noted that the ambient temperature from test to test varied slightly, with variations of order of 1 K. However, no major differences in the physics is expected due to these temperature variations. On the rib surface, zero heat flux was imposed due to the characteristics of the test section. The rib in the experimental setup was made of acrylic walls, which has low conductivity. For this

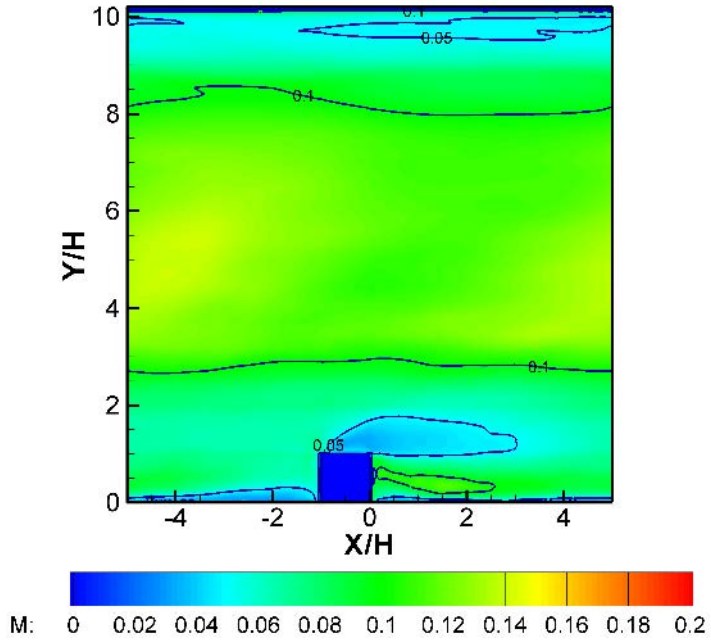

Figure 5.5 : Mean turbulence resolution magnitude ($\overline{M_T}$) contours in the symmetry plane ($Ro = 0.30$ counter-clockwise rotation)

reason, the heat flux from the rib to the fluid is assumed to be zero. In reality, the rib is heated by the heating foil on which it is installed, and that heat is released to the flow. The most accurate, but expensive approach would be to solve the conjugate heat transfer phenomena between the heating foil, the rib and the fluid. The temperature of the top and lateral walls was set to a value equal to 293 K, which is the typical ambient temperature in the laboratory. This setup results in a heat transfer from the bottom wall to the fluid, and from the fluid to the top and lateral walls. Therefore, the top and lateral walls act as a heat sink. The periodic boundary condition forces a balance between the heat fluxes, hence no source term is needed in Eq. (5.3), contrarily to what was done for the momentum equation.

The simulation was started using a coarse mesh of about 160,000 cells. The initial condition in the coarse mesh consists in a random velocity field superimposed to a uniform unidirectional velocity at ambient temperature. The initial velocity vector at a location (x, y, z) can be expressed as

$$\tilde{\mathbf{u}} = (U_b + u_r, u_r, u_r) \tag{5.11}$$

where u_r is a random variable following a normal distribution with mean equal to 0 and standard deviation equal to $0.2U_b$. Note that this velocity field does not represent a true turbulent field due to the fact that the magnitudes in adjacent cells are not correlated, it introduces however a level of randomness in the flow that results in a turbulent motion. Initially, the pressure gradient (without taking into account the factor

β) and SGS turbulent kinetic energy are set to zero, whereas the temperature field is set equal to 298 K. Then, the simulation is started until a stationary regime is reached. In order to evaluate the stabilization of the system, the velocity and temperature at several locations are monitored as well as the overall SGS kinetic energy, $< k_{sgs} >$ and temperature $< T >$:

$$< k_{sgs} >= \frac{1}{V} \iiint_D \frac{1}{2} \left(\tilde{u}^2 + \tilde{v}^2 + \tilde{w}^2 \right) dV \tag{5.12}$$

$$< T >= \frac{1}{V} \iiint_D \tilde{T}(x, y, z) dV \tag{5.13}$$

where D stands for the domain and V for its volume. Figure 5.6 shows the evolution of $< T >$ as a function normalized time, $t \times U_b/P$ (where P is the rib pitch). The characteristic time, U_b/P is also known as Flow Through Time, which is the typical time that the fluid employs to cross the domain. It can be observed that the characteristic time for the stabilization of the temperature is of the order of 10-20 FTTs. For a dimensionless time larger than 50, the standard deviation of $< T >$ is below 0.11 K, which represents about 0.5% of the temperature difference between the heated wall (314 K) and the cold walls (293 K).

The transient time is related to the effective diffusivity. The time scale of the energy equation (Eq. (5.3)) is $t_c \sim l^2 / \left(\frac{\nu}{Pr} + \frac{\nu_T}{Pr_t} \right)$, l being the characteristic length of the temperature variations, which is of the order of the rib height (15 mm). The order of magnitude of the turbulent eddy viscosity can be estimated from the Smagorinsky model [99]:

$$\nu_T = \left(C_S \tilde{\Delta} \right)^2 \| \tilde{S} \| \tag{5.14}$$

where $C_S \sim 0.2$ is the Smagorinsky constant, $\tilde{\Delta}$ is the characteristic length of the cell and $\| \tilde{S} \|$ is the magnitude of the resolved strain tensor. In the shear layer region, $\tilde{\Delta} \sim$ 2 mm, and $\| \tilde{S} \| \sim U_b/H$, resulting in $\nu_T \sim 1{\times}10^{-5}$ m^2/s. Actually, the eddy viscosity found in the present simulations shows similar values, about $3{\times}10^{-5}$ m^2/s. Therefore, the order of magnitude of the characteristic time is $t_c \sim 3$ s, which corresponds to about 30 FTT, very similar to what is observed in Fig. 5.6.

Once the simulation is established on the coarse mesh, the solution is interpolated onto the final mesh. After the establishment of the flow conditions on the final mesh, statistics of the main flow properties are collected for a time period of more than 60 FTT.

5.4 Solver

The CFD libraries employed to obtain the velocity, pressure and temperature fields issued by Eqs. (5.1)-(5.3) is based in the *SRFPimpleFoam* finite-volume solver available in the OpenFoam [100, 101] open source library. *SRFPimpleFoam* is a transient solver for incompressible flows in a rotating frame of reference, employing the PIMPLE algorithm

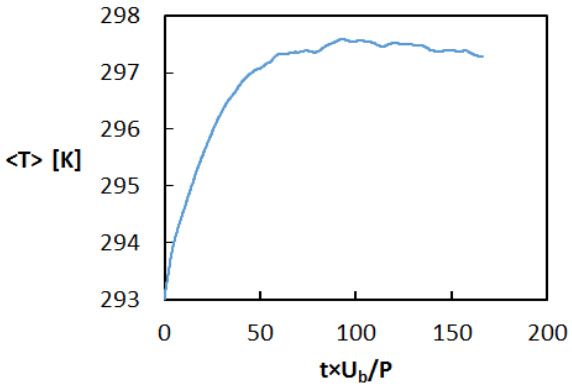

Figure 5.6 : Overall temperature in the domain as a function of the dimensionless time

[102]. The temperature equation has been added to the solver, since it was not initially included.

A second order implicit backward scheme was employed for temporal discretization. The convection and diffusion of the momentum and energy equations have been discretized with a second order central differencing scheme. The convergence criterion was set to 10^{-6} for the residuals in the continuity equation, and to 10^{-5} in the momentum and temperature equations. The time step is about 9×10^{-5}s resulting in a CFL number lower than 1.

Chapter 6

Results

6.1 Experimental results

6.1.1 Inlet conditions

To characterize the flow field at the inlet of the test section, PIV measurements were carried out in the symmetry plane of the channel, just upstream of the first rib. The mean stream-wise velocity contour in the measurement plane in static conditions is represented in Fig. 6.1. The in-plane streamlines, generated from the stream-wise and wall- normal velocities in the symmetry plane, are also represented in the figure. The frame of reference is the same as the one depicted in Fig. 3.10, with the origin at the trailing edge of the sixth rib of the channel. Due to the presence of the rib, the boundary layer on the ribbed wall is slightly thicker on the bottom wall ($Y/H = 0$). For the same reason, the stream-wise velocity is slightly larger closer to the top wall. As the flow moves downstream towards the rib, the velocity increases due to the area reduction introduced by the rib. Finally, a recirculation bubble is generated just upstream of the obstacle.

In order to compare the inlet velocity at the different rotating conditions, the experimental data was extracted from the line X/H = -56.0, corresponding to the dashed line in Fig. 6.1. The stream-wise velocity profiles are represented in Fig. 6.2. The uncertainty bars are shown in the static case for the sake of clarity. For the other cases, the uncertainty is very similar. The uncertainty in the central region is very low, with values u_{U/U_b} (95% C.L.) below 0.011. Near the walls, the uncertainty reaches values up to 0.04.

The ribbed wall (Y/H =0) acts as Leading Side when the rotation takes place in the clockwise sense, and as Trailing Side when rotation is in the opposite sense. Figure 6.2, shows that the slope of the mean velocity in the flow core increases as the Rotation number increases. Despite the sign of the slope is different if the channel rotates in the clockwise or counter-clockwise sense, the velocity magnitude is very similar for a given Rotation number. Since the flow is not fully developed, the resulting slope $\partial U/\partial y$ is lower than 2Ω [20]. Due to the symmetrical design of the test section with respect to

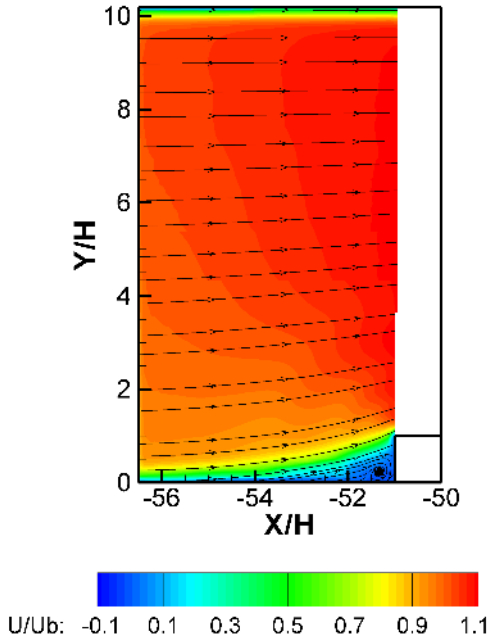

Figure 6.1 : Inlet mean stream-wise velocity contours in static conditions

the plane $Z = 0$, the inlet velocity field is expected to be symmetric with respect to $Z = 0$.

The stream-wise turbulent velocity profiles u_{rms}/U_b at X/H = -56.0 are presented in Fig. 6.3. In the core region, the turbulent velocity is lower than 1% due to the honeycombs and screens in the settling chamber as well as the contraction. In this region, the uncertainty u_{u_{rms}/U_b} is of order 0.003 (95% C.L.). Near the bottom wall, the turbulent velocity is large at every rotating condition due to the presence of the wall and the beginning of the recirculation bubble upstream of the first rib. On the other hand, the uncertainty of u_{rms}/U_b reaches values of about 0.2 (95% C.L.) in the region near the walls.

6.1.2 Isothermal velocity field

6.1.2.1 Comparison with previous experimental data

The velocity field in the present test section is firstly compared to the measurements by Coletti et al. [32] between the 6th and 7th ribs in Figs. 6.4 - 6.6. The flow topology and velocity magnitudes are very similar to the cases analyzed in Ref. [32] at Re = 15,000 and Ro = 0 - 0.30. The data represented in Fig. 6.4b reveals a reattachment length equal to 4.0 times the rib height. Here, the reattachment point is defined as the location where the stream-wise velocity immediately above the wall, i.e. the first measurement point, changes its sign from negative to positive. Note that this data was obtained with the 35 mm photo lens, presenting a spatial resolution equal to 2.85 mm in

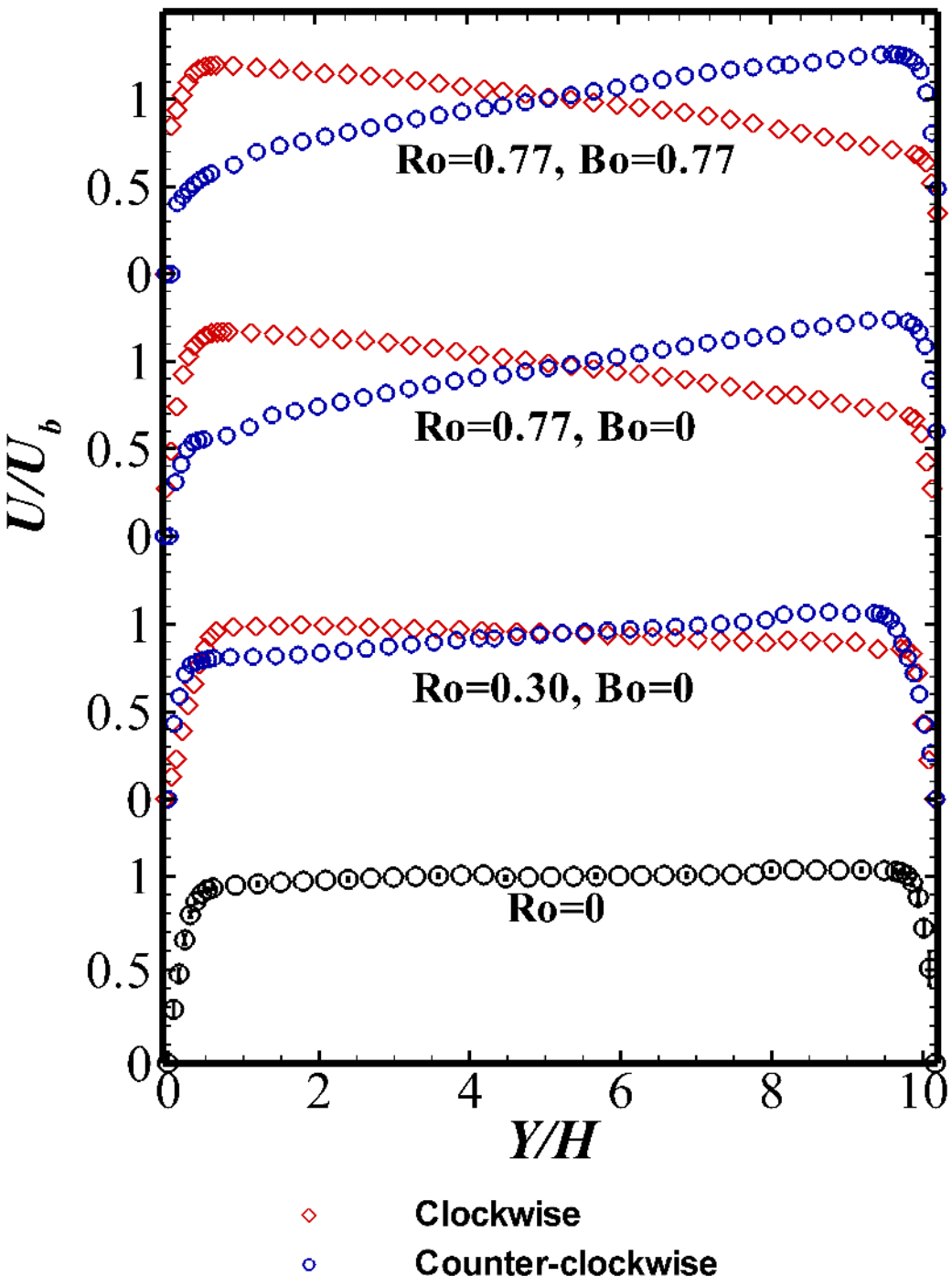

Figure 6.2 : Inlet mean stream-wise velocity profiles

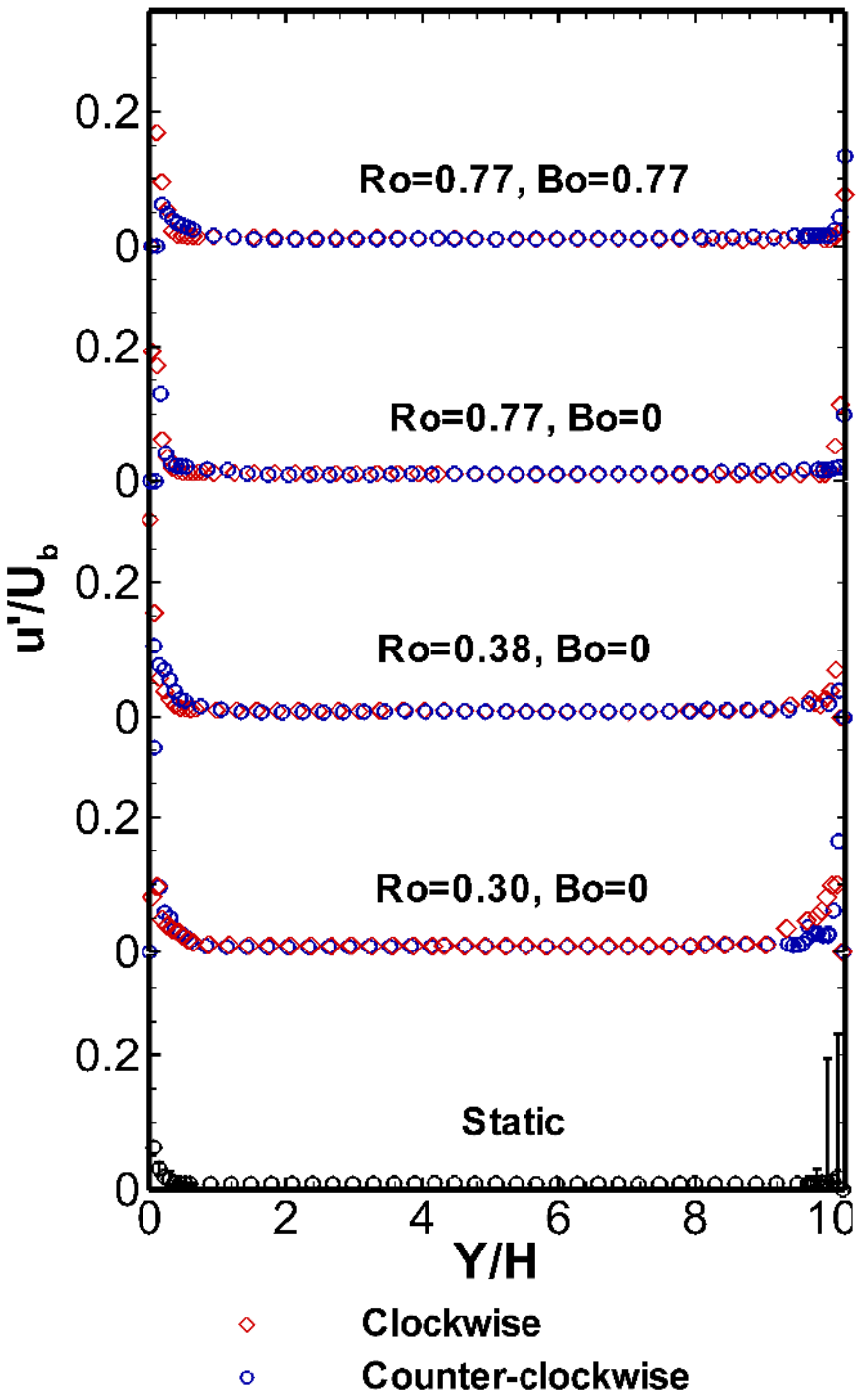

Figure 6.3 : Inlet turbulent stream-wise velocity profiles

the stream-wise direction, that is, almost 0.2 times the rib height. For the experiments performed with the 50 mm lens, the reattachment length is measured to be equal to 3.85 times the rib height (the spatial resolution in the stream-wise direction in this case is equal to 0.1 times the rib height). This distance is in good agreement with respect to the one found in Ref. [32], which reports it to be equal to 3.8 times the rib height. In the recirculation region behind the ribs, two vortices are visible: the largest one inducing a clockwise motion, and a reduced vortex in the corner downstream of the rib turning counter-clockwise. The length of the reduced vortex in the stream-wise direction is equal to $0.7H$ in the present experiments, whereas it is equal to $0.6H$ in Ref. [32]. As the flow moves downstream, the boundary layer develops, and the thickness of the low momentum region increases. Further downstream, as the fluid reaches the following obstacle, the flow is accelerated due to the area blockage introduced by the rib.

When rotation takes place in the clockwise sense, the ribbed wall acts as Leading Side, and the flow field is stabilized by rotation. As a result, the turbulent fluctuations are damped and the momentum exchange between the near wall and core flows is not as efficient as in the static case. The reattachment length of the shear layer generated by the rib is hence enlarged. It can be observed in Fig. 6.4 that the overall agreement of the data by Coletti et al. [32] and the one of this work is good. In the present experiments at $Ro = 0.30$ (Fig. 6.4a), the reattachment takes place 6.85 times the rib height downstream of the obstacle. At $X/H \simeq 7.15$, a second recirculation bubble starts, developing in front of the following rib. Using the same definition of the reattachment length as that expressed above, the data provided in Ref. [32] does not actually show a reattachment point. Instead, a saddle point is found at $(X/H, Y/H) = (7.08, 0.12)$, where the second recirculation bubble starts to develop. Therefore, the size of the recirculation bubble upstream of the 7th rib is almost the same in Ref. [32] and in the present work.

When the ribbed wall acts as Trailing Side (Figs. 6.4c and d), the shear layer generated by the rib is destabilized by rotation. The momentum exchange between the near wall and core regions is more effective, hence the size of the recirculation bubble behind the rib is reduced. The reattachment length in the present experiments is equal to $3.45H \pm 0.19H$, exactly the same as in Ref. [32]. As a result, the streamline curvature is larger under this rotating condition. It is noteworthy to mention that the momentum magnitude is larger in the proximity of the ribbed wall because of the high turbulence levels.

In order to compare in detail the data with the previous experimental results of Ref. [32], the stream-wise mean and turbulent velocities have been extracted along horizontal lines positioned at $X/H = 0$, 2 , 4, 6, 8 and 10, and represented in Figs. 6.5 - 6.6. As can be observed in the figures, the agreement between the represented data is fairly good. To quantify the agreement, the average difference between the profiles at a given X/H position has been calculated:

$$\delta_{U/U_b} = \int_0^3 \left| \left(\frac{U}{U_b} \right)_1 - \left(\frac{U}{U_b} \right)_2 \right| \mathrm{d} \left(\frac{Y}{H} \right) \tag{6.1}$$

where the subscripts 1 and 2 stand for the data of each experimental campaign. For

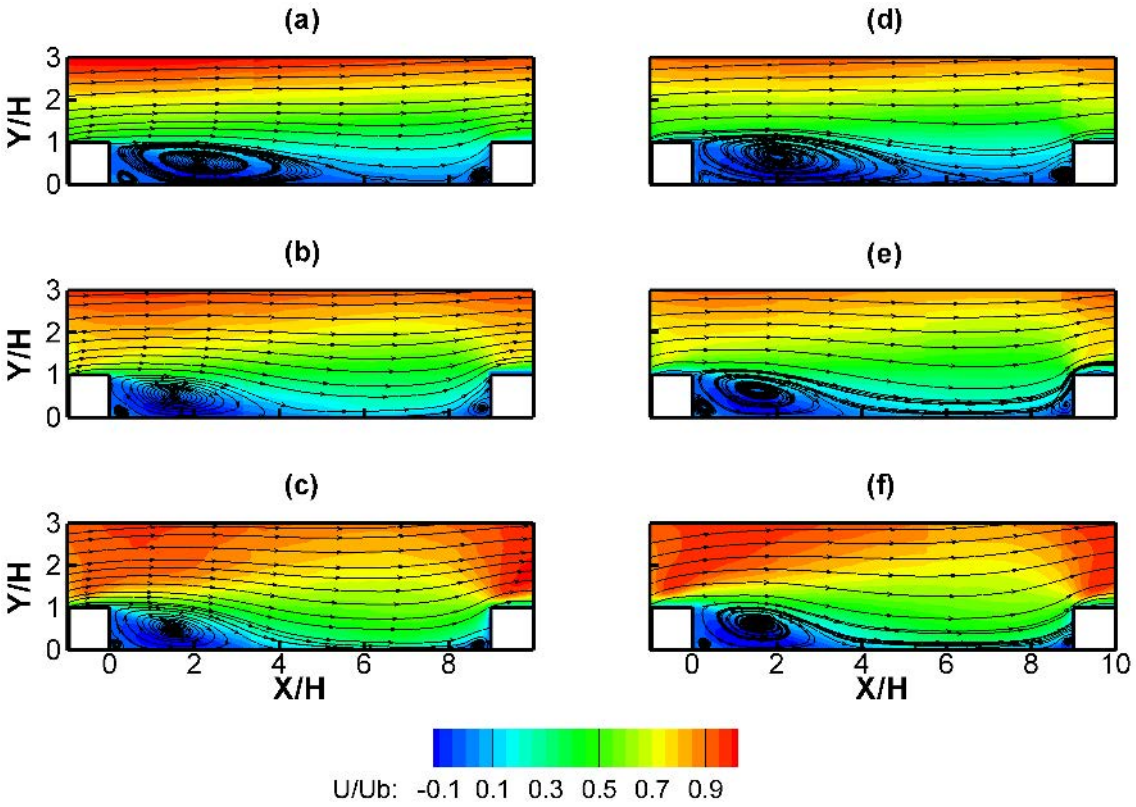

Figure 6.4 : Stream-wise velocity contours and in-plane streamlines, Re = 15,000: present investigation, Leading Side, Ro = 0.30 (a); present investigation, Static, Ro = 0 (b); present investigation, Trailing Side, Ro = 0.30 (c); Coletti et al. (2012), Leading Side, Ro = 0.30 (d); Coletti et al. (2012), Static, Ro = 0 (e); Coletti et al. (2012), Trailing Side, Ro = 0.30 (f)

instance, δ_{U/U_b} at X/H=4 shows values equal to 0.028, 0.023 and 0.035 in Figs. 6.6(a), (b) and (c), respectively. Therefore, the typical deviation of the stream-wise velocity between the different experimental campaigns is about 3% of the bulk velocity. The difference has been also computed in terms of the stream-wise turbulent velocity:

$$\delta_{u_{rms}/U_b} = \int_0^3 \left| \left(\frac{u_{rms}}{U_b} \right)_1 - \left(\frac{u_{rms}}{U_b} \right)_2 \right| \mathrm{d} \left(\frac{Y}{H} \right) \tag{6.2}$$

The difference δ_{u_{rms}/U_b} is equal to 0.015, 0.008 and 0.032 in Figs. 6.6a, b and c, respectively.

It is important to remark that the centrifugal forces were different in the experimental campaigns due to the difference in the rotational speed. In the case of the work by Coletti et al. [32], the rotational speed was about 104 rpm, providing a centrifugal acceleration equal to 9G in the investigated region. In the present case at $Ro = 0.30$, the rotational speed was about 31 rpm, providing a centrifugal acceleration of approximately 0.9G. However and although the ratio of the centrifugal forces to the inertia of the fluid is different, the results are the same. This is due to the fact that the centrifugal forces act as a pressure gradient in the case of isothermal flows, as demonstrated by Johnston el al. [21], and summarized in section 2.3. If the Reynolds and Rotation numbers are fixed in scaled geometries, the dimensionless velocity field is identical. This is confirmed by the fact that the dimensionless effective pressure gradient ends up to be the same. However, the actual pressure gradient is different due to the different rotational speeds. As a direct consequence, if static pressure measurements are taken in a rotating channel, the dimensionless results are required to be given in terms of the effective pressure to be representative.

6.1.2.2 Mean velocity field at high Rotation numbers

The in-plane velocity modulus contours, obtained from the stream-wise and wall-normal velocity components, in the cases Ro = 0 - 0.77 are represented in Figs. 6.7 and 6.8. The results were obtained in the two different experimental campaigns with the parameters shown in Tables 3.3 and 3.4, respectively. Additionally to the velocity contours, the in-plane streamlines are included in the figures. When the channel is rotated in the clockwise sense, the recirculation bubble grows as the Rotation number increases due to the shear layer stabilization. The center of the large vortex downstream of the rib moves from (X/H,Y/H)=(1.51,0.57) in static conditions to (X/H,Y/H)=(2.09,0.53) at $Ro = 0.30$, (X/H,Y/H)=(2.33,0.54) at $Ro = 0.38$ and (X/H,Y/H)=(3.12,0.53) at $Ro = 0.77$. Under the largest Rotation number (Leading Side, $Ro = 0.77$), the height of the recirculation bubble increases to reach almost the rib level. Therefore, there is little momentum interchange between the recirculation bubble and the core fluid. It is important to realize that the streamline curvature is reduced as the Rotation number increases. As the streamline curvature is reduced and the core fluid is isolated from the fluid in the recirculation bubble between the ribs, the core flow approaches the topology of a smooth channel flow in terms of flow curvature. As a consequence, the rib-induced secondary flows in static conditions are most likely weakened by the stabilization of the

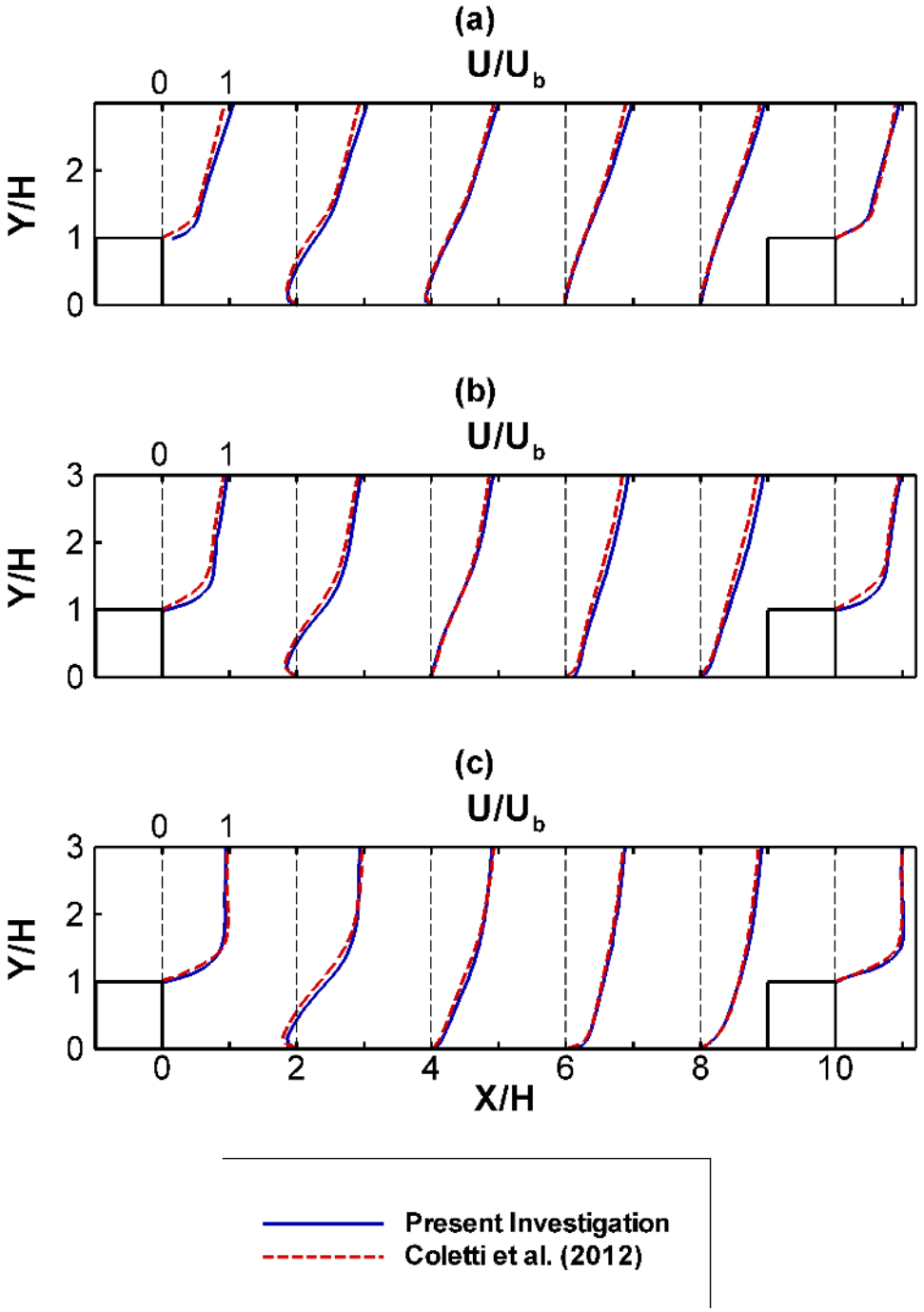

Figure 6.5 : Stream-wise velocity profiles: Leading Side, $Ro = 0.30$ (a); Static (b); Trailing Side, $Ro = 0.30$ (c)

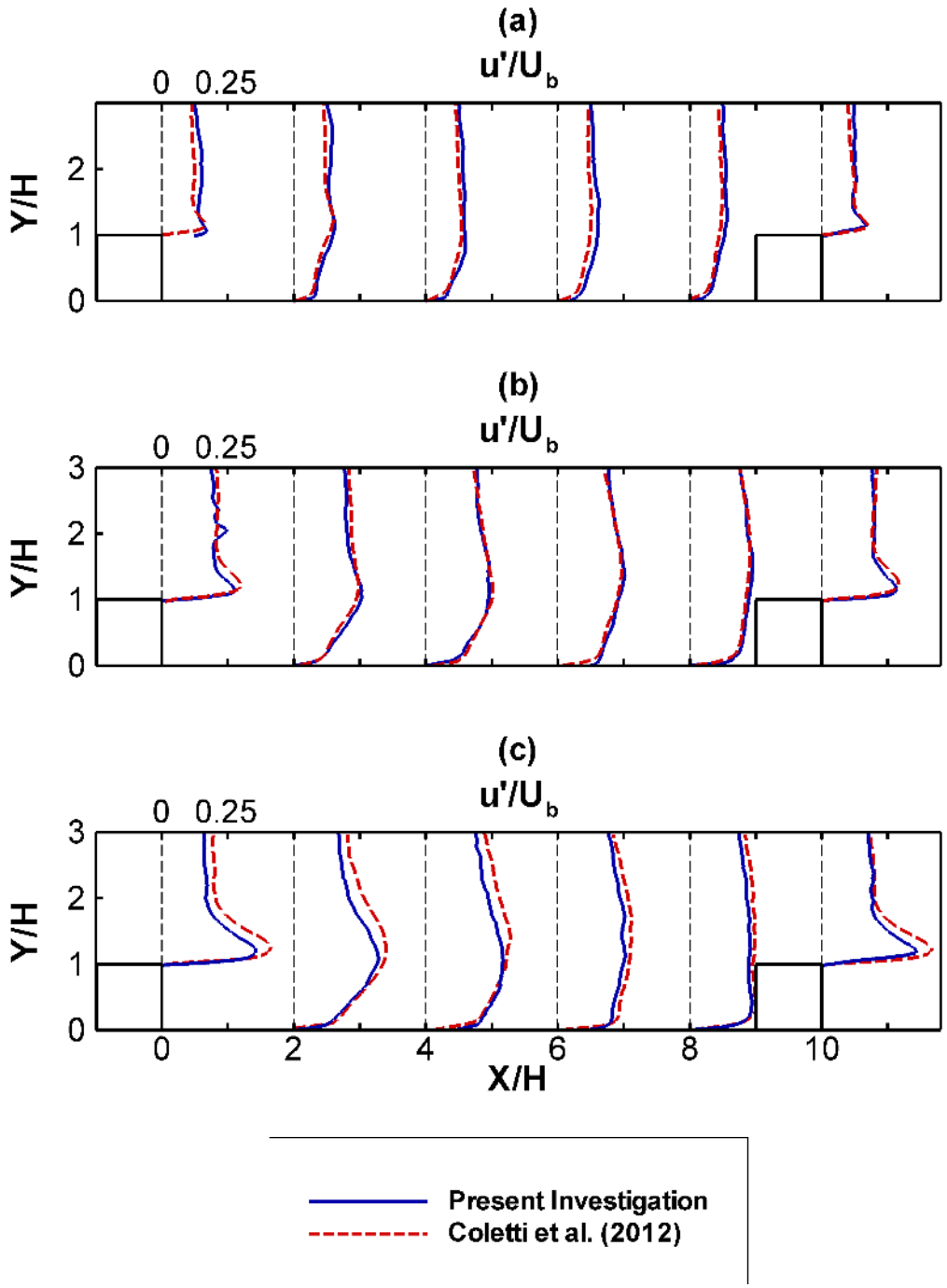

Figure 6.6 : Stream-wise turbulent velocity profiles: Leading Side, $Ro = 0.3$ (a); Static (b); Trailing Side, $Ro = 0.30$ (c)

flow and the reduction of streamline curvature when the ribbed wall acts as the Leading Side. The reduced vortex observed in the corner just downstream of the rib in static conditions still exists at $Ro = 0.30$ and 0.38. However, it is not observed at $Ro = 0.77$, probably due to the low momentum in the separation bubble. In parallel, the size of the vortex just upstream of the 7th rib grows as the Rotation number increases. The saddle point separating this vortex and the one downstream of the previous rib moves away from the wall, to reach a position (X/H,Y/H)=(7.51, 0.33) at $Ro = 0.77$.

When the ribbed wall acts as the Leading Side, the momentum distribution varies as the Rotation number increases. Close to the lower wall, the momentum under rotating conditions is lower than in the static case as a consequence of the larger recirculation bubble. Nevertheless, at a distance $Y/H \sim 3$ from the wall, the momentum on the stabilized cases is larger than under static conditions. This is in contrast with what was suggested in Refs. [32, 53, 78]: the secondary flows move fluid from the Trailing Side towards the Leading Side in the region near the lateral walls, whereas the fluid is pushed back towards the Trailing Side in the region of the symmetry plane due to the limited channel aspect ratio. This would be translated into a momentum decrease and an eventual positive wall-normal velocity near the Leading Side. However, the measurements of Refs. [32, 53] were limited to a region below $Y/H = 3$, and the momentum increase above this plane was not observed. With the measurements given in Figs. 6.8a and b, an alternative explanation needs to be provided. Most likely, the secondary flows are confined to a reduced region near the lateral wall and the influence on the momentum distribution in the measurement plane is low, at least under clock-wise rotation. The large momentum above the plane $Y/H = 3$ may be related to the tendency of the turbulence to generate regions of neutral stability, as demonstrated by Tritton[103] and Kristofferesen and Andersson [20]. The neutral stability region is characterized by a zero absolute vorticity, which is translated into a relative velocity gradient in the wall-normal direction ($\partial U/\partial y$) equal to twice the angular velocity. As shown in the DNS by Kristofferesen and Andersson [20], the momentum and shear in the stable region is lower than in static conditions. However, the maximum velocity in a rotating channel is larger than in the same channel at zero angular velocity due to the momentum redistribution. Moreover, the location of the region with the maximum momentum is closer to the Leading Side than to the Trailing Side. This would explain the larger momentum above $Y/H = 3$. When the Rotation number is increased from 0.3 to 0.77, the momentum is even larger in the region $Y/H > 3$. The large momentum can be explained firstly by the increase of the velocity gradient in the wall-normal direction due to the increase of the angular velocity. Additionally, the flow in the region near the opposite wall ($Y/H = 10.2$) might be re-stabilized by rapid rotation, which reduces the velocity in the near wall region. Since the Reynolds number is kept the same as the previous cases, the bulk velocity is the same, hence the fluid is accelerated in the core of the channel.

When the rotation takes place in the opposite sense, the ribbed walls acts as Trailing Side. As explained before, the fluid is destabilized, enhancing the entrainment of fluid from the main flow to the recirculation bubble, resulting in a shorter reattachment length as the Rotation number increases. The reattachment length is equal to $3.45H$,

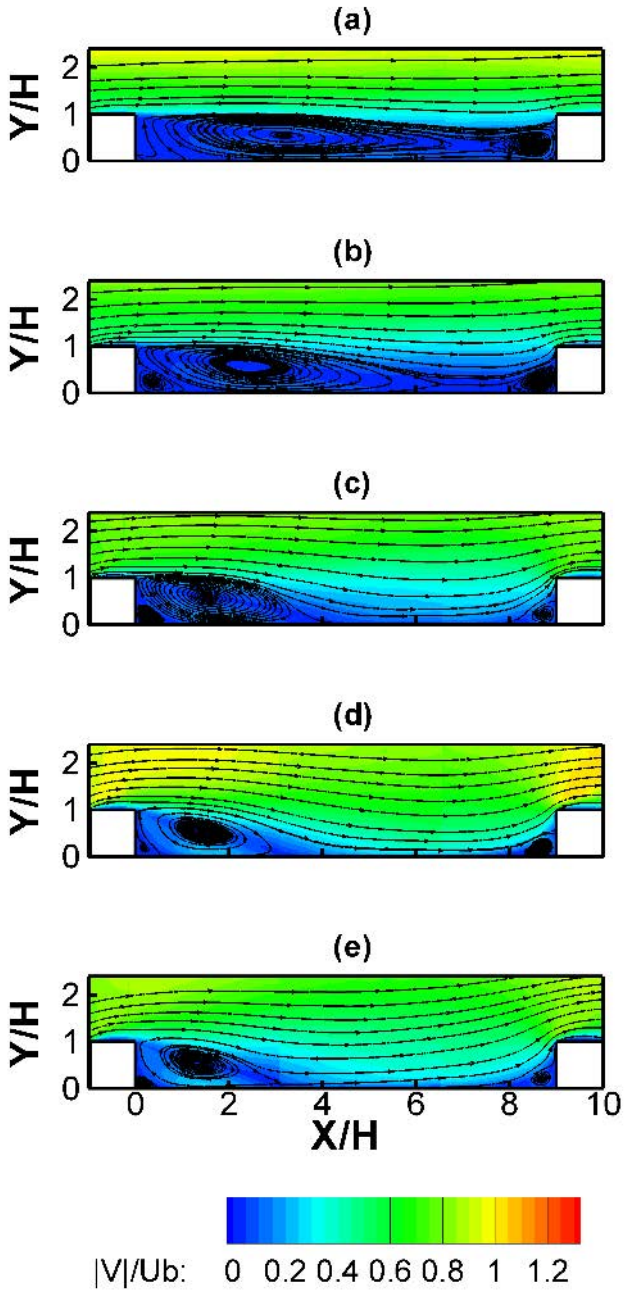

Figure 6.7 : In-plane velocity modulus contours and in-plane streamlines, $Re = 15{,}000$: Leading Side, $Ro = 0.77$ (a); Leading Side, $Ro = 0.38$ (b); Static, $Ro = 0$ (c); Trailing Side, $Ro = 0.38$ (d); Trailing Side, $Ro = 0.77$ (e). Data obtained with the 50 mm objective (Table 3.3)

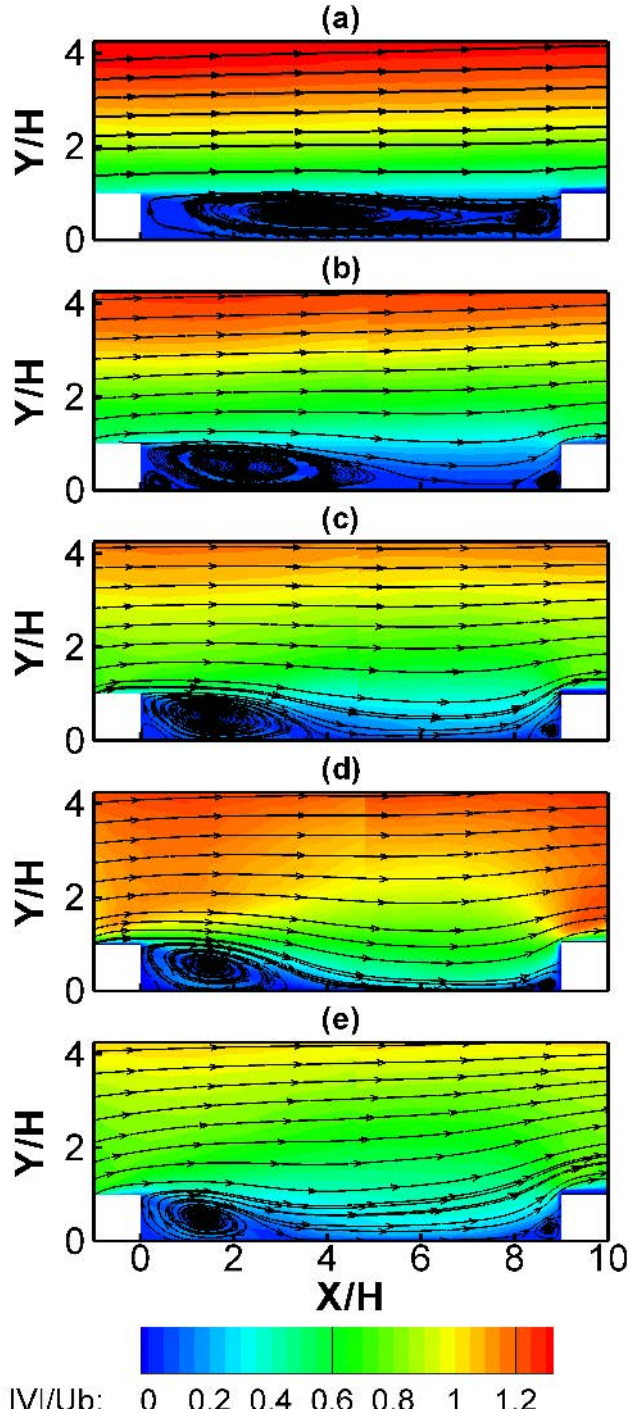

Figure 6.8 : In-plane velocity modulus contours and in-plane streamlines, $Re = 15{,}000$: Leading Side, $Ro = 0.77$ (a); Leading Side, $Ro = 0.30$ (b); Static, $Ro = 0$ (c); Trailing Side, $Ro = 0.30$ (d); Trailing Side, $Ro = 0.77$ (e). Data obtained with the 35 mm objective (Table 3.4)

$3.35H$ and $3.24H$ at Ro equal to 0.30, 0.38 and 0.77, respectively. The center of the large vortex in the recirculation bubble is located at $(X/H,Y/H)$=(1.49,0.51) at Ro = 0.30, $(X/H,Y/H)$=(1.38,0.51) at $Ro = 0.38$ and $(X/H,Y/H)$=(1.27,0.52). On the other hand, the reduced corner vortices just upstream and downstream of the ribs seem to be unaltered by the Rotation number. At $Ro = 0.30$ and 0.38, the momentum is larger than in the static case, especially in the near-wall region. Coletti et al. [32] relate the large momentum to the high turbulent fluctuations and to the effect of the secondary flows. The high turbulence enhances the mixing of the near-wall and core flows, leading to a high shear, especially on top of the ribs. In addition, the Coriolis-induced secondary flows sweep fluid from the top wall to push it to the bottom wall when the channel rotates in the counter-clockwise rotation, enhancing the momentum in the investigated region. Nevertheless, the streamlines do not seem to show an important wall-normal velocity component but only at the end of the recirculation bubble. Thus, the large momentum observed next to the Trailing Side at $Ro = 0.30$ and 0.38 is most likely caused by the turbulent entrainment of the core fluid into the near-wall flow enhanced by the Coriolis force. At $Ro = 0$, the momentum reaches even lower values than in the static cases. Moreover, the streamlines indicate a fluid motion away from the wall. This can be due to the re-stabilization of the flow at high Rotation numbers, and a variation of the secondary flow pattern. As it will be shown later, the stream-wise turbulence is largely reduced in the second half of the rib pitch. As demonstrated by Lezius [19] and Johnston et al. [21], the flow can be re-stabilized under anti-cyclonic rotation if the angular speed is large enough with respect to the flow shear $\partial U/\partial y$. In terms of the local gradient Richardson number,

$$Ri = \frac{-2\Omega\left(\partial U/\partial y - 2\Omega\right)}{\left(\partial U/\partial y\right)^2}$$

the flow is stable as long as Ri is positive. In such case, the turbulent mixing is reduced and so the momentum in the near wall region. However, the recirculation bubble shortening suggests a larger turbulent activity, hence the re-stabilization does not occur the entire near wall region. This is most probably due to the distribution of the mean flow shear, which is particularly high in the separated region. On the other hand, Kristoffersen and Andersson [20] demonstrated the change of the secondary flows pattern at high Rotation numbers in an infinite high aspect ratio channel flow. In that case, the boundary layer on the Leading Side thickens, reducing the effective cross section where the stream-wise vortex structures can grow. As a result, the size of the stream-wise Taylor-Görtler vortices on the Trailing wall is reduced, which leaves enough room in the span-wise direction to be occupied by another pair of stream-wise vortices. In the present case, the Coriolis-induced secondary flows would still induce a fluid motion from the Trailing Side to the Leading Side right near to the lateral walls. However, the fluid would go back to the Trailing Side in a region closer to the lateral walls, leaving room for two counter-rotating vortices in the center of the channel, near the Trailing Side. These central stream-wise vortices would revert the secondary flow motion in the symmetry plane, leading to a positive vertical velocity in the measurement plane, as observed in

Figs. 6.7 and 6.8.

The stream-wise mean velocity contours at the different rotating conditions are shown in Figs. 6.9 and 6.10. The contour line $U/U_b = 0$ is added to the figures to illustrate the evolution of the recirculation bubble as the rotation number increases. For the Leading Side case, the contour lines become more and more parallel as the rotation number increases, due to the enlargement of the separation bubble, and the low influence of the Coriolis-induced secondary flows. On the Trailing Side at $Ro = 0.30$ and 0.38, the iso-velocity contours are not parallel due to the acceleration of the flow on top of the ribs, the separation and reattachment of the shear layer generated by the rib, and the development of the boundary layer towards the following obstacle. At $Ro = 0.77$ on the Trailing Side, the contours are more uniform than in the previous case due to the probable turbulence reduction and the redistribution of the Coriolis-induced secondary flows.

Figures 6.11 and 6.12 show the wall-normal velocity contours at the different Rotation numbers. Additionally, the $V/U_b = 0$ contour line is represented in the figure to evidence the areas where the flow is pushed towards the wall or swept away from it. In static conditions, the area $2 < X/H < 6$ shows negative wall-normal velocity, due to the rib-induced secondary flows and the entrainment of the main flow into the recirculation bubble. In particular, the largest wall-normal velocity (in terms of the modulus) is located just upstream of the reattachment point, presenting a maximum value of about 7.6% of the bulk velocity. On the Leading Side, the area of negative wall-normal velocity is reduced as the Rotation number increases. The maximum magnitude of the wall-normal velocity is about 1.6% of the bulk velocity. For this reason, the streamline curvature is largely reduced at high Ro. Oppositely, the wall-normal velocity modulus slightly increases on the Trailing Side at $Ro = 0.30$ and 0.38. The modulus of the wall-normal velocity reaches levels up to 11.4% of the bulk velocity in the region where the main flow is reattaching. However, the region of negative wall-normal velocity presents a similar size to the static case, and the overall value of the negative wall-normal velocity is slightly larger. For this reason, the author believes that the Coriolis-induced secondary flows exert little influence on the flow in the measurement plane. Most of the flow in the symmetry plane is therefore under the influence of the destabilization induced by rotation. This hypothesis needs however to be confirmed by additional experiments or supported by high-fidelity CFD simulations. When the rotation number increases to $Ro = 0.77$, the region of negative wall-normal velocity is notably reduced and most of the velocity field presents a positive wall normal velocity. This may be caused by two mechanisms: the reduction of the turbulence intensity and the modification of the secondary flow pattern.

In order to further investigate the effects of rotation on the velocity field, the dimensionless stream-wise and wall normal turbulent velocity distributions (u_{rms}/U_b and v_{rms}/U_b, respectively) at the different rotating conditions have been represented in Figs. 6.13 and 6.14. On the Leading Side, the stream-wise and wall-normal turbulent velocities decrease as the Rotation number increases, due to the stabilizing effect of rotation. On the Trailing Side case at $Ro = 0.30$, the stream-wise and wall-normal turbulent velocities

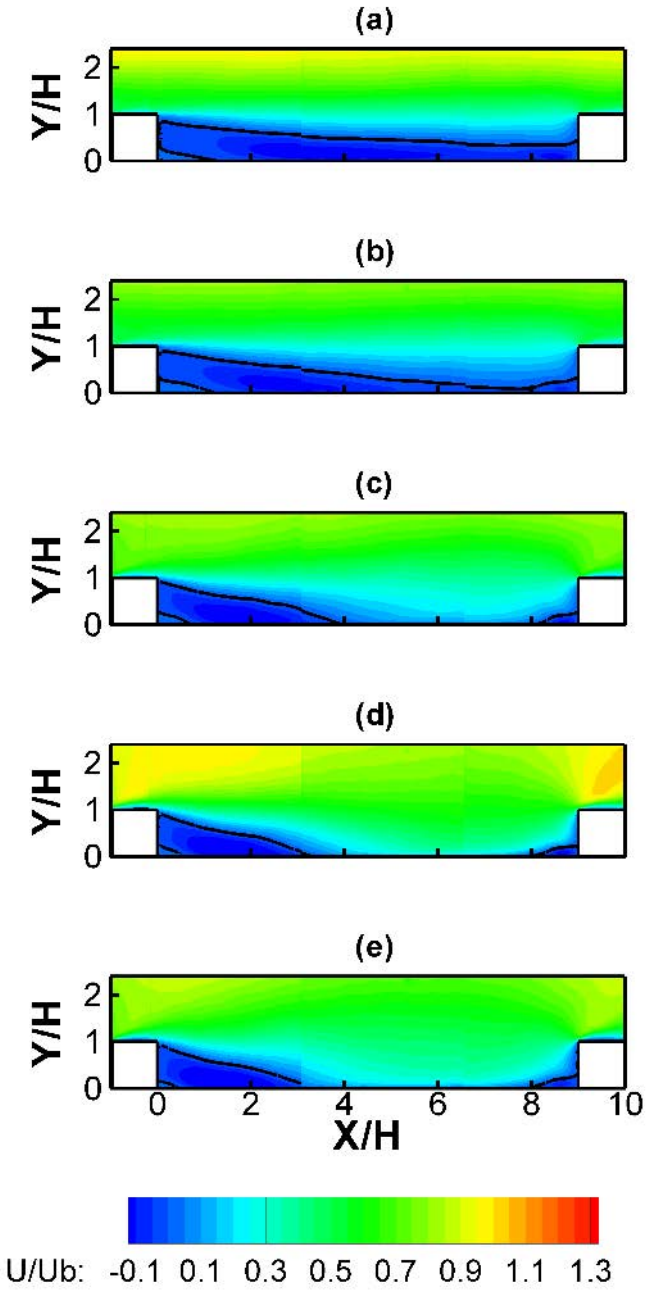

Figure 6.9 : Mean stream-wise velocity contours, Re = 15,000: Leading Side, Ro = 0.77 (a); Leading Side, Ro = 0.38 (b); Static, Ro = 0 (c); Trailing Side, Ro = 0.38 (d); Trailing Side, Ro = 0.77 (e). Data obtained with the 50 mm objective (Table 3.3)

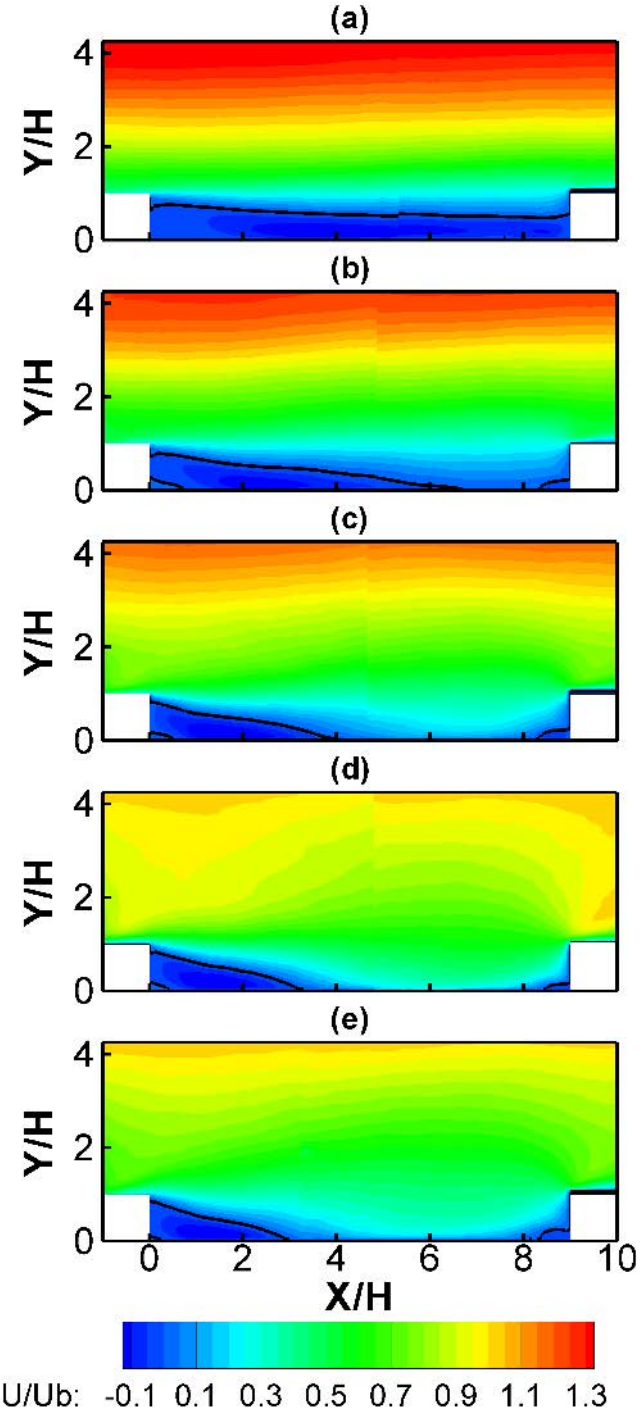

Figure 6.10 : Mean stream-wise velocity contours, Re = 15,000: Leading Side, Ro = 0.77 (a); Leading Side, Ro = 0.30 (b); Static, Ro = 0 (c); Trailing Side, Ro = 0.30 (d); Trailing Side, Ro = 0.77 (e). Data obtained with the 35 mm objective (Table 3.4)

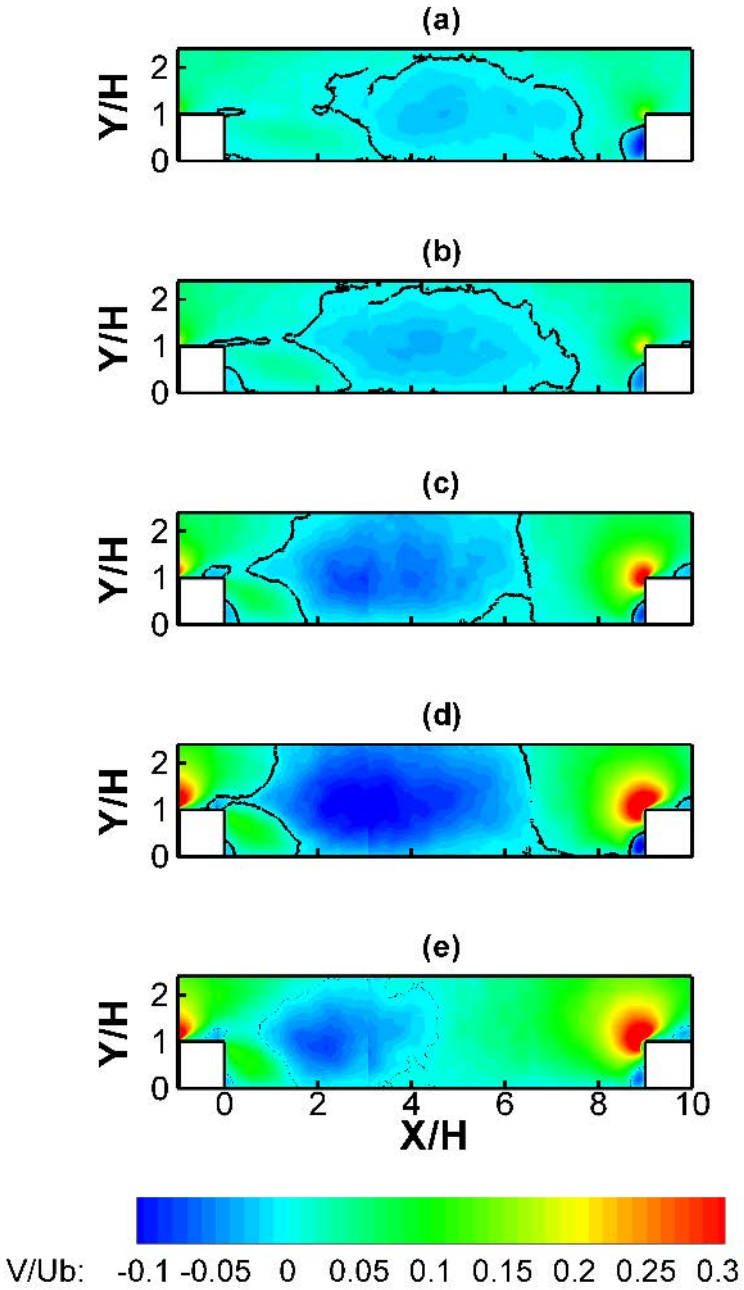

Figure 6.11 : Mean wall-normal velocity contours, Re = 15,000: Leading Side, Ro = 0.77 (a); Leading Side, Ro = 0.38 (b); Static, Ro = 0 (c); Trailing Side, Ro = 0.38 (d); Trailing Side, Ro = 0.77 (e). Data obtained with the 50 mm objective (Table 3.3)

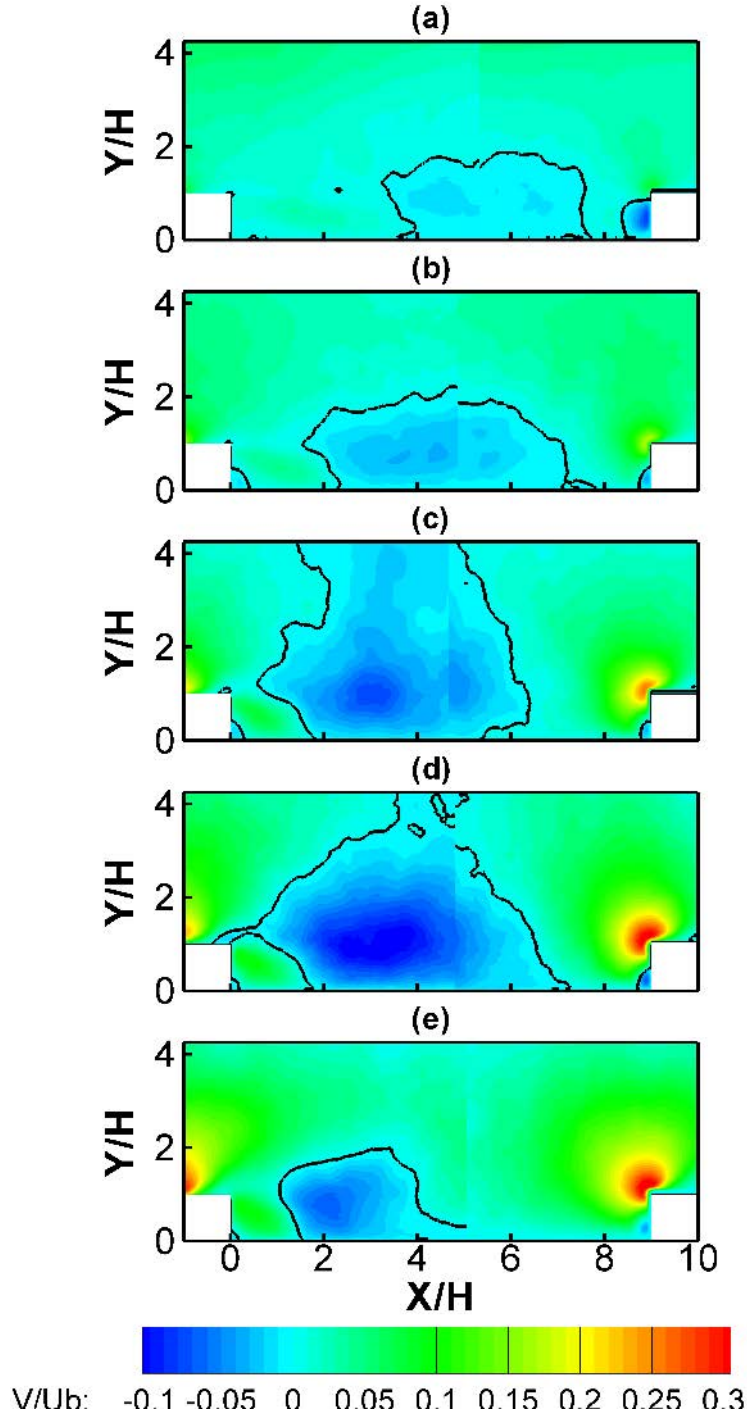

Figure 6.12 : Mean wall-normal velocity contours, Re = 15,000: Leading Side, Ro = 0.77 (a); Leading Side, Ro = 0.30 (b); Static, Ro = 0 (c); Trailing Side, Ro = 0.30 (d); Trailing Side, Ro = 0.77 (e). Data obtained with the 35 mm objective (Table 3.3)

are significantly increased with respect to the static case. At larger Rotation number however, $Ro = 0.77$, the stream-wise turbulent velocity decreases dramatically. Only in the region just above the rib, where the velocity gradient is the largest, the stream-wise turbulent velocity is larger than in the static case. In the rest of the flow field, u_{rms}/U_b is even lower than in the static case. On the other hand, v_{rms}/U_b increases in most of the area investigated. Only for $X/H > 5$, immediately above the wall, the wall-normal turbulent velocity decreases.

The dimensionless in-plane turbulent kinetic energy,

$$k_{in-plane} = \frac{1}{2U_b^2}\left(u_{rms}^2 + v_{rms}^2\right) \tag{6.3}$$

is displayed in Fig. 6.15 to study the final balance of the stream-wise and wall-normal turbulent velocities while varying the rotating conditions. In static conditions, the maximum turbulent kinetic energy reaches levels of about 0.04 in the shear layer area. On the Leading Side at $Ro = 0.30$, $k_{in-plane}$ shows values about 0.016 at the edge of the recirculation bubble and about 0.003 at $Y/H \sim 4$. At $Ro = 0.77$, the values are slightly lower, with the maximum $k_{in-plane}$ equal to 0.015 and a minimum value about 0.001 over the line $Y/H = 4$.

When the ribbed wall acts as Trailing Side and $Ro = 0.30$, $k_{in-plane}$ is enhanced over the whole investigated plane, as it is deducted from the increase of the stream-wise and wall- normal velocities. The maximum value of $k_{in-plane}$ is found as well along the shear layer, showing values of about 0.07-0.08. At $Ro = 0.77$, $k_{in-plane}$ is slightly higher than in the static case in the region of the separated shear layer, displaying values of about 0.05. The turbulent kinetic energy is even lower than in the static case in the rest of the investigated plane. Since the turbulence levels are lower than in the previous cases, a decrease in the momentum interchange between the near-wall region and the core is expected. As observed in Figs. 6.9 and 6.10, this results in a lower mean stream-wise velocity.

The Richardson number (Eq. (1.8)) has been calculated to investigate the origin of the observed mean and turbulent fields. The corresponding contours are displayed in Fig6.16, where also the contour line $Ri = 0$ has also been represented to discern the stable and unstable regions according to the Richardson number criterion. In the case of the Leading Side (Fig. 6.16a and b), the Richarson number is positive in most of the investigated plane. The mean span-wise vorticity presents the same orientation as the angular velocity vector, and therefore, the flow is stable. Only in a limited region of the flow field, directly near to the bottom wall, the span-wise vorticity and angular velocity present opposite senses. However, the momentum is so low in that region of the flow that no significant increase of the flow turbulence is observed there. As shown above, the streamline curvature is reduced on the Leading Side, especially if the Rotation number is high. In such case, the flow is expected to be similar to a two-dimensional flow, with low gradients in the span-wise direction (excluding the region near the lateral walls, where the Coriolis-induced secondary flows are confined). Therefore, the Richardson number criterion, established for (quasi) 2D flows, is able to explain the turbulence decrease as

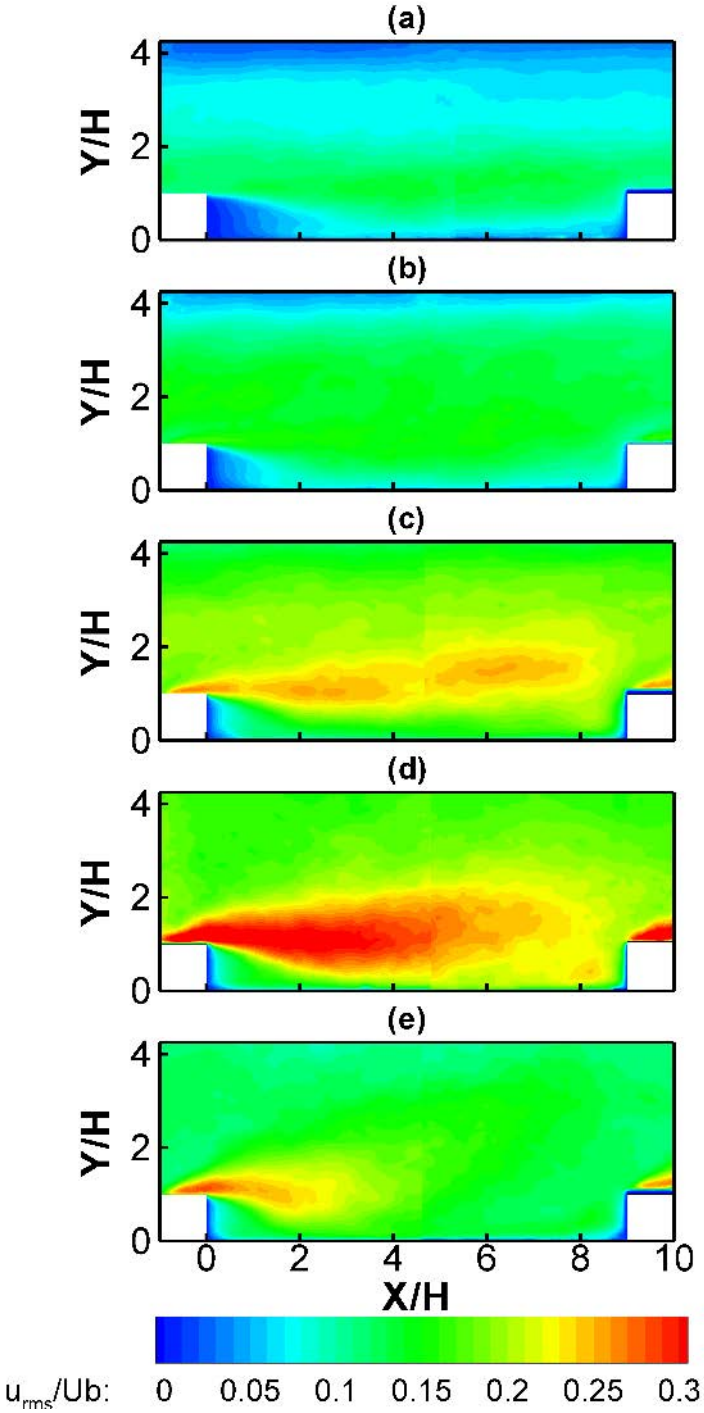

Figure 6.13 : Stream-wise turbulent velocity contours, Re = 15,000: Leading Side, Ro = 0.77 (a); Leading Side, Ro = 0.30 (b); Static, Ro = 0 (c); Trailing Side, Ro = 0.30 (d); Trailing Side, Ro = 0.77 (e). Data obtained with the 35 mm objective (Table 3.3)

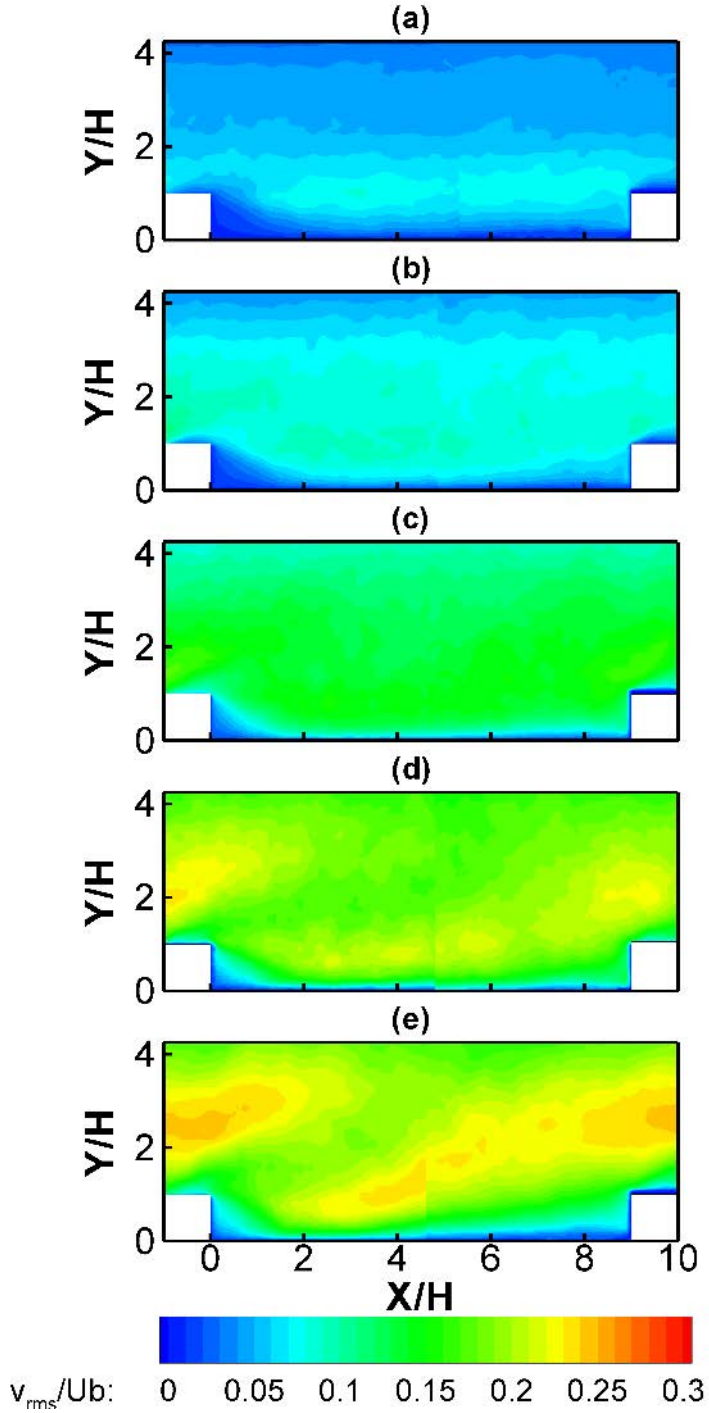

Figure 6.14 : Wall-normal turbulent velocity contours, Re = 15,000: Leading Side, Ro = 0.77 (a); Leading Side, Ro = 0.30 (b); Static, Ro = 0 (c); Trailing Side, Ro = 0.30 (d); Trailing Side, Ro = 0.77 (e). Data obtained with the 35 mm objective (Table 3.3)

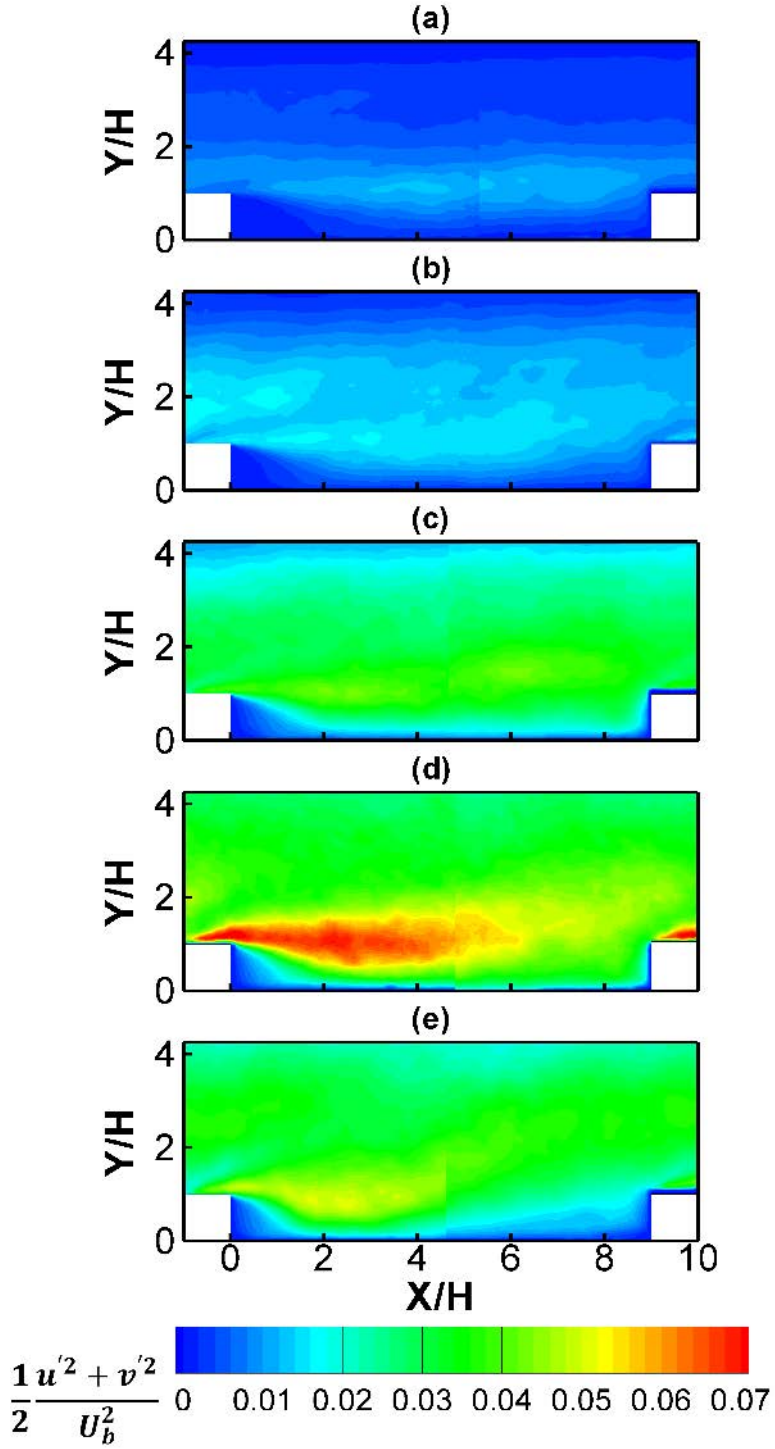

Figure 6.15 : In-plane turbulent kinetic energy contours, Re = 15,000: Leading Side, Ro = 0.77 (a); Leading Side, Ro = 0.30 (b); Static, Ro = 0 (c); Trailing Side, Ro = 0.30 (d); Trailing Side, Ro = 0.77 (e). Data obtained with the 35 mm objective (Table 3.3)

the Rotation number increases on the Leading Side case.

On the Trailing Side the status is the opposite: the mean span-wise vorticity and the angular velocity vector present different senses, and the flow is expected to be destabilized. Figures 6.16c and d show that the Richardson number is negative in a large region of the investigated plane. In the case at moderate rotation ($Ro = 0.30$), the Richardson number criterion explains the flow destabilization and the turbulence increase observed in Figs. 6.13c-6.15c. At $Ro = 0.77$, the Richarson number is also mostly negative. However, the in-plane turbulent kinetic energy was observed to be lower than in the previous case (in some regions, even lower than in the static case). Therefore, the Richardson number criterion seems ineffective to explain the flow behavior at high Rotation number. Only a limited region of the shear layer, located around $(X/H,Y/H)$=(6,1), shows a positive Richardson number, and therefore low turbulent kinetic energy is expected. Since the Richardson number criterion is based on (quasi) 2D flows, the mechanism that leads to the turbulence reduction at high Rotation number is expected to be of a three-dimensional nature. As observed in the mean velocity field, the streamlines show a fluid motion towards the top wall, which drives low momentum fluid from the wall to the core region. Due to the lower momentum and the main shear reduction ($\partial U/\partial y$), the turbulent kinetic energy is expected to decrease. Moreover, two additional stream-wise vortices are expected in the central, near-wall region, inducing the vertical motion. The presence of these stream-wise vortices would also impose a vortex compression (opposite to vortex stretching) to the span-wise vorticity, leading to a reduction of the overall turbulent kinetic energy in this area. The LES results presented in Fig. 6.48 (section 6.2) support this hypothesis.

Lastly, the energy spectrum in the shear layer region has been obtained from the time-resolved experiments. The Fast Fourier Transform has been applied to the stream-wise turbulent velocity, $u'(t) = u(t) - \overline{U}$, at $(X/H, Y/H) = (1, 1)$, and represented in Fig. 6.17. No dominant frequencies have been found in any of the cases, demonstrating the complexity of the flow and the interaction between the different turbulent length scales. However it is clear that the turbulent activity in the case of the Leading Side, both at Ro equal to 0.30 and 0.77, is lower than in static conditions. On the other hand, the energy level at $Ro = 0.30$ on the Trailing Side case increases if compared to that in static conditions, as expected from the flow statistics. At large Ro, the energy level on the Trailing Side goes back to the same level as the static case.

To summarize, it is evident that the channel rotation is responsible for a flow topology highly dependent on the sense of rotation and the corresponding rotational speed, characterized by the Rotation number. When the present channel rotates in the clock-wise sense, the flow mean vorticity in the region near the ribbed wall presents the same sense as the angular velocity vector. In such a case, the flow is often referred to as cyclonic rotation. According to the stability analysis performed by Lezius [19] in high-aspect ratio channel flows, the corresponding Richardson number is positive and the turbulent fluctuations are reduced. In the present case, the Richardson number observed on the Leading Side was mostly positive, and the turbulent fluctuations were significantly reduced with respect to the static case. As the Rotation number increases, the fluid

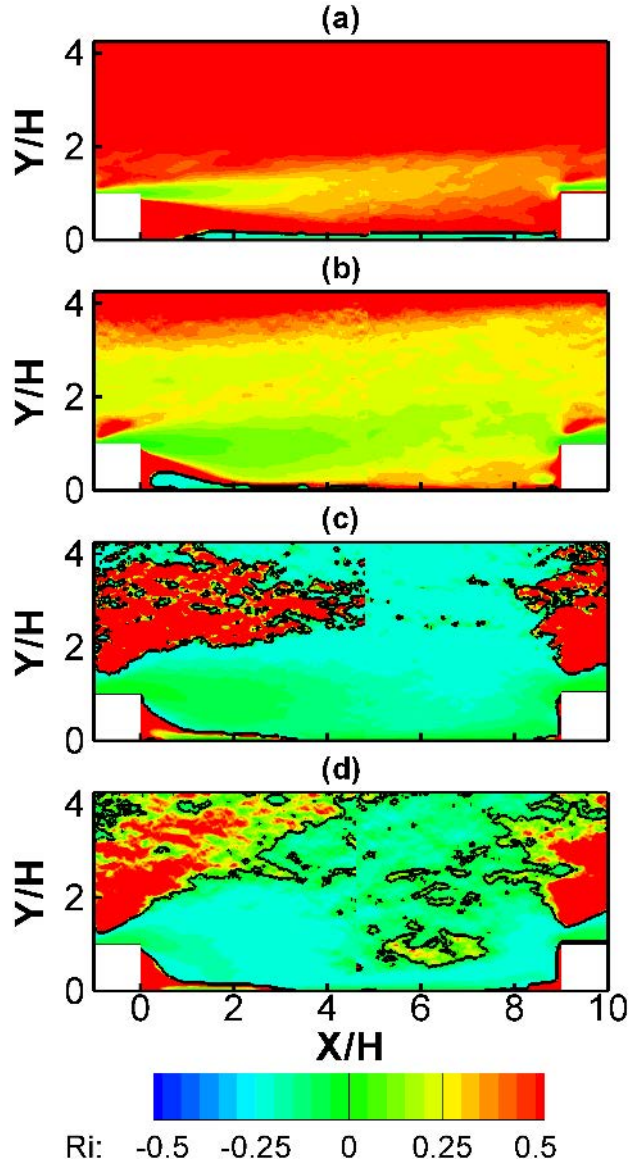

Figure 6.16 : Richardson number contours, Re = 15,000: Leading Side, Ro = 0.77 (a); Leading Side, Ro = 0.30 (b); Trailing Side, Ro = 0.30 (c); Trailing Side, Ro = 0.77 (d). Data obtained with the 35 mm objective (Table 3.3)

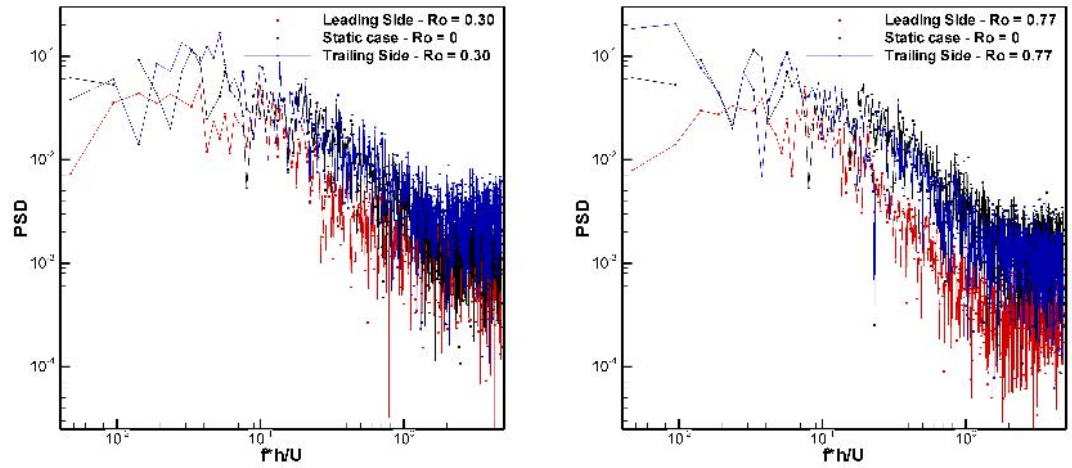

Figure 6.17 : Energy spectra at $(X/H, Y/H) = (1, 1)$

entrainment from the core flow to the recirculation bubble is reduced, resulting in a larger separated region. In addition, the streamline curvature is greatly reduced, especially at $Ro = 0.77$. The absence of stream-line curvature suggests that the impact of the Coriolis-induced and rib-induced secondary flows (Fig. 1.8 [32]) do not exert a large influence in the measurement region, located in the symmetry plane of the channel. The Coriolis-induced secondary flows, driving the fluid from the Trailing Side to the Leading side directly near the lateral walls, and then from the Trailing Side to the Leading Side, are expected to be confined to a limited region next to the lateral walls. It is also noted that it is probable that the rib-induced secondary flows are weakened as the Rotation number increases, since the stream-line curvature introduced by the rib is dramatically reduced. Finally, it is observed that the momentum near the Leading Side increases. This fact may be due to the tendency of the flow to lean the mean velocity profile as demonstrated by Johnston et al. [21] and Kristoffersen and Andersson [20], increasing the momentum near the Leading Side. Also, the increase of momentum could be caused by a change in the secondary flows pattern. However, these conjectures need to be confirmed by further experiments (like Stereoscopic-PIV) in rotating ribbed channels, or at least, to be supported by high-fidelity simulations (section 6.2).

When the channel rotates in the counter-clockwise direction, the ribbed wall acts as Trailing Side. The main flow vorticity shows the opposite direction to the angular velocity, and the flow is referred to as anti-cyclonic. The application of the stability criterion introduced by Lezius [19] and Johnston et al. [21], leads to a negative Richardson number in a large region of the investigated plane at every rotational speed investigated. For this reason, the flow is expected to be destabilized. At $Ro = 0.30$ - 0.38, the turbulence intensity in the shear layer generated by the rib is increased, enhancing the momentum exchange from the near wall region to the core flow. As a result, the recirculation bubble downstream of the rib is reduced, and the momentum directly in contact with the wall

shows larger values than in static conditions. Additionally, the stream-line curvature is increased. It is hence believed that the rib-induced secondary flows are still existing under counter-clockwise rotation. However, the wall-normal velocity in the measurement plane does not demonstrate a large impact from the Coriolis-induced secondary flows, since the wall-normal velocity levels are very similar to those in static conditions. When the rotation speed is augmented to reach $Ro = 0.77$, it is surprising to find low turbulence levels despite the Richardson number criterion suggesting flow destabilization. The in-plane turbulent kinetic energy presents values even lower than in static conditions in a large area of the investigated plane. However, the turbulence intensity in the shear layer generated by the rib is still large, and the recirculation bubble is smaller than in the static case. For these reasons, it is likely that the flow in the measurement plane is affected by a three-dimensional pattern. In particular, it is believed that an additional set of stream-wise vortices appears in the central section of the channel, similar to what was observed in the DNS by Kristoffersen and Andersson [20] at high rotational speeds. This pattern was also suggested by Abdel-Wahab and Tafti [36] in rotating ribbed channels. The presence of the additional stream-wise vortices would sweep fluid away from the Trailing side in the investigated region, reducing the local momentum and the main flow shear $(\partial U/\partial y)$, as observed in the experimental data. The lower momentum and flow shear are most likely the reasons of the turbulence decrease at $Ro = 0.77$ on the Trailing Side. However, as for the clockwise rotating cases, the conjectures about the flow topology in the regions away from the measurement plane need to be confirmed.

6.1.3 Heat transfer field

As demonstrated in the previous section, the flow in rotating channels strongly depends on the Rotation number. The corresponding variations of the mean velocity and turbulence fields result in a heat transfer enhancement or reduction, depending on the sense of rotation. In order to characterize the heat transfer process at the same conditions as in the PIV experiments, LCT measurements were performed in the same geometry. The TLC testing conditions are given in Table 3.5. The PIV and LCT data have been combined in static ($Ro = 0$), moderate rotation ($Ro = 0.30$) and high rotation ($Ro = 0.77$ - 0.83) conditions. At high rotation, the PIV data were obtained at $Ro = 0.77$, whereas the LCT data were obtained at $Ro = 0.83$.

Figure 6.18 shows the combination of the in-plane turbulent kinetic energy, streamlines and Enhancement Factor distribution at $Re = 15{,}000$ and $Ro = 0$. In the recirculation bubble downstream of the rib, EF is low due to the low momentum and turbulent kinetic energy. In the reattachment region, the main flow is directly in contact with the wall, resulting in a high EF. As the flow develops from the reattachment point, the turbulent kinetic energy decreases, which leads to a gradual EF decrease. Just upstream the vortex in front of the following rib, EF reaches a local minimum. However, EF slightly increases in the area of the vortex in front of the rib. This is likely due to the entrainment of flow from the main stream to the wall by action of the corner vortex. Moreover, the two-dimensional EF distribution reveals two maxima directly next to the lateral walls. As observed in the LES by Borello et al. [44], the set of stream-wise vortices (rib-induced

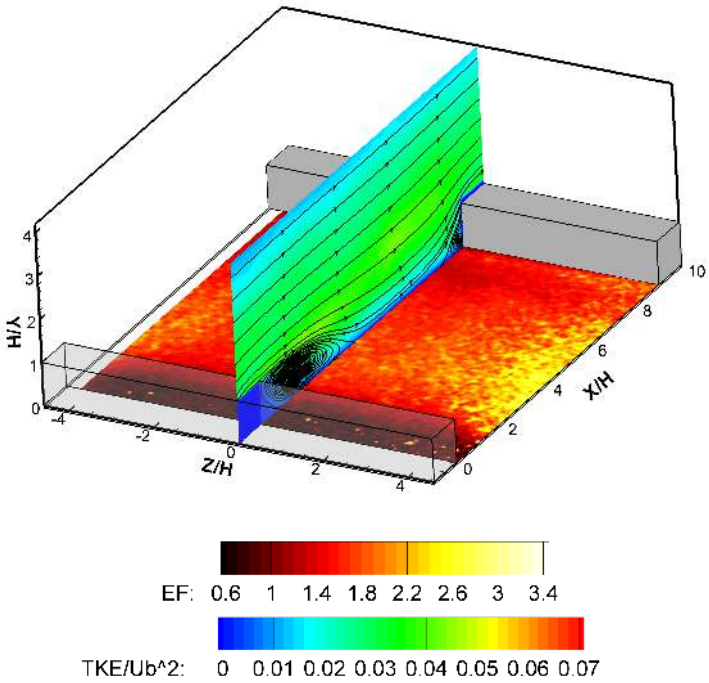

Figure 6.18 : Combination of the experimental Enhancement Factor and in-plane turbulent kinetic energy at $Re = 15000$, $Ro = 0$

secondary flows) drives the core fluid towards the bottom wall in the region near the lateral walls. As a result, the heat transfer is enhanced near the lateral walls, in the region $2 < X/H < 6$.

The Reynolds number effect on the Enhancement Factor has been first investigated in static conditions. The span-wise-averaged EF,

$$EF_{Z-av} = \frac{1}{9.2}\int_{-4.6}^{4.6} EF\left(\frac{X}{H}, \frac{Z}{H}\right) \mathrm{d}\left(\frac{Z}{H}\right) \tag{6.4}$$

has been calculated from the Enhancement Factor distribution in the investigated region at $Re = 15{,}000$, $30{,}000$ and $55{,}000$ and $Ro = 0$. The results are represented in Fig. 6.19. In the present experiments, the span-wise-averaged Enhancement Factor distribution presents almost the same values for each Reynolds number. Therefore, the Nusselt number in static conditions can be expressed as the product of a reference Nusselt number (given by the Dittus-Boelter correlation) and the Enhancement Factor for this geometry, within a wide Reynolds number range. In this way, the Reynolds number effect is taken into account by the reference Nusselt number, whereas the Enhancement Factor corresponds to the efficiency of the geometry to promote the heat transfer. The maximum value of the EF_{Z-av}, EF_{max}, barely varies with the Reynolds number: $EF_{max}(Re = 15{,}000) = 1.91$, $EF_{max}(Re = 30{,}000) = 1.96$ and $EF_{max}(Re = 55{,}000) = 2.00$. Note furthermore that the differences lie within the uncertainty on the Enhancement Factor.

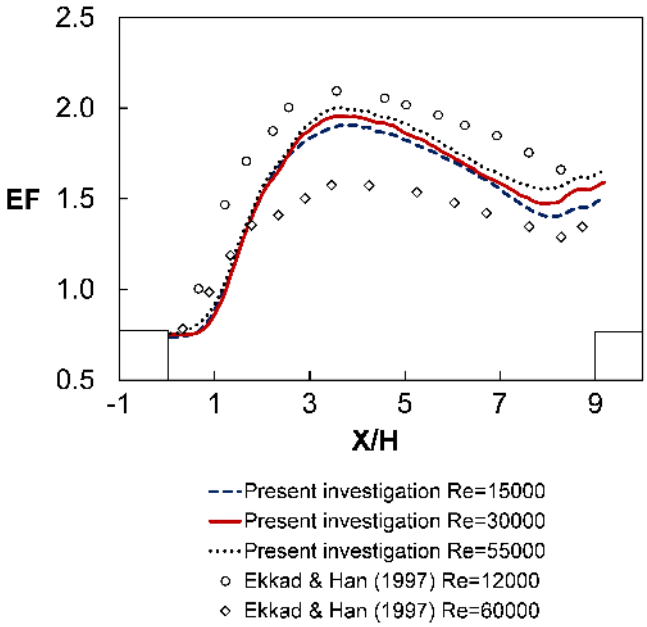

Figure 6.19 : Comparison of the present span-wise-averaged Enhancement Factor in static conditions with the data provided by Ekkad and Han [104], as shown in Ref. [78]

It is observed that as Re increases, EF_{max} is reached slightly closer to the 6th rib. At Re = 15,000 (resp. 30,000, 55,000), the reattachment point being located at X/H = 3.93 (resp. X/H = 3.5 - 3.7, X/H = 3.5).

The LCT data reduction methodology has been validated by comparing with the experimental data provided by Ekkad and Han [104] also in Figure 6.19. The data of Ref. [104] has been extracted between the 6th and 7th ribs of the first section in a two-pass internal cooling channel. The results provided by Ekkad and Han [104] are comparable to the present experiments given the experimental conditions, Re = 12,000 - 60,000, and the similar geometry. In Ref. [104], the channel cross section is squared, as well as that of the ribs. Additionally, the rib pitch to height ratio is equal to 10, and the blockage ratio is equal to 12.5%. The present measurements show a similar trend, with an agreement in the position of the maximum and minimum EF at about X/H = 3.8 and 8.0, respectively. The measured values fall inside the area delimited by the data of Ref. [104], but with a moderate bias of around 9.4% of the maximum EF at Re = 12,000 - 15,000, and around 21% of the maximum EF at Re = 55,000 - 60,000. Another comparison with the literature can be carried out by computing the surface-averaged EF, $\overline{EF}$. For Re = 15,000 (resp. 30,000, 55,000) the present work shows $\overline{EF}$ = 1.55 (resp. 1.59, 1.64) while Ekkad and Han [104] reported $\overline{EF}$ = 1.78 (resp. 1.84, 1.60).

The Enhancement Factor at the centerline of the investigated area (Z/H = 0) is represented in Fig. 6.20 on top of the in-plane turbulent kinetic energy contours and

streamlines at each of the PIV experimental conditions. Finally, the complete EF distribution on the wall is displayed in Figs. 6.21 and 6.22 together with the PIV data obtained in the symmetry plane of the channel. The direct correlation of the Enhancement factor with the momentum and turbulence distributions at the different rotating conditions appears clearly from the figures.

In the Leading Side case at $Ro = 0.30$, the turbulence level decreases with respect to the one in static conditions, and the recirculation bubbles are enlarged. As a result, the overall Enhancement Factor decreases, showing values below 1 in the area covered by the recirculation bubble and values about 1 when the main stream is in contact with the wall. In the EF distribution on the investigated wall (Fig. 6.21(a)), it can be observed that the extension of the low EF region downstream of the rib barely changes in the span-wise direction. Since this region of low EF is directly related to the recirculation bubble downstream of the obstacle, it seems that the recirculation bubble length is mostly uniform in the span-wise direction. The effect of the Coriolis-induced secondary flows is visible on the large EF near the lateral walls. According to the sketch shown in Fig. 1.8[32], the Coriolis-induced secondary flows drive fluid from the Trailing Side (top wall in this case) to the Leading Side. In the present channel, the impingement of the Coriolis-induced secondary flows on the Leading Side leads to high EF in the regions $Z/H <$ -4 and $Z/H > 4$. Therefore, the characteristic length of the Coriolis-induced secondary flows is of order of the rib height, that is, about 1/10 the hydraulic diameter. This length scale is similar to the dimension of the Coriolis-induced secondary flows observed in the LES by Borello et al. [44] near the Leading Side in smooth and ribbed channels, as well as in the LES carried out in the present work. Additionally, two large EF spots are found in the corner of the leading edge of the 7th rib and the lateral walls. These spots are related to the Coriolis-induced secondary flows with the constraint of the obstacle. In this area, the cold fluid driven by the Coriolis-induced secondary flows towards the Leading Side impacts the leading edge of the rib, inducing a local accumulation of cold fluid and resulting in a EF increase. It is likely that the vortex observed just upstream of the 7th rib in the symmetry plane does not extend over the whole span, as it is not very compatible with the high EF observed near the lateral walls. This observation is supported by the LES performed by Borello et al. [44], where no upstream vortex was detected in a plane close to the lateral walls on the Leading Side area at $Ro = 0.30$. When the rotational speed increases to reach $Ro = 0.77$ - 0.83, the turbulent kinetic energy on the Leading Side decreases and the recirculation bubble downstream of the rib is enlarged, occupying the whole area between the ribs. In this way, the Enhancement Factor shows even lower values than in the previous case, especially just downstream of the 6th rib (Fig. 6.20(a)). In the centerline EF distribution, the maximum value is found in the region where the second span-wise vortex lies ($X/H \sim 8$). This is the only region where EF shows values larger than 1. This EF local maximum could be caused by the entrainment of core fluid into the recirculation bubble, enhancing slightly the heat transfer. However, Fig. 6.21(b) shows that the footprint of the Coriolis-induced secondary flows is not observed under this regime, most probably due to the topology of the recirculation bubble. A thick recirculation bubble is expected to cover most of

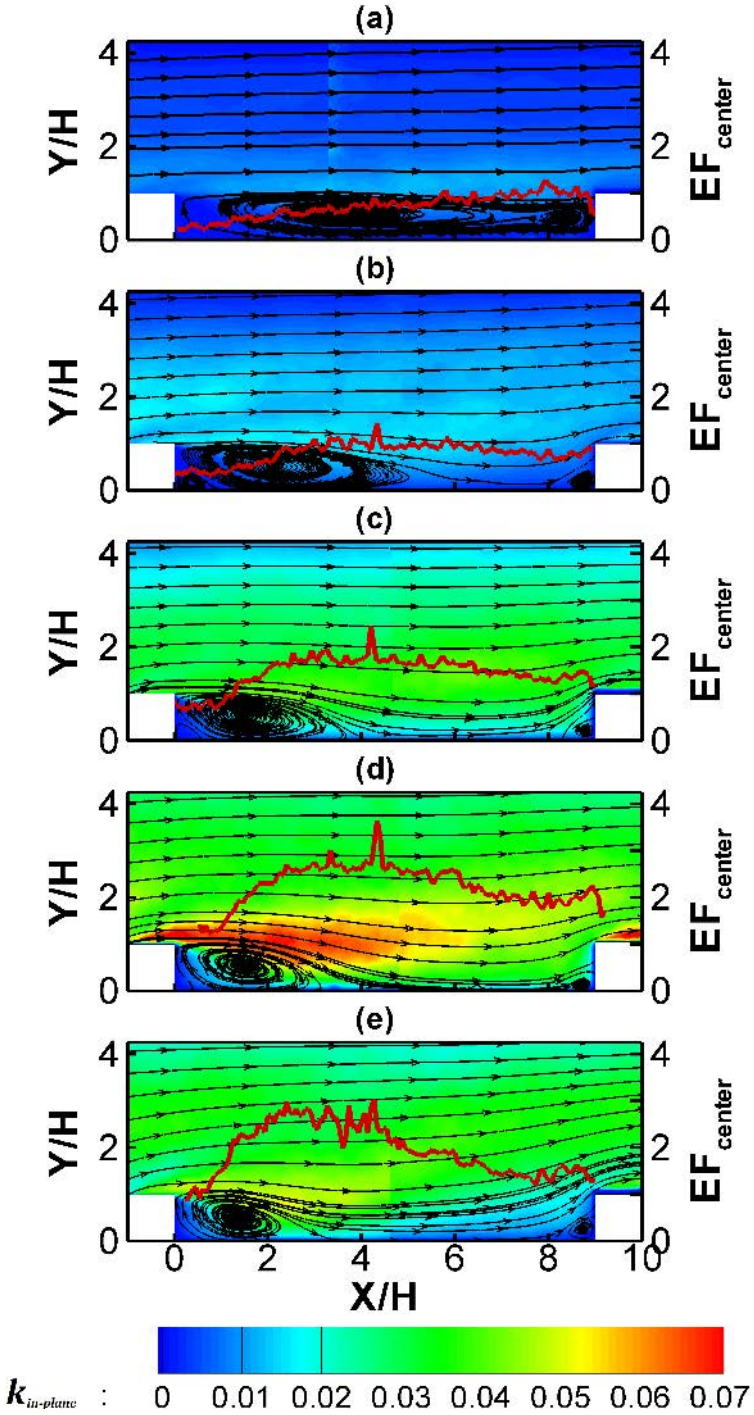

Figure 6.20 : Centerline Enhancement Factor, in-plane turbulent kinetic energy and streamlines at Re=15,000: Leading Side - Ro = 0.77 (PIV) - 0.83 (LCT) (a), Leading Side - Ro 0.30 (b), static case (c), Trailing Side - Ro = 0.30 (d) and Trailing Side - Ro = 0.77 (PIV) - 0.83 (LCT) (e)

the inter-rib area, leading to low EF and limited variations in the span-wise direction. The local maximum related to the vortex upstream of the rib is observed all along the Z direction, hence this vortex is expected to almost extend over the entire channel width. As in the case of $Ro = 0.30$, the maximum EF is found in the corner between the leading side of the rib and the lateral wall. In this region, the Coriolis-induced secondary flows are able to penetrate the recirculation bubble and provide cold fluid to the bottom wall, increasing the heat transfer.

When the channel rotates in the counter-clockwise sense (Trailing Side), the heat transfer increases. At $Ro = 0.30$ (Fig. 6.20(d)), the maximum EF in the centerline reaches levels of about 2.7 in the region around the reattachment point. Since the maximum EF in the centerline under static conditions is about 1.75, the heat transfer increase is about 50% of the original value. After the reattachment point and the decrease of turbulent kinetic energy, EF decreases. As in the previous cases, a local EF maximum is found just upstream of the 7th rib, corresponding to the entrainment of main stream fluid into the vortex in front of the obstacle. The EF map (Fig. 6.22(a)) reveals not only a local maximum in the reattachment point in the symmetry plane, but also near the lateral walls. With the picture given in Fig. 1.8[32], only one large EF spot is expected, corresponding to the combination of the flow reattachment and the Coriolis-induced secondary flows accelerating the fluid towards the Trailing Side in the region of the symmetry plane. Given the present EF distribution, it is believed that the Coriolis-induced secondary flows push the core fluid towards the corners between the bottom and lateral walls instead of the central region, combining with the rib-induced secondary flows and resulting in a larger heat transfer near the lateral walls. An alternative flow picture causing the present EF pattern may consist in the combination of Coriolis-induced secondary flows pushing the fluid in the symmetry plane and enhancing the heat transfer in the central region, and strong rib-induced secondary flows increasing the EF near the lateral walls. However, the LES performed in the present work and those produced by Borello et al. [44], suggest that the actual topology of the flow corresponds to the first flow picture. The EF distribution in Fig. 6.22(a) also shows a possible reduction of the separation bubble length close to the lateral walls, since the length of the low EF area is reduced in the span-wise direction. Additionally, the area of low EF just upstream of the vortex in front of the 7th rib extends over the entire channel width. Therefore, the vortex upstream of the rib is expected to exist over the whole span-wise direction. At a larger Rotation number ($Ro = 0.77$ - 0.83, Fig. 6.20(e)), the size of the recirculation bubble is slightly reduced, moving a bit forward the location of maximum EF. Even though the turbulent kinetic energy on the Trailing Side at large Ro is lower than in the precedent case, the generation of turbulence in the shear layer by effect of rotation is enough to reach a maximum EF of about 2.75. However, the turbulent kinetic energy decays abruptly after $X/H \sim 4$, which results in a continuous decrease of the EF towards the following rib. In fact, the Enhancement Factor in the centerline in the region $X/H > 6$ is very similar to the one found in static conditions, including the effect of the vortex in front of the rib. Away from the symmetry plane, the EF map presents a different distribution from the previous cases. In particular, two

(a) Leading Side, $Ro = 0.30$ (PIV & LCT)

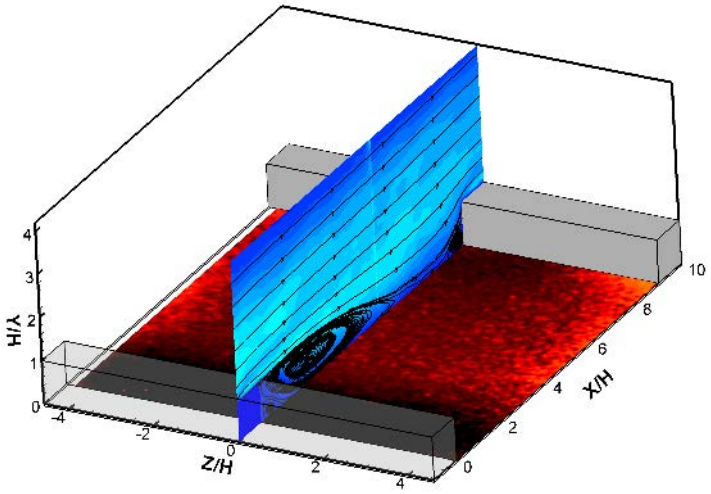

(b) Leading Side, $Ro = 0.77$ (PIV) - 0.83 (LCT)

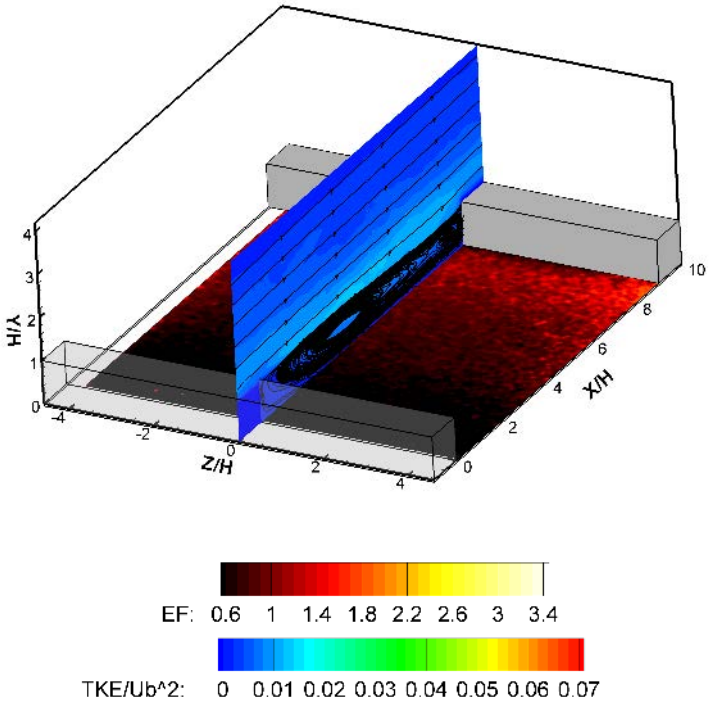

Figure 6.21 : Combination of the experimental Enhancement Factor and in-plane turbulent kinetic energy at $Re = 15000$

high EF spots (showing EF values of about 3) are found at $X/H \simeq 2.7$ at a distance $\sim 1.5H$ from the lateral walls. It is believed that the high rotation modifies the pattern of the secondary flows, similarly to what Kristoffersen and Andersson [20] observed in their DNS in a smooth channel at large Ro. In this case, four large stream-wise vortices are expected to coexist near the Trailing Side of the channel. Two of these vortices would be located near the lateral walls, inducing a secondary flow motion similar to the traditional flow picture in low-aspect ratio rotating channels (Fig. 1.8[32]): fluid moves from the Trailing Side towards the Leading Side in the area near the lateral walls. In the present case, the flow would go back from the Leading Side (top wall) to the Trailing Side to impinge in the mentioned high EF areas. Two additional counter-rotating vortices are expected in the central area of the flow, sweeping fluid out from the Trailing Side in the region of the symmetry plane, which leads to slightly lower EF in this area. In order to ease the comparison of the heat transfer performance at the different rotating conditions, Fig. 6.23 presents the top view of the EF contours in the investigated region at $Ro = 0$, 0.30 and 0.83.

The combined effects of rotation and Reynolds number are studied from th EF distributions shown in Figs. 6.24 - 6.26. In static conditions (Fig. 6.24), the Reynolds number does not show to have a major impact on the Enhancement Factor distribution. Only at $Re = 55{,}000$, as observed in Fig. 6.19, the overall Enhancement Factor is slightly larger than at lower Reynolds numbers. Another subtle difference corresponds to the decreasing span-wise variations as the Reynolds number increases. At $Re = 15{,}000$, the EF difference between the area near the lateral walls and the center of the investigated region is larger than at $Re = 30{,}000$ and 55,000. Moreover, the region of low EF in front of the vortex upstream of the 7th ($7 < X/H < 9$) shows large variations at $Re = 15{,}000$. The Enhancement Factor is particularly low in the intersection of this region with the symmetry plane at $Re = 15{,}000$. This span-wise EF gradients may be caused by slight differences in the secondary flow topology.

At $Ro = 0.20$, the EF distribution does not vary significantly as the Reynolds number increases from $Re = 15{,}000$ to $Re = 55{,}000$ (Fig. 6.25). When the channel is rotated in the clockwise sense (Leading Side case), the EF decreases due to the reduction of turbulence by the Coriolis forces and the enlargement of the separation bubble downstream of the rib. The region of low EF corresponding to the separation bubble presents a similar shape at the different investigated Reynolds numbers. Note that the effect of the Coriolis-induced secondary flows at every Reynolds number is evident in the area close to the lateral walls, where the fluid moves from the TS to the LS, generating a localized region of large EF. Therefore, the flow topology is likely to be the same in the range $Re = 15{,}000$ - 55,000 although the overall Enhancement Factor is slightly larger at $Re = 55{,}000$. Under counter-clockwise rotation (Trailing Side case), the overall Enhancement Factor increases due to the raise of turbulence intensity and the action of the Coriolis-induced secondary flows. The position of the maximum EF in the symmetry plane, related to the reattachment of the shear layer, takes place at $X/H \simeq 3.8$ in the case of $Re = 15{,}000$. As the Reynolds number increases, the location of the shear layer reattachment seems not to vary. Moreover, the footprint of the secondary flows does not

(a) Trailing Side, $Ro = 0.30$ (PIV & LCT)

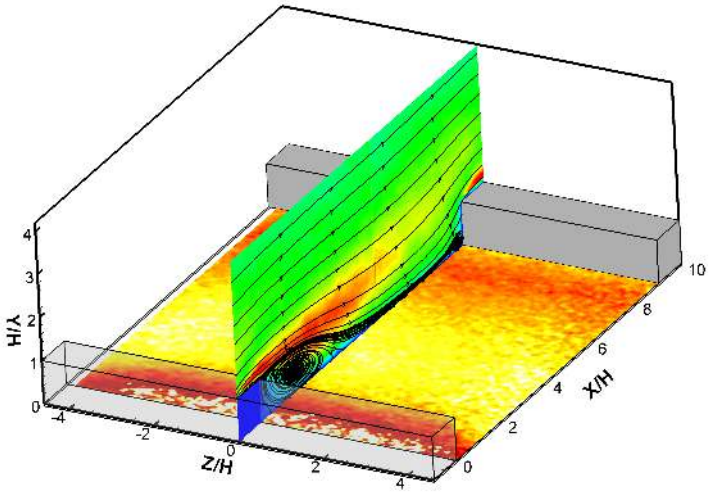

(b) Trailing Side, $Ro = 0.77$ (PIV) - 0.83 (LCT)

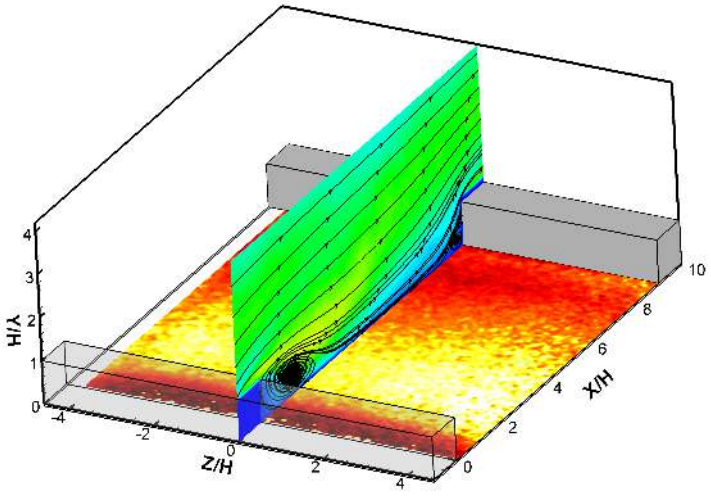

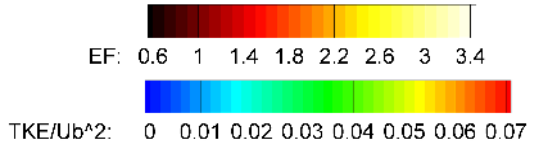

Figure 6.22 : Combination of the experimental Enhancement Factor and in-plane turbulent kinetic energy at $Re = 15000$

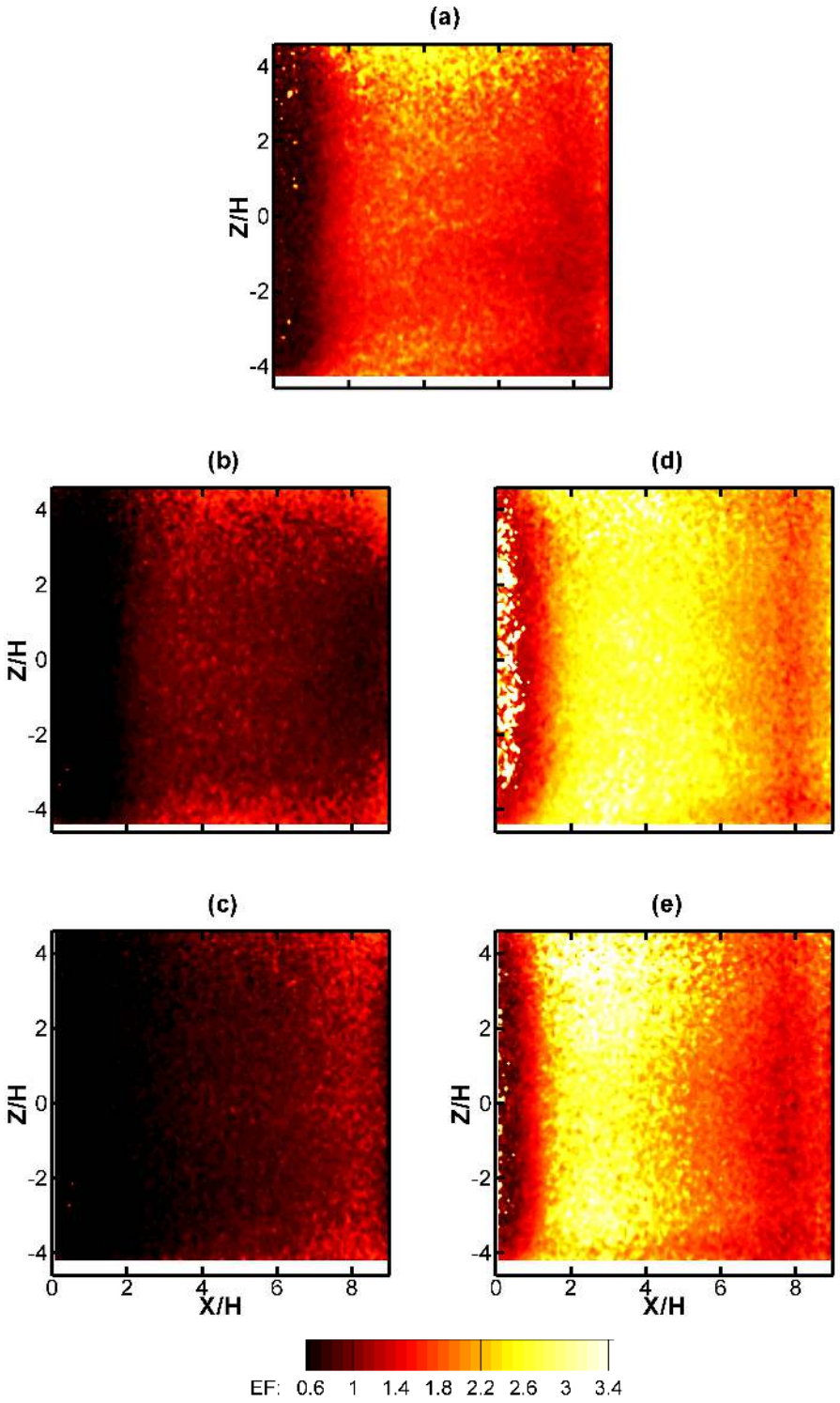

Figure 6.23 : Enhancement Factor contours at Re = 15,000: Static (a), Leading Side - Ro = 0.30 (b), Leading Side - Ro = 0.83 (c), Trailing Side - Ro = 0.30 (d), Trailing Side - Ro = 0.83 (e)

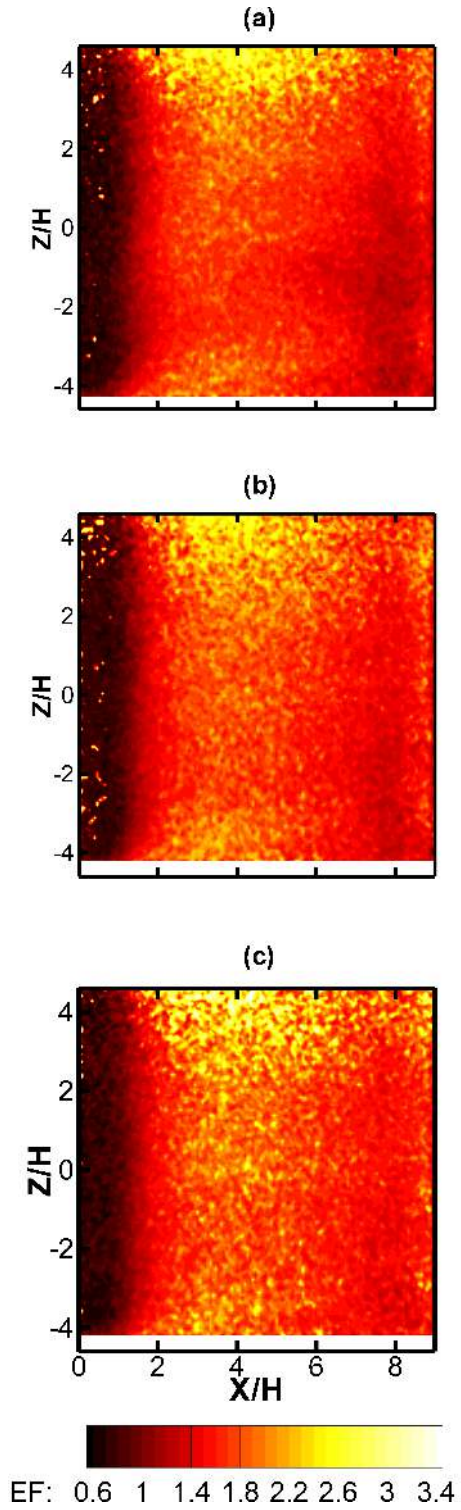

Figure 6.24 : Enhancement Factor contours at Re = 15,000 (a), 30,000 (b) and 55,000 (c)

change the EF distribution in the Trailing Side at the different Reynolds numbers. The region $2 < X/H < 6$ presents large EF values due to the reattachment of the shear layer generated by the rib and the action of the Coriolis-induced secondary flows. After this area of high heat transfer, the EF diminishes reaching a relative minimum on the line $X/H \sim 8$ which corresponds to the beginning of the span-wise vortex upstream of the 7th rib. Since the relative minimum is present all over the line $X/H \sim 8$, it is likely that this span-wise vortex extends over the whole span of the channel. For these reasons, limited differences in the turbulent field are expected as the Reynolds number increases.

At $Ro = 0.47$, the EF distribution is similar at $Re = 15{,}000$ and 30,000 in the case of the Leading Side. Only minor differences are found. In particular, the area of low EF corresponding to the recirculation bubble is considerably enlarged at $Re = 15{,}000$, whereas at $Re = 30{,}000$ the recirculation bubble size seems unchanged if compared to the case at $Ro = 0.20$. Additionally, the overall EF is larger at $Re = 30{,}000$ than at $Re = 15{,}000$. Most likely, the turbulent fluctuations at $Re = 30{,}000$ are not damped as efficiently by rotation as in the case at $Re = 15{,}000$. According to Lezius and Johnston [19], the stability criterion is actually affected by the Reynolds number. Therefore, the differences in the EF levels may be related to the Reynolds number effects on the flow stability. As a result of the presumed larger turbulence at $Re = 30{,}000$, the momentum exterchange between the core flow and the recirculating fluid is larger than at $Re = 15{,}000$, enhancing the heat transfer and reducing the separation bubble length. On the other hand, the Coriolis-induced secondary flows appear to have the same characteristic dimensions in both cases, given the area of slightly higher EF near the lateral walls.

On the Trailing Side at $Ro = 0.47$, the overall EF increases slightly from the case at $Ro = 0.20$, both at $Re = 15{,}000$ and 30,000. However, the EF distribution shows a different pattern in the cases at $Re = 15{,}000$ and 30,000. At $Re = 15{,}000$, the area of low EF corresponding to the recirculation bubble after the 6th rib is reduced and the maximum EF is found at $X/H \simeq 3.4$ in the symmetry plane. In this case, the secondary flow pattern appears to have changed with respect to the case at $Ro = 0.20$ since a large EF spot is found in the central region of the investigated area ($(X/H,\ Z/H) \simeq (4{,}0)$) and no large EF is found near the lateral walls. For this reason, it is likely that the Coriolis-induced secondary flows have increased in size and strength, setting aside the role of the rib-induced secondary flows in the heat transfer mechanism. On the other hand, the vortex upstream of the 7th rib seems not to move from its original position. The EF values on this zone ($X/H > 8$) are of the same level as in the previous case, showing that the flow field is not largely affected in this area. At $Re = 30{,}000$, the recirculation bubble size downstream of the 6th rib shows almost the same size as at $Re = 15{,}000$. However, the EF distribution in the region $2 < X/H < 6$ is different with respect to the case at $Re = 15{,}000$. Two large EF spots are found around the points $(X/H,\ Z/H) \sim (3{,}\pm 3)$, similarly to what was observed on the Trailing Side at $Re = 15{,}000$ and $Ro = 0.83$. Likely, the secondary flow pattern is similar to that at $Re = 15{,}000$ and $Ro = 0.83$ given that the shape of the EF distribution are akin. Therefore, the EF distributions suggest a change in the Coriolis-induced secondary flows pattern at different Rotation numbers if the Reynolds number is varied.

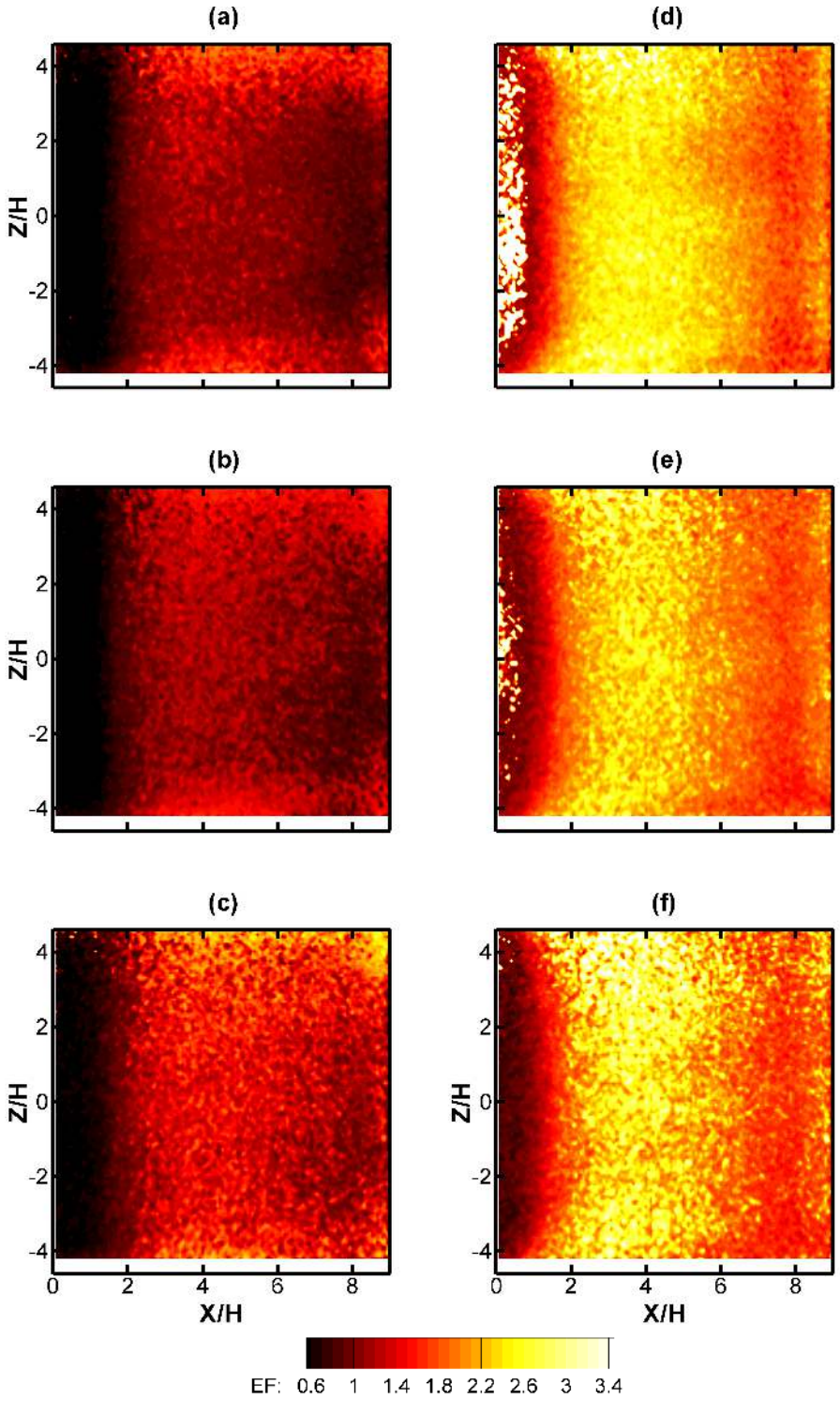

Figure 6.25 : Enhancement Factor contours at $Ro = 0.20$: Leading Side (LS) - $Re =$ 15,000 (a), LS - $Re =$ 30,000 (b), LS - $Re =$ 55,000 (c), Trailing Side (TS) - $Re =$ 15,000 (d), TS - $Re =$ 30,000 (e), TS - $Re =$ 55,000 (f)

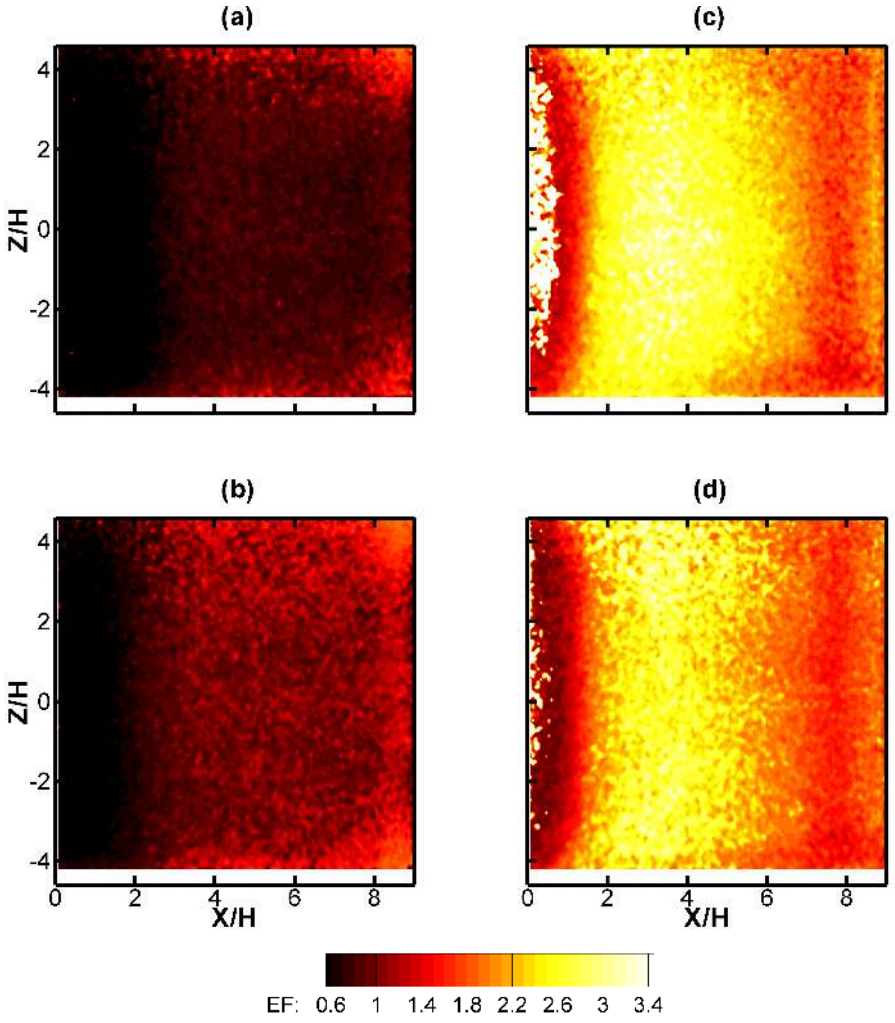

Figure 6.26 : Enhancement Factor contours at $Ro = 0.47$: Leading Side (LS) - $Re =$ 15,000 (a), LS - $Re =$ 30,000 (b), Trailing Side (TS) - $Re =$ 15,000 (c), TS - $Re =$ 30,000 (d)

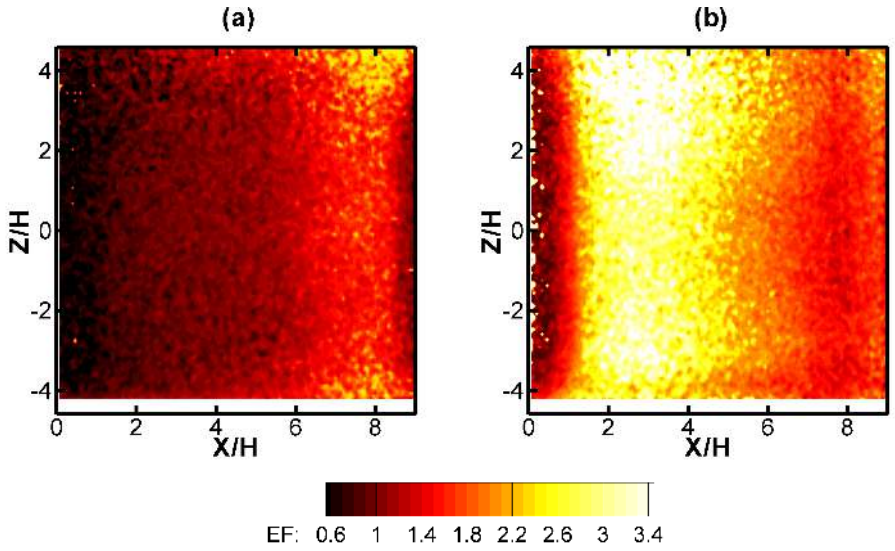

Figure 6.27 : Enhancement Factor contours at Re = 15,000, Ro = 1.0: Leading Side (a), Trailing Side (b)

Finally, the Enhancement Factor contours are represented at the largest Rotation number ($Ro = 1.0$, $Re = 15{,}000$) in Fig. 6.27. On the case of the Leading Side, the shape of the EF distribution is very similar to those already commented at lower rotational speeds, i.e. a large separation bubble and impact of the Coriolis-induced secondary flows. However, the overall EF is slightly larger than at lower Ro. This could be caused by the increasing importance of the centripetal buoyancy forces. At this regime, the Buoyancy number reaches a value of about 0.32. The fluid directly near the wall is at higher temperature than that in the core of the flow, leading to a centripetal force gradient in the Y direction. The centripetal force is larger in the core, which induces a large shear and therefore larger turbulent fluctuations. As a result, the heat transfer is slightly enhanced with respect to the previous case. On top of that, Coletti et al. [33] observed reversed flow when $Ro = 0.38$ and $Bo = 0.31$ caused by the shear layer stabilization and the high buoyancy forces on the Leading Side case. For this reason, it is possible that the flow is reversed near the Leading Side in the present case, which would lead to larger velocity gradients and turbulent fluctuations. On the Trailing Side, the EF distribution is similar to that observed at $Ro = 0.83$. The recirculation bubble size is reduced and the maximum EF is found at $X/H = 2.8$ in the symmetry plane. On the other hand, the highest EF is found in two symmetric spots at $(X/H,Z/H) \simeq (2.8, \pm 3)$ due to the doubling of the secondary flow cells from 2 to 4. Additionally, the region $X/H > 5$ presents lower EF than in the former situations due to the re-stabilization of the shear layer by the high angular velocity and the consequent decrease of turbulent kinetic energy.

The area averaged Enhancement Factor,

$$\overline{EF} = \frac{1}{9.2 \times 9} \int_0^9 \left[\int_{-4.6}^{4.6} EF\left(\frac{X}{H}, \frac{Z}{H}\right) \mathrm{d}\left(\frac{Z}{H}\right) \right] \mathrm{d}\left(\frac{X}{H}\right) \tag{6.5}$$

is displayed in Fig. 6.28 to compare the overall heat transfer performance at each regime. A sign criterion for the Rotation number has been chosen for the sake of clarity. Negative Ro stands for clockwise rotation (Leading Side cases), whereas positive Ro stands for counter-clockwise rotation (Trailing Side case). At $Re = 15{,}000$, $\overline{EF}$ shows approximately a linear dependency with respect to Ro in the range $|Ro| < 0.38$, with a sensitivity $\partial EF/\partial Ro \sim 2.37$. At larger Rotation numbers, EF presents an asymptotic behavior, with a value about 2.2 on the Trailing Side case and 0.75 on the Leading Side case. According to the PIV measurements of Coletti et al. [32] and in the present work, the position and extension of the recirculation bubble downstream of the 6th rib and upstream of the 7th rib vary very little with increasing rotation on the Trailing Side for $Ro > 0.3$, hence the zones of low EF are restricted to the same locations. At large Ro, the secondary flow cells are doubled and two symmetric spots of increased EF are present on the Trailing Side at a location $(X/H,\, Z/H) \simeq (2.8,\, \pm 3)$. However, the EF increase due to the secondary flows is balanced by a local reduction in the second half of the inter-rib area due to the re-stabilization of the shear layer. Therefore, the overall heat transfer enhancement is maintained on the Trailing Side at large Rotation numbers. On the Leading Side at $Re = 15{,}000$, $\overline{EF}$ is stable in the investigated region for $|Ro| > 0.4$, suggesting the isolation of the LS by the recirculation bubble from the bulk flow. Since the velocity at the border of the recirculation region is given by the bulk flow, fixed in turn by the Reynolds number, the EF reaches an asymptotic value. When the Reynolds number is increased to 30,000, the linear region is present in a smaller range of the Rotation number ($|Ro| < 0.20$) with a similar slope, $\partial EF/\partial Ro \sim 2.77$. In this situation, the asymptotic EF at $|Ro| > 0.20$, is about 2.0 on the Trailing Side case and 0.75 on the Leading Side case. At the highest Re no asymptotic performance is observed within the investigated range ($|Ro| < 0.20$), the dependence of the EF is linear with Ro with a sensitivity $\partial EF/\partial Ro \simeq 1.77$. According to the present results, the influence of rotation decreases as the Reynolds number increases.

Figure 6.29 shows the comparison of the present heat transfer results with data present in the literature with similar geometries and conditions. Since the overall Enhancement Factor ($\overline{EF}$) depends on the geometry, the data has been normalized with the overall Enhancement Factor in static conditions ($\overline{EF}_{static}$). The value of $\overline{EF}/\overline{EF}_{static}$ reaches a value around 1.5 on the Trailing Side and to 0.5 on the Leading Side at high rotation. Therefore, the net improvement and reduction of the heat transfer becomes 50% in the EF, depending on the sense of rotation. The data by Abdel-Wahab and Tafti [36], Kim et al. [105] and Johnson et al. [25] are comparable with the present investigation given the geometrical similarities and Reynolds numbers investigated (20,000, 10,000 and 25,000, respectively). Nonetheless, the boundary conditions and geometries employed in these reference works are slightly different from the present data (in particular, all of them present ribs on the top and bottom walls). In the case of Abdel-Wahab and Tafti

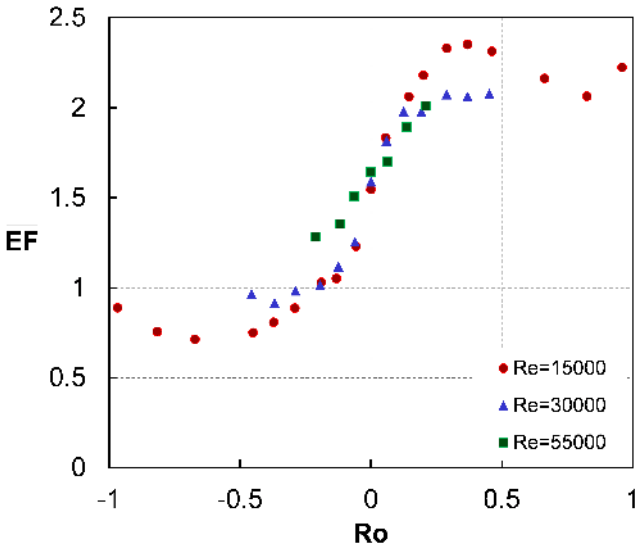

Figure 6.28 : Area-averaged Enhancement Factor as a function of the Rotation and Reynolds numbers[53]

[36], the LES computations are performed assuming periodic flow and heat transfer. In the case of the work by Johnson at al. [25], the ribs have different cross section and the channel walls are made of copper to apply a uniform temperature boundary condition. The channel employed by Kim et al. [105] presents a H/D_H slightly lower than in the present case whereas the boundary condition corresponds to uniform temperature. Despite these differences, Fig. 6.29 reveals an excellent agreement with the available data for all the investigated Ro range, except with respect to the LES computations by Abdel-Wahab and Tafti [36] at medium and high Buoyancy numbers, most likely due to the applied boundary conditions.

6.1.4 Buoyancy effects

In the following, the effect of centripetal buoyancy has been added by heating up the ribbed wall with the system described in section 3.3.2. To do so, the wall temperature is raised up to a maximum temperature of 95°C to achieve a Buoyancy number (Eq. (1.12)) of 0.77 when $Ro = 0.77$. Such a wall heating indeed generates a temperature gradient in the flow, and therefore differences in the centripetal force. Figures 6.30 - 6.32 present the mean flow statistics of the flow under large rotation and centripetal buoyancy ($Ro = 0.77$, $Bo = 0.77$) and compare them with the isothermal flow under rapid rotation described in the previous section ($Ro = 0.77$, $Bo = 0$). On the Leading Side case at $Ro = 0.77$ and $Bo = 0.77$, the flow field is totally different from the cases previously analyzed. The main characteristic of the fluid motion under these conditions is the large region of the flow field that shows a reverse sense. Figure 6.31 shows that the area $Y/H <$ 2 - 2.6 in the symmetry plane shows a negative mean stream-wise velocity. Moreover,

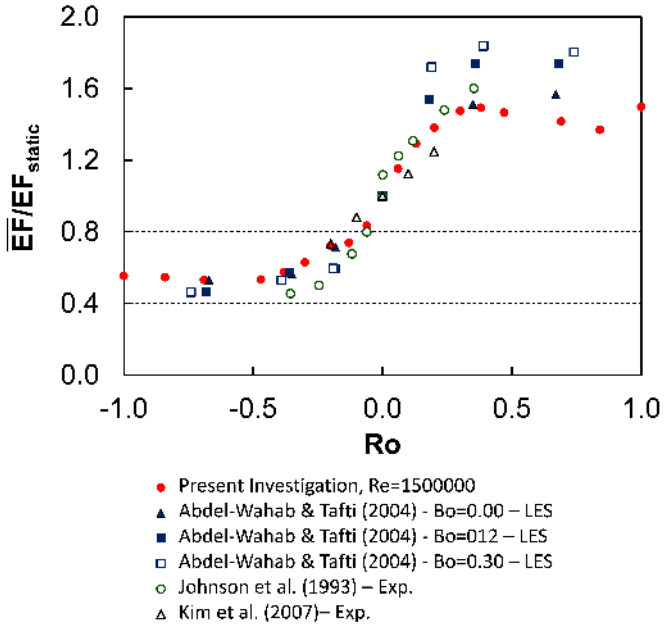

Figure 6.29 : Normalized average Enhancement Factor at Re = 15,000 and comparison with similar data present in the open literature[78]

the momentum in the reverse flow region presents a negative stream-wise velocity that reaches a value about 50% of the bulk velocity. Due to the temperature field, the density is lower in the near-wall region than in the core of the flow and the centripetal force is larger in the flow core. Similarly to the flow over a vertical heated plate subject to gravity force, the centripetal buoyancy force tends to push the fluid against the direction of the centripetal force. Due to the flow stabilization by the Coriolis force on the Leading Side and the action of the centripetal buoyancy, the negative velocity in the near-wall region between the ribs becomes so important that the flow near the Leading Side is completely reversed. It is the reduction of the turbulent fluctuations by the Coriolis force that avoids the mixing of the core and reversed flows. It is furthermore noted that the centripetal buoyancy force increases as the fluid moves radially outwards, which leads to a larger separated area further downstream. As observed in Fig. 6.31(a), the area of negative stream-wise velocity passes to cover the area $Y/H < 2$ at $X/H = 0$, to the area $Y/H < 2.6$ at $X/H = 10$. Since the Reynolds number is fixed, the negative velocity in the reverse flow region is balanced by a larger stream-wise velocity in the core of the flow, leading to a large stream-wise velocity gradient in the wall-normal direction. The ribs have also an impact in the reverse flow due to the reduction in the area of the cross section that they introduce, resulting in a large streamline curvature in the region around the obstacles and the appearance of two saddle points above them. The saddle points can be identified at (X/H, Y/H) = (-0.3, 2.1) and (9.5, 2.5) in Fig. 6.30, that shows in tun the in-plane streamlines and velocity modulus on the Leading Side at Ro = 0.77 and Bo = 0.77. As a result of the saddle points and the core flow, a large span-wise

vortex is generated in the inter-rib area, with a center at $(X/H,\, Y/H) = (5,\, 1.9)$. The momentum in the reverse flow region is so important that the flow is separated after passing the 7th rib, generating an additional span-wise vortex found in the near-wall region at $8 < X/H < 9$,

Three main differences are observed in the mean velocity field on the Leading Side under Buoyancy with respect to that in the study by Coletti et al. [33], carried out at Re = 15,000, $Ro = 0.38$ and $Bo = 0.31$. First, the reverse flow is sustained from rib to rib in the present experiments. Second, the ribs induce high stream-line curvature in the reversed flow region, which generates a saddle point just above the ribs. And finally, the wall-normal extension of the present reversed flow region is much larger. Therefore, it can be concluded that not only the Rotation number has a strong impact of the mean flow field on the Leading Side of rotating cooling channels, but the Buoyancy number can also generate critical differences.

On the contrary, Figs. 6.30(e)-6.32(e) show that the centripetal buoyancy has a very limited effect on the flow near the ribbed wall when it acts as Trailing Side. The same was found by Coletti et al. [33] at lower Rotation and Buoyancy numbers ($Ro = 0.38$ and $Bo = 0.31$). The reattachment point at $Ro = 0.77$ and $Bo = 0.77$ is located at $X/H = 3.2$, similarly to what was found in the isothermal case. The largest difference is found in the wall-normal velocity in the area just upstream of the reattachment of the shear layer generated by the rib (Figs. 6.32(d)-(e)): the wall normal velocity passes from about -0.06U_b at $Ro = 0.77$, $Bo = 0$ to about -0.11U_b at $Ro = 0.77$, $Bo = 0.77$. Most likely, the large turbulent fluctuations enhance the momentum exchange between the near-wall region and the main flow, leading to a high turbulent gradient near the wall and a more uniform temperature profile towards the core of the flow. Due to the uniformity of the hypothetical temperature profile, the gradients in the centripetal forces are drastically reduced, leading to a negligible centripetal buoyancy effect.

Concerning the turbulent velocity field, the changes on the Leading Side case under the effect of Buoyancy are also severe when compared to the distribution found in the isothermal flow. The stream-wise and wall-normal turbulent velocities on the Leading Side at $Ro = 0.77$ and $Bo = 0.77$, displayed respectively in Figs. 6.33(a) and 6.34(a), show the strong influence of the centripetal buoyancy force also on the turbulent field. First, the turbulence intensity is locally increased on the top of the rib and in the reduced shear layer generated by the 7th rib, located in the reversed flow region. Second, the reverse flow region generates a large velocity gradient in the y direction, which leads to a large strain field and turbulence production. Moreover, the near-wall flow is subject to anti-cyclonic rotation: the mean vorticity of the fluid directly in contact with the wall presents opposite sense to that of the angular velocity. In this region, the Coriolis force presents a destabilizing character and therefore the turbulence is increased with respect to the isothermal flow on the Leading Side (Figs. 6.33(b) and 6.34). It can be furthermore observed that the turbulent fluctuations are large in the region just upstream of the saddle points. In this area the mean velocity is close to zero, but the large velocity gradients generate high strain rates, hence providing large turbulent fluctuations. For these reasons, the overall turbulence intensity is notably larger than

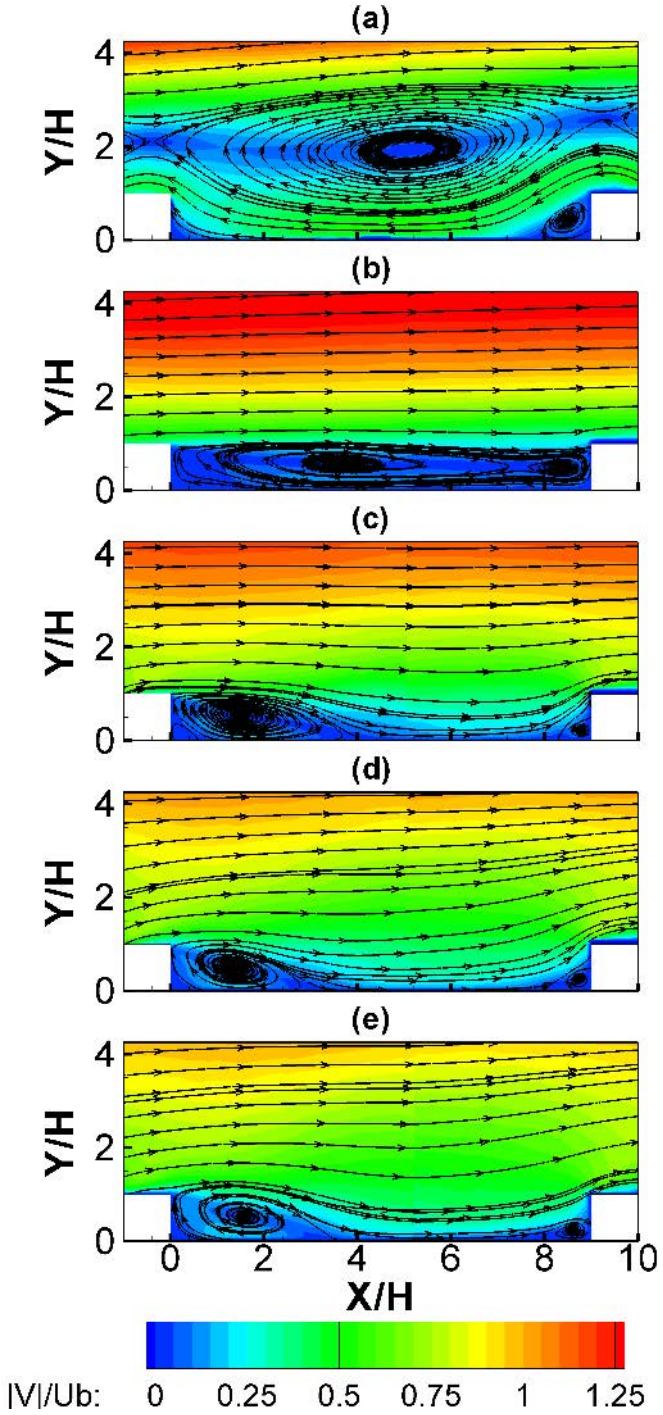

Figure 6.30 : Mean wall-normal velocity contours, Re = 15,000: Leading Side, Ro = 0.77, Bo = 0.77 (a); Leading Side, Ro = 0.77, Bo = 0 (b); Static, Ro = 0 (c); Trailing Side, Ro = 0.77, Bo = 0 (d); Trailing Side, Ro = 0.77, Bo = 0.77 (e)

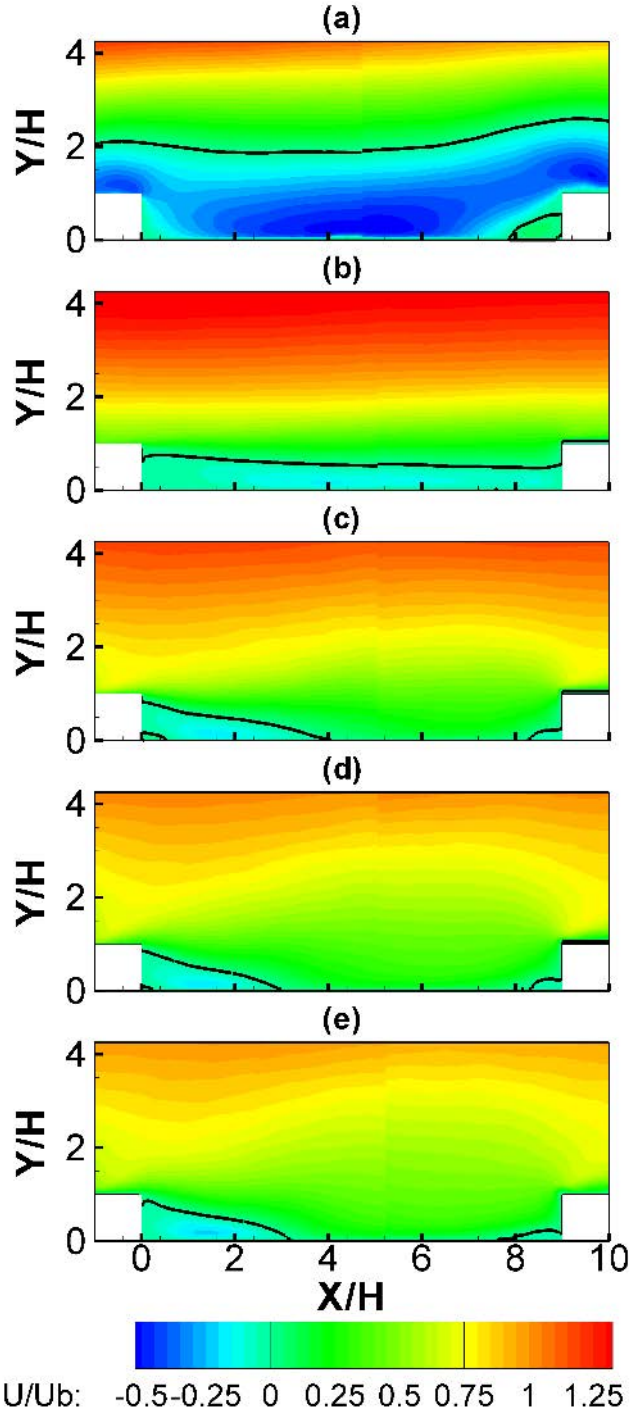

Figure 6.31 : Mean wall-normal velocity contours, Re = 15,000: Leading Side, Ro = 0.77, Bo = 0.77 (a); Leading Side, Ro = 0.77, Bo = 0 (b); Static, Ro = 0 (c); Trailing Side, Ro = 0.77, Bo = 0 (d); Trailing Side, Ro = 0.77, Bo = 0.77 (e)

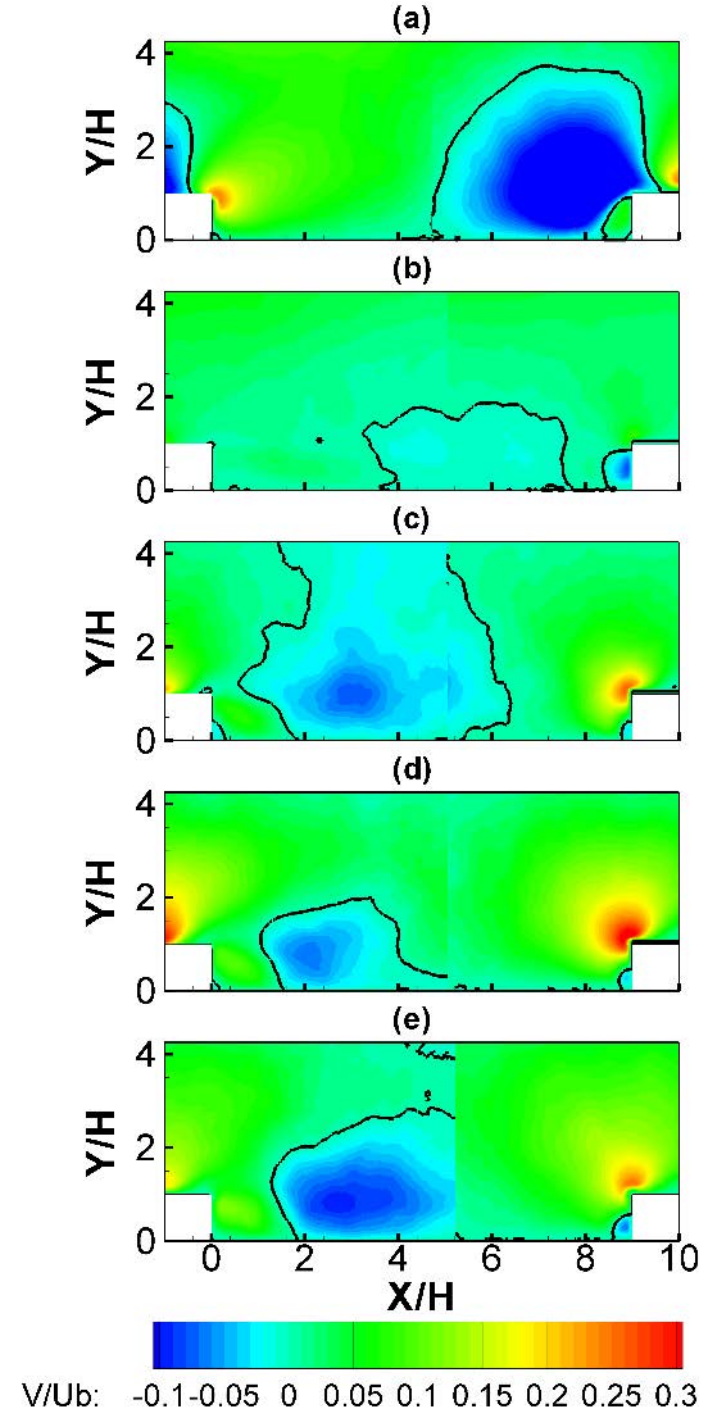

Figure 6.32 : Mean wall-normal velocity contours, Re = 15,000: Leading Side, Ro = 0.77, Bo = 0.77 (a); Leading Side, Ro = 0.77, Bo = 0 (b); Static, Ro = 0 (c); Trailing Side, Ro = 0.77, Bo = 0 (d); Trailing Side, Ro = 0.77, Bo = 0.77 (e)

in the isothermal case, reaching values similar to those found in static conditions in certain regions, i.e. near the saddle points. Note that although the turbulent velocity is relatively high in this case, it does not necessarily mean that the resulting wall heat flux is enhanced by buoyancy. It is indeed necessary to investigate simultaneously the velocity and temperature fields to fully characterize the flow stability and wall heat transfer under the effect of centripetal buoyancy.

On the Trailing Side under the effect of centripetal buoyancy, $Ro = Bo = 0.77$, the distribution of the stream-wise and wall-normal turbulent velocities (Figs. 6.33(e) - 6.34(e)) is akin to that in isothermal conditions (Figs. 6.33(d) - 6.34(d)), with slightly larger values, similarly to what was found by Coletti et al. [33] at $Ro = 0.38$ and $Bo = 0.31$. In particular, the increase of the stream-wise turbulent velocity is found in the shear layer generated by the rib and the in the region $4 < X/H < 8$ directly near the wall. Most likely, the temperature gradients are important in these regions, promoting the action of the centripetal buoyancy force. As a result, the centripetal buoyancy force tends to strain the velocity field, which leads to higher turbulence intensities. On the other hand, it can be observed that the wall-normal turbulent velocity distribution presents the same shape as that in isothermal conditions with a modest increase of the order of 0.03 - $0.05U_b$. In summary, the limited increase of the turbulent activity with respect to the isothermal case is not sufficient to alter significantly the mean flow field.

The energy spectrum at $(X/H, Y/H) = (1, 1)$ under the effects of buoyancy is compared with the one in the isothermal flow in Fig. 6.36. Despite the fact that the flow is totally different on the Leading Side at $Ro, Bo = 0.77$, the energy spectrum is very similar to that at $Bo = 0$. This is most likely due to the similar velocity fluctuations at $(X/H, Y/H) = (1, 1)$, as observed in the turbulence statistics. In the Trailing Side case, the spectrum under the effect of the centripetal buoyancy presents slightly larger energy levels, as expected from the turbulent kinetic energy shown in Fig.6.35. No dominant frequency has been found in any of the cases presented, which is likely related to the complexity of the flow and the interaction between the turbulent length scales.

6.2 Numerical results

Clearly, the previous experimental data provides useful information about the flow in rotating cooling channels. Nevertheless, the measured velocity field is limited to a reduced region in the symmetry plane of the channel. Therefore, it is indispensable to carry out measurements in planes away from this region in order to fully characterize the flow field in rotating conditions. However, this is highly complex with a two-component PIV system like the one employed here, since the fluid motion is highly three-dimensional. The preferred approach that is followed in this work is to validate LES in the same conditions, and to study the three-dimensional flow field in the regions where the PIV is not able to provide the information.

The sensitivity of the simulations with respect to the mesh resolution is studied by comparing the mean flow and heat transfer statistics for meshes with different degrees of refinement. The numerical data presented in the present thesis is based on the mean

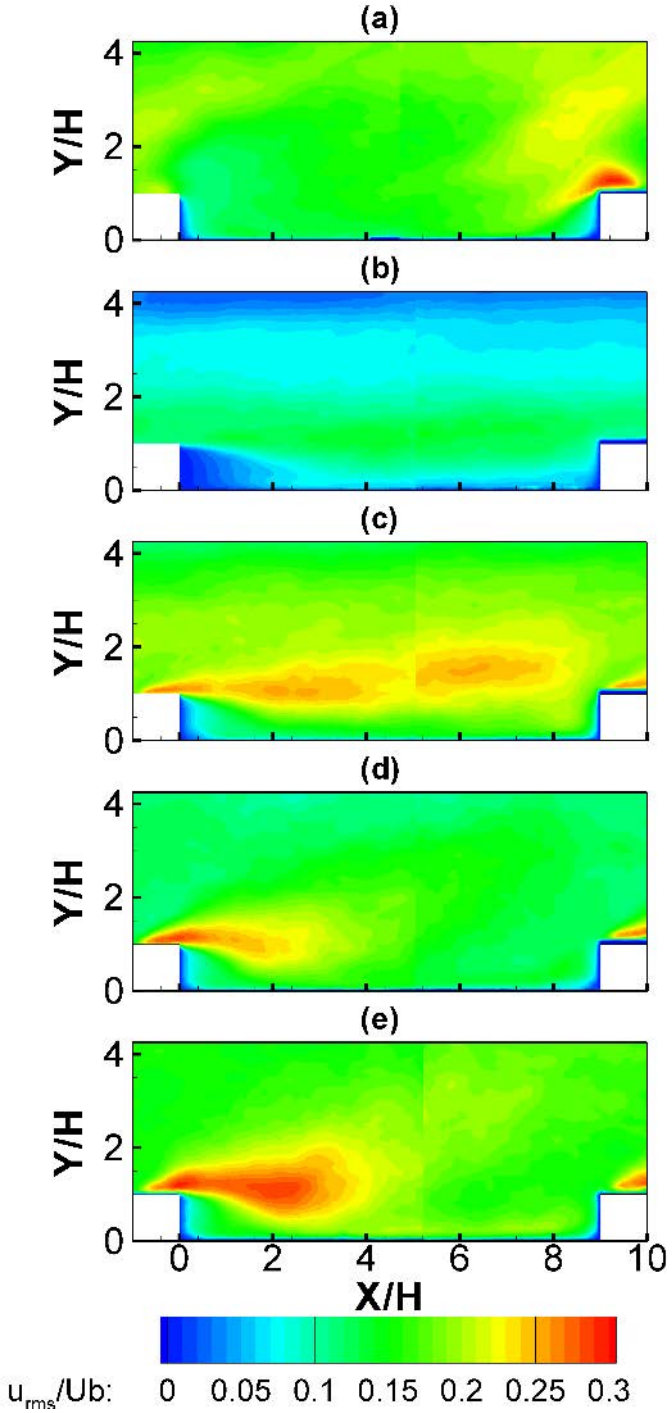

Figure 6.33 : Stream-wise turbulent velocity contours, Re = 15,000: Leading Side, Ro = 0.77, Bo = 0.77 (a); Leading Side, Ro = 0.77, Bo = 0 (b); Static, Ro = 0 (c); Trailing Side, Ro = 0.77, Bo = 0 (d); Trailing Side, Ro = 0.77, Bo = 0.77 (e)

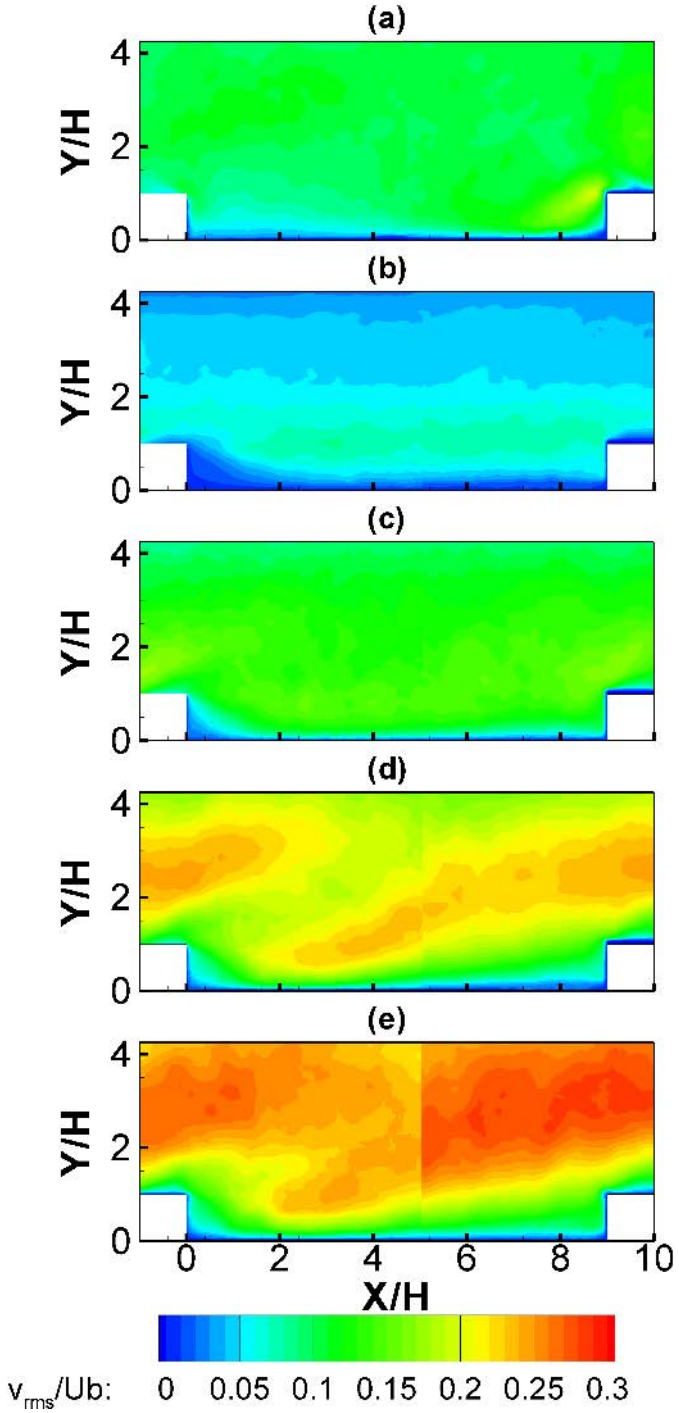

Figure 6.34 : Wall-normal turbulent velocity contours, Re = 15,000: Leading Side, Ro = 0.77, Bo = 0.77 (a); Leading Side, Ro = 0.77, Bo = 0 (b); Static, Ro = 0 (c); Trailing Side, Ro = 0.77, Bo = 0 (d); Trailing Side, Ro = 0.77, Bo = 0.77 (e)

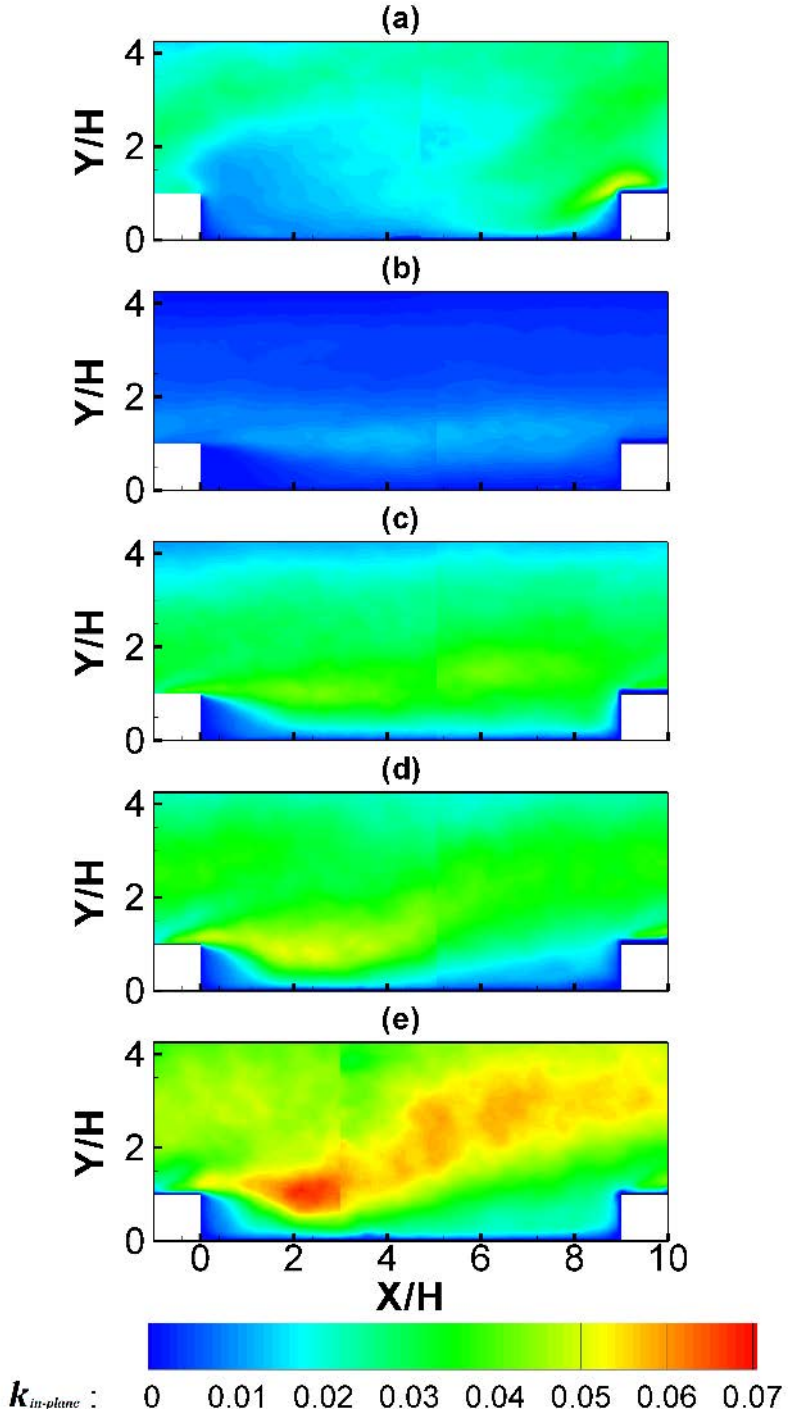

Figure 6.35 : In-plane turbulent kinetic energy contours, Re = 15,000: Leading Side, Ro = 0.77, Bo = 0.77 (a); Leading Side, Ro = 0.77, Bo = 0 (b); Static, Ro = 0 (c); Trailing Side, Ro = 0.77, Bo = 0 (d); Trailing Side, Ro = 0.77, Bo = 0.77 (e)

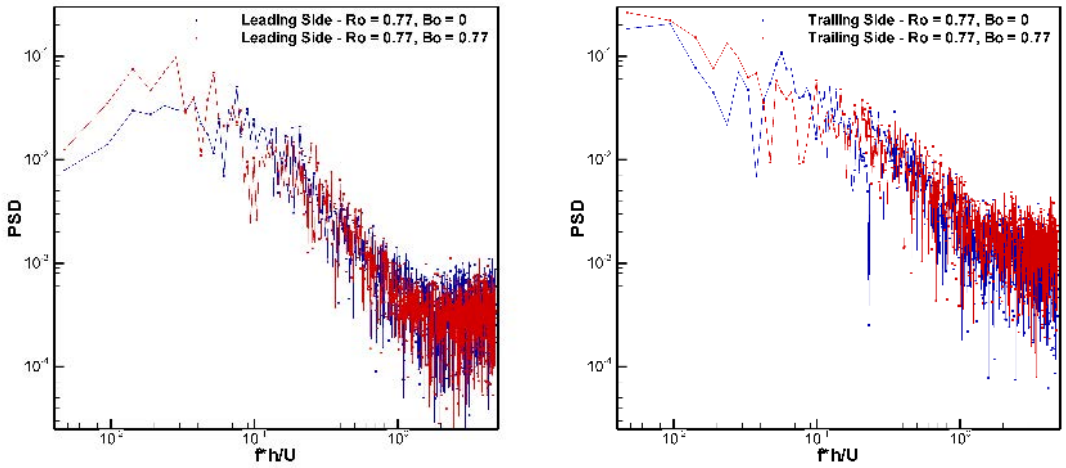

Figure 6.36 : Energy spectra under the buoyancy effects at $(X/H, Y/H) = (1, 1)$

statistics of the velocity and heat transfer field collected after the stabilization of the flow along a time period of more than 60 Flow-Through Times. Figure 6.37 displays the mean stream-wise velocity profiles in the symmetry plane and the mean Enhancement Factor in the line $(Y/H, Z/H) = (0, 0)$ in static conditions. For the sake of clarity, only the results provided by two different meshes are represented in Fig. 6.37. The first mesh (mesh A) has about 477,000 cells in total, whereas the second one (mesh B) is composed by 958,000 cells. The details of mesh B are reported in section 5.2. Additionally, both the PIV and LCT data are represented in order to assess the accuracy of the present numerical methodology at equivalent conditions. It is observed that the velocity profiles provided by the simulations are very close to each other, only minor differences are found in the shear layer region. It is likely that the separation bubble present on top of the rib is slightly larger than in the experiments, leading to a momentum deficit, which is reduced as the slow fluid is mixed in the shear layer with the core flow. The centerline Enhancement Factor for both simulations present a good agreement with the experimental data, with differences only near the ribs. Most probably, the thermal boundary condition imposed on the rib surface (adiabatic wall) is the factor that leads to the difference with respect to the experimental data. Nevertheless, the Enhancement Factor gets closer to the experimental data near the rib as the mesh is refined.

Next, the three-dimensional flow field is investigated by representing the dimensionless time-averaged λ_2 [106] iso-surface (λ_2=500) in static conditions in Fig. 6.38. To characterize the position of the different coherent structures, the represented λ_2 iso-surface is colored by the distance to the bottom wall. Firstly, it can be observed that the corner vortex upstream of the rib extends all over the channel span, with a uniform shape and parallel to the Z axis. According to the λ_2 criterion, the vortex on top of the rib is identified as well with a uniform strength in the Z direction. Downstream of the rib, a large λ_2 iso-surface describes the recirculation area. This iso-surface is not as uniform as

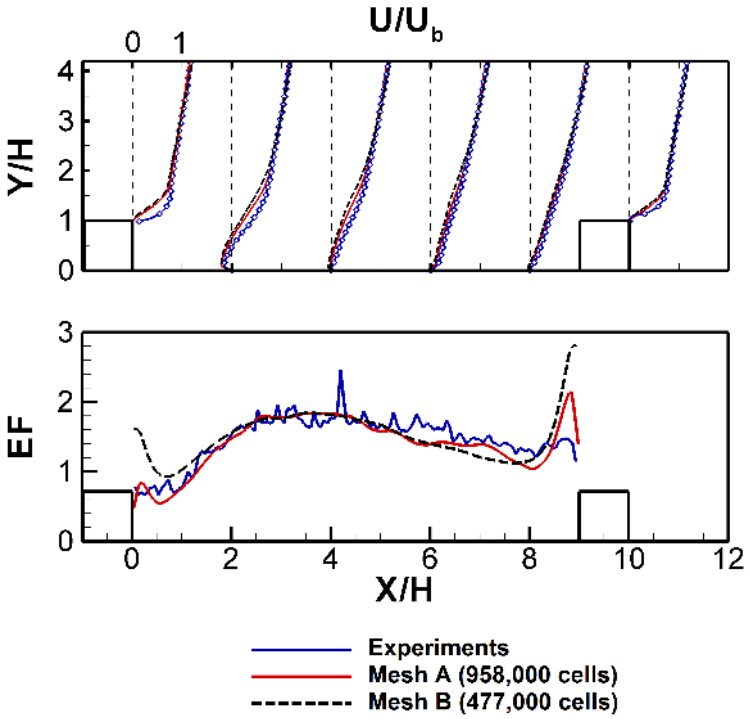

Figure 6.37 : Mean stream-wise velocity profiles (top) and centerline Enhancement Factor (bottom) obtained in static conditions (Re = 15,000, Ro = 0) during the experimental campaign and by means of LES in Mesh A and Mesh B.

the previous ones, due to the unsteadiness of the flow and the need for a larger data set to converge towards a uniform iso-surface in this region. Probably, the most interesting information that Fig. 6.38 provides is the origin of the rib-induced secondary flows. Similarly to the vortex generated on the bottom wall at the leading edge of the rib, the boundary layer in the region below $Y/H \sim 1$ is constrained by the rib, which generates a swirling motion about the Y axis in the corner between the rib and the lateral walls. Then, the vortex is convected towards the top of the rib, reaching a maximum height of about $2H$. It is observed that this structure losses its coherence downstream of the rib. Indeed, the flow in this region is highly turbulent, promoting the destruction of large-scale structures. Nevertheless, the strength of this vortex is such that it is able to induce a large vertical velocity near the lateral walls. The contours of the dimensionless vertical velocity, V/U_b, in the plane X/H = -0.5 have been represented also in Fig. 6.38. The iso-line $V = 0$ has been also represented to separate the areas of positive and negative vertical velocity. It is shown that the maximum vertical velocity is caused by the latter vortex in the region directly on top of the rib, near the lateral wall, reaching a value about 30% of the bulk velocity. The vertical velocity induced by this vortex is so high that positive V/U_b values are found near the top wall. The swirling motion generated by these vortices induces on the other hand a negative vertical velocity on top of the rib, in the region $|Z/H| \sim 3.5$. Due to this feature, the positive vertical velocity imposed by the presence of the rib in the region $|Z/H| < 3.5$ is interrupted by the rib-induced secondary flows.

Figure 6.39 represents the dimensionless temperature contour in the plane X/H = 3.33 and the in-plane mean streamlines, corresponding to the vertical and span-wise velocity components. The dimensionless temperature is defined here as

$$\Theta = \frac{T - T_c}{T_h - T_c} \tag{6.6}$$

where T_h is the temperature of the bottom wall (equal to 314 K) and T_c is the temperature of the top and lateral walls (equal to 293 K). In order to provide a clear picture of the flow and temperature fields, the results given in Fig. 6.39 are obtained by averaging the CFD data at each side of the symmetry plane ($Z/H = 0$). Figure 6.39 shows the presence of two large-scale counter-rotating swirling motions in the region above $Y/H \sim$ 6. The center of these counter-rotating swirling structures is located at about (Y/H, Z/H) $\simeq$ (7.2, $\pm$ 3). Despite the fact that these swirling motions can be though as the flow around the vortices generated in the corner between the rib and the lateral walls, the locations of the structures are somewhat distant, and therefore, they are not the same. However, the large swirling motions in the region $Y/H > 6$ are a consequence of the vortices generated in the corner between the rib and the lateral walls: the large vertical momentum generated by the rib lateral vortex reaches the top wall, then the fluid is directed in the central region of the channel towards the bottom wall. Since these motions would not exist without ribs, the terminology often used to refer to these secondary flow motions, 'rib-induced secondary flows', is totally valid. The time scales of these motions are also significantly different. Since the rib lateral vortex presents a

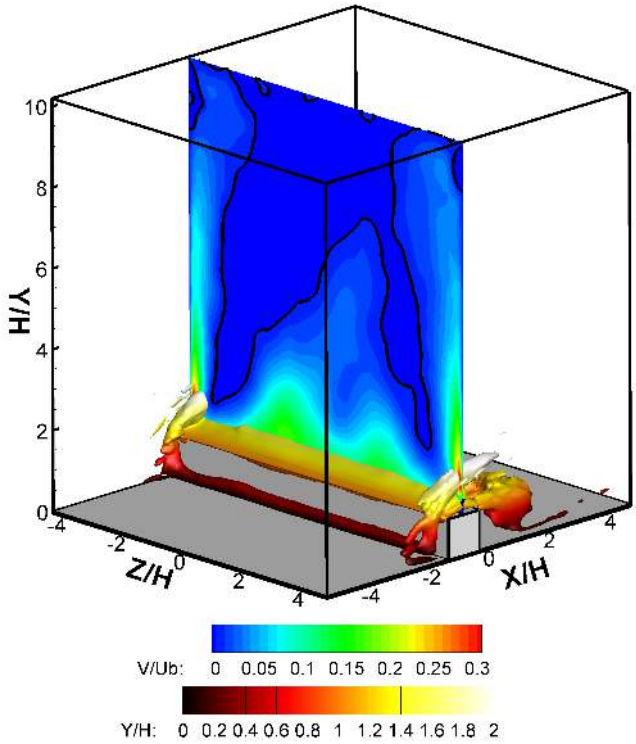

Figure 6.38 : Mean λ_2 iso-surface and vertical velocity contour in the plane X/H = -0.5, static case

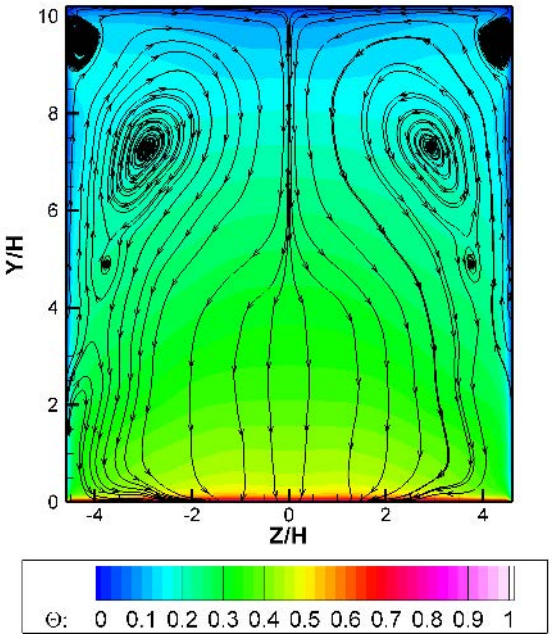

Figure 6.39 : Dimensionless temperature contour and in-plane streamline in the plane $X/H = 3.33$ in static conditions

characteristic velocity of about $0.3U_b$ and a length scale H, the time scale is of order $t \sim \pi H/(0.3U_b) \sim 3H/U_b$. With a convective velocity of order Ub, the fluid particles around the lateral vortex make a full turn in a length $l \sim \delta t \cdot U_b \sim 3H$. Here, the large top vortices present a characteristic length and velocity of order $3H$ and $0.02U_b$. Therefore, the time scale is about $150H/U_b$, that is, 50 times larger than in the lateral corner vortex. In this way, a fluid particle would complete a entire loop in a distance of the order of $150\times(H/U_b) \times U_b \sim 15D_H$.

The secondary flows induced by the ribs lead to a high temperature gradient on the bottom wall. In this way, the value $\partial\Theta/\partial(Y/H)$ on the bottom wall is much larger near the lateral walls than in the central region. Due to the imposed boundary conditions (314 K on the bottom wall and 293 K on the lateral walls), the temperature gradient in the bottom corners turns to be the highest in the cross section. As the distance to the bottom wall increases, the temperature gradients in the span-wise direction are reduced. Near the top wall, two additional stream-wise corner vortices appear, similarly to those observed by Lohász [107].

The corresponding heat transfer Enhancement Factor has been calculated similarly to the experiments. In the simulations, q_{conv} is calculated as

$$q_{conv} = k(T_w) \cdot \frac{\partial T}{\partial y} \tag{6.7}$$

where $k(T_w)$ is the air thermal conductivity at the wall temperature (T_w). Then the

heat transfer coefficient is simply determined as

$$h = \frac{q_{conv}}{T_w - T_c} \tag{6.8}$$

Note that in the latter expression, the temperature at the center of the cross section, T_c, varies depending on the rotating condition. However, the stream-wise variations of T_c in a given simulation are found to be negligible. Finally, the Nusselt number and Enhancement Factor have been calculated as

$$Nu = \frac{h \cdot D_H}{k_f} \tag{6.9}$$

$$EF = \frac{Nu}{Nu_0} \tag{6.10}$$

where k_f is the thermal conductivity at the film temperature, $T_{film} = \frac{1}{2}(T_w + T_c)$, and Nu_0 is the value of the reference Nusselt number [80]. Figure 6.40 compares the experimental and numerical Enhancement Factor Distributions. The agreement of the LES predictions with the experimental data is very positive both in terms of quantitative values and distribution. The footprints of the recirculation bubble downstream of the rib and the rib-induced secondary flows present the same shape and dimensions. After the reattachment point, $X/H \sim 4$, EF decreases due to the boundary layer development and is also well captured by LES. Only minor differences are found near the boundaries, likely due to the conditions imposed in the simulations. Concerning the high EF predicted just upstream of the rib, it is necessary to consider that the rib walls are considered adiabatic in the simulations. In the experimental test section, the ribs are made of acrylic glass, which presents relatively low conductivity. For this reason, the considered boundary condition has been approximated by a non-conductive (adiabatic) solid. However, the base of the rib is heated by the heating foil (see Fig. 3.15) and part of this heat is conducted by the rib and transferred to the fluid. Through this process, the fluid temperature around the rib is expected to be higher than in the simulations. In parallel, the vortex upstream of the rib pushes relatively cold fluid towards the corner in the simulations, leading to a higher EF than in the experiments. The combination of the velocity field and the heat transfer on the bottom wall obtained by means of LES is presented in Fig. 6.41. The mean stream-wise velocity contours have been represented in the planes $Z/H = 0$ and $X/H = 3.33$, together with the in-plane streamlines.

After the investigation of the static case, the simulations including the rotational effects are validated with the experimental data obtained in the present thesis at Ro = 0.3 - 0.8, and that provided by Coletti et al. [32] at $Ro = 0.30$. Figures 6.42, 6.43 compares the stream-wise mean and turbulent velocities in the symmetry plane, whereas Fig. 6.40 compares the Enhancement Factor along the centerline of the bottom wall at different rotational speeds. On the Trailing Side, the agreement is excellent both at moderate (Ro =0.30) and high rotation. The turbulence increase and the large shear near the wall is thoroughly captured by LES at $Ro = 0.30$. Additionally, the centerline

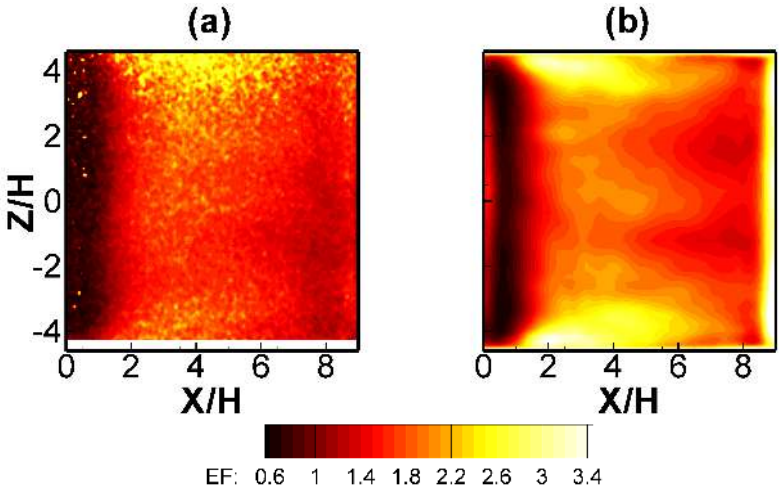

Figure 6.40 : Enhancement Factor contours in the static case ($Ro = 0$): experiments (a), LES (b)

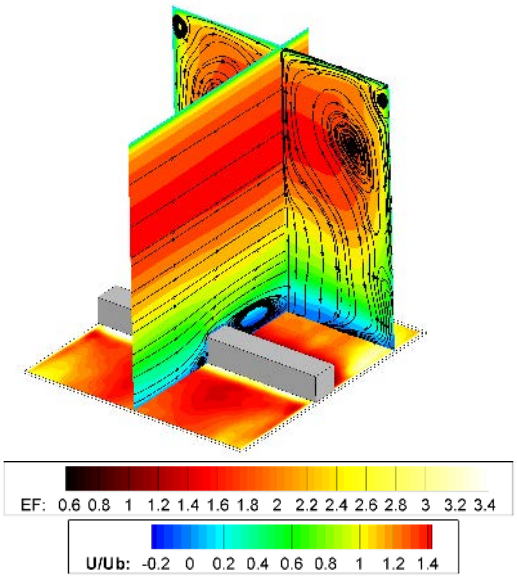

Figure 6.41 : 3D representation of the flow field and heat transfer provided by the LES in static conditions

EF provided by LES follows perfectly the EF observed in the experimental campaign, with a limited deviation just downstream of the rib ($0 < X/H < 1$) and a larger one in the region just upstream of the rib ($8 < X/H < 9$). The deviation just downstream of the rib is most likely due to the large temperature and the corresponding uncertainty. On the other hand, the deviation just upstream of the rib is probably due to the action of the upstream corner vortex similarly to the static case. In this way, low temperature fluid is introduced into the corner region, leading to high heat transfer. At $Ro = 0.77$, the increase of turbulence by rotation in the shear layer generated by the rib is also captured, as well as the turbulence reduction in the second half of the inter-rib area already commented in section 6.1.2. At $X/H = 0$ and 2, the area of high stream-wise turbulent velocity in LES is slightly larger than in the experiments. Therefore, small differences in the velocity and heat transfer distributions can be expected in this region. However, the Enhancement Factor obtained by LES presents once again an excellent agreement with the experimental data, including the high EF in the reattachment region, and the abrupt decrease after it due to the decrease of turbulent kinetic energy.

On the Leading Side at $Ro = 0.30$, the agreement of the stream-wise velocity profiles with the data is positive in the region Y/H <3 , especially if compared to the data by Coletti et al. [32]. The differences between LES results may be first due to the degree of development of the flow in the experimental test section. As can been seen in Fig. 6.42 at $Ro = 0.30$ on in the Leading Side case, the velocity profiles are closer at $X/H = 10$, that is, the flow is not fully established in the test section. Likewise, the turbulence levels obtained by LES are slightly lower than in the experiments. The momentum interchange between the near-wall fluid and the core flow is hence not as efficient as in the experimental case, which leads to a larger momentum deficit in the recirculation area. Since the bulk velocity is fixed by the Reynolds number (mass flow) and the momentum in the near-wall region is limited, the velocity in the core region is slightly larger. As a result, the Enhancement Factor given by LES is slightly lower than in the LCT experiments. Another cause of the velocity profile differences may be related to the mesh resolution near the top wall. Under these conditions, the flow near the top wall is destabilized, increasing the turbulence levels and the velocity gradients, hence requiring finer resolutions. Nonetheless, the distributions presents almost the same shape, with an extremely low EF just downstream of the rib, then a maximum EF around $X/H \sim 4$ and a slight and steady decrease towards the following obstacle. As in the previous cases, the EF is somewhat larger just upstream of the rib.

The situation is very similar in the Leading Side case at $Ro = 0.77$. The decrease of turbulence and momentum due to rotation is captured by LES, but the stream-wise mean and turbulent velocities present lower values than in the experimental campaign. Again, the reasons of this mismatch can be due to the degree of development of the flow in the test section, the lower turbulence intensity obtained in LES under these conditions and the eventual grid requirements near the top wall. Despite the differences in the velocity and turbulence profiles, the main physical mechanisms are simulated, driving to an EF distribution with very similar values as in the LCT experiments. The EF is extremely low just downstream of the rib, and increases monotonously towards

the following obstacle. In this case, the EF shows also slightly lower values than in the experiments.

The dimensionless temperature contours and in-plane streamlines obtained in the LES at $X/H = 3.33$ in the Leading Side case at $Ro = 0.30$ and 0.77 are represented in Fig. 6.45. In both cases, there is a large difference of secondary flows with respect to those in the static case. The most characteristic feature of the flow in this plane is the lack of rib-induced secondary flows and the presence of the Coriolis-induced secondary flows, which consist in the fluid motion from the top (Trailing Side) to the bottom wall (Leading Side) near the lateral walls and then the fluid is swept back towards the core of the flow. These structures are oriented in the stream-wise direction and span over a large space on the lateral walls. The downward motion of the fluid near the lateral walls pushes cold fluid from the top and lateral areas of the channel towards the bottom wall, generating a large temperature gradient $\partial T/\partial y$ in the bottom corner. Due to the low momentum and turbulence near the bottom wall with respect to those found in static conditions, the temperature gradients in the y direction are significantly lower than in the static case. In particular, it can be observed that the cold fluid can penetrate into the separated recirculation bubble downstream of the rib only near the lateral wall. In the central region of the channel, the hot fluid is moved from the bottom to the top, which leads to high temperature gradients in the span-wise direction. As the Rotation number is increased from 0.30 to 0.77, $\partial\Theta/\partial y$ presents slightly lower values over the bottom wall. However, the span-wise temperature gradients away from the recirculation bubble are significantly higher at $Ro = 0.77$. The secondary flows pattern is also significantly different from the static case. At $Ro = 0.30$ two counter-rotating swirling structures appear around $(Y/H,\ Z/H) = (8.5,\ \pm 1.5)$, whereas four counter-rotating structures appear at $(Y/H,\ Z/H) = (9,\ \pm 1)$ and $(Y/H,\ Z/H) = (9.5,\ \pm 3)$. It is believed that these structures are Taylor-Görtler vortices, similarly to what was found by Johnston et al. [21] and Kristoffersen and Andersson [20] near the unstable wall in high aspect ratio rotating channels. Due to the low aspect ratio of the present channel, the amount of Taylor-Görtler vortices covering the unstable wall is additionally influenced by the Coriolis-induced secondary flows (not existing in Refs. [21] and [20]). Due to the relative strength of the instability leading to the Taylor-Görtler vortices with respect to the Coriolis-induced secondary flows, the number of cells near the unstable wall is increased from two at $Ro = 0.30$ to four at $Ro = 0.77$.

The resulting Enhancement Factor distribution at $Ro = 0.30$ and 0.77 on the bottom wall is shown in Fig. 6.46 and compared with the experimental data. As already shown in Fig. 6.44, the EF provided by LES is slightly lower than in the test section. However, the main heat transfer mechanism is well simulated. As the Rotation number increases, the size of the recirculation bubble downstream of the rib increases. As a result, the region of low EF is extended to a larger surface behind the rib. At $Ro = 0.30$, the footprint of the Coriolis-induced secondary flows is evident in the region near the lateral wall, presenting a slightly larger EF. The maximum EF is found in the corner between the leading face of the rib and the lateral walls. In this region, the Coriolis-induced secondary flows and the vortex upstream of the rib combine their strength to direct cold

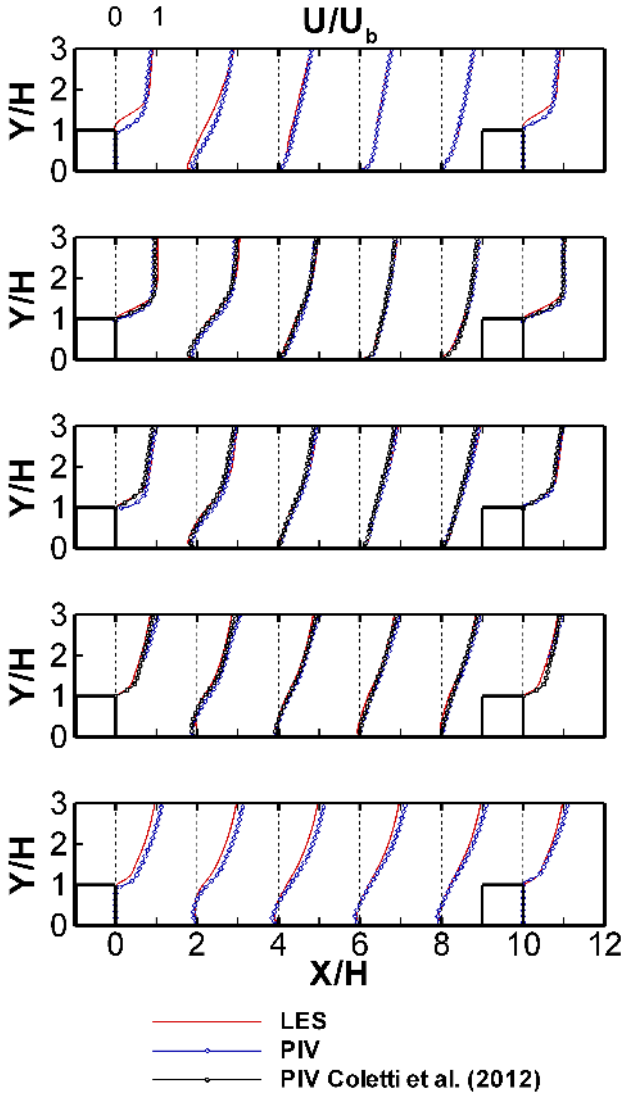

Figure 6.42 : Mean stream-wise velocity profiles, from top to bottom: Trailing Side - Ro = 0.77, Trailing Side - Ro = 0.30, static case, Leading Side - Ro = 0.30 and Leading Side - Ro = 0.77

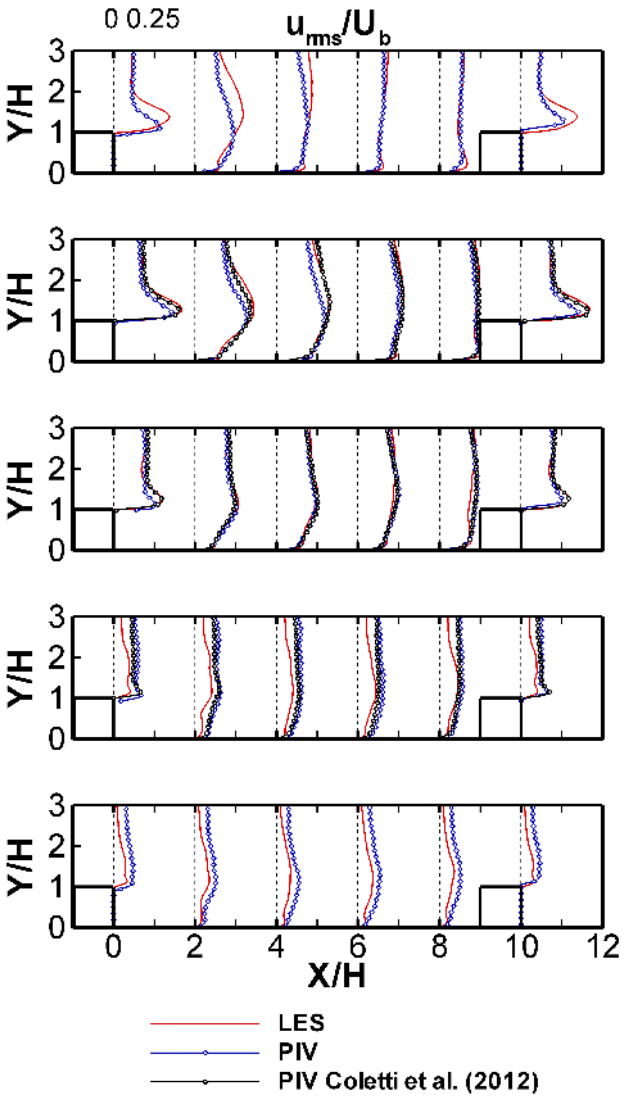

Figure 6.43 : Stream-wise turbulent velocity profiles, from top to bottom: Trailing Side - $Ro = 0.77$, Trailing Side - $Ro = 0.30$, static case, Leading Side - $Ro = 0.30$ and Leading Side - $Ro = 0.77$

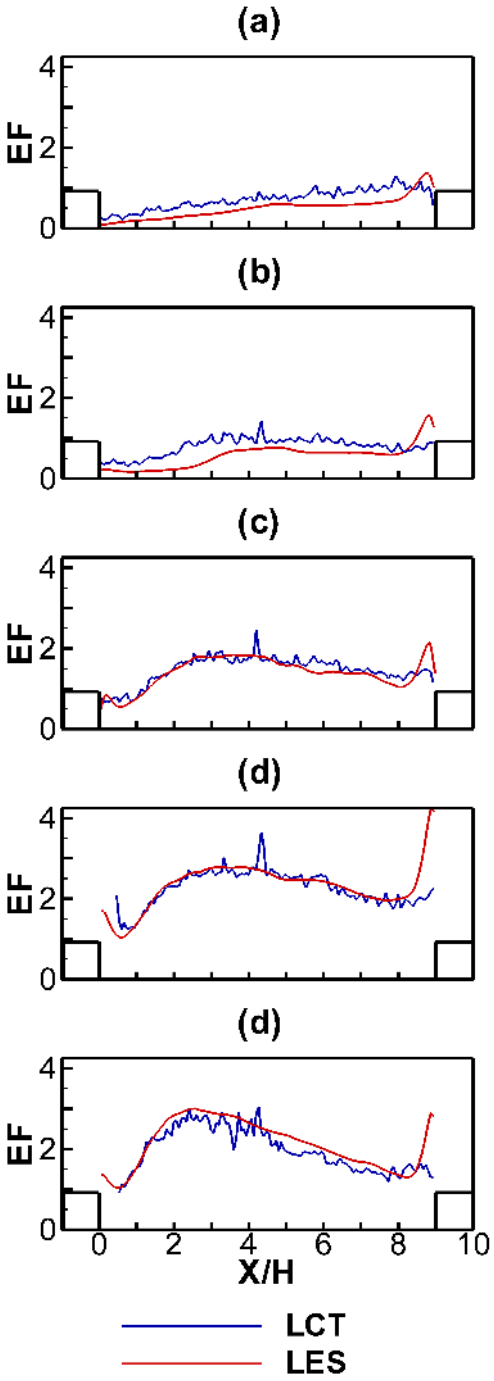

Figure 6.44 : Centerline Enhancement Factor: Leading Side - $Ro \simeq 0.8$ (a), Leading Side - $Ro \simeq 0.3$ (b), static (c), Trailing Side - $Ro \simeq 0.3$ (d), Trailing Side - $Ro \simeq 0.8$ (d)

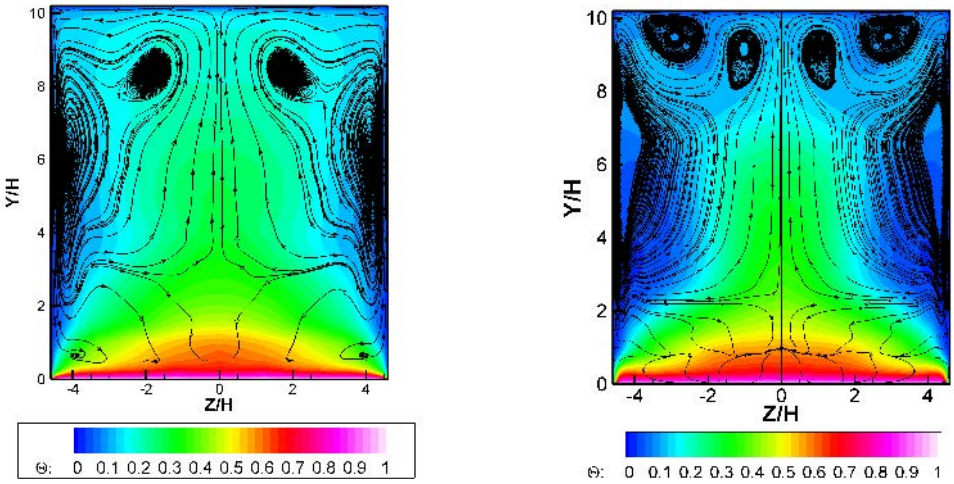

Figure 6.45 : Dimensionless temperature contours and in-plane streamlines in the plane $X/H = 3.33$, Leading Side case (clockwise rotation): $Ro = 0.30$ (left), $Ro = 0.77$ (right)

fluid towards the wall, resulting in a high heat transfer. Since the boundary conditions set in the numerical investigation provide most likely lower temperatures than in the experiments, the Enhancement Factor near the boundaries is slightly larger than in the experiments. The representations of the flow field and heat transfer at $Ro = 0.30$ and 0.77 under clockwise rotation given by the LES are shown in Fig. 6.47.

The secondary flows pattern and dimensionless temperature distribution at $X/H = 3.33$ in the case of counter-clockwise rotation at $Ro = 0.30$ and 0.77 are shown in Fig. 6.48. Similarly to the case under clockwise rotation, the Coriolis force alters the secondary flow pattern in the channel. Under counter-clockwise rotation, the Coriolis-induced secondary flows move the fluid from the bottom wall (Trailing Side) towards the top wall (Leading Side) in the region near the lateral walls. In this way, the rib-induced and Coriolis-induced secondary flows are combined to increase the vertical velocity near the lateral walls. At $Ro = 0.30$, the fluid that reaches the top wall, is directed back towards the bottom wall, mainly to the bottom corners. As a result of the secondary flows and the increase of the turbulence near the bottom wall, the temperature gradients in the vertical direction, $\partial\Theta/\partial y$, are significantly larger than in the previous cases near the bottom wall. For the same reason, the temperature gradients in the span-wise direction, $\partial\Theta/\partial z$, are lower than in the case of clockwise rotation.

At $Ro = 0.77$, the secondary flow pattern is different from the previous case. Despite the fact that the Coriolis force pushes the flow from the bottom wall towards the top region to go back to the bottom wall, two additional counter-rotating structures appear in the central region of the channel. The lateral secondary flows are pushed towards the side walls, resulting in a flat structure elongated in the y direction. The central secondary flows tend to sweep the fluid away from the bottom wall in the area near the symmetry plane, resulting in a slightly positive wall-normal velocity. Then, the fluid

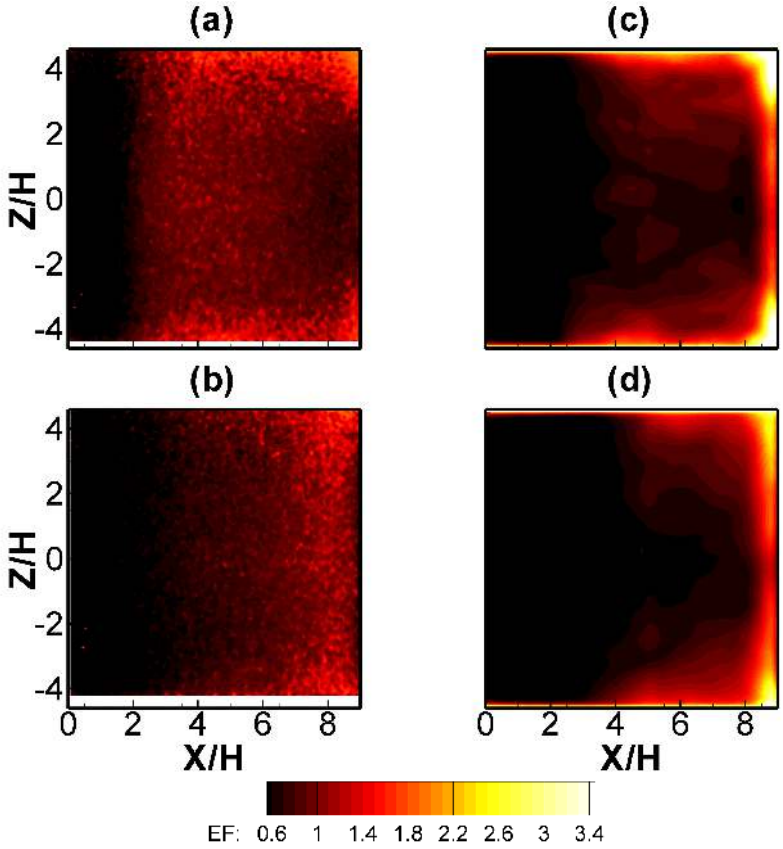

Figure 6.46 : Enhancement Factor contours in the Leading Side case: Experiments - Ro = 0.29 (a), Experiments - Ro = 0.82 (b), LES - Ro = 0.30 (c), LES - Ro = 0.77 (d)

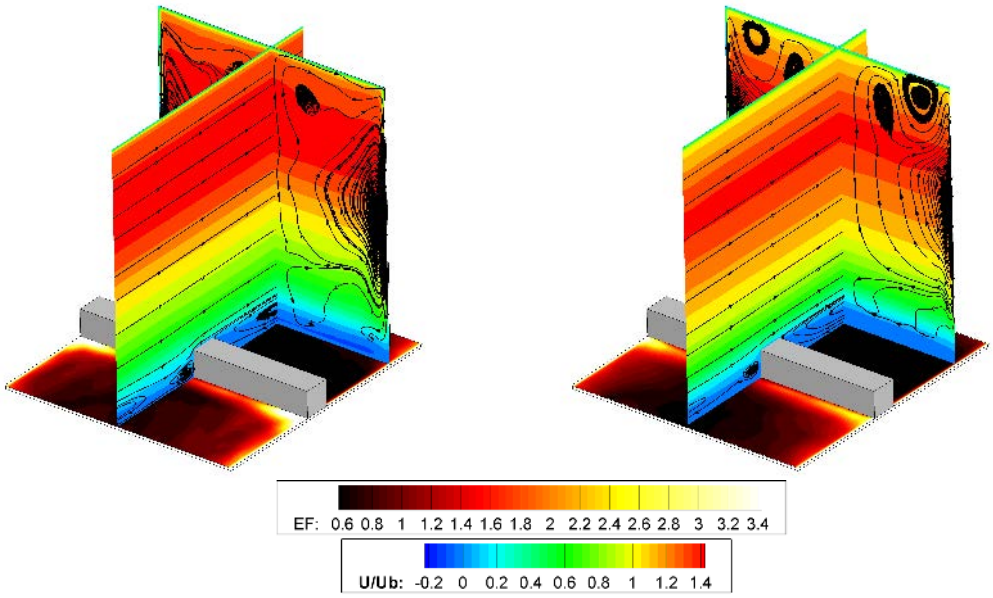

Figure 6.47 : 3D representation of the flow field and heat transfer provided by the LES under clockwise rotation: $Ro = 0.30$ (left), $Ro = 0.77$ (right)

returns back to the bottom wall in an area around $Z/H \sim 3$. As at $Ro = 0.30$, $\partial\Theta/\partial y$ is higher than in static case due to the larger turbulence levels and the action the secondary flows. In this plane, the vertical temperature gradients are similar at $Ro = 0.30$ and 0.77, which explains the low difference of EF in the first half of the inter-rib area.

The corresponding EF distributions at $Ro = 0.30$ and 0.77 are displayed in Fig. 6.49 and compared with the experimental data. In both cases, the agreement of the numerical data with the experiments is excellent. Firstly, the increase of the heat transfer with respect to the static case is evident in both cases due to the increase of the turbulence intensity and the secondary flows. At $Ro = 0.30$, the reduction of the recirculation bubble size leads to the reduction of the area with low EF. The footprint of the secondary flows also appears next to the lateral walls, with slightly higher EF values. The EF reduction as the flow develops downstream of the reattachment of the shear layer generated by the rib is also correctly predicted by LES. At $Ro = 0.77$, the small reduction of the recirculation bubble is also captured by LES. In this way, the area of maximum EF is moved slightly upstream. Due to the secondary flows system observed in LES, the points of maximum EF are displaced slightly towards the center of the channel. Additionally, an area of low EF is found between $X/H = 1$ and 5 in the region of the symmetry plane. This region would correspond to the are where the secondary flows tend to sweep the fluid away from the wall, leading to a reduction of the heat transfer. Downstream of $X/H \simeq 5$ the drastic EF reduction due to the turbulent kinetic energy decay is also correctly simulated by LES. As in the static and clockwise-rotating cases, higher EF's are found near the ribs and the lateral walls, likely due to the selection of the boundary

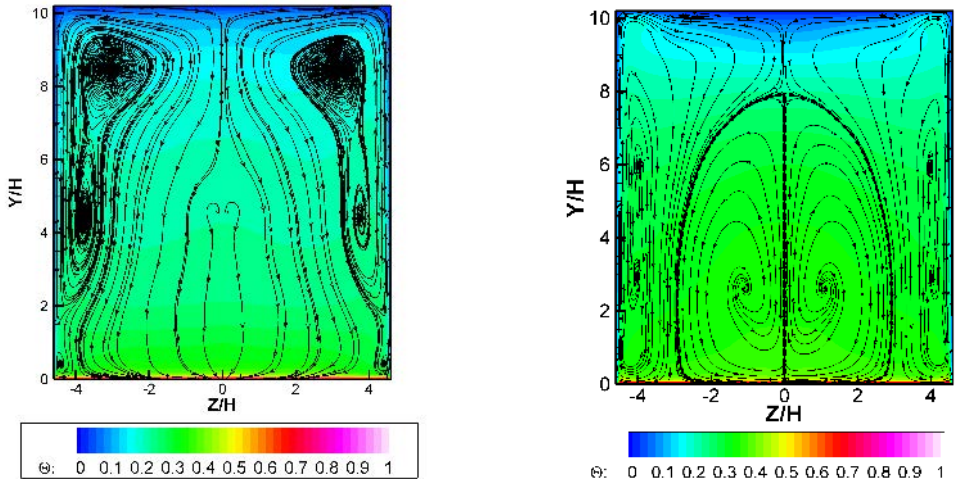

Figure 6.48 : Dimensionless temperature contours and in-plane streamlines in the plane $X/H = 3.33$, Trailing Side case (counter-clockwise rotation): $Ro = 0.30$ (left), $Ro = 0.77$ (right)

conditions. The resulting velocity field and Enhancement Factor map are represented together in Fig. 6.50 for the counter-clockwise rotation case.

The surface-averaged EF on the bottom wall has been represented against the experimental results and the data present in the literature in Fig. 6.51. In the figure, positive Ro corresponds to counter-clockwise rotation, and negative Ro to clockwise rotation. The agreement of the present numerical data is very positive, presenting only minor differences due to the local variations of EF near the domain boundaries.

On the other hand, the overall performance of the channel in terms of pressure drop is evaluated by calculating the friction factor at each rotating condition. The friction factor, f, is defined in this work as

$$f = \frac{\Delta\tilde{p}_{eff} D_H}{2 \cdot \rho \cdot P \cdot U_b^2} \tag{6.11}$$

where $\tilde{p}_{eff} = \tilde{p} - \beta x - \frac{1}{2}\rho\Omega^2 r^2$ is the effective pressure, as designated by Johnston et al. [21], and Δp_{eff} the effective pressure difference between the inlet and outlet of the domain. The friction factor is normalized with respect to the friction factor of a smooth pipe at large Reynolds numbers ($Re \gtrsim 20{,}000$) as given by Incropera et al. [108]:

$$f_0 = 0.046 \cdot Re^{-0.2}. \tag{6.12}$$

The friction factor enhancement, f/f_0 is displayed in Fig. 6.52 as a function of the Rotation number. Since the value of f/f_0 is unsteady, its standard deviation within the simulation time has been also included at each Ro in order to assess the overall unsteadiness of the flow. At $Ro = 0.30$ in the counter-clockwise sense, the f/f_0 and

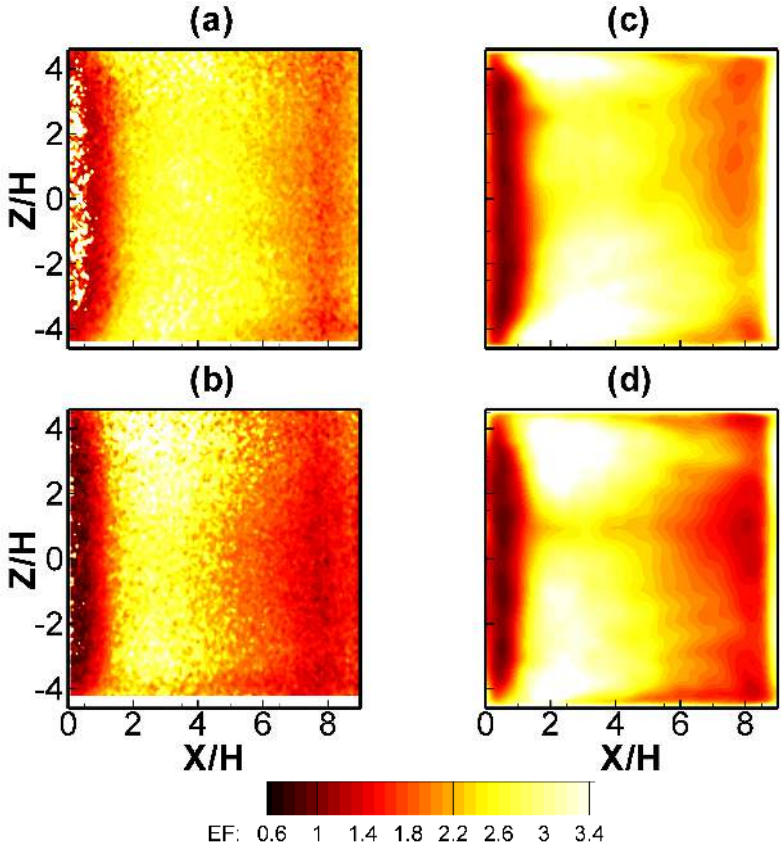

Figure 6.49 : Enhancement Factor contours in the Trailing Side case: Experiments - Ro = 0.29 (a), Experiments - Ro = 0.83 (b), LES - Ro = 0.30 (c), LES - Ro = 0.77 (d)

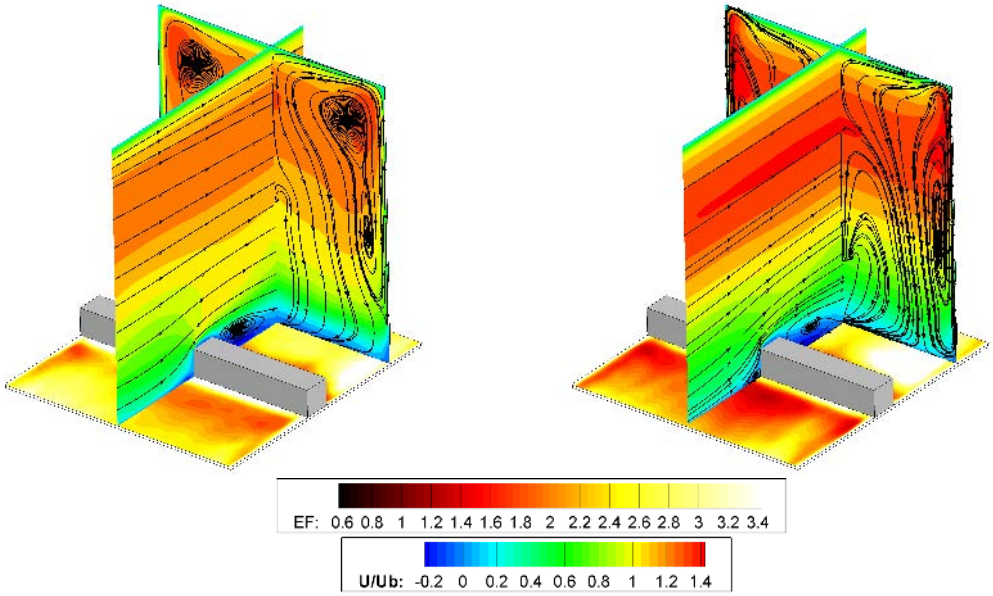

Figure 6.50 : 3D representation of the flow field and heat transfer provided by the LES under counter-clockwise rotation: $Ro = 0.30$ (left), $Ro = 0.77$ (right)

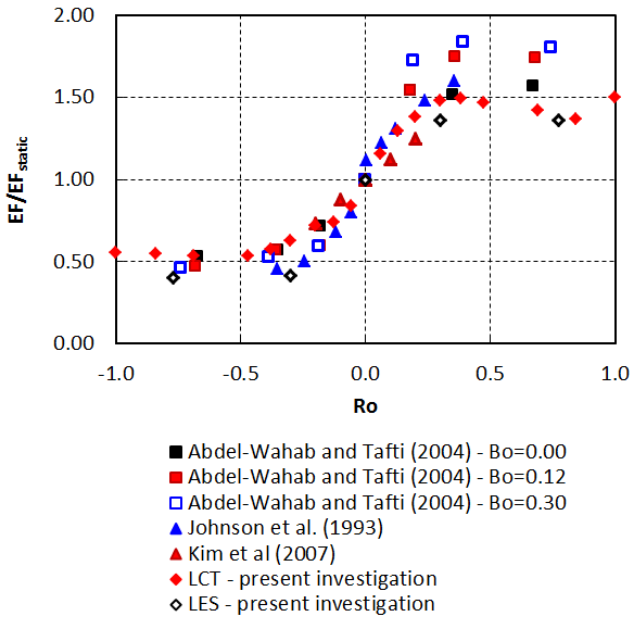

Figure 6.51 : Normalized EF on the bottom wall as a function of the Rotation number

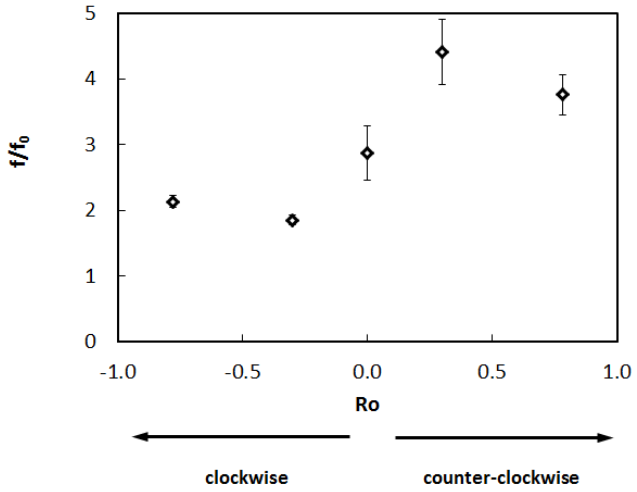

Figure 6.52 : Normalized mean friction factor as a function of the Rotation number

its fluctuations increase with respect to those in static conditions due to the general increase of turbulence near the bottom wall. As a result of the flow re-stabilization in the second half of the inter-rib area at $Ro = 0.77$ in the counter-clockwise sense, f/f_0 is slightly lower than that at $Ro = 0.30$, but still larger than in static conditions. On the other hand, f/f_0 is significantly reduced when rotation takes place in the clockwise case. At $Ro = 0.77$, the friction factor enhancement is slightly larger than at Ro =0.30. Due to the turbulence reduction, the fluctuations of the friction factor enhancement are suppressed in the case of clockwise rotation.

Chapter 7

Concluding remarks

7.1 Conclusions

The present work has introduced an advanced experimental setup that allows reliable and accurate measurements of the velocity and heat transfer in rotating cooling channels. The RC-1 facility at the VKI has been modified in order to achieve a large operational range, based on the Reynolds, Rotation and Buoyancy numbers in the investigated geometry. The unique characteristics of the present setup are:

- the possibility of investigating Reynolds number up to 55,000, Rotation numbers up to 1.0 and Buoyancy numbers up to 0.8;
- versatile design: different geometries can be easily adapted and tested in the facility;
- combination of velocity and heat transfer measurements along different planes in the test section;
- the measurements are performed in the rotating frame of reference, hence providing the same accuracy and resolution as in a stationary facility,

The geometry selected for this investigation consisted in a low aspect ratio channel with ribs on one wall, and placed perpendicularly to the main flow direction to simulate the aero-thermodynamics in the internal cooling channels of turbine blades. Despite the fact that the geometry does not replicate the exact shape of a modern internal cooling channel it reproduces the main flow physics that govern the aero-thermal performance of the component. At the same time, the geometry allows the comparison of a part of the experimental data with results present in the open literature, as well as the fine tuning of the experimental techniques.

A large effort has been made to determine the main measurement error sources and estimate the corresponding uncertainty. The main error source in the dimensionless velocity measurement is caused by the uncertainty of the bulk velocity, U_b. The overall

impact of the uncertainty in the bulk velocity can lead to a relative error of about 1 - 1.6% (in terms of the bulk velocity) at a confidence level of 95%, even reaching levels of about 2.7% in the regions where the velocity is maximum. This error is due to the uncertainty in the discharge coefficient of the Venturi nozzle employed to measure the mass flow and to the corresponding pressure drop in the nozzle. On the other hand, the error due to the PIV particle displacement gradient is the dominant error source in regions where the velocity gradients are large, such as the flow near the ribbed walls, reaching maximum levels of about 3.6% of the bulk velocity. Due to the dependency of the measurement error with respect to the Field of View, two different experimental campaigns were carried out. The first experimental campaign consisted in experiments with a reduced field of view, obtaining the velocity field up to about 2.4 times the rib height from the top wall, which led to measurements with an overall error of about 1.2% of the bulk velocity. The second experimental campaign provided the velocity distribution in a larger area, reaching wall distances about 4.2 times the rib height. In this case, the overall error was about 1.8% of the bulk velocity.

In parallel, a detailed uncertainty analysis of the temperature and heat transfer measurements has been carried out. The largest error source in the wall temperature measurement by the TCLs is related to the intensity resolution of the camera (8 bits) and the high TLC color sensitivity at high temperatures, and presents a maximum contribution of 0.70 K to the maximum temperature uncertainty at a 95% C.L.. The other error sources present a contribution of less than 0.1 K, which results in an overall temperature uncertainty equal to 0.45 K and a maximum temperature uncertainty equal to 0.82 K at a 95% Confidence Level (C.L.). Since the TLC activation temperature is about 308 K and the minimum temperature measurement uncertainty is found in the range 308 - 318 K, the wall heating was controlled to keep the TLC temperature at about 311 K. In this range, the temperature measurement uncertainty is approximately 0.35 K (95% C.L.). When dealing with heat transfer measurements, the overall contribution of the wall temperature measurement on the normalized heat transfer coefficient is 3 - 4%, presenting values as high as 13% in regions where the temperature difference between the wall and the core flow is minimum. Another important error source in the heat transfer measurement is the uncertainty of the TLC emissivity, which contributes to the radiative heat loss. With an uncertainty on ε_{TLC} equal to 0.05, the corresponding EF measurement error reaches values about 1.5 - 3.1% of the mean EF. Adding the contribution of the secondary error sources, the overall measurement uncertainty on the EF is about 5 - 6% of the measured value, reaching values as high as 14% when the temperature difference between the wall and the fluid is low. As the Reynolds number increases, the convective heat flux increases, whereas the conductive and radiative heat losses barely change. As a result, the contributions of the heat losses to the heat transfer balance and to the measurement error are reduced.

The heat transfer data in the present test section at $Ro = 0$ have been compared with the measurements of Ekkad and Han [104], showing similar values. In the present case, the heat transfer Enhancement Factor does not show a large dependency on the Reynolds number. Equivalently, this means that the Reynolds number effect on the

dimensionless heat transfer coefficient follows the Dittus-Boelter correlation. Under rotating conditions, the heat transfer data was averaged in the investigated surface and compared with the results given by Johnson et al. [25], Kim et al. [105] and Abdel-Wahab and Tafti [36], showing an excellent agreement even though the geometries and boundary conditions were not exactly the same. Concerning the velocity measurements, additional comparisons were done with the PIV data provided by Coletti et al. [32] at Re = 15,000. The agreement of the dimensionless mean and turbulent velocities was excellent not only in static conditions, but also at Ro = 0.30. These experiments also confirmed that the determining parameters in an isothermal rotating flow are the Reynolds and Rotation numbers, even if the centrifugal force is completely different.

The experiments have allowed comparing the flow physics that takes place when the channel is rotated in clockwise and counter-clockwise directions, at moderate and high rotational speeds. When the channel is rotated in the clockwise sense, the ribbed wall acts as Leading Side. At Re = 15,000 and moderate rotation (Ro = 0.30-0.38), the Coriolis force induces the stabilization of the flow near the ribbed wall, which reduces the turbulence intensity and increases the size of the recirculation bubble downstream of the rib with respect to that in static conditions, covering the entire inter-rib area. As a result, the heat transfer is reduced by about 40% with respect to the overall EF at Re = 0. Moreover, the footprint of the Coriolis-induced secondary flows is observed near the lateral walls, since high EF values are found in this region. At large Rotation numbers (that is, $Ro > 0.38$) the heat transfer level on the Leading Side is stabilized at a level almost 50% lower than in static conditions. The PIV measurements reveal a minor turbulence reduction with respect to the case at Ro = 0.38, but the recirculation bubble size increases. On the other hand, the velocity profile in the core of the flow tends to be tilted due to rotation, which leads to a higher momentum near the Leading Side and lower near the Trailing Side. By this process, the velocity above the recirculation bubble increases as Ro increases. Despite the corresponding velocity gradient increases and hence higher turbulence levels can be expected, the larger Coriolis force tends to stabilize the flow. This leaves the turbulence field near the Leading Side almost unchanged.

When the channel rotates counter-clockwise, the flow at Ro = 0.30 - 0.38 and Re = 15,000 is destabilized by rotation. As a result, the turbulence increases, reducing the length of the recirculation bubble behind the rib and increasing the heat transfer. The overall heat transfer at Ro = 0.30 - 0.38 is almost 50% larger than in static conditions. If the Rotation number is further increased to 0.77, no change in the overall EF is observed. The Coriolis-induced secondary flows contribute to increasing the heat transfer, whereas the momentum deficit near the Trailing Side due rotation tends to reduce the heat transfer. In the plane investigated experimentally, it is observed that the velocity shear $\partial U/\partial y$ is drastically reduced at Ro = 0.77, leading to low turbulence production and therefore lower heat transfer. As a result, the Coriolis-induced secondary flows and turbulence reduction at Ro = 0.77 are balanced to provide a stable mean EF as the Rotation number is further varied. The two-dimensional EF distribution suggests a new pattern of the rotation-induced secondary flows near the Trailing Side at high rotation. Indeed, two vortices appear in the central region of the channel, between the Coriolis-

induced secondary flows (confined to the lateral regions). Consequently, the location of the maximum EF values - which correspond to the areas where the secondary flows push the fluid towards the wall - varies as the Rotation number increases.

For these specific cases, the effect of the Reynolds number on the dimensionless heat transfer has been investigated at different Rotation numbers. It has been observed that the sensitivity of the Enhancement Factor with respect to Ro decreases as Re increases. On the Leading Side cases, the flow pattern results to be similar, resulting in a low EF due to the stabilization of the flow and the increase of the recirculation bubble size, and slightly higher EF near the lateral walls due to the Coriolis-induced secondary flows. However, the impact of the secondary flows pattern on the EF distribution is different as the Reynolds number varies. In particular, it is observed that the Rotation number from which the monotonous EF increase stops occurs at different Reynolds numbers.

The effect of the centripetal buoyancy forces has been studied by heating the ribbed wall at a temperature of about 85 - 95°C (358 - 368 K). On the Trailing Side case, no major changes in the mean velocity and turbulence fields are found. However, the flow on the Leading Side is massively affected since a large region of reverse flow is present on the Leading Wall. Considering that the Reynolds number is fixed and that a large region shows a negative velocity, large velocities appear above the reverse flow region, leading to a large velocity shear. Furthermore, the flow near the wall is anti-cyclonic, inducing a turbulence level much larger than in the isothermal case.

The present work also introduces a solid methodology to perform high-fidelity CFD simulations of internal cooling channels. It has been demonstrated that the present numerical method is a powerful tool to support and complement the experimental observations. Since the experimental data is only available in a limited region of the symmetry plane and the ribbed wall, the numerical results are helpful in providing the three-dimensional view of the flow in the investigated volume. The turbulence modeling employed in this investigation shows that both the velocity and heat transfer can be correctly predicted by LES in rotating ribbed channels, with minor localized differences with respect to the experimental data. In particular, the rotation-induced secondary flows have been characterized at the different rotating conditions, and their impact on the wall heat transfer has been evaluated. When rotation takes place in the clockwise sense, the Coriolis-induced secondary flows are confined to a region near the lateral walls, moving fluid from the top (Trailing Side) to the bottom wall (Leading Side), and increasing the EF on the lateral region of the bottom wall. Due to the strength of these secondary flows and the increase of the recirculation bubble upstream of the obstacle, no rib-induced secondary flows arise. Also, Taylor-Görtler vortices have been identified near the top wall, due to the destabilization of the boundary layer. Under counter-clockwise rotation, the Coriolis secondary flows move fluid from the bottom to the top wall, merging with the rib-induced secondary flows. As the rotation number increases, two additional stream-wise vortices appear near the bottom wall in the central region of the flow, likely due to the Taylor-Görtler instability near the Trailing Side.

7.2 Future work

The present investigation has focused on the flow physics in a simplified model of internal cooling channel, which has allowed to study the main flow physics governing the the performance of the cooling system. The next natural step in the investigation of the aero-thermal performance of rotating internal cooling channels is to provide the detailed flow field and heat transfer in a geometry closer to those in contemporary cooling schemes present in turbine blades. Due to the versatile design of the experimental setup, different geometries can be easily fitted in the facility, and the velocity field and heat transfer can be provided as in the present work. Channels with different aspect ratio, cross section, number of ribbed walls, rib shape, etc. can be studied in the RC-1 facility for a wide Reynolds and Rotation number ranges. Currently, the test section has been modified to study the rotational effects in the flow of a two-pass cooling channel.

The experimental setup can be further upgraded to allow Stereoscopic PIV measurements. This kind of experiments would provide the three components of the velocity vector in a plane, also reducing the measurement error when the velocity component normal to the plane is important. This solution is particularly interesting when investigating the flow in a U-bend, where a large separation bubble and secondary flows are produced. The combination of the rotational effects and the flow in a U-bend provides a complex velocity field, for which the use of Stereoscopic PIV seems an essential tool to perform accurate measurements.

A major step forward would be the design of an experimental facility that does not only match the Reynolds and Rotation numbers with the ones in turbine cooling channels, but also the correct Buoyancy number distribution. In the present facility, the distance of the channel inlet to the axis of rotation is close to zero, whereas in a real gas turbine, this distance is much larger. This makes the Buoyancy number distribution along the channel different in both cases. To overcome this issue there are two possible solutions. The first one is to consider the similarity on the distance to the axis of rotation and on the temperature gradients. The second is to apply a non-uniform wall temperature, so that the variation of the radial position is balanced by the temperature difference between the wall and the fluid, leading to the desired Buoyancy number distribution.

In parallel, the computational setup has demonstrated to be highly reliable. Nevertheless, different boundary conditions need to be addressed to mimic the behavior of modern turbine blades. In particular, buoyancy effects and conjugate heat transfer need to be included. Different channel geometries can also be investigated by means of LES in to find an optimum geometry in terms of pressure drop and heat transfer. Eventually, optimization algorithms can be employed to maximize the aero-thermal performance of the rotating channel. Nevertheless, an optimization corresponding to the present numerical setup would lead to a relatively large computational cost, even if the simulated domain is restricted to a rib pitch. In order to reduce the computational cost, alternative turbulence models need to be addressed. The experimental velocity and heat transfer results delivered in the present work are actually a solid data base that can be used for CFD validation and code comparison.

Bibliography

[1] M. P. Boyce. *Gas Turbine Engineering Handbook, 4th Edition*. Butterworth-Heinemann, 2011.

[2] A. García. *Diseño de motores de aviación comercial*. Aeropuertos Españoles y Navegación Aérea (AENA), 2008.

[3] N. T. Birch. 2020 Vision: The Prospects for Large Civil Aircraft Propulsion. In *22nd Congress of the International Council of the Aeronautical Sciences*, Harrogate International Conference Centre, United Kingdom, August-September 2000.

[4] F. Haselbach and R. Parker. Hot End Technology for Advanced, Low Emission Large Civil Aircraft Engines. In 28th *Congress of the International Council of the Aeronautical Sciences*, Brisbane, Australia, September 2012.

[5] Rolls-Royce Holdings Limited. Rolls-Royce Trent XWB augmented reality application. `https://itunes.apple.com/WebObjects/MZStore.woa/wa/viewSoftware?id=988798634&mt=8`, June 2015.

[6] J. D. Mattingly. *Elements of Propulsion: Gas Turbines and Rockets*. AIAA Education Series, Virginia, 2006.

[7] E. Torenbeek and H. Wittenberg. *Flight Physics*. Springer Netherlands, 2009.

[8] N. Cumpsty. *Jet Propulsion*. Cambridge University Press, Cambridge, 2001.

[9] S.A. International Consolidated Airlines Group. Annual report and accounts 2015, March 2016.

[10] B. Pearce. Economic performance of the airline industry. Mid-year report, International Air Transport Association, 2016.

[11] D. Unger and H. Herzog. Comparative Study on Energy R&D Performance: Gas Turbine Case Study. Technical report, Energy Laboratory, Massachusetts Institute of Technology, 08 1998.

[12] S. J. Donachie M. J. Donachie. *Superalloys: A Technical Guide*. ASM International, Ohio, 2002.

[13] T. A. Auxier. The importance of cooling technology in propulsion & power systems. In *Proceedings of the RTO AVT Symposium, held in Loen, Norway*, May 2001.

[14] R. S. Bunker. Cooling design analysis. In National Energy Technology Lab U.S. Dept. of Energy, Office of Fossil Energy, editor, *The Gas Turbine Handbook*, 2006.

[15] P. Ligrani. Heat Transfer Augmentation Technologies for Internal Cooling of Turbine Components of Gas Turbine Engines. *International Journal of Rotating Machinery*, 20(3):493–499, 2013.

[16] J. C. Han, S. Dutta and S. Ekkad. *Gas turbine Heat Transfer and Cooling Technology*. Taylor & Francis, London, 2012.

[17] R. S. Bunker. Turbine heat transfer and cooling: An overview. In *Proceedings of the ASME Turbo Expo 2013, paper GT2013-94174*, San Antonio, TX, USA, 6 2013.

[18] Rolls-Royce Holdings Limited. Rolls-Royce Trent 1000 augmented reality application. `https://itunes.apple.com/us/app/rolls-royce-trent-1000-augmented/id988737956?mt=8`, June 2015.

[19] D. K. Lezius and J. P. Johnston. The structure and stability of turbulent wall layers in rotating channel flow. Report MD 29, Stanford University, 08 1971.

[20] R. Kristoffersen and H. I. Andersson. Direct simulations of low-reynolds-number turbulent flow in a rotating channel. *Journal of Fluid Mechanics*, 256:163–197, 11 1993.

[21] J. P. Johnston, R. M. Halleen, and D. K. Lezius. Effects of spanwise rotation on the structure of two-dimensional fully developed turbulent channel flow. *Journal of Fluid Mechanics*, 56:533–557, 12 1972.

[22] J. P. Johnston. Effects of system rotation on turbulence structure: a review relevant to turbomachinery flows. *International Journal of Rotating Machinery*, 4(2):97–112, 1998.

[23] W. Sha, K. Tsuchiya, and K. Nakabayashi. The linear stability of thermally stratified rotating channel flow. *Physics of Fluids*, 11(2):439–449, 1999.

[24] T. J. Hajek, J. H. Wagner, B. V. Johnson, A. W. Higgins, and G. D. Steuber. Effects of rotation on coolant passage heat transfer. Volume 1: Coolant passages with smooth walls. NASA Contractor Report 4396, Vol.I, National Aeronautics and Space Administration, 09 1991.

[25] B. V. Johnson, J. H. Wagner, and G. D. Steuber. Effects of rotation on coolant passage heat transfer. Volume 2: Coolant passages with trips normal and skewed to the flow. NASA Contractor Report 4396, Vol.II, National Aeronautics and Space Administration, 10 1993.

[26] J. P. Bons and J. L. Kerrebrock. Complementary velocity and heat transfer measurements in a rotating cooling passage with smooth walls. *Journal of Turbomachinery*, 121(4):651–662, 1998.

[27] M. Elfert, M. Schroll, and W. Förster. Piv measurement of secondary flow in a rotating two-pass cooling system with an improved sequencer technique. *Journal of Turbomachinery*, 134(3):031001–1–031001–12, 7 2011.

[28] A. Armellini, L. Casarsa, and C. Mucignat. Flow field analysis inside a gas turbine trailing edge cooling channel under static and rotating conditions. *International Journal of Heat and Fluid Flow*, 32(6):1147 – 1159, 2011.

[29] L. Furlani, A. Armellini, and L. Casarsa. Rotational effects on the flow field inside a leading edge impingement cooling passage. *Experimental Thermal and Fluid Science*, 76:57 – 66, 2016.

[30] A. Di Sante. *Time Resolved PIV Measurements of Low Reynolds Number Flow in Rotating Channels*. PhD thesis, von Karman Institute for Fluid Dynamics and Università Politecnica delle Marche, 2007.

[31] A. Di Sante, Raf Theunissen, and R. A. Van den Braembussche. A new facility for time-resolved piv measurements in rotating channels. *Experiments in Fluids*, 44(2):179–188, 2008.

[32] F. Coletti, T. Maurer, T. Arts, and A. Di Sante. Flow field investigation in rotating rib-roughened channel by means of particle image velocimetry. *Experiments in Fluids*, 52(4):1043–1061, 2012.

[33] F. Coletti, D. Lo Jacono, I. Cresci, and T. Arts. Turbulent flow in rib-roughened channel under the effect of coriolis and rotational buoyancy forces. *Physics of Fluids*, 26(4), 2014.

[34] G. Rau, M. Çakan, D. Moeller, and T. Arts. The effect of periodic ribs on the local aerodynamic and heat transfer performance of a straight cooling channel. *Journal of Turbomachinery*, 120(2):368–375, 1998.

[35] L. Casarsa and T. Arts. Experimental investigation of the aerothermal performance of a high blockage rib-roughened cooling channel. *Journal of Turbomachinery*, 127(3):580–588, 2005.

[36] S. Abdel-Wahab and D. K. Tafti. Large eddy simulation of flow and heat transfer in a 90 deg ribbed duct with rotation: Effect of coriolis and centrifugal buoyancy forces. *Journal of Turbomachinery*, 126(4):627–636, 12 2004.

[37] H. Iacovides. Computation of flow and heat transfer through rotating ribbed passages. *International Journal of Heat and Fluid Flow*, 19(5):393–400, 1998.

[38] A. K. Saha and S. Acharya. Unsteady RANS simulation of turbulent flow and heat transfer in ribbed coolant passages of different aspect ratios. *International Journal of Heat and Mass Transfer*, 48(23 and 24):4704 – 4725, 2005.

[39] A.K. Sleiti and J.S. Kapat. Effect of coriolis and centrifugal forces on turbulence and transport at high rotation and density ratios in a rib-roughened channel. *International Journal of Thermal Sciences*, 47(5):609 – 619, 2008.

[40] A. Murata and S. Mochizuki. Large eddy simulation with a dynamic subgrid-scale model of turbulent heat transfer in an orthogonally rotating rectangular duct with transverse rib turbulators. *International Journal of Heat and Mass Transfer*, 43(7):1243 – 1259, 2000.

[41] A. Murata and S. Mochizuki. Aiding and opposing contributions of centrifugal buoyancy on turbulent heat transfer in a two-pass transverse- or angled-rib-roughened channel with sharp 180° turns. *International Journal of Heat and Mass Transfer*, 47(17 and 18):3721 – 3743, 2004.

[42] E. A. Sewall and D. K. Tafti. Large eddy simulation of flow and heat transfer in the developing flow region of a rotating gas turbine blade internal cooling duct with coriolis and buoyancy forces. *Journal of Turbomachinery*, 130(1):011005–1–011005–7, 12 2007.

[43] R. Fransen, L. Vial, and L. Y. M. Gicquel. Large eddy simulation of rotating ribbed channel. In *Proceedings of the ASME Turbo Expo 2013, paper GT2013-95076*, San Antonio, TX, USA, 6 2013.

[44] D. Borello, A. Salvagni, and K. Hanjalić. Effects of rotation on flow in an asymmetric rib-roughened duct: LES study. *International Journal of Heat and Fluid Flow*, 55:104–119, 2015.

[45] S. Kubacki, J. Rokicki, and E. Dick. Simulation of the flow in a ribbed rotating duct with a hybrid k-ω RANS/LES model. *Flow, Turbulence and Combustion*, 97(1):45–78, 2016.

[46] Q.-Q. Xun and B.-C. Wang. Hybrid RANS/LES of turbulent flow in a rotating rib-roughened channel. *Physics of Fluids*, 28(7), 2016.

[47] V. D. Narasimhamurthy and H. I. Andersson. Turbulence statistics in a rotating ribbed channel. *International Journal of Heat and Fluid Flow*, 51:29 – 41, 2015.

[48] E. Buckingham. On physically similar systems; illustrations of the use of dimensional equations. *Phys. Rev.*, 4:345–376, Oct 1914.

[49] R. D. Thulin, D. C. Howe, and I. D. Singer. Energy efficient engine high-pressure turbine detailed design report. NASA Contractor Report 165608, National Aeronautics and Space Administration, 1 1982.

[50] P.T. Lott, I. Lepot, E. Chérière, F. Thirifay, K. Semmler, and L. Bénet. Internal cooling channels design investigations: Aerothermal optimisation of ribbed u-bends. In *Proceedings of the ASME Turbo Expo 2013, paper GT2013-95545*, San Antonio, TX, USA, 6 2013.

[51] R. Theunissen, A. Di Sante, M. L. Riethmuller, and R. A. Van den Braembussche. Confidence estimation using dependent circular block bootstrapping: application to the statistical analysis of piv measurements. *Experiments in Fluids*, 44(4):591–596, 2008.

[52] F. Coletti, I. Cresci, and T. Arts. Spatio-temporal analysis of the turbulent flow in a ribbed channel. *International Journal of Heat and Fluid Flow*, 44:181 – 196, 2013.

[53] I. Mayo, G. L. Gori, A. Lahalle, and T. Arts. Aerothermal characterization of a rotating ribbed channel at engine representative conditions: Part I– high resolution PIV measurements. *Journal of Turbomachinery*, 138(10), 2016.

[54] D. W. Holder R. C. Pankhurs and. *Wind Tunnel Technique*. Pitman & Sons, London, 1952.

[55] J. Scheiman. Comparison of experimental and theoretical turbulence reduction characteristics for screens, honeycomb and honeycomb-screens combinations. TP 1958, NASA, 1981.

[56] C. Farell and S. Youssef. Experiments on turbulence management using screens and honeycombs. *ASME Journal of Fluids Engineering*, 118:26–32, 1996.

[57] H. M. Nagib R. I. Loehrke, R. I. Experiments on management of free-stream turbulence. Report No. 598, AGARD, 1972.

[58] P. S. Klevanoff G. B. Schubauer, W. G. Spangenburg. Aerodynamic characteristics of damping screens. TN 2001, NACA, 1950.

[59] G. Casterman. Conception d'un convergent rod-carre pur soufflerie et verification experimentale de l'uniformite de l'encoulement. Stagiaire Report 2003-39, von Karman Institute, 2003.

[60] R. J. Adrian and J. Westerweel. *Particle Image Velocimetry*. Cambridge University Press, Cambridge, New York, 2011.

[61] M. Raffel, C. E. Willert, S. Wereley, and J. Kompenhans. *Particle Image Velocimetry*. Springer-Verlag, 2nd edition, 2007.

[62] R. J. Adrian. Particle-imaging techniques for experimental fluid mechanics. *Annual Review of Fluid Mechanics*, 23:261–304, 1991.

[63] R. J. Adrian. Twenty years of particle image velocimetry. *Experiments in Fluids*, 39:159–169, 2005.

[64] F. Scarano and M. L. Riethmuller. Iterative multigrid approach in piv image processing with discrete window offset. *Experiments in Fluids*, 26:513–523, 1999.

[65] Nikon Corp. Af nikkor 50mm f/1.8d specifications.

[66] Canon Inc. Canon ef 50mm f/1.4 usm specifications. `http://www.canon.co.uk/lenses/ef-50mm-f-1-4-usm-lens/specification.aspx`.

[67] S. T. Wereley, L. Gui, and C. D. Meinhart. Advanced algorithms for microscale particle image velocimetry. *AIAA Journal*, 40(60):1047–1055, 2002.

[68] F. Scarano and M. L. Riethmuller. Advances in iterative multigrid piv image processing. *Experiments in Fluids*, 29:S51–S60, 2000.

[69] L. Casarsa. *Aerodynamic Performance Investigation of a Fixed Rib-Roughened Internal Cooling Passage*. PhD thesis, von Karman Institute for Fluid Dynamics and Università degli Studi di Udine, 2003.

[70] A. K. Prasad. Stereoscopic particle image velocimetry. *Experiments in Fluids*, 29(2):103–116, Aug 2000.

[71] P T Ireland and T V Jones. Liquid crystal measurements of heat transfer and surface shear stress. *Measurement Science and Technology*, 11(7):969, 2000.

[72] N. Abdullah, A. R. Abu Talib, A. A. Jaafar, M. A. Mohd Salleh, and W. T. Chong. The basics and issues of thermochromic liquid crystal calibrations. *Experimental Thermal and Fluid Science*, 34(8):1089 – 1121, 2010.

[73] B. Cukurel, C. Selcan, and T. Arts. Color theory perception of steady wide band liquid crystal thermometry. *Experimental Thermal and Fluid Science*, 39:112 – 122, 2012.

[74] R. Wiberg and N. Lior. Errors in thermochromic liquid crystal thermometry. *Review of Scientific Instruments*, 75(9):2985–2994, 2004.

[75] Y. Rao and Y. Xu. Liquid crystal thermography measurement uncertainty analysis and its application to turbulent heat transfer measurements. *Advances in Condensed Matter Physics*, 2012:Article ID 898104 (8 pages), 2012.

[76] M. Çakan. *Aero-thermal Investigation of Fixed Rib-roughened Internal Cooling Passages*. PhD thesis, von Karman Institute for Fluid Dynamics and Université Catholique de Louvain, 2000.

[77] F. Coletti. *Coupled Flow Field and Heat Transfer in an Advanced Internal Cooling Scheme*. PhD thesis, von Karman Institute for Fluid Dynamics and Universität Stuttgart, 2010.

[78] I. Mayo, G. L. Gori, A. Lahalle, and T. Arts. Aerothermal characterization of a rotating ribbed channel at engine representative conditions: Part II âĂŤ detailed LCT measurements. *Journal of Turbomachinery*, 138(10), 2016.

[79] K. Batchelder and R.J. Moffat. Towards a method for measuring heat transfer in complex 3-d flows. Technical Report TSD 108, Stanford University, 1997.

[80] W.H. McAdams. *Heat transmission*. McGraw-Hill series in chemical engineering. McGraw-Hill, 1954.

[81] F.W. Dittus and L.M.K. Boelter. Heat transfer in automobile radiators of the tubular type. 2(13), 1930.

[82] Test Uncertainty. Standard, American Society of Mechanical Engineers, New York, NY, U.S.A., 2005.

[83] Uncertainty of measurement – Part 3: Guide to the expression of uncertainty in measurement (GUM:1995). Standard, International Organization for Standardization, Geneva, CH, 2008.

[84] Measuring and Test Equipment Specifications – NASA Measurement Quality Assurance Handbook âĂŞ ANNEX 2 . Standard, National Aeronautics and Space Administration, Washington DC, U.S.A., July 2010.

[85] Measurement of fluid flow by means of pressure differential devices inserted in circular cross-section conduits running full. Standard, International Organization for Standardization, Geneva, CH, 2003.

[86] P. M. Kodzwa and J. K. Eaton. Heat Transfer Coefficient Measurements on the Film-Cooled Pressure Surface of a Transonic Airfoil. *Journal of Turbomachinery*, 135(6):061011–061011–16, September 2013.

[87] C. Camci. Liquid crystal thermography on the fluid solid interface of rotating systems. In *Temperature Measurements, von Karman Institute for Fluid Dynamics Lecture Series 1996-09*, April 1996.

[88] A. Murata and S. Mochizuki. Effect of rib orientation and channel rotation on turbulent heat transfer in a two-pass square channel with sharp 180 DEG turns investigated by using large eddy simulation. *International Journal of Heat and Mass Transfer*, 47(12 and 13):2599 – 2618, 2004.

[89] P. Sagaut. *Large Eddy Simulation for Incompressible Flows: an Introduction*. Springer-Verlag Berlin Heidelberg, 2006.

[90] S. B. Pope. *Turbulent flows*. Cambridge Univ. Press, Cambridge, 2011.

[91] J. P. A. J. van Beeck U. Piomelli, C. Benocci, editor. *Large Eddy Simulation: Theory and Applications*, volume 2016-01 of *VKI Lecture Series*, Rhode-Saint-Genese, Belgium, 2016. von Karman Institute for Fluid Dynamics.

[92] S. V. Patankar, C. H. Liu, and E. M. Sparrow. Fully developed flow and heat transfer in ducts having streamwise-periodic variations of cross-sectional area. *Journal of Heat Transfer*, 99(2):180–186, 1977.

[93] W.-W. Kim and S. Menon. A new dynamic one-equation subgrid-scale model for large eddy simulations. In *Proceedings of the 33rd Aerospace Sciences Meeting and Exhibit, paper AIAA 95-0356*, Reno, NV, USA, 1 1995.

[94] A. Yoshizawa. Bridging between eddy-viscosity-type and second-order turbulence models through a two-scale turbulence theory. *Phys. Rev. E*, 48:273–281, Jul 1993.

[95] D. K. Lilly. A proposed modification of the germano subgridâĂŘscale closure method. *Physics of Fluids A*, 4(3):633–635, 1992.

[96] P. Moin, K. Squires, W. Cabot, and S. Lee. A dynamic subgridâĂŘscale model for compressible turbulence and scalar transport. *Physics of Fluids A*, 3(11):2746–2757, 1991.

[97] E. A. Sewall and D. K. Tafti. Large eddy simulation of flow and heat transfer in the developing flow region of a rotating gas turbine blade internal cooling duct with coriolis and buoyancy forces. *Journal of Turbomachinery*, 130(1):011005–011005–7, 2007.

[98] S. B. Pope. Ten questions concerning the large-eddy simulation of turbulent flows. *New Journal of Physics*, 6:35, march 2004.

[99] J. Smagorinsky. General circulation experiments with the primitive equations. *Monthly Weather Review*, 91(3):99–164, 1963.

[100] The OpenFOAM Foundation Ltd. `http://openfoam.org/`, 2016. [Online; accessed December-2016].

[101] H. G. Weller, G. Tabor, H. Jasak, and C. Fureby. A tensorial approach to computational continuum mechanics using object-oriented techniques. *Computers in Physics*, 12(6):620–631, 1998.

[102] OpenFOAMWiki. `https://openfoamwiki.net/index.php/OpenFOAM_guide/The_PIMPLE_algorithm_in_OpenFOAM/`, 2016. [Online; accessed December-2016].

[103] D. J. Tritton. Turbulence in rotating fluids. In P. H. Roberts and A. M. Soward, editors, *Rotating Fluids in Geophysics*, pages 105–138. Academic, 1978.

[104] S. V. Ekkad and J. C. Han. Detailed heat transfer distributions in two-pass square channels with rib turbulators. *International Journal of Heat and Mass Transfer*, 40(11):2525 – 2537, 1997.

[105] K. M. Kim, Y. Y. Kim, D. H. Lee, D. H. Rhee, and H. H. Cho. Influence of duct aspect ratio on heat/mass transfer in coolant passages with rotation. *International Journal of Heat and Fluid Flow*, 28(3):357 – 373, 2007.

[106] J. Jeong and F. Hussain. On the identification of a vortex. *Journal of Fluid Mechanics*, 285:69–94, 1 1995.

[107] M. Lohász, P. Rambaud, and C. Benocci. Flow features in a fully developed ribbed duct flow as a result of miles. *Flow, Turbulence and Combustion*, 77(1):59–76, 2006.

[108] F. P. Incropera, D. P. DeWitt, T. L. Bergman, and A. S. Lavine. *Fundamentals of Heat and Mass Transfer*. John Wiley & Sons, Inc., New York City, New York, 6th edition edition, 2007.